Interaction entre deformation et percolation de magma ou de fluide dans le manteau à l'aplomb des zones de subduction

Vincent Soustelle

UNIVERSITÉ MONTPELLIER II
SCIENCES ET TECHNIQUES DU LANGUEDOC

THÈSE
Pour obtenir le grade de

DOCTEUR DE L'UNIVERSITÉ MONTPELLIER II

Discipline : Structure et évolution de la Terre et des autres planètes
École Doctorale : SIBAGHE

Présentée et soutenue publiquement

Par

Vincent Soustelle

Le 2 Décembre 2010

Interaction entre déformation et percolation de magma ou de fluide dans le manteau à l'aplomb des zones de subductions

JURY

Michel Grégoire	Chargé de recherche (LDTP-OMP)	Examinateur
Ben Holtzman	Assistant research professor (LDEO)	Rapporteur
David Mainprice	Directeur de recherche (Géosciences Montpellier)	Examinateur
Karel Schulmann	Professeur (IPG Strasbourg)	Rapporteur
Andréa Tommasi	Directrice de recherche (Géosciences Montpellier)	Directrice de thèse

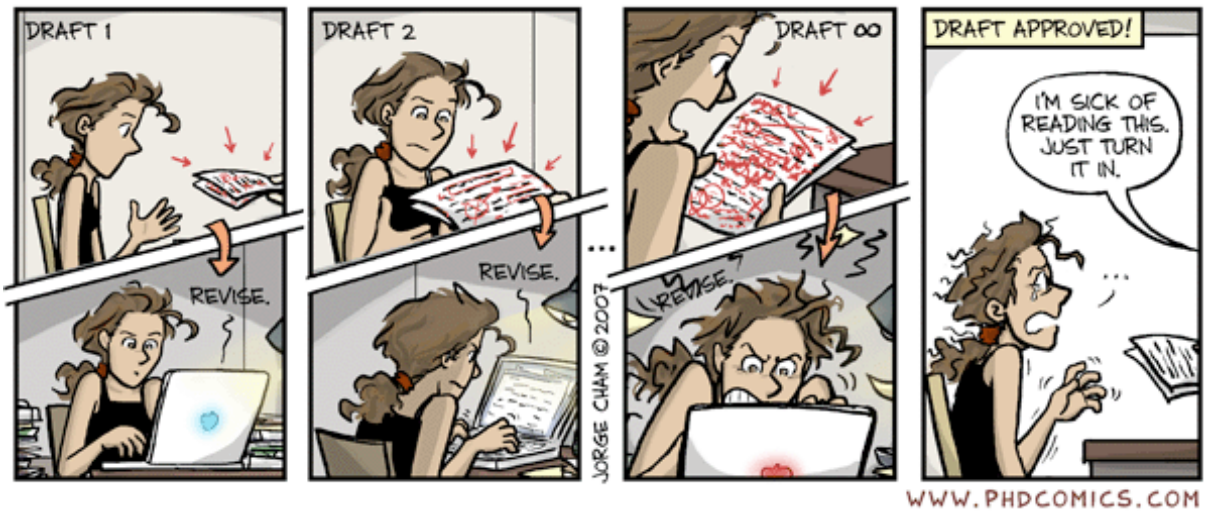

« En Science, la phrase la plus excitante que l'on peut entendre, celle qui annonce de nouvelles découvertes, ce n'est pas "Eurêka" mais "c'est drôle". » Isaac Asimov

Remerciements

Pour m'avoir supporter depuis le stage de master 2, pour tout ce qu'elle m'a enseigné, pour avoir cru en moi et soutenu, pour sa disponibilité, et pour tous les moments agréables que nous avons partagés, la première personne que je tiens à remercie énormément pour cette thèse ma est directrice de thèse **Andréa Tommasi**. Grâce à elle, mes années de thèse ont été géniales, je ne regrette rien et si on me demande de résigner, je le ferais sans hésiter! J'espère que cette relation durera encore longtemps et que nous continuerons à collaborer dans le futur.

Je tiens à remercier **David Mainprice, Michel Grégoire, Ben Holtzman et Karel Schulmann** d'avoir accepter d'être mes examinateurs ou rapporteurs, et d'avoir pris de leur temps pour s'intéresser à mes travaux de thèse.

De toutes les personnes avec qui ont collaborés à ma thèse, je tiens à remercier en premier **Sylvie Demouchy** qui s'est énormément investie, particulièrement lors de la dernière année où elle m'a initié et donner gout à l'expérimental. Je la remercie aussi pour ses nombreuses relectures. Mais tout le temps que nous avons passé ensemble n'a pas toujours été tout rose, nos deux mauvais caractères ont été à l'origine de nombreuses engueulades qui n'ont pourtant jamais réussies à entacher nôtre bonne entente. Je remercie **Alain Vauchez** pour nos nombreuses discussions, qu'elles aient été scientifiques ou pas, pour tous les bons moments de rigolade qu'on a partagé, et pour son ordinateur (promis je te le rendrais en partant). Merci aussi à **Jean-Louis Bodinier**, **Carlos Garrido, Dmitri Ionov et Leander Franz** (même si nous ne nous sommes jamais rencontrés) pour leur collaboration. Je remercie aussi **Christophe Nevado** grâce qui j'ai toujours pu avoir de superbes lames minces en temps et en heure.

Je tiens aussi à remercier l'ensemble de **l'équipe Manteau-Noyau** du laboratoire Géosciences Montpellier qui m'a permis de faire ma thèse dans une ambiance très agréable. Je pense surtout au nombre de gâteaux que nous avons partagés durant les pauses café, et pendant lesquelles j'ai souvent eu tendance à exposer ma vie privée. J'espère d'ailleurs que certains détails seront vite oubliés.

Je remercie tous les enseignants que j'ai eus durant mon parcours universitaire, avec une pensée particulière pour **Phillipe Laurent** grâce à qui je me suis passionné pour la géologie, ainsi que pour **Jean-Marie Dautria** et **André Leyreloup** qui m'ont permis de ne plus douter de cette passion. Ce n'est que plus tard, lors du master, qu'**Alain, Andréa** et **Jean-louis** ont éveillé ma curiosité pour les processus mantelliques.

Je remercie bien entendu toute ma famille, et surtout mon frère **Julien** et mes parents **Marc** et **Jocelyne**. Tout au long de mes études ils m'ont soutenu financièrement et moralement. Le fait qu'ils aient toujours cru en ma réussite a vraiment été d'une grande aide dans les moments difficiles. Réussir cette thèse est donc une façon pour moi de les remercier de tous leurs efforts durant ces années.

J'en arrive maintenant à remercier tous mes potes. Tout d'abord mon compère **Thibault Candela** avec qui on se tire la bourre sur tous les plans depuis le master mais avec qui on se marre bien. Toujours de bon conseil (à part pour les filles), nous nous sommes toujours soutenus mutuellement durant nôtre thèse et particulièrement sur la fin. Grâce à facebook, nous avons pu garder une vie sociale (même virtuelle) durant les derniers mois alors que nous bossions de nuit. Aller Tibo fini vite qu'on puisse s'en payer une tranche, assis peinard à la terrasse d'un café en train de mater des gonzesses. Et n'oublie pas l'objectif ultime: finir l'alphabet! Je remercie aussi mon pote **Johan** avec qui nous avons partagé tant de murges sur Montpellier durant toutes ces années que je ne m'en rappelle même pas de la moitié. Grâce à toi poulet ma vie montpelliéraine fut douce et tranquille. Je remercie aussi **Jos** mon ami de toujours et pour encore longtemps. Je fais aussi un bisou à mes grands copains de thèse **Dr Knoll**, **MatMond,** et **Lara** avec qui je me suis bien amusé au labo et en dehors. Je remercie bien entendu mes deux cher co-bureaux. Il y a eu tout d'abord **Marion** avec qui nous formions le bureau des râleurs, puis **MikeB,** certe plus calme mais pas moins râleur. C'est la personne avec qui j'ai passer le plus de temps ces deux dernières année donc là Mike je te dis un grand merci. Et si je pars, surtout ne pleure pas, soit fort et essaie d'être gentil avec ton prochain co-bureau.

Je souhaite bonne chance pour la suite à mes amis thésard du cristal2plate **Roberto**, **Kate** et **Erwin.** Courages les gars! Maman veille sur vous! Un conseil : aimez le manteau, et le manteau vous le rendra bien…

Je tiens aussi à remercier tous les thésards, post-docs, ATER de Géosciences et d'ailleurs avec qui j'ai fait un bout de chemin, qui ont terminer avant moi, ou terminerons

plus tard: **Bruno, Flo, Théo, Clémence, Pierre, Titou, Zoltan, Karoly, Claudio, Ductile Shear, Francis, Mag, Tom, Philou, Luiz, Véro, Camille** etc.… Évidement j'en oublie plein, mais ne vous sentez pas lésé, je pense aussi à vous.

Parmi les gens qui m'ont fait passer d'agréables moments durant cette thèse je n'oublie pas de remercier **Eric, Laurent, Romain, Julie, Mickeal, Medhi, Alex et les autres de la bande,** toute **la Compagnie Mercès, les Arlesiens et les Saint Martinois** (Promis les gars, j'essaie de plus raté de férias).

Je tiens aussi à remercier les principaux "sponsors" de ma vie montpelliéraine qui sont: **La Barrique** (merci Olive!!), **l'alternatif**, **La Distillerie** et bien sur le **LoveStore.**

Pour finir, je remercie Célia…

Table des matières

Résumé :

Ce travail apporte de nouvelles contraintes sur les interactions entre déformation et processus d'hydratation et de percolation de magma ou de fluides dans le manteau à l'aplomb d'une zone de subduction et leurs implications sur les propriétés sismiques dans le coin mantellique. Il se base sur l'analyse de péridotites à spinelle provenant du massif de Ronda (Espagne) et deux séries de xénolites issues de zones de subduction actives (Kamchatka, Papouasie-Nouvelle-Guinée). L'étude structurale, pétrologique et géochimique de ces échantillons montrent qu'ils ont subit une percolation réactive de magma ou de fluide synchrone d'une déformation de haute température basse contrainte cohérente avec les condition PT de la base de la lithosphère ou de l'asthénosphère. Cette percolation réactive est responsable d'un enrichissement en pyroxènes, qui est souvent localisé dans des bandes parallèles à la foliation. Cet enrichissement est associé à une dispersion de l'orientation cristallographique de l'olivine. Les systèmes de glissement dominant dans l'olivine sont dans tous les cas {0kl}[100], ce qui implique que la direction de polarisation rapide des ondes S dans la partie supérieure du coin mantellique est parallèle à la direction d'écoulement dans le manteau. La décroissance de l'intensité des OPR de l'olivine associée à l'enrichissement en pyroxènes a pour conséquence une réduction non négligeable de l'anisotropie sismique qui peut induire jusqu'à 33% d'erreur sur l'interprétation de l'épaisseur de la couche anisotrope. Un enrichissement en orthopyroxène peut aussi entraîner une baisse du rapport Vp/Vs, mais ne peut expliquer les rapports Vp/Vs <1,7 cartés dans certains avant-arcs. Cependant de telles valeurs peuvent être expliquées si l'anisotropie des péridotites du coin mantellique est prise en compte. Les analyses par spectroscopie infra-rouge montrent que les olivines des deux séries de xénolites étudiées contiennent moins d'eau que la saturation théorique calculée pour leurs températures d'équilibre dans le domaine du spinelle. Ces faibles concentrations en eau sont similaires à celles observées dans les olivines des péridotites à spinelle des autres zones de subduction. Elles enregistrent probablement la faible solubilité de l'eau dans l'olivine à des pressions relativement basses et la déshydratation au cours de l'exhumation des xénolites. Ces teneurs en eau mesurées ainsi que les estimations de la saturation théorique ne sont pas suffisantes pour changer la direction de glissement dominante dans l'olivine de [100] à [001].

MOTS CLÉS: olivine, pyroxène, déformation, OPR, subduction, coin mantellique, percolation réactive, fluides, magma, propriétés sismiques.

Abstract

This work provides new constraints on the interactions between deformation and percolation of melt or fluids, as well as on the implications of these processes for the seismic properties of the mantle wedge. It is based on the analysis of spinel peridotites from the massif of Ronda (Spain) and two xenolith suites from active subduction zones (Kamchatka, Papua New Guinea). A coupled structural, petrological and geochemical study of these samples shows that they underwent a reactive percolation of melts or Si-rich fluids, which was synchronous to a deformation event occurring under high temperature and low stress conditions, consistent with the PT conditions at the base of the lithosphere or in the asthenosphere. This reactive percolation is responsible for enrichment in pyroxenes, mainly orthopyroxene, which is often localized in bands parallel to the high-temperature foliation. This enrichment is associated with grain size reduction and dispersion of the crystallographic orientation of olivine. The dominant slip system in olivine is {0kl}[100], which results in fast S-wave polarization parallel to the flow direction in the mantle. The decrease in the intensity of the olivine crystal preferred orientations associated with the enrichment in pyroxene results in significant decrease of the anisotropy that may induce an underestimation of the thickness of the anisotropic layer by up to 33%. The observed orthopyroxene enrichment also lowers the Vp/Vs ratio, but cannot explain Vp/Vs < 1.7 mapped locally in the fore-arc mantle in Japan and the Andes. Such low Vp/Vs ratios may however be explained by considering the intrinsic anisotropy of the peridotites, which is generally ignored in large-scale Vp/Vs ratio mapping of the mantle wedge. Infrared analyses show that olivine from the both xenolith collections contains less water than the theoretical saturation calculated for their estimated equilibrium temperature in the spinel stability field. These low water content are similar to those observed in spinel peridotites from other subduction zones and probably record both the low solubility of water in olivine at relatively low pressure and dehydration during exhumation of the xenoliths. These measured water contents as well as theoretical saturation estimations are not sufficient to change the dominant slip direction of in olivine from [100] to [001].

KEYWORDS: olivine, pyroxene, deformation, CPO, subduction, mantle wedge, reactive percolation, fluids, melt, seismic properties.

Chapitre 1

Introduction

1.1. Introduction générale

1.1.1. Subduction et tectonique des plaques

La subduction est un processus fondamental de la tectonique des plaques qui témoigne de l'activité interne de la Terre. Le terme "subduction" désigne l'enfoncement d'une portion de plaque lithosphérique sous une autre. Dans plus de 80% des cas, la plaque subduite est d'origine océanique, on parle alors de "subduction océanique" qui diffère en de nombreux points de la moins fréquente "subduction continentale".

Au cours de son accrétion, la Terre a emmagasiné une immense quantité de chaleur et elle continue à en produire principalement par la présence d'éléments radioactifs dans les roches du manteau. Cette chaleur interne est évacuée de différentes manières : conduction, convection et radiation. Dans le manteau terrestre, la température est assez importante (d'environs 700 °C à 30 km de profondeur à 3500°C à 2900 km de profondeur) et les vitesses de déformation faibles (de 10^{-11} à 10^{-14} s^{-1}) ce qui induit la déformation ductile des minéraux du manteau. À l'échelle de plusieurs millions d'années, le manteau peut donc être considéré comme un fluide visqueux. Ce comportement mécanique et la différence de température entre la surface (quelques degrés Celsius) et la base du manteau provoquent une évacuation de la chaleur interne par convection. La couche limite supérieure de ce système, où le transfert de chaleur se fait par conduction, est la lithosphère. Comme la viscosité des roches dépend exponentiellement de l'inverse de la température, cette couche supérieure a un comportement mécanique rigide; elle constitue les plaques tectoniques. Les panaches mantelliques qui forment les points chauds observés en surface correspondent aux courants convectifs ascendants et l'enfouissement des plaques lithosphériques par subduction représentent les courants descendants des cellules de convection. Le processus d'accrétion lithosphérique aux dorsales océaniques reste localisé dans le manteau supérieur, correspondant ainsi à une remontée passive compensant le flux descendant dans les zones de subductions dans un système avec une source de chaleur interne dû à la production radiogénique dans le manteau convectif (Fig. 1.1).

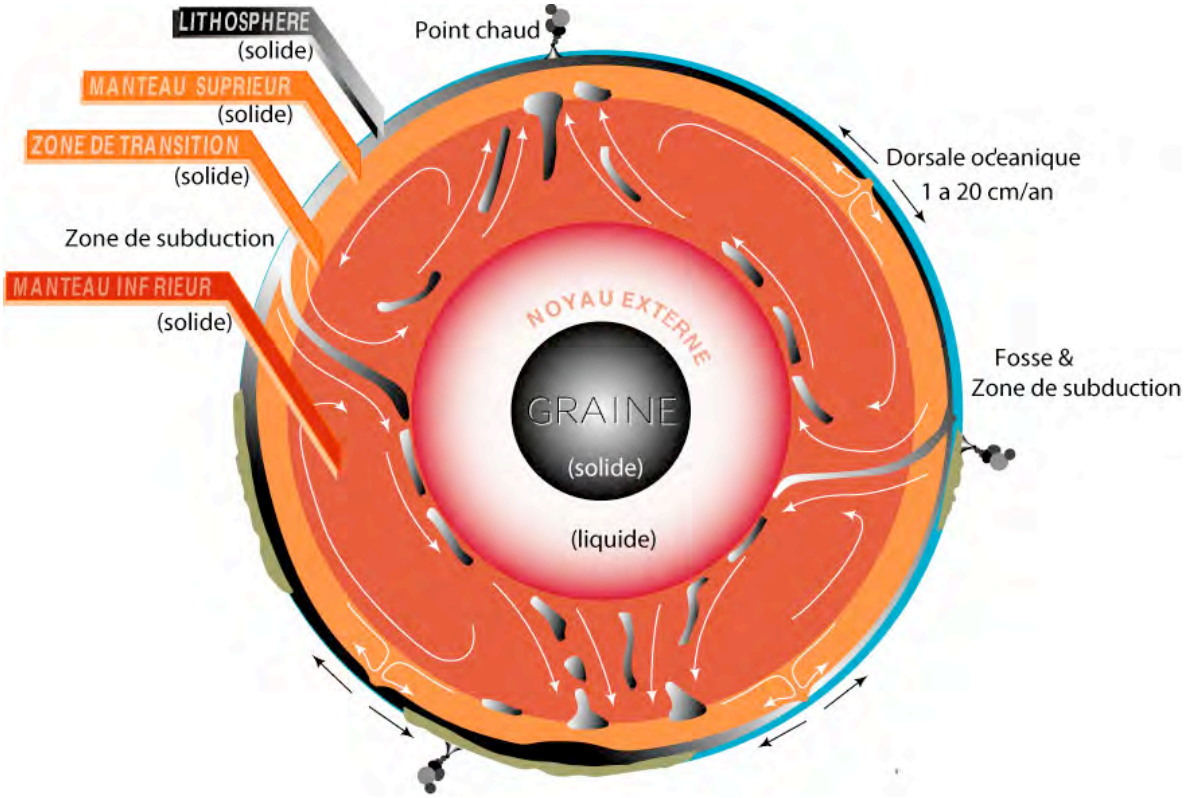

Figure 1.1 : Schéma illustrant la structure interne de la Terre avec les courants de convection affectant l'ensemble du manteau.

Au même titre que les failles transformantes et les dorsales océaniques, les zones de subduction sont donc des frontières de plaques. Cependant, la force exercée par la descente de plaque subduite dans le manteau serait au moins deux fois supérieure à l'extension au niveau d'une dorsale océanique (e.g., Forsyth & Uyeda, 1975; Schellart, 2004). Les forces associées aux zones de subduction constituent donc le principal moteur de la tectonique des plaques. Ces zones concentrent la majeure partie de l'activité sismique sur Terre dont les séismes les plus violents ayant des conséquences directes ou indirectes, comme les tsunamis, sur les hommes et leurs habitats (Fig. 1.2.). Les zones de subductions sont également le lieu d'une intense activité volcanique et concentrent aussi les éruptions les plus violentes et les plus destructrices. Elles jouent d'ailleurs un rôle essentiel dans la formation des continents (Stern, 2002). Les zones de subduction permettent enfin le recyclage des plaques océaniques et l'enfouissement à des grandes profondeurs d'une partie des sédiments transportés par ces dernières dans le manteau; contrôlant le cycle de l'eau et du carbone dans la Terre. Toutes ces caractéristiques font des zones de subductions un sujet primordial étudié par tous les domaines des sciences de la Terre, que ce soit dans un but sociétal ou purement fondamental.

1.1.2. Structures des zones de subduction océaniques

Une zone de subduction est formée par trois domaines: les plaques lithosphériques, supérieure et inférieure (celle qui est subduite), et le coin mantellique. Ce dernier correspond à la partie convective du manteau supérieur (l'asthénosphère) serré entre la plaque subduite et la plaque supérieure (Fig. 1.3.). En surface, une subduction se caractérise par la présence d'une fosse océanique pouvant atteindre une dizaine de kilomètres de profondeur (~12 km pour la fosse des Mariannes) et par la formation d'un prisme d'accrétion dû à l'accumulation des sédiments tractés par la plaque inférieure contre la plaque supérieure. Cette dernière porte généralement un arc volcanique situé entre 100 et 500 km de la fosse en fonction de la géométrie de la subduction (Lallemand, 1999). Une subduction en contexte compressif provoque, sur la plaque supérieure, la formation d'une chaîne de montagne, alors qu'en contexte extensif se forme un bassin d'arrière-arc, souvent caractérisé par un centre d'accrétion de lithosphère océanique au niveau d'une dorsale (Fig. 1.3.).

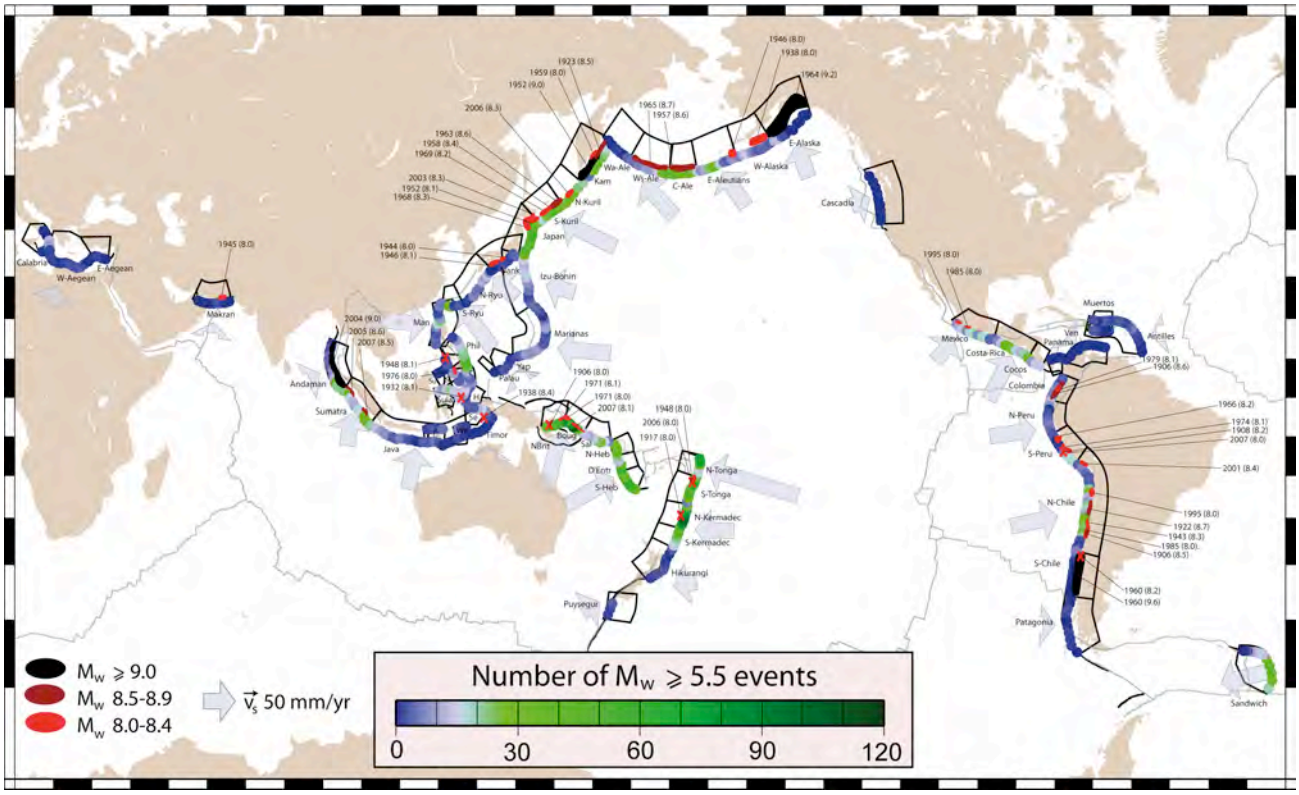

Figure 1.2. : Localisation des séismes de magnitude ≥ 5,5 dans les zones de subduction depuis 1976, ainsi que les zone de rupture pour tous les séismes de magnitude ≥8 depuis 1900 (ellipses noires et rouges). Les flèches bleues correspondent aux vitesses de subduction. Figure d'après (Heuret et al., soumis).

Les roches de la plaque océanique inférieure, c'est-à-dire, la croûte océanique et une partie du manteau lithosphérique, ont été hydratées depuis leur création à la dorsale. Lors de leur enfouissement, un métamorphisme de basse température et haute pression provoque la formation de nouveaux minéraux dont la structure cristalline plus dense ne permet plus l'intégration de fluides, ceux-ci, en partie composés de H_2O et OH^-, sont donc expulsés. Cette réaction de déstabilisation induisant une déshydratation se produit massivement entre 70 et 300 km de profondeur, en fonction du gradient géothermique de la plaque subduite. La présence d'hydrogène dans une matrice rocheuse abaisse son solidus (Yoder & Tilley, 1962), ce qui provoque la fusion des péridotites de l'asthénosphère formant ainsi les magmas qui vont donner naissance aux arcs volcaniques. Ces derniers sont positionnés parallèlement à la fosse et situés à une distance qui dépend de l'angle de la plaque plongeante, ce qui corrobore l'influence de la libération de H_2O par la plaque subduite sur la fusion partielle dans le manteau. La présence de fluides ou de magma dans une matrice rocheuse affecte également les mécanismes de déformation et donc sa rhéologie, ainsi que d'autres propriétés physiques, comme la conduction électrique. De nombreuses études expérimentales ou numériques ont analysé ces interactions et leurs impacts sur la dynamique mantellique (Blacic, 1972; Mackwell et al., 1985 ; Karato et al., 1986; Hirth & Kohlstedt, 1995a; Hirth & Kohlstedt, 1995b ; Mei & Kohlstedt, 2000a; Mei & Kohlstedt, 2000b; Honda et al., 2002; Mei et al., 2002; Gerya & Yuen, 2003; Zimmerman & Kohlstedt, 2004; Arcay et al., 2006; Cagnioncle et al., 2007; Currie et al., 2008). Ce mémoire, basé sur l'étude d'échantillons naturels, discute l'effet de la percolation de fluides et de magmas sur les mécanismes de déformation du coin mantellique supérieur, à l'interface lithosphère-asthénosphère, et son impact sur les propriétés sismiques du coin mantellique.

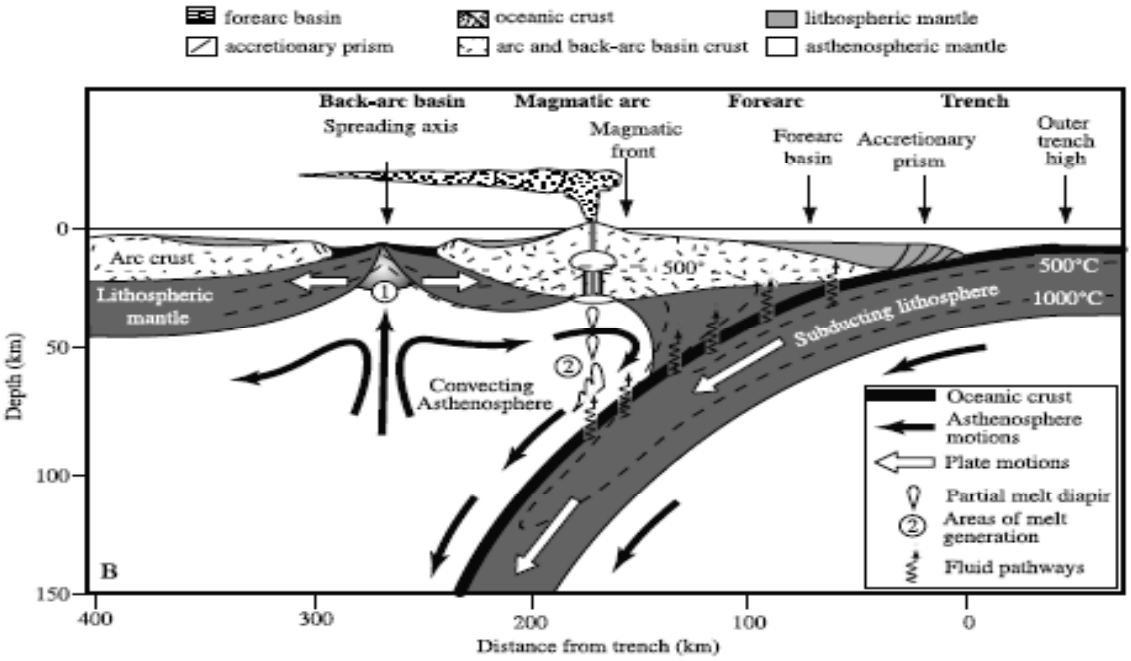

Figure 1.3. : Coupe schématique d'une zone de subduction intra-océanique d'après Stern (2002). Le régime tectonique de la plaque supérieure est en extension.

1.1.3. Les outils d'étude du coin mantellique

Le coin mantellique des zones de subduction peut être étudié par différentes approches/méthodes. Beaucoup d'entre-elles sont indirectes et les observations directes restent rares. La sismologie est la méthode la plus efficace pour observer, imager et comprendre la structure et la dynamique du coin mantellique à petite comme à grande échelle. C'est par exemple par l'observation d'une bande de sismicité inclinée dans le manteau supérieur, le plan de Wadati-Benioff (Wadati, 1928; Wadati, 1935; Benioff, 1949), que le processus de subduction a en partie été démontré. Par l'observation des anomalies de vitesses sismiques, des mesures d'atténuation ou des rapports de vitesses des ondes de compression et cisaillement, les méthodes de tomographie permettent d'imager la structure thermique d'une zone de subduction, les anomalies de densité, et la présence de fluides ou de magma dans le manteau. L'étude de l'anisotropie sismique permet de carter les flux mantelliques et d'étudier la déformation du manteau à grande échelle. Les fluides ayant une forte influence sur les propriétés physiques des roches du manteau (voir les chapitres 1.2.2 et 1.2.3), l'interprétation des observations sismiques dans le coin mantellique reste toutefois délicate. L'analyse des laves issues du volcanisme d'arc constitue un autre moyen indirect de contraindre la composition du coin mantellique et les caractéristiques des fluides responsables de la fusion de l'asthénosphère. En effet, la composition de ces laves dépend de la composition de la

source mantellique, de la nature des fluides responsables de la fusion, mais aussi des processus d'interactions pétrologiques et chimiques entre le magma et les roches qu'il a percolées. Enfin, les échantillons d'ultra-haute pression exhumés (éclogite) dans les zones de sutures des chaînes de montagne fournissent aussi d'importants renseignements sur les réactions métamorphiques qui se produisent lors de l'enfouissement de la plaque subduite, ainsi que sur les mécanismes d'expulsion des fluides. À toutes ces méthodes indirectes, il faut aussi ajouter l'apport de la pétrologie, géochimie et déformation expérimentale, ainsi que les résultats des modélisations numériques et analogiques.

L'un des moyens direct de comprendre le coin mantellique est l'étude des xénolites de roches mantelliques remontés par les magmas d'arc dans des zones de subduction. Ils permettent d'étudier directement la composition chimique et minéralogique ainsi que la déformation du coin mantellique. Cependant, ces roches sont rares, généralement petites (au maximum plusieurs dizaines de centimètres) et surtout elles ne sont pas « en place ». Tout cela pose donc le problème de la représentativité de ces échantillons ponctuels du coin mantellique.

Tous ces outils d'observation ont des avantages et des inconvénients. Ils apportent tous des informations importantes, qui, une fois combinées, permettent d'établir des interprétations robustes sur la dynamique du coin mantellique.

1.2. Les processus d'interaction fluide-roche dans le coin mantellique.

1.2.1. Les fluides, magmas et réactions dans le coin mantellique.

Déshydratation de la plaque plongeante et hydratation du coin mantellique

Le magmatisme d'arc résulte en partie de l'hydratation du coin mantellique par les fluides aqueux expulsés par la plaque subduite. L'eau interstitielle contenue dans les pores et les fractures va être évacuée par simple compaction dès les premiers kilomètres d'enfouissement de la lithosphère dans le manteau. L'augmentation de pression et de température lors de l'enfouissement va ensuite provoquer une série de réactions de déshydratation successives. Les premiers minéraux hydratés qui vont se déstabiliser sont le talc, la chlorite et l'amphibole contenus dans la croûte océanique métamorphisée, ils se déstabilisent au-delà de 5 GPa (Fig. 1.4; Poli & Schmidt, 2002). Le phlogopite subsiste à plus grande profondeur, et se déstabilise entre 6,5 et 11 GPa selon le régime thermique de la

plaque plongeante (Kawamoto, 2006). Une partie de l'eau issue de ces réactions de déstabilisation peut serpentiniser les péridotites de la base du coin mantellique qui sont entraînées par la plaque subduite. On retrouve donc dans ces péridotites, ainsi que dans celles de la plaque plongeante altérée, un phyllosilicate très riche en eau: l'antigorite (12 poids % d'H_2O). Elle se déstabilisée entre 2,5 et 6 GPa selon la température (Kawamoto, 2006). La plaque subduite devrait donc être presque totalement déshydratée entre 175 et 300 km de profondeur selon le régime thermique du coin mantellique.

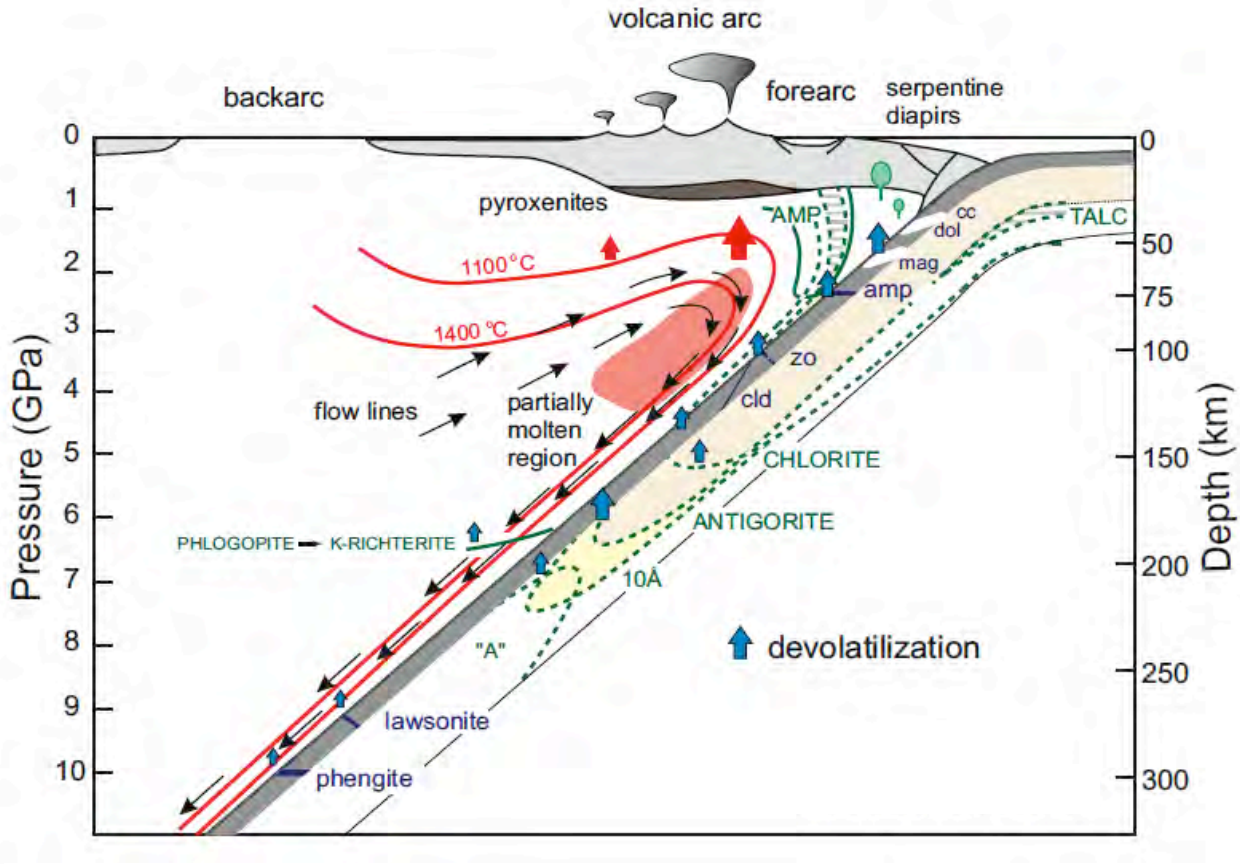

Figure 1.4 : Schéma d'une subduction "chaude" montrant les domaines de stabilité des minéraux hydratés et la zone supposée de fusion partielle. D'après Poli & Schmidt, 2002

Le transport d'eau dans le coin mantellique est fortement dépendant de l'angle dièdre de mouillage entre le fluide aqueux et les cristaux. Si cet angle est inférieur à 60°, une percolation diffuse est possible (Figure 1.5). L'angle dièdre entre l'olivine et un fluide aqueux change de >60° à <60° à 1 et 3 GPa pour des températures de, respectivement, 1200 et 1000°C (Watson et al., 1990; Mibe et al., 1998; Mibe et al., 1999). Cette variation est due au changement de composition du fluide aqueux en fonction de la pression et de la température (Mibe et al., 1998; Mibe et al., 1999). À haute pression, les fluides issus de la déshydratation

vont donc pouvoir circuler verticalement, alors qu'à plus basse pression, ils vont être bloqués et participer à la cristallisation de minéraux hydratés. Les fluides aqueux seront ensuite relâchés lorsque ces phases, entraînées par le flux mantellique descendant (entraînement par le mouvement de la plaque plongeante), seront à leur tour au-delà de leur champ de stabilité. Ce processus est appelé le transport d'eau latéral (Davies & Stevenson, 1992).

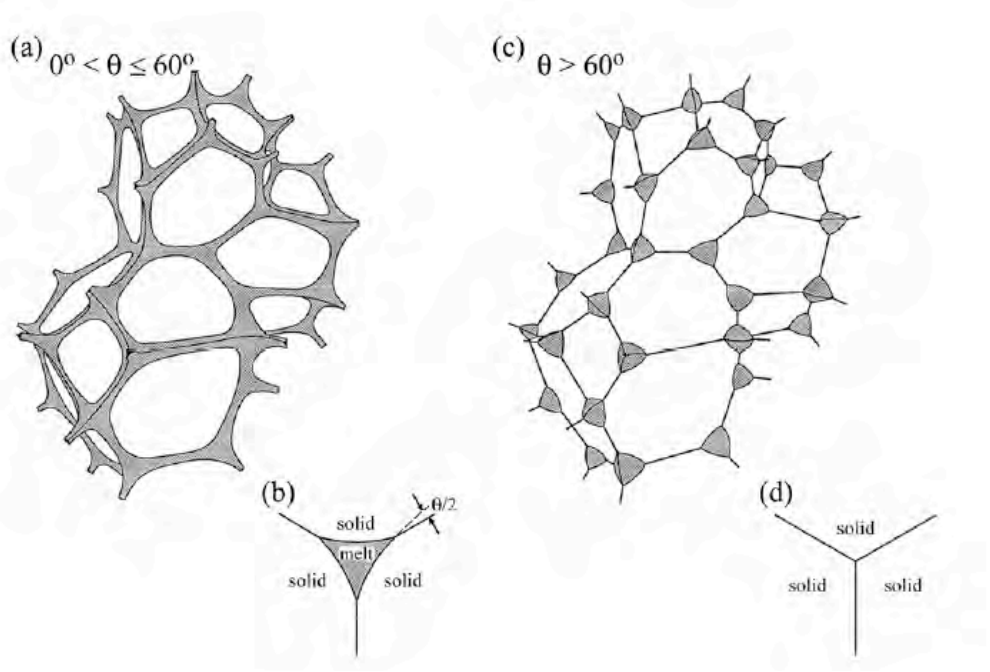

Figure 1.5 : Schéma de la distribution du magma (melt sur la figure) dans une roche partiellement fondue pour des énergies d'interface isotropes. (a) l'angle dièdre θ est compris entre 0 et 60° ; le magma mouille tous les joints triples et quadruples. (c) l'angle dièdre θ est supérieur à 60° ; le magma est confiné au dans les joints quadruple. (b) et (c) sont des coupe au niveau des joints triples pour, respectivement, les cas (a) et (b). Figure d'après Riley & Kohlstedt (1990).

L'eau expulsée dans le coin mantellique par les réactions de déshydratation successives qui affectent la plaque plongeante et les péridotites de la base du coin mantellique peut donc être stockée de trois manières différentes : (1) par la serpentinisation de la partie avant arc du coin mantellique, (2) par la cristallisation de minéraux hydratés néoformés et (3) par l'intégration d'hydrogène en infime quantité (quelque ppm) dans les minéraux « dits » anhydres (NAMs : nominally anhydrous minerals). La cristallisation de minéraux hydratés néoformés dans les péridotites du manteau supérieur ne se produit que lorsque les NAMs sont saturés en hydrogène. Il reste alors de l'eau libre contenu dans les fluides supercritiques ou des magmas hydratés qui va pouvoir former de l'amphibole (pargasite) ou du phlogopite en fonction de la composition et des conditions de pression et de température.

Une partie de cette eau sera évacuée vers la surface dans les magmas d'arc. L'hydratation d'une péridotite abaisse son solidus (Yoder & Tilley, 1962), ce qui implique la formation d'une zone de fusion partielle au-dessus de la plaque subduite dont l'extension verticale est contrôlée par le régime thermique dans le coin mantellique. La zone principale d'hydratation du manteau et donc de fusion partielle se situe alors au-dessus de la plaque subduite entre 75 et 125 km de profondeur (Fig. 1.4). La fusion hydratée des péridotites du coin mantellique produit en grande majorité des magmas de composition tholéithique ou calco-alcaline. Les premiers sont caractérisés par un enrichissement continu en fer depuis les basaltes jusqu'aux termes intermédiaires (andésites), alors que les seconds présentent une décroissance précoce et continue de la concentration en fer au cours de la différenciation.

Percolation de magmas dans le manteau

La migration des magmas dans le manteau se fait par différents processus physiques. Un premier processus est la fracturation hydraulique, qui entraine la formation de dykes (Weertman, 1971; Nicolas, 1986). Cependant, le volume minimum de magma doit d'être important afin que la pression hydrostatique devienne supérieure à la pression lithostatique (e.g., Spence & Turcotte, 1985; Spence et al., 1987; Sleep, 1988) et provoque la fracturation des roches sus-jacentes. Ce processus se produit logiquement dans la lithosphère plus froide et plus rigide. À plus haute température, dans l'asthénosphère, le magma percole par flux poreux diffus à travers une matrice polycristalline visqueuse. Dans ce régime, du fait de la relaxation des contraintes de la matrice par des processus de fluage de haute température, les forces imposées par le magma ne sont jamais suffisamment importantes pour produire de la fracturation (Kohlstedt & Holtzman, 2009). Ce type de migration peut aboutir à la ségrégation des magmas. Cette dernière peut résulter de trois processus différents:

(1) des vagues de compaction-décompaction induites par le couplage entre déformation viscoélastique et porosité du solide et flux de fluide, qui produit une alternance de zones à haute et faible porosité (e.g., Drew, 1983; McKenzie, 1984; Ribe, 1986; Spiegelman, 1993; Connolly & Podladchikov, 1998; Connolly & Podladchicov, 2007).

(2) un déséquilibre chimique entre le magma et la matrice rocheuse menant à une réaction. Si cette réaction produit une augmentation de porosité, elle peut mener à une instabilité qui grandit jusqu'à former un chenal de haute perméabilité (e.g.,McKenzie, 1984; Richter and McKenzie, 1984; Kelemen et al., 1995; Kelemen et al., 1997).

(3) une interaction entre la migration des magmas et la déformation de l'agrégat cristallin. Le liquide est alors ségrégé et auto-organisé en bandes riches en magma dont

l'orientation et géométrie est guidée par le champ de contraintes (e.g.,Stevenson, 1989; Hall & Parmentier, 2000; Holtzman et al., 2003a; Holtzman et al., 2003b; Holtzman & Kohlstedt, 2007; King et al., 2010).

Le métasomatisme

Le coin mantellique des zones de subduction est le lieu d'une intense percolation de fluides aqueux ou de magma. Ces liquides n'étant pas forcement en équilibre chimique ou pétrologique avec la péridotite encaissante, cette percolation peut produire un métasomatisme cryptique ou modal. Dans le premier cas, il se produit seulement un échange d'éléments chimiques, alors que dans le second cas, l'échange est si important qu'il produit une modification de la composition minéralogique de la péridotite. C'est ce dernier qui nous intéresse particulièrement dans cette étude. Un premier exemple de métasomatisme modal correspond aux réactions entre les fluides aqueux et les roches du coin mantellique entraînant la formation de minéraux hydratés comme la phlogopite et l'amphibole. L'étude des xénolites extraites par des volcans d'arc montre que le métasomatisme modal dans les zones de subduction se traduit essentiellement par un enrichissement conséquent en orthopyroxène, clinopyroxène, et, de façon mineure, en amphibole et phlogopite (e.g.,Arai and Kida, 2000; Gregoire et al., 2001; McInnes et al., 2001; Arai et al., 2003; Grégoire et al., 2007; Ionov et al., 2007; Ishimaru et al., 2007; Ionov, 2010). La cristallisation de pyroxènes aux dépens de l'olivine dans ces péridotites est due à la réaction entre les péridotites réfractaires du coin mantellique et des fluides aqueux riches en SiO_2 ou des magmas siliceux riches en H_2O (aux pressions du manteau il n'est actuellement pas possible de différencier les deux, (Kawamoto et al., 2004). Ces fluides peuvent aussi contenir selon les cas, des teneurs variables en Al, Ca, Na et/ou K.

1.2.2. Effets sur la rhéologie et les mécanismes de déformation du coin mantellique

Dans la section précédente, nous avons vu que le coin mantellique dans les zones de subduction est affecté par un grand nombre de processus pétrologiques allant de la déshydratation du matériel subduit à l'hydratation et la fusion partielle des péridotites, ainsi qu'aux réactions entre ces fluides et les péridotites percolées. Dans ces zones, le manteau asthénosphérique est aussi soumis à des mouvements convectifs, les roches du coin mantellique sont donc intensément déformées. Cette section propose un bref résumé de l'état des connaissances sur l'effet de la percolation de magma et la présence d'eau sur la rhéologie et les mécanismes de déformation du manteau.

Effet sur la rhéologie

L'olivine est le minéral dominant dans le manteau supérieur, il est généralement admis que sa rhéologie contrôle celle du manteau supérieur. Pour un agrégat cristallin, elle peut être décrite par une loi de puissance semi-empirique où la vitesse de déformation ($\dot{\varepsilon}$) est dépendante de la contrainte déviatorique σ (Hirth & Kohlstedt, 2003):

$$\dot{\varepsilon} = A\sigma^n d^{-p} f H_2O^r e^{(\alpha\phi)} e^{(-\frac{E^* + PV^*}{RT})} \quad (1)$$

A est une constante pour le solide donné, *n* est l'exposant de la contrainte, *d* est la taille de grain, *p* est l'exposant de la taille de grain, fH_2O est la fugacité d'eau, *r* est l'exposant de la fugacité, ϕ est la fraction de magma, α est une constante, *E** est l'énergie d'activation, *V** est le volume d'activation, *P* est la pression, *R* est la constante des gaz rares, et *T* est la température absolue. La déformation ductile des cristaux se fait selon deux mécanismes : le fluage diffusion et le fluage dislocation. Pour des conditions thermodynamiques données, la rhéologie d'un agrégat d'olivine correspond à la combinaison des lois de ces deux mécanismes de déformation. On écrit alors la relation suivante :

$$\dot{\varepsilon} = \dot{\varepsilon}_{diffusion} + \dot{\varepsilon}_{dislocation} \quad (2)$$

L'équation (1) permet d'identifier l'effet des différents paramètres thermodynamiques sur la rhéologie de l'agrégat cristallin. Cette équation prédit une baisse de viscosité lorsque la fugacité d'eau, la proportion de magma ou la température augmentent ou que la pression ou taille de grain baisse. Pour cette étude, ce sont principalement les effets de la présence de fluides et d'eau sur la rhéologie du manteau qui nous intéressent.

Des études expérimentales sur la déformation des péridotites montrent en effet que la présence de faibles proportions de magma et l'incorporation d'eau dans l'olivine baisse significativement la résistance mécanique des roches du manteau supérieur de plusieurs ordres de grandeur (Blacic, 1972; Mackwell et al., 1985; Karato et al., 1986; Hirth & Kohlstedt, 1995a; Hirth & Kohlstedt, 1995b; Mei & Kohlstedt, 2000a; Mei & Kohlstedt, 2000b; Mei et al., 2002; Zimmerman & Kohlstedt, 2004). Des expériences en laboratoire montrent également que l'incorporation d'eau dans NAMs tels que l'olivine (Hier-Majumder et al., 2004; Demouchy et al., 2007; Costa & Chakraborty, 2008), ou la présence d'une faible proportion de magma interconnecté favorisent les processus contrôlés par la diffusion ionique comme la restauration des dislocations (Karato et al., 1993), la recristallisation (Avé-Lallemant & Carter, 1970; Jung & Karato, 2001b) et la croissance de grains (Karato, 1989).

Ces résultats sont cohérents avec les études récentes sur des xénolites de péridotites ou des massifs péridotitiques, qui suggèrent que la percolation de magmas en conditions statiques ou dynamiques modifie les microstructures et la distribution de la déformation dans les péridotites (e.g., Vauchez & Garrido, 2001; Tommasi et al., 2006; Le Roux et al., 2008; Tommasi et al., 2008).

Effet sur les orientations préférentielles de réseau (OPR) de l'olivine

Lorsque l'olivine se déforme par fluage dislocation dans les conditions de pression et température du manteau supérieur les systèmes de glissement activés sont {0kl}[100] et {hk0}[001]. Cependant l'activation préférentielle d'un de ces systèmes par rapport aux autres dépend des conditions de pression, température, contrainte déviatorique, fugacité d'oxygène et de la présence de magma. Dans le manteau supérieur, sous condition anhydres et sans magma, à basse (<1000°C) et à haute température (>1000°C) ce sont, respectivement, les systèmes de glissement avec des vecteurs de Burgers [001] et [100] qui dominent (Durham et al., 1977; Bai et al., 1991). Dans l'asthénosphère et la base de la lithosphère, les axes [100] de l'olivine auront donc tendance à s'orienter parallèlement à la direction d'écoulement dans le manteau. Cependant, des études expérimentales suggèrent que la présence d'eau ou de magma peut provoquer un changement de l'orientation préférentielle de réseau (OPR) de l'olivine qui montre un alignement préférentiel des axes [001], au lieu des axes [100], dans la direction de fluage (Jung and Karato, 2001a; Holtzman et al., 2003b; Jung et al., 2006). Dans le premier cas, cette variation résulte d'un changement de direction de glissement dominante (Jung et al., 2006), alors que dans le second cas elle est due à un phénomène de partitionnement de la déformation entre les domaines riches et pauvres en magma (Holtzman et al., 2003b). Quoiqu'il en soit, ces variations d'OPR dues à la présence d'eau ou de magma n'ont jamais été concrètement observées dans des échantillons naturels. Des OPR qui peuvent résulter de l'activation préférentielle de systèmes [001]{hk0} ont été décrites dans plusieurs études (Mizukami et al., 2004; Skemer et al., 2006; Tasaka et al., 2008) et attribuées à une déformation dans des conditions hydratées. Cependant, elles sont toujours observées dans des péridotites à grenat associées à des éclogites, donc le changement de système de glissement peut aussi résulter de l'augmentation de la pression (e.g., Mainprice et al., 2005).

1.2.3. Effets sur les propriétés sismiques du manteau

La percolation de fluides ou de magmas et l'hydratation des péridotites dans le coin mantellique ont un impact important sur la composition du manteau et sur sa déformation. Ces processus peuvent avoir un effet non négligeable sur les propriétés sismiques du manteau. La compréhension de cet effet est donc essentielle pour l'interprétation des données sismologiques en termes de structure du coin mantellique. Cette section résume les effets de la présence de magma ou de fluide, d'eau et des variations de composition sur les propriétés sismiques du manteau.

Effets sur les vitesses sismiques et sur l'atténuation

Des expériences sur des péridotites à haute pression et température ont montré que les vitesses des ondes P et S baissent fortement dès qu'un faible pourcentage (2%) de magma est présent (e.g., Sato et al., 1989). Cette réduction est bien plus importante pour les ondes S que pour les ondes P impliquant des rapports Vp/Vs élevés dans les zones de fusion partielle. Ces variations sont aussi dépendantes de la forme des inclusions magmatiques dans l'agrégat. Du magma, même en très faible quantité, organisé sous forme de films micrométriques ou selon de fines fractures orientés produit une réduction considérable de la vitesse des ondes S, alors que des inclusions de forme sphérique ont un impact plus faible (O'Connell & Budianski, 1974; Mavko, 1980; Schmeling, 1985; Takei, 1998; Takei, 2000).

L'atténuation sismique mesure la décroissance d'amplitude des ondes sismiques due à l'absorption d'énergie dans un milieu anélastique. Elle augmente en présence de magma, cependant pour des faibles fractions de liquide (<5%), elle reste moins significative que si l'on a des anomalies de haute proches du solidus (Schmeling, 1985; Hammond & Humphreys, 2000). La présence de faibles quantités d'eau dans les minéraux composant les péridotites augmente aussi fortement leur anélasticité, ce qui provoque une hausse de l'atténuation et une baisse des vitesses sismiques (Karato and Jung, 1998; Karato, 2002). Les anomalies de hautes températures ou la présence d'eau peuvent provoqué la même atténuation. Par exemple, entre 50 et 100 km de profondeur, une augmentation de température de 100 °C ou l'incorporation d'environs 30 ppm en poids d'OH dans l'olivine augmente l'atténuation d'un ordre de grandeur. La présence d'eau à un effet similaire sur les ondes P et S; elle n'a donc que très peu d'influence sur les rapport Vp/Vs (Jacobsen et al., 2008). Enfin, les variations de composition ont un effet très limité sur l'atténuation et les vitesses sismiques (Sobolev et al., 1996), mais elles sont détectables en utilisant les rapports Vp/Vs, car elles affectent de façon différente les ondes P et S (e.g., Wagner et al., 2006).

En conclusion, les anomalies de température, la concentration en l'eau, ou la présence de magma produisent toutes une décroissance des vitesses sismiques et une augmentation de l'attenuation. Pour identifier une zone de fusion partielle dans le manteau, il faut donc combiner différents observables sismiques, plus particulièrement l'atténuation et les vitesses sismiques des ondes P et S. Le magma a un effet plus important sur les ondes S que sur les ondes P, et un très faible impact sur l'atténuation selon la proportion de phase liquide. Les zones de fusion partielle montreront donc de forts rapports Vp/Vs et de forte atténuation dans les zones de fusion partielle, mais elle sera plus faible dans les zones de transport de magma.

Effets sur l'anisotropie sismique

L'anisotropie sismique définit la dépendance entre les vitesses des ondes sismiques et leur direction de propagation ou de polarisation. Elle peut avoir différentes origines: une alternance de différentes couches isotropes (e.g., Backus, 1965), des fractures orientées remplies par du magma ou des fluides (e.g., Crampin & Booth, 1985; Kendall, 1994), ou l'OPR des minéraux anisotropes, tel que l'olivine dans le manteau (e.g., Hess, 1964; Nicolas & Christensen, 1987; Silver & Chan, 1988; Mainprice & Silver, 1993; Ben Ismail & Mainprice, 1998).

Les données d'anisotropie sismique dans les zones de subduction, principalement obtenues à partir de l'analyse de la biréfringence des ondes S, montrent que la direction de polarisation de l'onde S rapide est soit perpendiculaire soit parallèle à la fosse (Figure 1.6). Ce travail étant focalisé sur le coin mantellique, nous allons réviser ci-dessous les processus produisant une anisotropie sismique dans cette région du manteau.

Dans l'asthénosphère, un agrégat d'olivine se déforme en acquérant une OPR où les axes [100] ont tendance à s'orienter parallèlement à la direction de fluage du manteau. Les cas où les directions rapides de propagation et de polarisation des ondes sismiques sont perpendiculaires à la fosse peuvent donc être expliqués par la déformation du coin mantellique dû à la subduction.

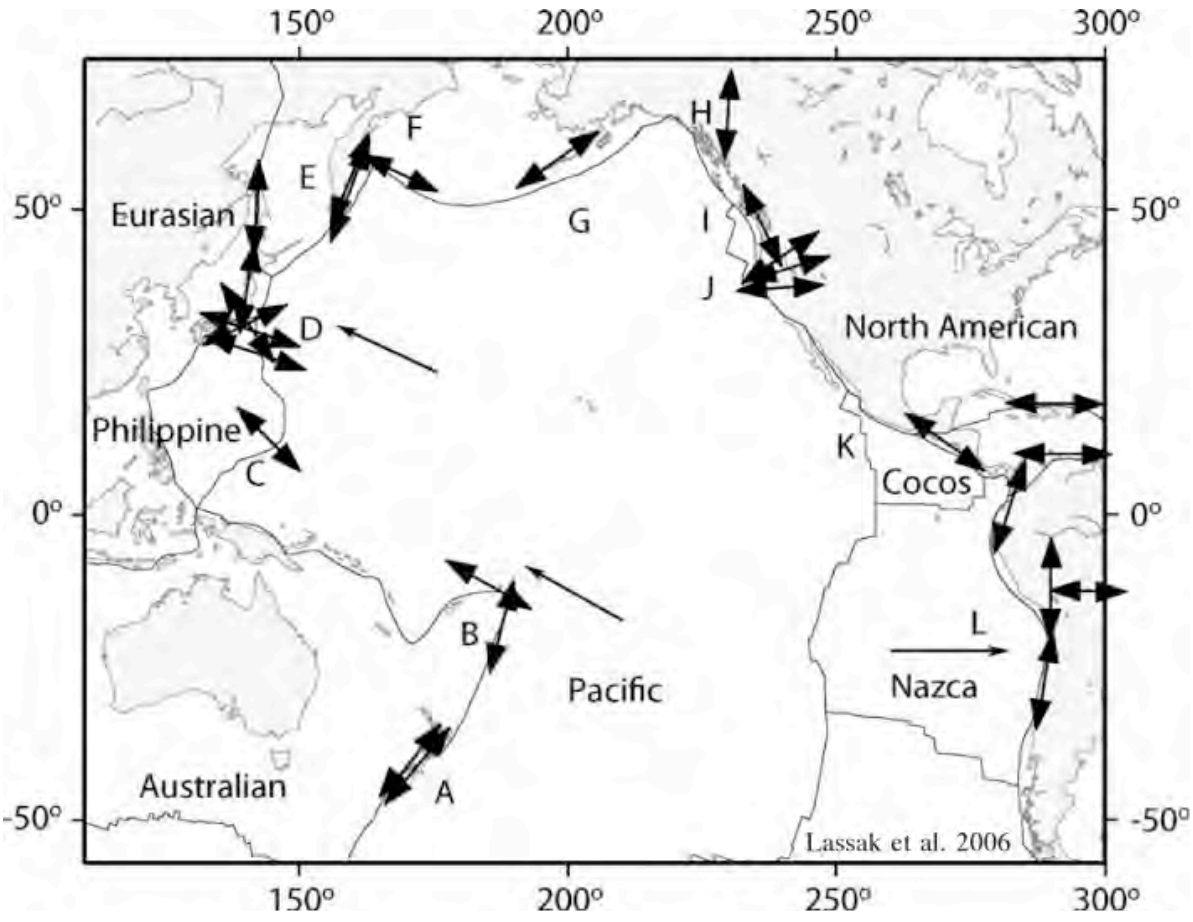

Figure 1.6 : Direction de polarisation rapide moyenne des ondes S (doubles flèches) au niveau des zones de subduction péri-Pacifique. D'après Lassak et al. (2006).

Pour les directions rapides parallèles à la fosse, plusieurs explications sont possibles:

- Si la plaque en subduction à des bords libres et qu'elle est soumise à des mouvements horizontaux (retrait ou avancée), l'asthénosphère est alors soumise à des mouvements toroïdaux pouvant être localement parallèles à la fosse (e.g., Buttles & Olson, 1998; Peyton et al., 2001; Funiciello et al., 2003; Levin et al., 2004).
- Le changement de système de glissement de l'olivine dû à la présence d'eau (Jung et al., 2006; Karato et al., 2008) ou de magma (Holtzman et al., 2003b) menant à une orientation des axes [001] et des axes [100], respectivement, parallèlement et perpendiculairement à la direction de fluage du manteau.
- La présence de magma ou de fluides dans des dykes, fractures ou chenaux alignés parallèlement à la fosse (e.g., Greve & Savage, 2008; Greve & Savage, 2009).
- La géométrie de la plaque en subduction joue un rôle important sur le fluage du coin mantellique. Kneller & van Keken (2008) ont démontré que, pour un faible pendage (>15°) ou un courbure importante de la plaque subduite, un flux de manteau oblique ou normal à la fosse pouvait créer des linéation dans le manteau parallèles à la fosse.

Ceci induit donc une direction de propagation et de polarisation rapide des ondes sismiques parallèle à la fosse.

- La flexion de la plaque subduite provoque la formation de fractures sub-verticales dans sa croûte et son manteau supérieur. Ces fractures sont scellées par des minéraux très anisotropes (serpentines, talc). L'orientation de ces fractures ainsi que les délais de temps de temps d'arrivé des ondes S provoquées par ce modèle concordent avec les données d'anisotropie sismique mesurées dans de nombreuses zones de subduction (Faccenda et al., 2008).
- Lors de l'hydratation de la plaque en subduction et du coin mantellique, de l'antigorite cristallise aux dépens de l'olivine. L'antigorite cristallise en formant des lamelles orientées parallèlement au plan (100) de l'olivine. Étant donné que l'olivine, dans le manteau déformé, montre le plus souvent une OPR ou les plan (100) sont parallèles à la linéation. Les lamelles formant le réseaux cristallin de l'antigorite cristallisent alors préférentiellement perpendiculairement à la direction de fluage. Dans l'antigorite, la direction de polarisation rapide des ondes S est parallèle à ces lamelles. Cette dernière sera alors parallèle à la direction longitudinale de la fosse dans les zones de subduction et l'anisotropie sera corrélée au degré de serpentinisation (Boudier et al., 2010).

1.3. Objectif de la thèse et structure du mémoire

L'objectif de cette étude est de comprendre comment les processus d'hydratation et de percolation de magma ou de fluides affectent la déformation et les propriétés sismiques du coin mantellique à partir de l'analyse d'échantillons naturels: un massif de péridotites (Ronda, Espagne) et deux séries de xénolites issues de zones de subduction actives (Kamchatka, Papouasie-Nouvelle-Guinée). En effet, jusqu'à maintenant cette question a été abordée presque uniquement par l'intermédiaire d'études expérimentales. La présente étude se base donc sur l'observation des structures et microstructures de ces péridotites, ainsi que sur la mesure d'orientations préférentielles du réseau cristallin (OPR) et de la concentration en eau des minéraux qui les composent (olivine et pyroxènes). Les propriétés sismiques de ces échantillons ont ensuite été calculées pour quantifier les effets des réactions minéralogiques associées au transport de fluides ou de magma sur celles-ci, ainsi que pour contraindre les relations entre anisotropie sismique et direction d'écoulement dans la partie supérieure du coin mantellique. De plus, cette étude montre que les échantillons de cette partie du manteau ont subi des réactions minéralogiques liées à la circulation de fluides. Or les travaux

expérimentaux qui traitent des interactions entre déformation et percolation de magma utilisent le plus souvent des fluides en équilibre avec la matrice solide. J'ai donc réalisé une série d'expériences afin de mieux comprendre si une percolation réactive peut expliquer les incohérences observées entre les résultats expérimentaux et les échantillons naturels.

Ce mémoire est présenté sous la forme de 6 chapitres. Il comporte trois articles publiés dans des revues internationales (*Journal of Petrology* et *Geophysical Research Letters*) et un article en phase finale de rédaction (soumission à *Tectonophysics*).

Le chapitre 2 : **"Interactions entre fusion partielle, transport de magma et déformation à la limite lithosphère-asthénosphère"** présente une étude pétro-structurale et géochimique des tectonites à spinelles du massif de Ronda situé au sud de l'Espagne publiée dans *Journal of Petrology* (Soustelle et al., 2009). La zone d'étude est située en amont d'une limite lithosphère-asthénosphère fossile. La partie asthénosphérique était partiellement fondue et une partie des magmas ont percolé la zone sus-jacente. Cette étude montre que cet événement a provoqué une refertilisation du domaine des tectonites à spinelle qui constitue la base de la lithosphère et qu'il était synchrone d'un épisode de déformation. Le but de ce travail fut donc de caractériser les transformations chimiques et minéralogiques associées à la percolation réactive de magma dans le manteau, et d'identifier les relations avec la déformation. Cette étude présente un avantage majeur comparer aux suivantes, elle permet de faire des observations à l'échelle du kilomètre.

Le chapitre 3 : "**Effets des interactions fluides-roche sur la déformation et les propriétés sismiques du coin mantellique : exemple de la subduction du Kamchatka"** est constitué de deux parties. La première est une étude de 23 xénolites de péridotite à spinelle exhumées de la base de lithosphère par les laves du volcan Avacha, situé au sud-est de la péninsule du Kamchatka. Ce travail publié dans *Journal of Petrology* (Soustelle et al., 2010) se base sur des observations microstructurales et des mesures des teneurs en eau et des OPR de l'olivine et l'orthopyroxene dans ces péridotites. Il a pour but de contraindre l'effet de la percolation réactionnelle de fluides enrichis en silice sur les mécanismes de déformation des roches du coin mantellique. La deuxième partie analyse l'impact de cette percolation sur les propriétés sismiques du manteau situé au-dessus d'une plaque subduite. Les résultats ont été publiés dans la revue *Geopysical Research Letters* (Soustelle & Tommasi, 2010).

Le chapitre 4 : "**Effet des interactions fluides-roche sur la déformation et les propriétés sismiques du coin mantellique: exemple de la subduction de Papouasie-Nouvelle-Guinée"** est une étude basée sur 8 échantillons de xénolites de péridotites à spinelle provenant de la base de la lithosphère et transporter par les laves de deux volcans sous-marins

proche de l'ile de Lihir situé dans le nord-ouest de l'archipel de Papouasie-Nouvelle-Guinée. Ce travail complète l'étude précédente sur les xénolites du volcan Avacha; les mêmes méthodes ont été appliquées et les résultats obtenus sur ces deux collections sont cohérents. Ils sont détaillés dans un article actuellement en phase finale préparation pour *Tectonophysics*, qui forme le corps de ce chapitre.

Le chapitre 5 : **"Caractérisation des interactions entre déformation et transport réactionnel de fluides enrichis en silice par une approche expérimentale"** décrit une série d'expériences menée dans la presse Paterson du laboratoire Géosciences Montpellier. Elles consistent à déformer un agrégat d'olivine en présence d'un fluide riche en silice à des températures similaires à celles du coin mantellique. Le but est de caractériser l'impact de ces fluides sur la déformation et de tester si ces fluides réagissent avec l'olivine entraînant la cristallisation d'orthopyroxene, et ainsi mieux contraindre les hypothèses faites à partir des échantillons naturels. Ce chapitre détaille les résultats préliminaires de ces expériences.

Enfin le chapitre 6 '**Conclusions et perspectives'** synthétise l'ensemble des résultats obtenus sur les interactions entre déformation et percolation réactionnelle de fluides ou de magma et leurs implications sur les propriétés sismiques du coin mantellique. Ce chapitre expose aussi les nouvelles questions induites par ces résultats et suggère des moyens d'y répondre.

Chapitre 2

Interactions entre fusion partielle, transport de magma et déformation à la limite lithosphère asthénosphère.

Le massif de péridotites de Ronda situé dans le sud de l'Espagne présente une limite lithosphère-asthénosphère fossile définie par un front de recristallisation bien marqué (Van der Wal & Bodinier, 1996; Lenoir et al., 2001). Celui-ci sépare un domaine asthénosphérique où la lithosphère a subi un événement de fusion partielle et de recristallisation de grande ampleur d'une zone lithosphérique où elle est "préservée" (Van der Wal & Bodinier, 1996; Van der Wal & Vissers, 1996; Garrido & Bodinier, 1999; Lenoir et al., 2001; Vauchez & Garrido, 2001). C'est un événement d'érosion thermique, lié à un amincissement lithosphérique qui est responsable de la configuration actuelle du massif. Une étude en cours montre que des pyroxénites, qui se sont formées dans la lithosphère "préservée" durant la formation du front de recristallisation, ont une signature isotopique caractéristique de sédiments océaniques (C. Marchesi, communication personnelle, 2010). Ceci montre que la source des magmas parents de ces pyroxénites été alors située à l'aplomb d'une subduction. Le massif de Ronda est donc un lieu idéal pour étudier, à l'échelle kilométrique, les relations entre transfert de chaleur, percolation de magma et déformation dans le manteau lors d'un processus d'érosion lithosphérique au-dessus d'une zone de subduction.

Le travail présenté dans ce chapitre se base sur l'étude pétro-structurale et géochimique d'une zone d'environs 2,5 km^2 s'étendant du front de recristallisation aux mylonites qui marquent la bordure ouest du massif. Les observations pétrographiques et les donnés géochimiques montrent que les magmas produits dans la partie asthénosphérique ont percolé de manière hétérogène la lithosphère et qu'ils ont réagi avec les péridotites

lithosphériques entraînant la refertilisation de la base de la lithosphère sur une distance d'environ 1,5 km. Cette réaction est responsable de l'alternance plurimétrique de roches mantelliques fertiles (lherzolites) et réfractaires (harzburgites) dans le domaine lithosphérique. On observe également la présence de pyroxénites à grenat partiellement fondues sur une distance d'environ 800 m en avant du front. Ceci est dû au fait que les pyroxénites ont un solidus plus bas que celui des péridotites. Les magmas résultant de leur fusion ont aussi pu contribuer à la refertilisation du domaine lithosphérique.

Un travail de cartographie structurale de détail, l'analyse des microstructures ainsi que les mesures d'orientations préférentielles de réseau (OPR) des minéraux constitutifs des roches mantelliques ont permis de mettre en évidence les interactions entre transport réactionnel de magma et déformation, ainsi que l'effet du gradient thermique sur ces deux processus. Le parallélisme observé entre le front de recristallisation, les limites compositionnelles et les structures de déformations (foliation, linéation), ainsi que les intensités de déformation variables des pyroxènes et spinelles, suggèrent que le transport de magma était syn- à tardi-cinématique, et qu'il était guidé par la déformation et le gradient thermique. Les péridotites les plus fertiles présentent des intensités d'OPR de l'olivine très variables, ce qui suggère une contribution plus importante des mécanismes de diffusion dans ces derniers et constitue donc un argument supplémentaire pour l'hypothèse d'une déformation en présence de magma.

JOURNAL OF PETROLOGY | VOLUME 50 | NUMBER 7 | PAGES 1235–1266 | 2009 | doi:10.1093/petrology/egp032

Deformation and Reactive Melt Transport in the Mantle Lithosphere above a Large-scale Partial Melting Domain: the Ronda Peridotite Massif, Southern Spain

V. SOUSTELLE[1]*, A. TOMMASI[1], J. L. BODINIER[1], C. J. GARRIDO[2] AND A. VAUCHEZ[1]

[1]GÉOSCIENCES MONTPELLIER, UNIVERSITÉ MONTPELLIER II & CNRS, CC 60, PLACE E. BATAILLON, 34095 MONTPELLIER CEDEX 5, FRANCE

[2]INSTITUTO ANDALUZ DE CIENCIAS DE LA TIERRA (IACT), CSIC & UGR, FACULTAD DE CIENCIAS, FUENTENUEVA S/N, 18002 GRANADA, SPAIN

RECEIVED MAY 17, 2008; ACCEPTED MAY 6, 2009

The Ronda peridotite massif in Southern Spain shows a well-defined 'recrystallization' front that separates a large-scale partial melting domain formed at the expense of the continental lithospheric mantle from a 'preserved' lithospheric domain. To investigate the processes allowing a transient lithosphere–asthenosphere boundary to propagate in the lithospheric mantle, we performed a joint petrostructural and geochemical study of an ~2·5 km^2 zone extending from the melting front to the mylonites that mark the western limit of the massif. This study emphasizes a feedback between heat transfer, melt percolation, and deformation in the lithospheric mantle. Petrographical observations and geochemical data show that heterogeneous reactive percolation of melts produced in the underlying partial melting domain led to refertilization of lithospheric peridotites up to 1·5 km ahead from the melting front, producing metre-scale layering of fertile and refractory mantle rocks. Within 800 m from the front, pre-existing garnet pyroxenite layers were partially molten and the resulting melts probably contributed to the refertilization process. Detailed structural mapping and analysis of the microstructures and crystal preferred orientations highlight the relations between reactive melt transport and deformation, and the control of the temperature gradient on both processes. Parallelism between the recrystallization front, compositional boundaries, and deformation structures, as well as variations in the deformation intensity of pyroxenes and spinels, suggest syn- to late-tectonic melt transport controlled by both the deformation and the thermal gradient. Variations in the strength of olivine crystal preferred orientations as a function of the modal and chemical composition of the spinel tectonites point to a higher contribution of diffusion to deformation in the most fertile rocks, corroborating the hypothesis that deformation occurred in presence of melt. Finally, the systematic dispersion of olivine [100] and orthopyroxene [001] axes in the foliation plane suggests a dominantly transpressive deformation regime.

KEY WORDS: *asthenosphere–lithosphere boundary; deformation; lithosphere; melt percolation; microstructure; olivine; CPO; mylonites; partial melting; peridotite; refertilization; transient heating*

INTRODUCTION

The processes leading to thinning of the continental lithosphere are still poorly understood. Analysis of lithosphere strength envelopes constructed using laboratory-based flow laws (e.g. Kohlstedt *et al.*, 1995) shows that plate-tectonic or plume-related forces do not suffice to deform a 100 km thick lithosphere. Numerical models of the interaction of a mantle plume with a moving lithospheric plate highlight that enhanced small-scale convection in the plume impact zone results in a high transient thermal gradient at the base of the lithosphere, but has no effect on

*Corresponding author. Telephone: +33-(0)467143941. Fax: +33-(0)467143603. E-mail: vsoustel@gm.univ-montp2.fr

the shallow, higher strength mantle lithosphere (Thoraval *et al.*, 2006).

Seismic anisotropy measurements in the East African rift indicate that magmas play an essential role in the rifting process at all depths (Kendall *et al.*, 2005). The presence of melt results in significant decrease of the mantle viscosity (e.g. Hirth & Kohlstedt, 1995*a*). Weakening of the lithospheric mantle by a combination of melt percolation and thermo-mechanical erosion of the base of the lithosphere atop an asthenospheric upwelling is thus a good candidate to account for the deformation of an initially 100 km thick lithospheric plate.

Reactive melt percolation in the lithospheric mantle has been described in several peridotite massifs, such as Horoman, Lherz, or Lanzo, where it resulted in refertilization of an ancient, refractory lithosphere (Saal *et al.*, 2001; Muntener *et al.*, 2005; Le Roux *et al.*, 2007) and controlled the strain distribution (Kaczmarek & Müntener, 2008; Le Roux *et al.*, 2008). However, these massifs expose only the 'refertilized' lithosphere. In contrast, the Ronda peridotite massif in Southern Spain contains a well-defined 'recrystallization' front that separates a large-scale partial melting domain formed at the expense of the continental lithospheric mantle from a 'preserved' lithospheric domain (Van der Wal & Bodinier, 1996; Van der Wal & Vissers, 1996; Garrido & Bodinier, 1999; Lenoir *et al.*, 2001; Vauchez & Garrido, 2001). The Ronda recrystallization front represents an exhumed transient lithosphere–asthenosphere boundary. A detailed petrostructural and geochemical study of a $\sim$2·5 km^2 zone in the southwestern part of the massif, extending from the melting front to the mylonites (Fig. 1), allows us to study the extent of melt infiltration and the relations between melt percolation, heat transfer, and deformation above a partial melting domain in the mantle. Detailed structural mapping and analysis of the microstructures and crystal preferred orientations highlight the relations between reactive melt transport and deformation, and the control of the temperature gradient on both processes. In addition, petrographical observations and geochemical data allow us to constrain the contribution of reactive melt transport to the development of compositional heterogeneities in the lithosphere.

GEOLOGICAL SETTING

The Ronda peridotite is the largest ($\sim$300 km^2) orogenic ultramafic massif cropping out at the Earth's surface. It is located in the western part of the Betic Cordillera (Southern Spain), which forms the northern part of the Gibraltar arc (Fig. 1). This orogenic system is the westernmost segment of the Alpine belt in Europe and contains a series of large ultramafic massifs (Ronda, Ojén, Carratraca in the Betics, and Beni Boussera in the Rif).

The Ronda peridotite massif is characterized by kilometre-scale petrological, geochemical and structural zoning (Obata, 1980). Van der Wal & Vissers (1996) reinterpreted Obata's (1980) zoning, defining three tectonometamorphic domains (Fig. 1), which they interpreted as recording the thermal evolution of the lithospheric mantle during the late stages of extension in the Alboran Basin, aborted by the final emplacement of the massif in the crust.

(1) The spinel (±garnet) tectonite domain is the oldest. It is divided in two sub-domains: the garnet–spinel mylonites that mark the northern and western boundaries of the massif and the foliated spinel tectonites. They correspond respectively to Obata's garnet lherzolite facies and ariegite subfacies. Both spinel tectonites and mylonites display a pervasive steeply dipping foliation that trends almost parallel to the melting front and a shallowing dipping lineation (Fig. 1).

(2) The coarse-granular peridotite domain roughly coincides with Obata's Seiland subfacies. It is located in the central part of the Ronda peridotite and is separated from the spinel tectonites by the recrystallization front (Lenoir *et al.*, 2001). Structural and geochemical data imply that the coarse-granular peridotites were developed at the expense of the spinel tectonites by partial melting and annealing (Van der Wal & Bodinier, 1996; Van der Wal & Vissers, 1996; Garrido & Bodinier, 1999; Lenoir *et al.*, 2001; Vauchez & Garrido, 2001). The coarse-granular peridotites display a mainly northward, steeply dipping. foliation and a shallowly dipping lineation (Fig. 1).

(3) The plagioclase tectonite domain, which corresponds to Obata's (1980) plagioclase lherzolite facies, is the youngest of the three structural domains. It formed at the expense of the granular peridotites during the emplacement of the massif in the crust. It constitutes the largest part of the massif and is exposed in the southern and eastern part of the Ronda peridotite.

More recently, detailed structural and petrological studies of the garnet- and spinel-bearing mylonites indicate that the spinel (±garnet) mylonites formed during a decompression and cooling event in the lithospheric mantle from 1150°C and 2·7 GPa to 900°C and 1·9 GPa (Garrido *et al.*, 2006). Based on these data, Precigout *et al.* (2007) proposed that the petrological, geochemical, and structural zoning of the Ronda massif records thinning of an old sub-continental lithospheric mantle accommodated by ductile shear zones. This thinning was followed by a thermal event resulting in the propagation of a partial melting and recrystallization front (Lenoir *et al.*, 2001). For Van der Wal & Bodinier (1996), the recrystallization front represented a permeability barrier for basaltic melts, which accumulated in the coarse-granular peridotites. However, Lenoir *et al.* (2001) suggested that a strong thermal gradient existed across the Ronda massif during the formation of the recrystallization front. This gradient

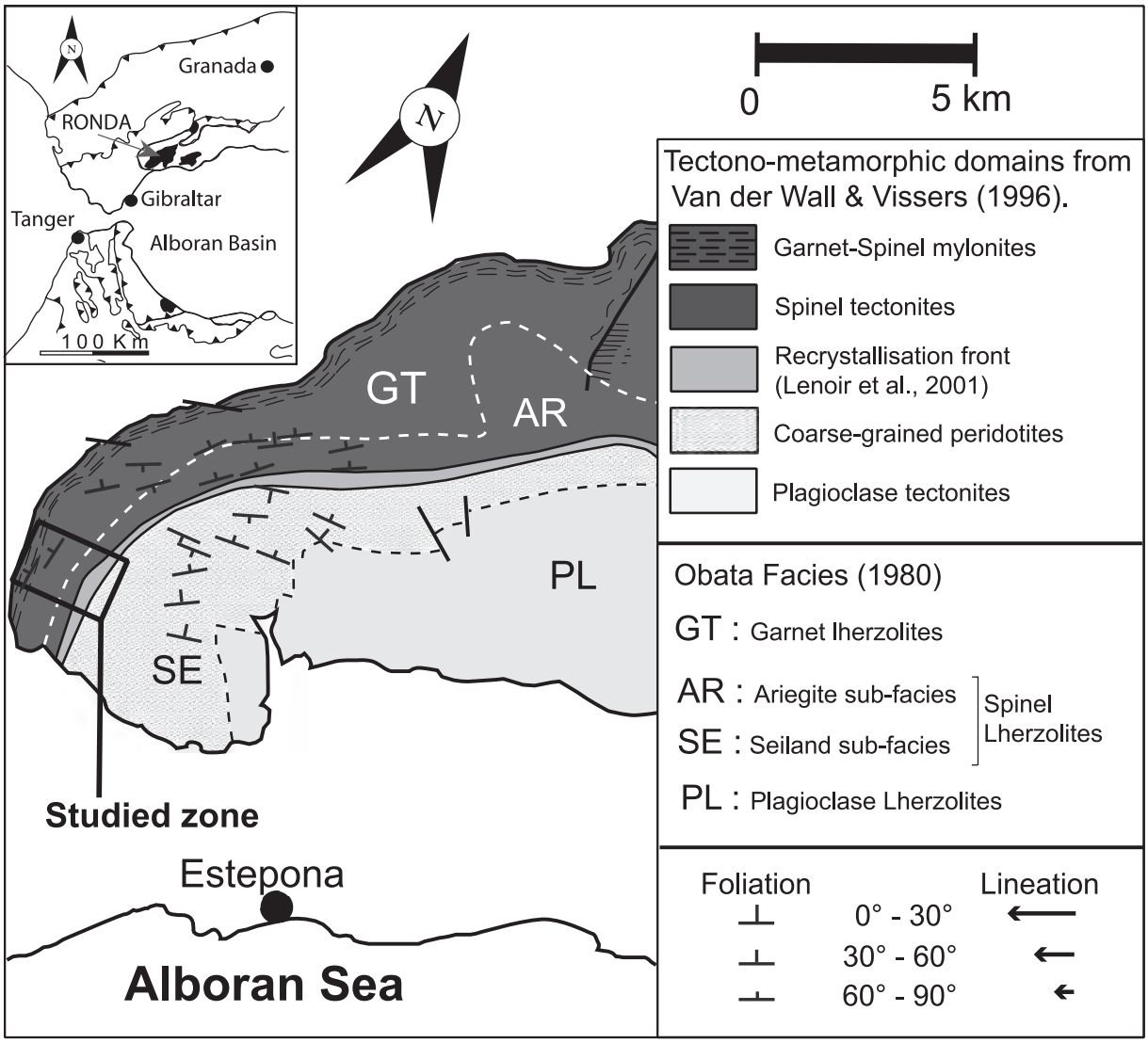

Fig. 1. Simplified geological map of the Ronda peridotite massif (Southern Spain) showing the location of the study area in the westernmost part of the massif, the tectono-metamorphic domains, and the recrystallization front mapped by Obata (1980), Van der Wal & Vissers (1996) and Lenoir *et al.* (2001). Lineations and foliations from Darot (1973).

allowed small melt fractions to percolate up to a few hundred metres ahead of the melting front, reacting with the spinel tectonites.

FIELD OBSERVATIONS: LITHOLOGICAL RELATIONS AND DEFORMATION STRUCTURES

We performed detailed structural mapping of a 2·5 km^2 area in the westernmost part of the massif, including, from east to west, the transition between granular peridotites and spinel tectonites, the spinel tectonites, and the garnet–spinel mylonites (Figs 2 and 3). In the studied zone, lherzolites are dominant. They enclose discontinuous harzburgite bodies, 15–90 m thick, elongated in a north–south to NNE–SSW direction. Lherzolite–harzburgite contacts occur as a metre-scale transition characterized either by alternating decimetre-scale lherzolite–harzburgite layers (Fig. 2a) or by alternating harzburgites and centimetre-scale olivine websterite layers (Fig. 2b).

In the spinel tectonite domain, both harzburgites and lherzolites display a penetrative, steeply dipping foliation (65°W to 75°E) that trends N350E–N40E, and a shallowly dipping lineation (0–30°S) marked by the alignment of spinel and pyroxene aggregates (Fig. 3). These orientations

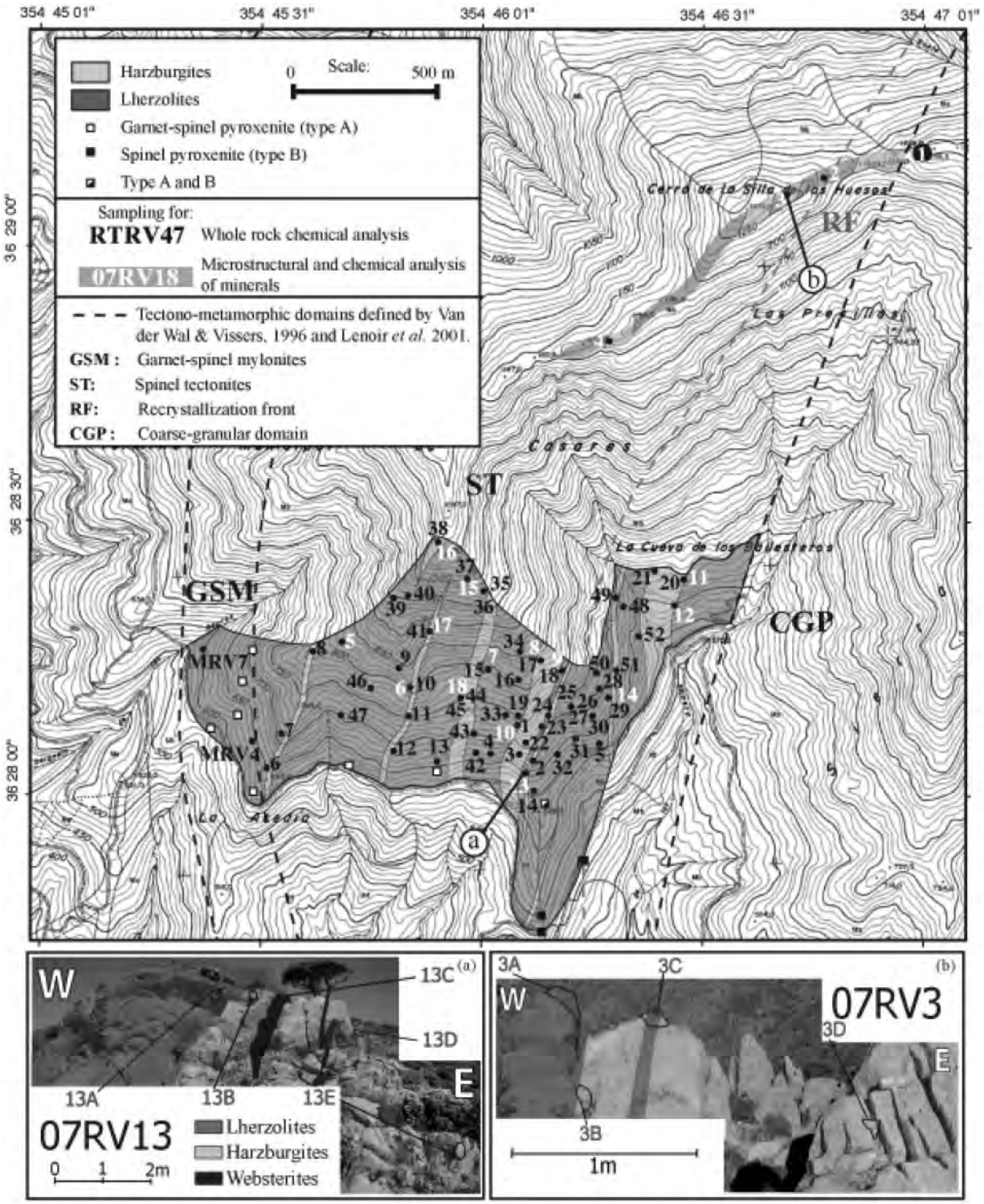

Fig. 2. Geological map of the studied zone showing the samples location. Inserts are photographs of representative lherzolite–harzburgite contacts: (a) 07RV13; (b) 07RV3.

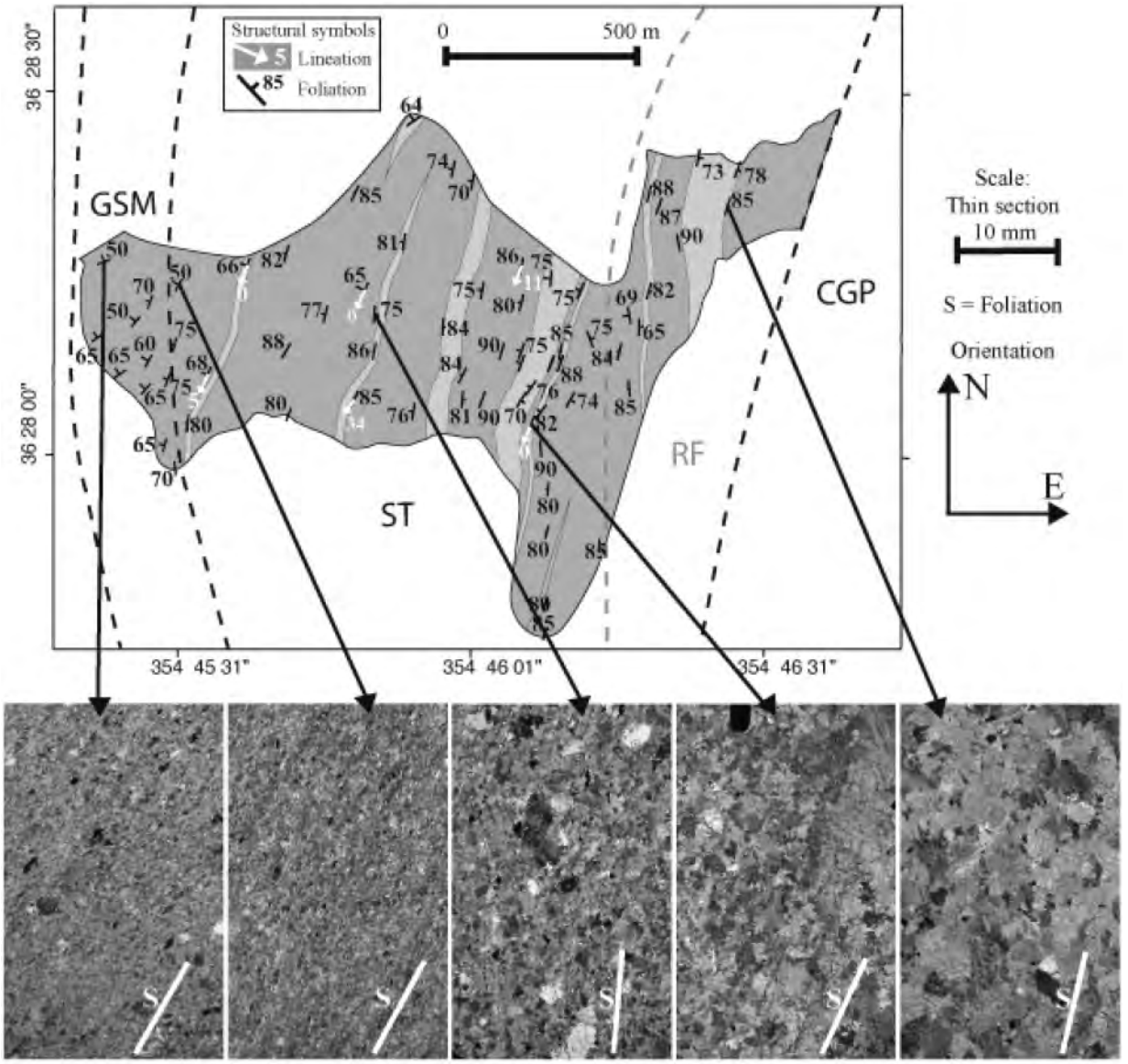

Fig. 3. Structural map of the studied domain and photomicrographs showing the evolution of the microstructure as a function of the distance to the recrystallization front.

are consistent with the foliations and lineations reported at the scale of the massif (Darot, 1973; Van der Wal, 1993; Van der Wal & Bodinier, 1996; Van der Wal & Vissers, 1996; Vauchez & Garrido, 2001; Precigout *et al.*, 2007). Variations in the foliation orientation are gradual, occurring at the tens of metres scale, and may result from either strain heterogeneity or large-scale open folds. Crosscutting relations between mylonites and spinel tectonites have not been observed. A clear change in the orientation of the deformation structures is observed only within the garnet–spinel mylonites, where the foliation progressively rotates from parallel to the spinel tectonites' foliation to N70E–50°NW at the western boundary of the massif. The orientation of the foliation and lineation does not change across lherzolite–harzburgite contacts.

In addition to the centimetre-scale olivine websterite layers that underline the lherzolite–harzburgite contacts, lherzolites also contain decimetre- to metre-scale garnet and spinel pyroxenite layers. These pyroxenites correspond to the types A and B from Garrido & Bodinier (1999), respectively. Spinel pyroxenites are observed within 800 m from the front, whereas garnet pyroxenites occur farther away from the front within spinel tectonites or garnet–spinel mylonites (Fig. 2). A composite layer a few metres

wide formed by garnet pyroxenites enclosed in spinel pyroxenites occurs at ca. 400 m from the melting front. These observations are in agreement with the interpretation of Garrido & Bodinier (1999) that type B spinel pyroxenites result from partial melting of type A garnet pyroxenites. Both pyroxenites and olivine websterites form bands parallel to the peridotite foliation. However, the pyroxenites are boudinaged and show sharp contacts with the peridotite, whereas the olivine websterites usually do not display boudinage and their contact with the peridotites is irregular and diffuse.

It is worth noticing that all tectonic structures (foliation, lineation), pyroxenite layers, and lherzolite–harzburgite contacts are parallel. In the eastern part of the mapped area, they are also parallel to the recrystallization front (Fig. 3). To investigate the relations between partial melting, melt transport, and deformation in this fossil lithosphere–asthenosphere boundary, we performed coupled petrological, microstructural, and geochemical analyses on four series of 4–7 samples collected along metre-scale transects across lherzolite–harzburgite contacts, at variable distance from the recrystallization front, as well as in a few additional samples remote from any lithological contact (Fig. 2). To refine the lithological mapping, additional major-element analyses of whole-rocks and minerals were performed on smaller samples collected on a roughly ~50 m scale grid, depending on outcrop availability.

MICROSTRUCTURES

Deformation-related microstructures

At the thin-section scale, the lineation and foliation are marked by alignment of spinel and pyroxene aggregates and by the elongation of olivine crystals. From the western border of the massif to the recrystallization front, we observe a continuous increase in grain size (Fig. 3). This variation in grain size agrees with that observed at the scale of the massif by Van der Wal & Bodinier (1996) and Vauchez & Garrido (2001). Those workers showed that a further increase in grain size occurs across the recrystallization front in the coarse-grained peridotites. In the easternmost part of the studied domain, close to the recrystallization front, the spinel tectonites have a coarse-grained porphyroclastic microstructure. Fine-grained porphyroclastic microstructures dominate in the central part of the spinel tectonite domain. In the westernmost part of the studied zone, the microstructure is mylonitic. A weak variation in the microstructure is also observed across the harzburgite–lherzolite contacts in the coarse-grained porphyroclastic domain: harzburgites display on average coarser olivine grains than lherzolites.

The coarse-grained porphyroclastic microstructure is characterized by a heterogeneous olivine grain size ranging from 1 to 15 mm. Olivine crystals display irregular shapes with sinuous grain boundaries, undulose extinction and well-developed subgrain boundaries (Fig. 4a). Subgrains are more commonly observed in large grains than in small ones (Fig 4b). Olivine crystals are usually elongated parallel to the lineation with aspect ratios varying between 1:1·5 and 1:2, but reaching 1:10 for the largest grains. Pyroxenes occur either as isolated crystals or form aggregates often aligned parallel to the lineation trend. Orthopyroxenes (opx) are 0·5–5 mm in size. They have irregular shapes and may show undulose extinction and kink bands (Fig. 4c). Clinopyroxene (cpx) grain-size distribution is bimodal. Coarse cpx crystals (0·5–2 mm) usually form clusters with opx and display the same deformation features, whereas small interstitial cpx crystals (0·1–1 mm) show no evidence of deformation. Spinels display heterogeneous grain sizes (0·1–2 mm) and shapes. Small grains are sub-euhedral, whereas coarse grains have irregular, holly-leaf shapes, and are often aligned parallel to the lineation (Fig. 4d).

The fine-grained porphyroclastic microstructure is similar to the coarse-grained porphyroclastic one, but olivine crystals are on average smaller (<2 mm). Some coarse olivine porphyroclasts up to 10 mm long and 2 mm wide elongated parallel to the lineation are nevertheless preserved. Olivine crystals display irregular shapes with sinuous grain boundaries, undulose extinction and closely spaced sub-grains (Fig. 4f). The pyroxene and spinel microstructures are similar to those in the coarse-grained porphyroclastic peridotites.

Mylonites are characterized by a bimodal olivine grain-size distribution with few relict porphyroclasts (0·5–1 mm long) elongated parallel to the lineation (aspect ratios generally around 1:5). Olivine porphyroclasts are surrounded by a matrix of small recrystallized grains (~200 μm), which are also elongated (aspect ratios of 1:2) parallel to the lineation. Both porphyroclasts and recrystallized grains present irregular shapes with sinuous grain boundaries, closely spaced subgrain boundaries, and undulose extinction (Fig. 4g and h). Opx and cpx occur essentially as isolated crystals; grain sizes range from 0·1 to 1 mm. Some opx crystals have been highly stretched parallel to the lineation, attaining aspect ratios of 1:10 or higher. They display undulose extinction and well-developed kink bands. Spinels are similar to those in the fine-grained porphyroclastic peridotites, but smaller (0·1–1 mm).

Olivine websterites are constituted essentially of pyroxenes 0·5–2 mm across that have irregular shapes and sinuous grain boundaries. Most opx grains display undulose extinction, as is shown also by the coarser cpx crystals. Olivine crystals are relatively small (<1 mm) and show undulose extinction and subgrains. Spinels are larger than in the peridotites and can up to 3 mm in size. They display holly-leaf shapes. At the thin-section scale, the boundary between peridotites and websterites is sinuous and characterized by a gradual increase in pyroxene content (Fig. 4e).

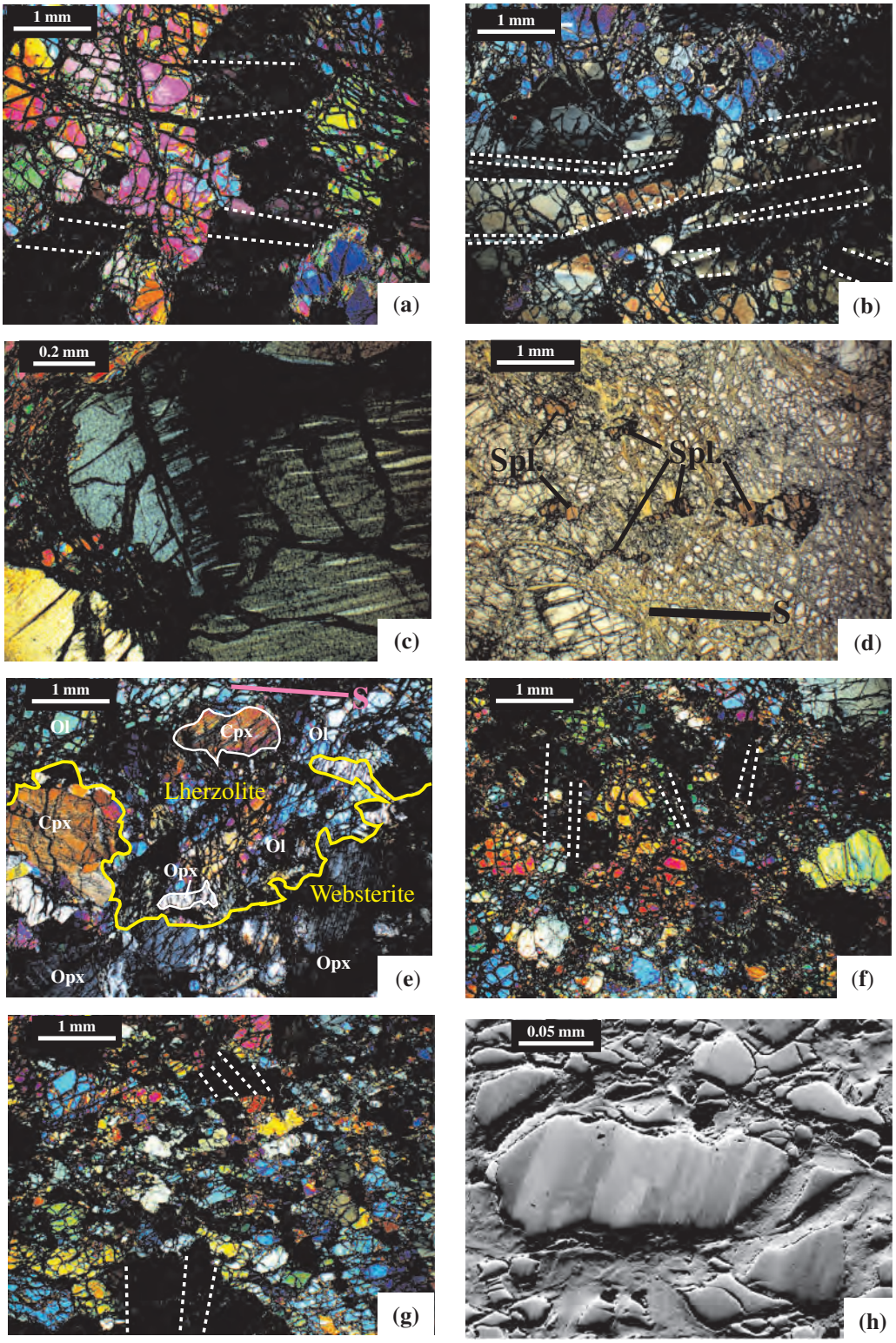

Fig. 4. Photomicrographs illustrating the variation in microstructures in the spinel tectonite domain from the coarse-grained porphyroclastic peridotites close to the front to garnet–spinel mylonites. (a, b) Coarse-grained porphyroclastic microstructure with (a) widely spaced subgrain boundaries in olivine grains in a lherzolite (07RV12D) and (b) closely spaced subgrain boundaries in olivines in a harzburgite (07RV12Ce). (c) Kink-bands and coarse clinopyroxene exsolution in an opx crystal (07RV12Bc). (d) Trail of holly-leaf spinels in a coarse-grained porphyroclastic spinel tectonite (07RV3C). (e) Lherzolite–websterite contact (07RV12Be); S marks the pervasive foliation. (f) Fine-grained porphyroclastic microstructure with closely spaced subgrain boundaries in olivine (07RV6). (g) Garnet–spinel mylonite RX8 from Lenoir *et al.* (2001) showing olivine porphyroclasts with clear (100) subgrain boundaries (indicated by dashed lines) and undulose extinction surrounded by small recrystallized grains. (h) Closely spaced polygonal subgrain boundaries in an olivine fragment from a serpentinized (low-relief domains) spinel mylonite (MRV7); FSE orientation contrast image obtained using the CamScan X500FE CrystalProbe at Geosciences Montpellier.

Garnet pyroxenites (type A pyroxenites) have a porphyroclastic microstructure characterized by large porphyroclasts of cpx (± opx, gt) in a fine matrix of gt and cpx crystals. Spinel pyroxenites (type B pyroxenites) present a granoblastic microstructure and do not show evidence of deformation (e.g. Garrido & Bodinier, 1999, fig. 3).

Melt–rock reaction-related microstructures

Melt–rock reactions in the mantle may lead either to consumption of pyroxenes and olivine crystallization during incongruent partial melting or interaction with Si-undersaturated magmas (Kelemen *et al.*, 1992), or to crystallization of pyroxenes (±spinel or garnet or plagioclase) at the expense of olivine during refertilization reactions (Lenoir *et al.*, 2001; Dijkstra *et al.*, 2003; Le Roux *et al.*, 2007; Bodinier *et al.*, 2008; Kaczmarek & Müntener, 2008). Analysis of pyroxene morphology and deformation thus provides information on the reactions that affected the peridotites.

Spinel tectonites show dominantly 0·5–5 mm wide opx grains characterized by irregular shapes that occur either isolated or in opx–cpx–sp clusters. Some of these pyroxenes display concave grain boundaries filled with olivine (Fig. 5a and b), suggesting the occurrence of melt–rock reactions that consumed pyroxenes and crystallized olivine. These opx crystals usually display undulose extinction and kink bands, implying deformation by dislocation creep. However, the secondary crystallization of opx is also suggested by rare, undeformed opx forming overgrowth rims on isolated crystals (Fig. 5c). Undeformed opx is also present as small (<0·5 mm) interstitial crystals along olivine–olivine grain boundaries (Fig. 5d).

In harzburgites, cpx occurs essentially as isolated interstitial grains (0·1–1 mm wide), which located along olivine–olivine grain boundaries or at triple junctions, sometimes forming large poikilitic crystals (Fig. 5e). Lherzolites also show isolated interstitial cpx, but most cpx occurs in opx–cpx–sp aggregates where cpx is predominant (Fig. 5f). These aggregates are sometimes flattened in the foliation plane, but show no intracrystalline deformation features. We interpret the interstitial pyroxenes and the aggregates as formed by secondary crystallization of pyroxenes from percolating melt, suggesting that most lherzolites in the study area result from refertilization reactions. Similar microstructures were described by Lenoir *et al.* (2001) in the lherzolites located a few hundreds of metres ahead of the recrystallization front; they were similarly ascribed to igneous refertilization.

CRYSTAL PREFERRED ORIENTATIONS

Olivine and pyroxene crystal preferred orientations (CPO) were determined by indexation of electron-backscattered diffraction (EBSD) patterns using the SEM-EBSD facility at Geosciences Montpellier. EBSD patterns are generated by interaction of a vertical incident electron beam with a carefully polished thin section tilted at 70° in a scanning electron microscope (JEOL JSM 5600). The diffraction pattern is projected onto a phosphor screen and recorded by a digital CCD camera. The image is then processed and indexed in terms of crystal orientation using the CHANNEL5 software from Oxford Instruments HKL. For each sample, we obtained crystallographic orientation maps covering almost the entire thin section (usually 20 mm × 35 mm) with a sampling step ranging from 30 to 100 μm. Indexation rates in the raw maps range from 30 to 60% depending mostly on the extent of serpentinization. Post-acquisition data treatment allowed a further increase in the indexation rate by (1) filling the non-indexed pixels that have up to eight identical neighbours with this orientation, (2) repeating this operation using respectively seven, six and five identical neighbours, (3) identifying the grains (i.e. continuous domains characterized by an internal misorientation of $< 15°$) and (4) within each olivine crystal, searching and correcting for systematic indexation errors related to the olivine's hexagonal pseudosymmetry, which results in closely similar diffraction patterns for orientations differing by a rotation of 60° around [100]. At each step, the resulting orientation maps were verified by the operator to avoid over-extrapolation of the data.

The studied peridotites show clear olivine and pyroxene crystal preferred orientations, implying a significant contribution of dislocation creep to deformation (Fig. 6). In all samples, olivine [100] axes are dispersed in the foliation plane with a well-marked maximum within 10° of the lineation, and a strong concentration of [010] almost normal to the foliation. The [001] axes are more dispersed, but they present a weak maximum normal to the lineation within the foliation plane. It should be noticed that in most studied samples [010] axes are more concentrated than the [100] axes, characterizing well-developed [010]-fibre patterns (Bunge, 1982).

In the spinel tectonites, opx [001] axes are dispersed in a plane close to the foliation with a weak maximum close to the lineation and [100] axes are concentrated close to the normal to the foliation. The [010] axes have an almost random repartition (Fig. 6). Cpx displays a very weak CPO, which is related to the opx CPO, but with a larger dispersion. In garnet–spinel mylonites (Fig. 6), cpx and opx show similar CPO patterns, although weaker for the cpx: [001] is either dispersed in a plane at low angle to the foliation or concentrated close to the lineation and [010] tends to be oriented at high angle to the foliation (Fig. 6).

The observed olivine and opx CPO imply deformation by dislocation creep with dominant activation of the high-temperature, low-stress (010)[100] and (100)[001] slip systems for olivine and opx, respectively (Tommasi *et al.*,

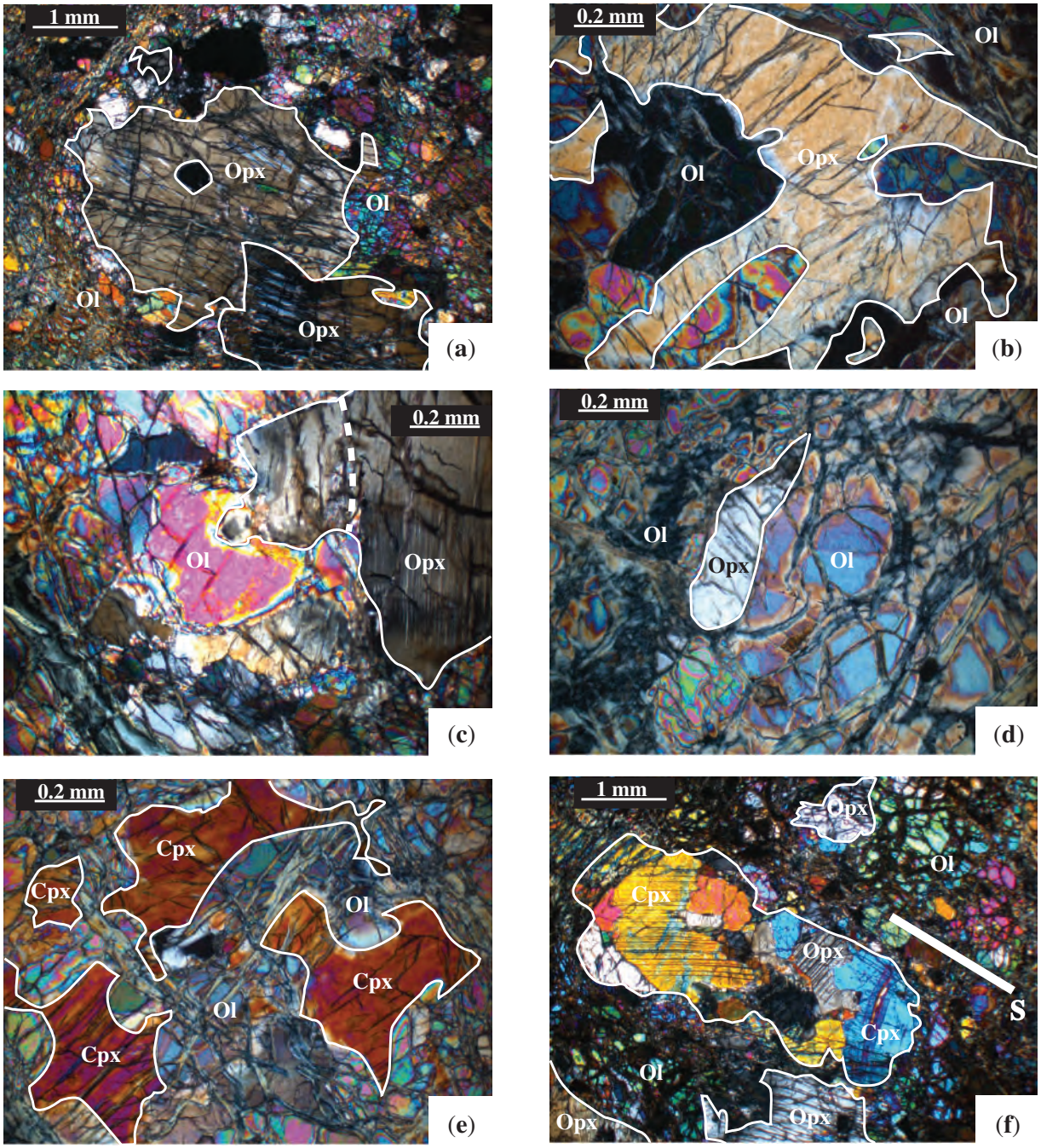

Fig. 5. Photomicrographs (crossed polarizers) showing the variation in pyroxene morphology in the studied samples. (a, b) Corroded orthopyroxenes (opx), corrosion embayments filled by olivine (ol), samples 07RV10A and 07RV3C, respectively; (c) opx crystal with fine clinopyroxene exsolution and undulose extinction and an exsolution-free overgrowth at the expense of an olivine (ol) crystal (sample 07RV12Cw); (d) undeformed interstitial opx (07RV13A); (e) undeformed interstitial cpx in an olivine matrix (07RV13B); (f) undeformed aggregate of cpx and opx with granoblastic texture (07RV13A), S marks the trace of the foliation.

2000). Moreover, the systematic dispersion of olivine [100] axes and opx [001] within the foliation and the small obliquity between the olivine [100] and opx [001] maxima and the lineation are characteristic of transpressional deformation (Tommasi *et al.*, 1999).

Analysis of the intensity of the olivine CPO, characterized by the dimensionless J-index (Bunge, 1982), as a function of the modal proportion of clinopyroxenes allows investigation of the relation between deformation and melt–rock reaction (Fig. 7). The J-index is the

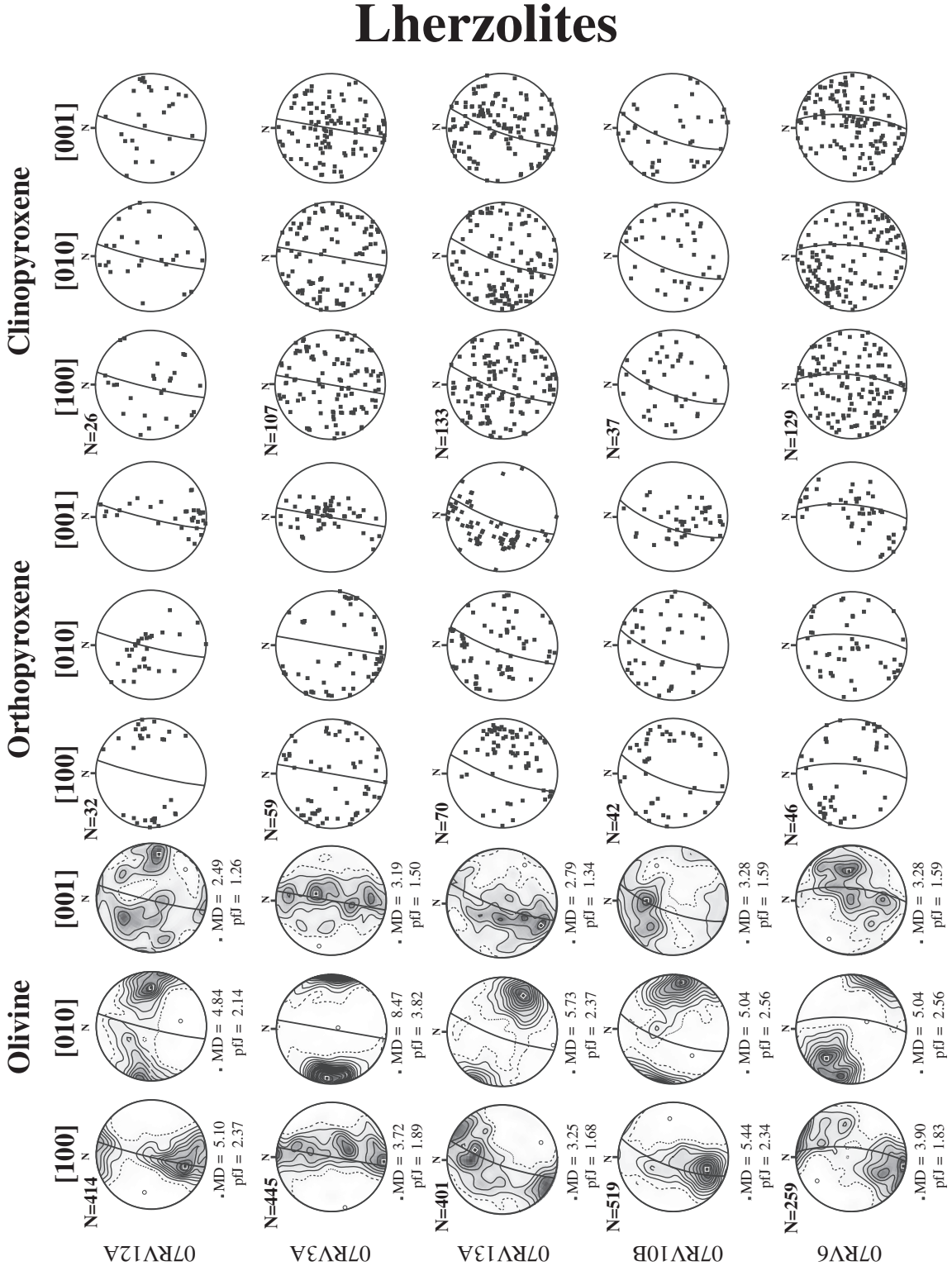

Fig. 6. Olivine, orthopyroxene, and clinopyroxene crystal preferred orientations (CPO) in representative lherzolite and harzburgite samples of the spinel tectonites domain and of the mylonites. Lower hemisphere, equal area stereographic projection in the geographical reference frame. The opx and cpx CPO from lherzolites and harzburgites were not contoured because fewer than 150 grains could be measured in the thin-section. Continuous line represents the foliation. N, number of measured grains; MD, maximum density.

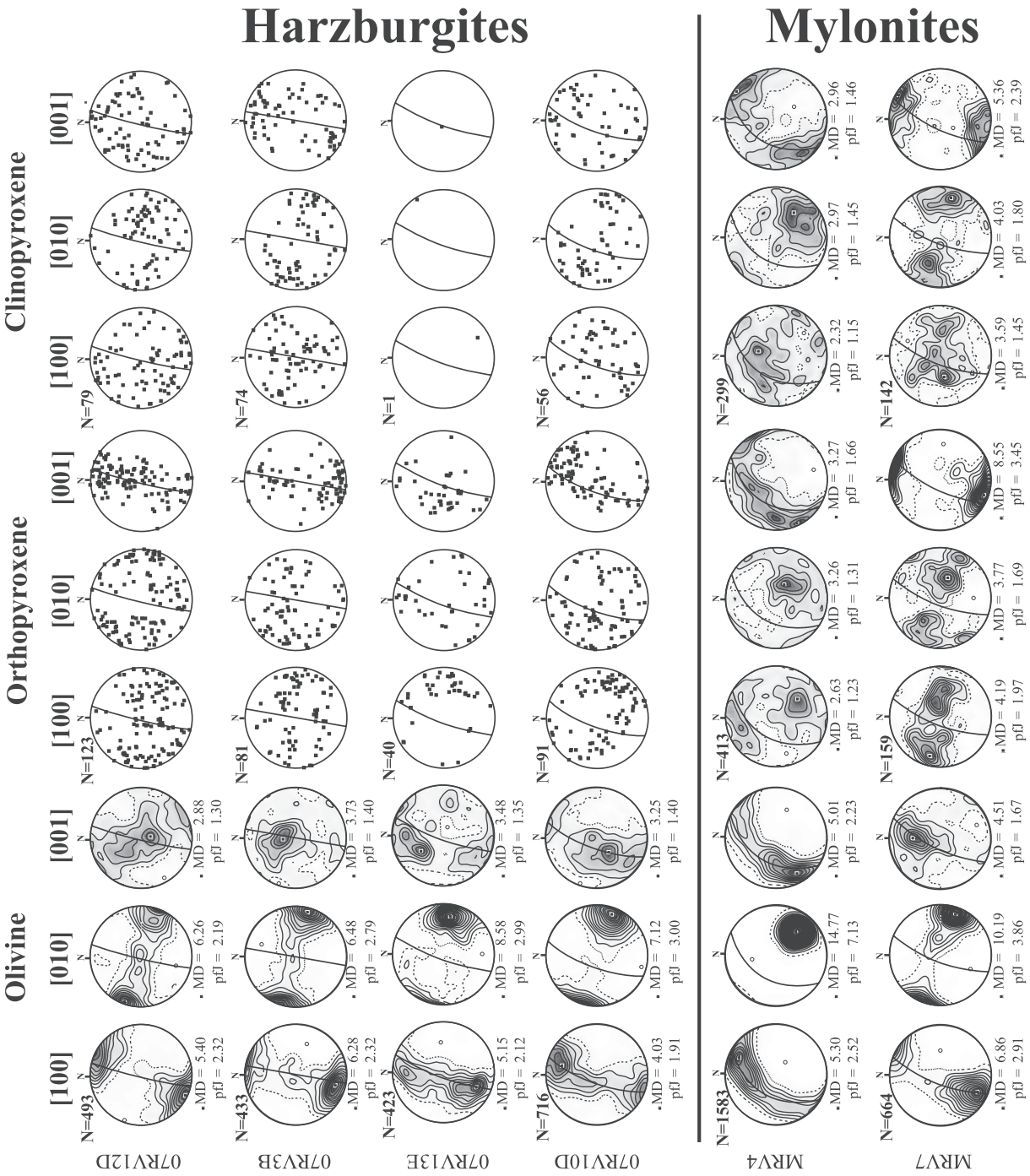

Fig. 6. Continued.

volume-averaged integral of the squared orientation densities. It has a value of unity for a random CPO and infinity for a single crystal. Most natural peridotites show values between 2 and 20 (Ben Ismail & Mainprice, 1998; Tommasi *et al.*, 2000). In the study area, harzburgites and cpx-poor lherzolites (>8% cpx) display a rather homogeneous J-index ranging from 4·5 to 6·5. The more fertile types (<8% cpx), in contrast, display a large variation in the J-index in the range of 3–8·5 with a bimodal distribution: one population has very weak olivine CPO, with a J-index <4, and the other has rather strong olivine CPO, with J-index >6. At the scale of a single lherzolite–harzburgite contact, one may observe either an increase or a decrease in J-index from the harzburgites to the

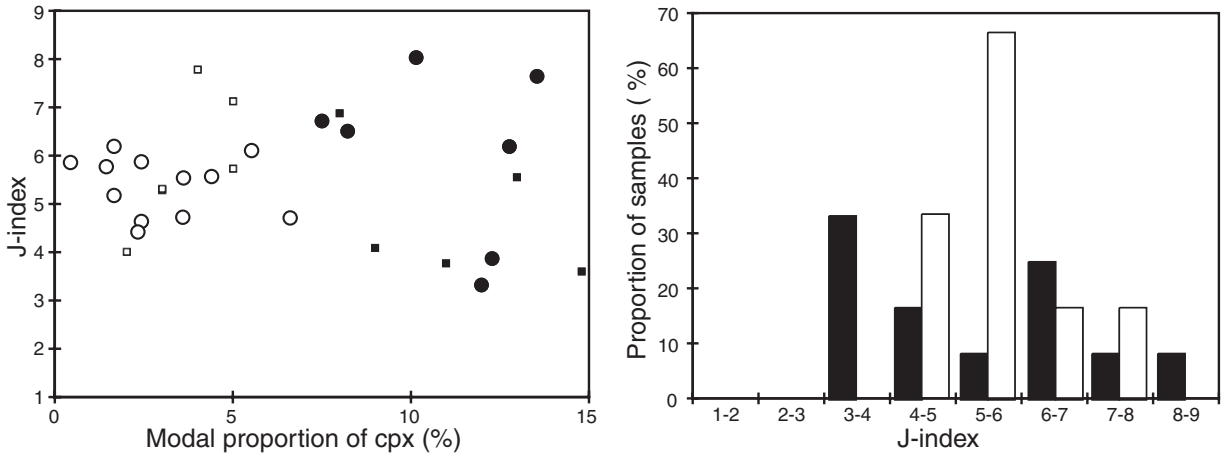

Fig. 7. (a) J-index of the olivine CPO as a function of the clinopyroxene modal content in the sample. Cpx-rich lherzolites and harzburgites/cpx-poor lherzolites are indicated by filled and open symbols, respectively. Data from this study are given as large circles; previous measurements by Vauchez & Garrido (2001) are indicated by small squares. (b) Histogram showing the variation of J-index in the cpx-rich lherzolites (in black) and in the harzburgites and cpx-poor lherzolites (in white).

lherzolites. For instance, at the contact 07RV3 (Fig. 6) the harzburgites have a J-index around six and the lherzolites between 6·3 and 7·7, whereas at the contact 07RV13, the J-index decreases from 5·9 in the harzburgites to 3·9 in the lherzolites. The observed short-scale variations in J-index may be explained by strain gradients or by a higher contribution of melt-enhanced diffusion processes that result in a weaker CPO (Tommasi *et al.*, 2000).

MAJOR- AND MINOR-ELEMENT COMPOSITIONS OF WHOLE-ROCKS AND MINERALS

X-ray fluorescence (XRF) analysis of major and minor transition elements (Ni, Cr) in whole-rocks was performed at the CIC (Scientific Instrument Centre) of the University of Granada (Spain). Data are reported in Table 1. Major-element compositions of olivine, pyroxenes, and spinel were determined by electron microprobe analysis (EPMA) using a CAMECA SX100 at the 'Microsonde Sud' facility, University of Montpellier 2. Analytical conditions were an accelerating voltage of 20 kV, a 10 nA focused beam, and counting times of 20–30 s.

The studied spinel tectonites show a wide range of major-element contents from highly refractory (44·67 wt % MgO, 0·27 wt % Al_2O_3, 0·18 wt % CaO) to very fertile compositions (33·73 wt % MgO, 4·55 wt % Al_2O_3, 3·9 wt % CaO; Table 1, Fig. 8). The observed values encompass the whole range of compositions reported for the Ronda peridotites (Frey *et al.*, 1985; Van der Wal & Bodinier, 1996; Lenoir *et al.*, 2001). However, some lherzolites in the study area tend to be even more fertile in term of Al, Ca and Ti contents than the most fertile compositions reported previously (Fig. 8).

Al, Ca, Ti and Na decrease, and Ni increases slightly with increasing Mg content from fertile lherzolites to harzburgites (Fig. 8). These element co-variations coupled with the modal changes are typical of the majority of peridotite suites worldwide. However, in the studied peridotites these co-variations are linear. The Na and Ti variations are therefore inconsistent with those produced by partial melting (Fig. 8). Cr shows a more complex variation, marked by almost constant content in lherzolites and decreasing—although scattered—concentrations with increasing Mg contents in harzburgites (Fig. 8). Decreasing Cr contents in refractory peridotites have been observed previously in orogenic peridotites, including the Ronda massif (Frey *et al.*, 1985; Van der Wal & Bodinier, 1996) and the Lherz massif, where Le Roux *et al.* (2007) ascribed the Cr variation to refertilization processes.

Significant variations in mineral compositions as a function of whole-rock modal and chemical compositions are observed only for the Mg-number [Mg/(Mg + Fe) cationic ratio] of silicates and the Cr-number [Cr/(Cr + Al) cationic ratio] of spinel (Table 2). The olivine forsterite content (Fo) or Mg-number decreases from 0·92–0·91 in the harzburgites to 0·91–0·89 in lherzolites and olivine websterites. Similar variations are observed for the Mg-number of orthopyroxenes and clinopyroxenes. The Cr-number in spinel strongly decreases from 0·67–0·17 in the harzburgites to 0·25–0·07 in the lherzolites and 0·07–0·03 in the websterites.

To investigate small-scale heterogeneity in mineral compositions, we performed detailed EPMA analyses of pyroxenes in two samples: the harzburgite 07RV13B and the lherzolite 07RV12Cw (Table 3). These samples were

Table 1: Whole-rock major-element and modal compositions of the studied Ronda peridotites and websterites

Rock type:	Lherzolite													
Sample:	RTR-V2	RTR-V4	RTR-V5	RTR-V7	RTR-V9	RTR-V12	RTR-V13	RTR-V14	RTR-V15	RTR-V36	RTR-V37	RTR-V39	RTR-V40	RTR-V43
wt %														
SiO_2	39·80	43·61	44·17	43·76	42·75	41·69	43·96	43·73	42·77	42·75	38·47	43·47	41·91	42·81
TiO_2	0·10	0·17	0·23	0·04	0·07	0·06	0·18	0·18	0·12	0·14	0·05	0·17	0·06	0·16
Al_2O_3	2·90	3·68	4·48	1·66	2·42	2·17	3·94	3·84	3·02	3·37	1·75	3·75	2·31	3·65
Fe_2O_3	8·16	8·81	9·15	8·39	8·44	8·77	8·54	8·78	8·74	8·66	8·52	8·76	8·46	8·47
MgO	35·18	35·50	33·73	40·27	38·00	37·60	35·59	34·41	36·74	37·62	39·42	34·66	38·27	36·45
CaO	2·36	3·13	3·65	1·60	2·31	1·81	3·57	3·33	2·37	3·02	1·17	3·04	2·24	3·04
Na_2O	0·14	0·26	0·31	0·07	0·14	0·11	0·28	0·28	0·20	0·24	0·08	0·26	0·13	0·25
K_2O	0·01	0·01	0·01	0·01	0·00	0·01	0·01	0·03	0·01	0·00	0·01	0·01	0·01	0·01
MnO	0·13	0·14	0·14	0·13	0·14	0·14	0·14	0·14	0·13	0·13	0·13	0·14	0·13	0·13
NiO	0·27	0·32	0·24	0·28	0·30	0·30	0·26	0·26	0·28	0·24	0·26	0·25	0·26	0·23
Cr_2O_3	0·34	0·33	0·33	0·43	0·35	0·33	0·38	0·34	0·36	0·36	0·42	0·33	0·36	0·37
LOI	11·52	4·92	4·84	4·64	6·11	7·82	4·10	5·53	6·27	4·39	10·54	6·45	6·58	5·44
Total	100·91	100·87	101·29	101·28	101·04	100·83	100·94	100·84	101·02	100·92	100·81	101·30	100·70	100·99
Mg-no.	89·61	88·96	88·05	90·57	90·01	89·56	89·29	88·68	89·37	89·68	90·25	88·78	90·05	89·59
wt %														
Ol %	62·5	54·8	48·5	67·5	53·0	66·2	53·6	51·8	63·5	61·3	77·8	55·2	66·8	58·0
Opx %	23·9	28·5	31·4	26·8	27·8	25·2	27·2	30·4	23·6	22·4	15·0	28·0	22·0	25·2
Cpx %	12·1	15·1	17·7	5·1	17·7	7·9	17·3	16·2	11·5	14·6	5·4	14·9	10·4	14·8
Sp %	1·5	1·6	2·4	0·5	1·5	0·7	1·9	1·6	1·5	1·8	1·7	1·9	0·8	2·0

Rock type:	Lherzolite											
Sample:	RTR-V46	RTR-V47	RTR-V48	RTR-V52	RTR-V19	RTR-V24	RTR-V26	RTR-V29	RTR-V30	RTR-V31	RTR-V32	RTR-V34
wt %												
SiO_2	43·13	42·56	41·93	43·75	44·29	43·80	40·52	43·25	43·09	42·47	42·49	43·71
TiO_2	0·16	0·14	0·15	0·15	0·24	0·19	0·12	0·15	0·09	0·04	0·15	0·16
Al_2O_3	3·41	3·34	3·18	3·16	4·55	3·82	1·84	3·27	2·05	1·21	3·14	3·30
Fe_2O_3	8·66	8·55	8·63	8·55	8·56	9·22	8·05	8·62	9·06	7·98	9·07	8·75
MgO	36·61	37·03	37·19	37·92	33·95	35·53	39·24	35·80	37·44	38·37	36·50	37·12
CaO	2·87	2·85	2·63	2·78	3·90	3·29	1·53	2·56	1·45	1·05	2·54	2·83
Na_2O	0·25	0·23	0·21	0·22	0·33	0·29	0·14	0·19	0·14	0·08	0·22	0·24
K_2O	0·01	0·01	0·01	0·02	0·01	0·01	0·01	0·02	0·01	0·01	0·02	0·01
MnO	0·14	0·13	0·13	0·13	0·13	0·14	0·12	0·13	0·13	0·12	0·13	0·14
NiO	0·25	0·24	0·26	0·24	0·23	0·28	0·26	0·26	0·27	0·27	0·27	0·24
Cr_2O_3	0·34	0·35	0·35	0·35	0·33	0·32	0·35	0·33	0·26	0·30	0·30	0·31
LOI	5·08	5·46	6·43	4·11	4·70	4·27	8·81	6·69	7·26	8·82	5·98	4·50
Total	100·88	100·87	101·11	101·40	101·21	101·17	100·99	101·28	101·25	100·72	100·81	101·31
Mg-no.	89·43	89·65	89·60	89·86	88·81	88·51	90·69	89·25	89·20	90·58	88·95	89·45
wt %												
Ol %	60·7	61·5	63·8	61·8	47·2	55·8	71·8	55·8	64·6	65·6	63·6	60·7
Opx %	23·6	22·7	21·5	23·5	31·5	26·4	20·4	30·9	29·9	27·7	22·3	24·2
Cpx %	14·0	14·0	13·0	13·3	18·9	15·9	6·9	12·2	5·5	6·6	12·4	13·6
Sp %	1·8	1·8	1·8	1·4	2·3	1·9	0·9	1·1	0·0	0·0	1·7	1·5

(continued)

Table 1: Continued

Rock type:	lherzolite						Harzburgite						
Sample:	RTR-V35	07RV-3A	07RV-3C	07RV-10C	07RV-12C	07RV-13A	RTR-V11	RTR-V21	RTR-V23	RTR-V38	RTR-V49	RTR-V51	07RV-3B
wt %													
SiO_2	42·53	41·87	41·59	41·04	42·27	42·54	41·63	42·09	42·07	39·14	39·93	41·82	41·35
TiO_2	0·14	0·12	0·09	0·04	0·07	0·14	0·03	0·08	0·01	0·05	0·04	0·03	0·05
Al_2O_3	2·86	2·93	3·14	1·88	1·50	3·08	0·57	1·58	1·05	0·70	0·70	0·93	0·79
Fe_2O_3	8·64	8·30	7·30	9·13	8·11	8·80	8·37	8·18	8·43	8·37	7·53	7·85	7·52
MgO	36·93	38·21	38·46	38·17	41·87	36·73	40·28	41·21	40·20	40·62	41·04	41·71	41·02
CaO	2·23	2·64	2·75	1·52	1·40	2·56	0·45	1·37	0·81	0·48	0·50	0·85	0·47
Na_2O	0·19	0·19	0·15	0·11	0·11	0·22	0·05	0·12	0·05	0·06	0·06	0·07	0·06
K_2O	0·01	0·00	0·00	0·01	0·00	0·01	0·01	0·00	0·01	0·01	0·01	0·00	0·00
MnO	0·13	0·13	0·12	0·16	0·12	0·13	0·13	0·12	0·13	0·10	0·12	0·12	0·12
NiO	0·25	0·24	0·24	0·28	0·26	0·26	0·39	0·27	0·27	0·27	0·26	0·27	0·27
Cr_2O_3	0·26	0·34	0·35	0·32	0·35	0·29	0·27	0·34	0·28	0·20	0·30	0·31	0·27
LOI	6·58	5·79	6·98	8·47	5·11	5·63	9·12	5·39	8·00	10·94	10·22	6·66	8·58
Total	100·74	100·75	101·18	101·11	101·17	100·40	101·29	100·75	101·31	100·94	100·71	100·62	100·49
Mg-no.	89·53	90·21	91·34	89·32	91·17	89·30	90·59	90·97	90·51	90·66	91·60	91·40	91·60
wt %													
Ol %	64·4	61·8	60·6	70·3	76·4	61·7	76·8	71·7	76·0	77·2	82·7	80·3	76·4
Opx %	23·5	24·2	24·4	22·4	17·6	24·8	21·4	23·3	19·6	20·6	14·4	15·0	21·3
Cpx %	10·8	12·8	13·6	6·6	5·5	12·3	1·5	4·3	3·2	1·7	2·0	3·6	1·6
Sp %	1·3	1·2	1·4	0·7	0·5	1·2	0·3	0·8	1·2	0·4	0·9	1·1	0·7

Rock type:	Harzburgite												Websterite
Sample:	07RV-3D	RTR-V3	RTR-V6	RTR-V8	07RV-10A	07RV-10B	07RV-10D	07RV-12A	07RV-12B	07RV-13B	07RV-13D	07RV-13E	07RV-13C
wt %													
SiO_2	40·74	43·93	42·71	42·31	40·56	40·80	42·85	41·05	40·99	40·27	39·71	39·11	43·15
TiO_2	0·02	0·06	0·04	0·04	0·02	0·03	0·07	0·03	0·08	0·05	0·04	0·03	0·26
Al_2O_3	0·64	0·99	0·83	1·13	0·61	1·49	1·77	0·26	1·10	0·68	0·56	0·42	7·48
Fe_2O_3	7·14	8·53	8·21	8·34	8·05	8·67	8·31	7·60	8·53	8·06	8·04	7·95	8·11
MgO	40·93	41·07	40·14	39·25	42·21	41·60	41·17	44·67	43·35	42·53	41·59	40·43	29·66
CaO	0·44	0·51	0·66	0·77	0·53	1·10	1·45	0·18	0·55	0·63	0·57	0·39	6·10
Na_2O	0·05	0·08	0·06	0·05	0·06	0·10	0·14	0·05	0·08	0·06	0·06	0·05	0·44
K_2O	0·00	0·01	0·01	0·01	0·00	0·01	0·00	0·00	0·00	0·00	0·00	0·01	0·01
MnO	0·12	0·12	0·13	0·13	0·12	0·13	0·12	0·11	0·13	0·12	0·12	0·12	0·13
NiO	0·26	0·30	0·29	0·29	0·27	0·27	0·26	0·29	0·27	0·27	0·28	0·27	0·17
Cr_2O_3	0·29	0·32	0·33	0·34	0·29	0·39	0·33	0·20	0·19	0·34	0·32	0·25	0·46
LOI	10·28	4·92	7·12	8·04	8·41	6·83	5·21	6·65	6·33	7·06	8·01	10·74	4·63
Total	100·90	100·84	100·52	100·69	101·14	101·43	101·67	101·09	101·58	100·08	99·29	99·76	100·60
Mg-no.	91·98	90·60	90·73	90·40	91·29	90·56	90·84	92·16	91·04	91·34	91·18	91·05	87·97
wt %													
Ol %	77·0	77·7	73·1	67·3	84·4	76·2	69·7	88·2	82·6	82·6	81·4	81·7	25·6
Opx %	21·0	19·5	23·6	28·4	12·5	19·2	25·2	10·5	15·3	13·9	15·4	16·5	37·7
Cpx %	1·5	1·8	2·4	4·0	1·8	3·6	4·4	0·4	1·6	2·4	2·3	1·4	31·2
Sp %	0·5	1·0	0·9	0·3	1·3	1·0	0·8	0·9	0·4	1·2	0·9	0·4	5·4

The modes were reconstructed by mass-balance of whole-rock and mineral major-element compositions, using the total inversion method of Tarantola & Valette (1982). LOI, loss on ignition; ol, olivine; opx, orthopyroxene; cpx, clinopyroxene; Sp, spinel; Mg-number = Mg/(Mg + Fe) cationic ratio.

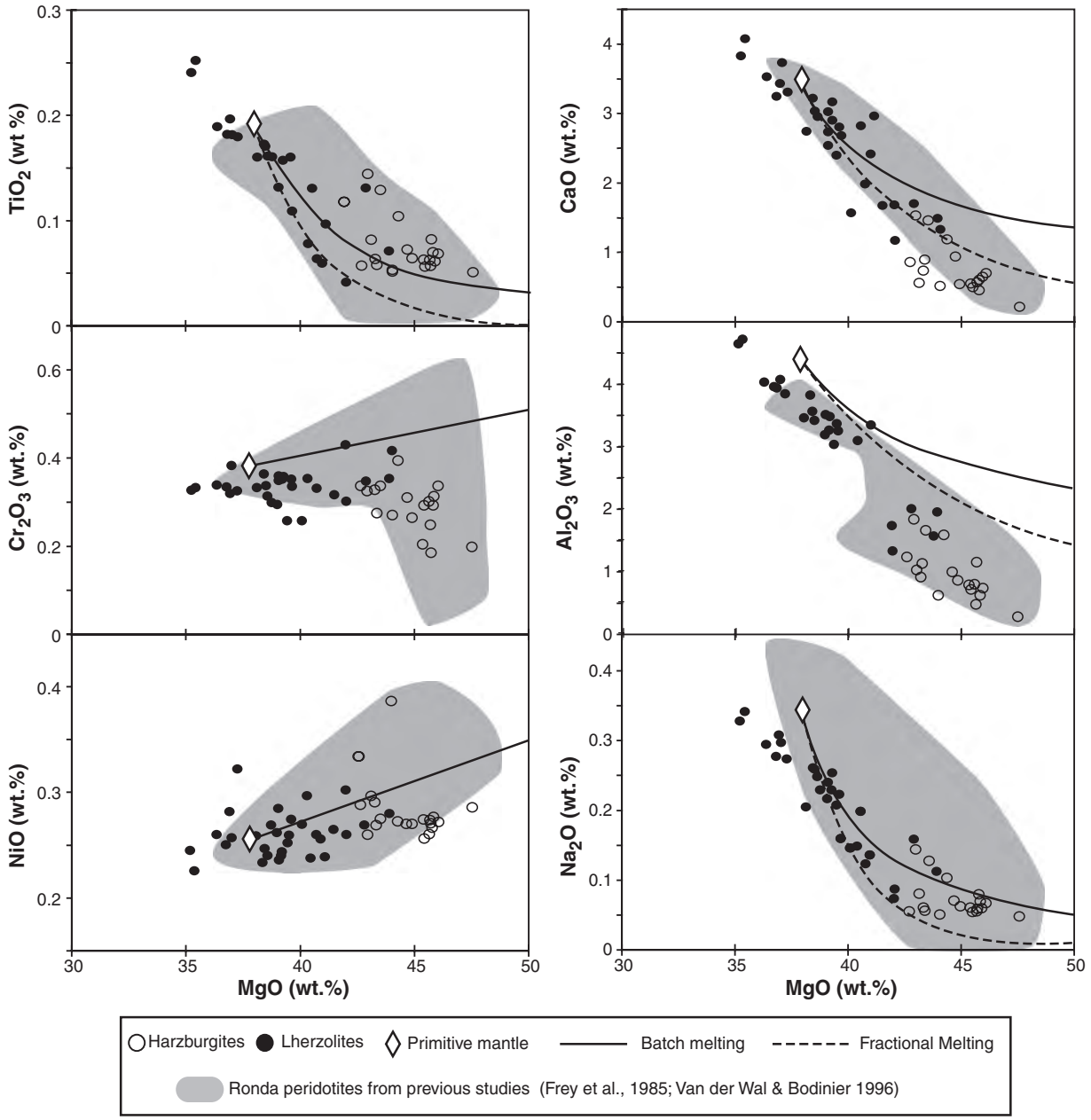

Fig. 8. Covariation diagrams for major (CaO, Al_2O_3) and minor (Na_2O, TiO_2, Cr_2O_3, NiO) elements vs MgO (wt %) in the studied peridotites, compared with major- and minor-element compositions in the entire Ronda peridotite massif (Frey *et al.*, 1985; Van der Wal & Bodinier 1996) and with the evolution predicted by batch and fractional melting models (Gast, 1968; Shaw, 1970). Primitive upper mantle composition from McDonough & Sun (1995).

selected because they show unambiguous evidence for coexisting primary and secondary pyroxenes, hence allowing a search for chemical variations related to interaction with percolating melts. No significant variation was observed between the various pyroxenes types. The only small-scale variations observed within and between grains are those classically ascribed to cooling, notably the opposite core-to-rim variations of CaO in opx and cpx.

RARE EARTH ELEMENTS IN CLINOPYROXENE

In situ trace-element analyses of clinopyroxenes were performed by laser ablation induced coupled plasma mass spectroscopy (LA-ICP-MS) on thick (*c.* 150 μm) sections at the AETE facility, Geosciences Montpellier, using a single-collector double-focusing sector field Element XR

Table 2: Major-element compositions of minerals from the studied Ronda peridotites and websterites

	07RV3A Lherzolite				07RV3C Lherzolite				07RV6 Lherzolite				07RV12Cw Lherzolite				07RV12D Lherzolite			
	Ol	Opx	Cpx	Spl	Ol	Opx	Cpx	Spl	Ol	Opx	Cpx	Spl	Ol	Opx	Cpx	Spl	Ol	Opx	Cpx	Spl
Crystal:	0	4	3	3	3	3	4	3	2	5	3	3	3	3	4	3	3	3	3	3
wt %																				
Al_2O_3	—	5·4	7·4	57·4	—	5·7	7·2	59·1	0·0	5·6	7·6	57·6	—	4·2	6·1	48·5	—	4·1	5·5	46·5
SiO_2	—	54·3	51·8	0·2	41·0	54·3	51·2	0·2	40·9	54·3	51·6	0·2	41·0	55·0	51·4	0·2	41·5	55·4	52·3	0·2
TiO_2	—	0·14	0·53	0·05	—	0·12	0·43	0·05	0·01	0·15	0·64	0·06	—	0·12	0·45	0·08	—	0·09	0·30	0·07
Na_2O	—	0·08	1·90	—	—	0·06	1·35	0·01	—	0·08	2·07	—	—	0·03	1·34	—	0·01	0·06	1·41	—
MgO	—	32·0	14·4	19·4	49·0	32·2	14·6	20·1	47·7	31·6	13·8	19·0	48·7	32·8	14·8	17·8	48·0	32·0	14·7	16·8
FeO	—	6·1	2·3	10·5	8·7	5·5	2·0	9·2	9·9	6·4	2·5	11·0	9·0	5·7	2·0	11·5	8·8	5·8	2·1	11·7
MnO	—	0·15	0·10	0·12	0·13	0·12	0·08	0·09	0·14	0·15	0·07	0·11	0·14	0·14	0·09	0·17	0·13	0·15	0·09	0·16
K_2O	—	—	—	—	0·02	—	—	0·01	—	0·01	0·02	—	—	—	—	—	—	—	—	0·01
CaO	—	0·8	20·1	—	0·0	0·8	21·3	0·0	0·0	0·7	19·9	0·0	—	0·4	21·2	—	0·0	0·7	21·6	0·0
Cr_2O_3	—	0·52	0·98	10·57	—	0·47	0·81	8·96	—	0·46	0·83	9·93	—	0·70	1·44	20·00	0·01	0·66	1·36	21·57
NiO	—	0·09	0·03	0·34	0·36	0·09	0·04	0·33	0·35	0·09	0·05	0·35	0·39	0·12	0·03	0·23	0·36	0·07	0·03	0·20
Total	—	99·54	99·63	98·52	99·23	99·41	99·01	97·97	99·13	99·50	99·21	98·37	99·26	99·20	98·89	98·54	98·80	99·03	99·31	97·18
Standard deviation (wt %)																				
Al_2O_3	—	0·5	0·3	0·6	—	0·4	0·3	0·6	0·0	0·8	0·1	0·5	—	1·0	0·3	0·6	—	0·3	0·2	0·7
SiO_2	—	0·4	0·1	0·0	0·1	0·4	0·5	0·0	0·5	0·4	0·1	0·0	0·2	0·4	0·4	0·0	0·4	0·3	0·4	0·0
TiO_2	—	0·04	0·04	0·02	—	0·03	0·04	0·02	0·01	0·02	0·12	0·02	—	0·05	0·03	0·02	—	0·01	0·02	0·02
Na_2O	—	0·03	0·07	0·02	—	0·03	0·07	0·01	—	0·02	0·09	—	—	0·01	0·06	—	0·01	0·01	0·07	—
MgO	—	0·4	0·2	0·3	0·2	0·4	0·3	0·4	0·3	0·4	0·3	0·1	0·1	0·7	0·5	0·1	0·6	0·4	0·2	0·3
FeO	—	0·1	0·1	0·3	0·0	0·2	0·1	0·6	0·2	0·1	0·3	0·2	0·1	0·1	0·2	0·2	0·2	0·0	0·1	0·3
MnO	—	0·02	0·02	0·01	0·02	0·01	0·01	0·02	—	0·02	0·01	0·03	0·02	—	0·01	0·01	0·01	0·01	0·01	—
K_2O	—	—	—	—	0·02	0·02	—	0·02	—	0·02	0·03	—	—	—	—	—	—	—	—	0·01
CaO	—	0·2	0·2	—	0·0	—	—	0·0	—	0·2	0·7	—	—	0·3	0·6	—	0·0	3·0	0·2	—
Cr_2O_3	—	0·09	0·07	0·44	—	0·03	0·05	0·18	0·01	0·11	0·05	0·59	—	0·13	0·08	0·54	0·01	0·09	0·08	1·11
NiO	—	0·02	—	0·02	0·02	0·02	0·02	0·03	0·03	0·01	0·02	0·02	0·01	0·01	0·01	0·02	0·02	0·00	0·00	0·01

(continued)

Table 2: Continued

	07RV13A Lherzolite				07RV3B Harzburgite				07RV3C Harzburgite				07RV12A Harzburgite				07RV12Bc Harzburgite			
	Ol	Opx	Cpx	Spl	Ol	Opx	Cpx	Spl	Ol	Opx	Cpx	Spl	Ol	Opx	Cpx	Spl	Ol	Opx	Cpx	Spl
Crystal:	3	3	3	4	3	3	3	3	3	3	3	3	5	2	1	2	4	3	2	5
wt %																				
Al_2O_3	—	6·1	7·9	58·5	—	3·4	5·2	44·8	—	2·2	2·8	31·0	—	1·3	1·5	17·6	—	4·7	6·7	50·5
SiO_2	41·1	53·9	51·5	0·2	41·3	55·9	52·6	0·2	41·3	56·6	53·8	0·2	41·3	56·9	54·0	0·2	41·1	54·4	50·6	0·2
TiO_2	—	0·18	0·61	0·08	—	0·06	0·19	0·05	—	0·04	0·11	0·07	—	0·03	0·02	0·04	0·01	0·24	0·84	0·07
Na_2O	0·01	0·10	2·12	—	—	0·15	1·57	—	—	0·04	1·06	—	0·01	0·06	0·59	—	0·01	0·14	1·53	—
MgO	47·7	30·9	13·7	19·2	49·1	32·6	15·0	17·0	49·7	34·0	16·6	13·9	49·6	34·2	17·3	11·9	48·6	31·8	15·3	17·9
FeO	10·1	6·4	2·7	11·2	8·4	5·3	1·9	12·0	7·9	5·0	1·7	15·1	7·8	4·9	1·9	16·2	8·9	5·5	2·1	11·3
MnO	0·14	0·16	0·10	0·11	0·11	0·12	0·08	0·18	0·11	0·13	0·08	0·24	0·12	0·13	0·05	0·29	0·14	0·13	0·07	0·14
K_2O	—	—	0·02	0·01	—	—	—	—	—	—	—	—	—	—	—	—	—	0·01	—	—
CaO	0·0	1·0	19·9	0·0	0·0	1·0	20·8	—	0·0	0·8	22·0	—	0·0	0·8	22·6	—	0·0	1·4	20·0	—
Cr_2O_3	—	0·47	0·81	8·67	—	0·76	1·59	23·86	0·01	0·67	1·36	37·72	0·01	0·64	0·99	51·78	0·00	0·71	1·32	17·96
NiO	0·36	0·09	0·05	0·40	0·39	0·08	0·04	0·20	0·39	0·09	0·05	0·07	0·37	0·09	0·07	0·06	0·35	0·09	0·04	0·23
Total	99·34	99·29	99·42	98·46	99·30	99·35	98·97	98·34	99·46	99·60	99·54	98·20	99·24	99·07	99·02	98·01	99·16	99·24	98·44	98·30
Standard deviation (wt %)																				
Al_2O_3	—	0·1	0·2	1·0	—	0·5	1·3	9·3	—	0·3	0·2	4·2	—	0·1	—	17·6	—	0·3	0·4	1·3
SiO_2	0·2	0·3	0·3	0·0	0·0	0·3	0·5	0·0	0·1	0·3	0·2	0·0	0·3	0·1	—	0·2	0·2	0·4	0·6	0·0
TiO_2	—	0·04	0·03	0·02	—	0·02	0·07	0·04	—	0·01	0·02	0·02	—	0·01	—	0·04	0·01	0·05	0·13	0·03
Na_2O	0·01	0·05	0·09	—	—	0·16	0·05	—	—	0·02	0·06	—	0·00	0·03	—	—	0·01	0·06	0·14	—
MgO	0·1	0·6	0·5	0·3	0·2	0·5	0·6	2·2	0·2	0·4	0·2	0·6	0·2	0·0	—	11·9	0·2	0·4	0·4	0·3
FeO	0·2	0·1	0·3	0·4	0·2	0·2	0·1	2·3	0·1	0·1	0·1	0·6	0·2	0·1	—	16·2	0·1	0·2	0·0	0·3
MnO	0·01	0·01	0·01	0·00	0·01	0·02	0·02	0·03	0·01	0·01	—	0·03	0·01	0·02	—	0·29	0·02	0·01	0·02	0·02
K_2O	—	—	0·02	0·02	—	—	—	—	—	—	—	—	—	—	—	—	—	0·02	—	—
CaO	0·0	0·7	0·7	0·0	0·0	0·6	0·2	—	0·0	0·2	0·3	—	0·0	0·0	—	—	0·0	0·6	0·5	—
Cr_2O_3	—	0·02	0·09	0·91	—	0·20	0·32	9·04	0·01	0·09	0·16	4·37	0·01	0·04	—	51·78	0·02	0·12	0·04	1·24
NiO	0·01	0·02	0·01	0·03	0·03	—	0·02	0·09	0·01	0·01	0·02	0·02	0·02	0·00	—	0·06	0·02	0·01	0·02	0·03

(continued)

Table 2: Continued

	07RV12Ce Harzburgite				07RV13B Harzburgite				07RV13D Harzburgite				07RV12Be Websterite				07RV13C Websterite			
	Ol	Opx	Cpx	Spl	Ol	Opx	Cpx	Spl	Ol	Opx	Cpx	Spl	Ol	Opx	Cpx	Spl	Ol	Opx	Cpx	Spl
Crystal:	3	2	4	3	3	3	3	3	3	3	3	3	2	3	4	3	3	3	3	4
wt %																				
Al_2O_3	—	4·3	5·3	45·2	—	2·1	2·6	25·9	—	2·4	2·6	26·4	0·0	5·9	7·8	63·6	—	5·9	7·8	61·3
SiO_2	41·3	55·1	52·1	0·2	41·2	56·5	53·0	0·2	41·1	56·1	53·4	0·2	40·9	53·9	50·7	0·3	40·8	53·8	50·9	0·3
TiO_2	—	0·09	0·24	0·06	—	0·06	0·10	0·20	—	0·03	0·07	0·13	0·01	0·17	0·61	0·03	—	0·14	0·55	0·05
Na_2O	—	0·17	1·41	—	—	0·04	0·66	—	0·01	0·02	0·74	—	0·01	0·11	1·11	—	—	0·04	1·66	—
MgO	49·1	32·9	15·4	17·0	49·0	33·4	16·8	13·0	49·0	33·4	16·9	12·8	48·4	31·3	14·15	21·2	46·6	30·9	14·2	19·0
FeO	8·4	5·2	2·2	12·1	8·5	5·5	2·3	17·7	8·5	5·6	2·3	17·9	9·0	5·7	2·2	8·4	11·3	7·4	3·2	12·4
MnO	0·11	0·13	0·07	0·18	0·12	0·13	0·08	0·28	0·14	0·15	0·08	0·28	0·13	0·13	0·10	0·09	0·15	0·16	0·10	0·11
K_2O	—	0·02	—	—	—	—	—	—	—	—	—	—	—	0·01	—	—	—	—	0·01	—
CaO	0·0	1·0	20·3	—	0·0	1·0	21·8	—	0·0	0·7	21·7	—	0·0	1·3	22·12	—	0·0	0·7	19·9	—
Cr_2O_3	—	1·19	1·51	23·62	—	0·54	1·08	40·85	0·01	0·70	1·08	40·44	—	0·28	0·44	4·65	0·01	0·26	0·50	5·36
NiO	0·39	0·09	0·03	0·19	0·37	0·09	0·05	0·11	0·37	0·08	0·07	0·11	0·38	0·09	0·04	0·38	0·32	0·10	0·03	0·42
Total	99·30	98·71	98·57	98·66	99·16	99·34	98·61	98·31	99·07	99·14	98·94	98·27	98·89	98·84	99·26	98·64	99·15	99·29	98·76	98·89
Standard deviation (wt %)																				
Al_2O_3	—	0·4	0·2	1·6	—	0·0	0·2	0·3	—	0·2	0·2	1·1	0·0	0·3	1·1	1·1	—	0·4	0·1	1·8
SiO_2	0·0	0·4	0·3	0·0	0·1	0·2	0·0	0·0	0·3	0·3	0·0	0·0	0·1	0·8	0·6	0·0	0·2	0·5	0·6	0·0
TiO_2	—	0·03	0·01	0·02	—	0·01	0·01	0·02	—	0·01	0·02	0·01	0·01	0·05	0·11	0·02	—	0·02	0·10	0·01
Na_2O	—	0·15	0·07	—	—	0·02	0·07	0·02	0·03	0·01	0·04	—	0·02	0·08	0·26	—	—	0·03	0·11	—
MgO	0·2	1·7	1·0	0·2	0·1	0·3	0·4	0·0	0·1	0·1	0·3	0·4	0·1	0·8	0·4	0·3	0·4	0·2	0·4	0·5
FeO	0·2	0·4	0·4	0·2	0·1	0·0	0·1	0·2	0·1	0·1	0·1	0·3	0·0	0·2	0·5	0·2	0·4	0·3	0·2	0·9
MnO	0·01	0·01	0·02	0·01	0·02	0·02	0·02	0·02	0·02	0·01	0·02	0·03	—	0·02	0·02	0·01	0·03	0·01	0·01	0·01
K_2O	—	0·03	—	—	—	—	—	—	—	—	—	—	—	0·01	—	—	—	—	0·02	—
CaO	0·0	0·45	1·8	—	0·0	0·4	0·2	—	—	0·0	0·4	—	0·0	0·6	0·2	—	—	0·1	0·2	—
Cr_2O_3	—	0·19	0·06	1·76	—	0·02	0·10	0·44	0·01	0·13	0·14	0·89	—	0·10	0·11	1·14	—	0·10	0·16	1·51
NiO	0·03	0·01	0·01	0·01	0·01	0·00	0·01	0·01	0·03	0·02	0·03	0·03	0·01	0·01	0·01	0·03	0·02	0·02	—	0·03

'Crystal' indicates number of analysed crystals. Ol, olivine; Opx, orthopyroxene; Cpx, clinopyroxene; Sp, spinel.

Table 3: Major- and minor-element concentrations (in wt %) in pyroxenes as a function of their texture in one lherzolite and one harzburgite

	07RV12Cw; lherzolite													
Group:	Primary									Secondary				
	opx1(c)	opx1(r)	opx2	cpx1(c)	cpx1(r)	cpx2(c)	cpx2(r)	cpx3(c)	cpx3(r)	opx1	opx2	opx3	cpx1	cpx2
SiO_2	55·24	55·67	55·60	51·98	51·36	51·78	52·98	51·65	52·03	55·52	55·07	56·09	51·80	51·76
Al_2O_3	4·05	3·71	3·99	6·00	5·79	5·69	3·75	6·26	5·30	4·08	4·18	3·26	5·96	6·10
Na_2O	0·09	0·03	0·05	1·43	1·16	1·34	0·90	1·53	1·22	0·04	0·07	0·04	1·31	1·32
MgO	32·41	32·93	32·77	14·64	15·15	14·90	15·95	14·55	15·28	32·37	32·50	33·17	14·89	14·82
MnO	0·15	0·17	0·14	0·08	0·07	0·10	0·09	0·09	0·09	0·16	0·16	0·13	0·08	0·09
FeO	5·84	5·81	5·95	2·15	2·07	1·97	2·08	2·09	2·08	5·93	5·83	5·86	2·30	1·94
K_2O	0·02	0·00	0·00	0·00	0·00	0·01	0·00	0·00	0·01	0·00	0·00	0·00	0·01	0·00
CaO	0·84	0·58	0·65	21·55	21·42	21·77	22·72	21·39	21·82	0·85	0·95	0·66	21·65	21·98
NiO	0·04	0·05	0·07	0·02	0·02	0·04	0·03	0·05	0·06	0·08	0·11	0·06	0·06	0·03
Cr_2O_3	0·61	0·50	0·61	1·47	1·31	1·46	0·91	1·57	1·13	0·63	0·66	0·57	1·31	1·47
TiO_2	0·11	0·09	0·12	0·43	0·43	0·47	0·27	0·46	0·41	0·13	0·09	0·10	0·52	0·48
Total	99·40	99·54	99·95	99·75	98·75	99·53	99·67	99·64	99·42	99·79	99·61	99·94	99·89	99·99

	07RV13B; harzburgite						
Group:	Primary			Secondary			
	opx1(c)	opx1(r)	opx2	opx1	opx2	cpx1	cpx2
SiO_2	56·64	57·02	56·63	56·59	56·79	52·81	53·12
Al_2O_3	2·32	1·93	2·16	2·11	2·18	2·82	2·85
Na_2O	0·03	0·00	0·03	0·04	0·04	0·83	0·85
MgO	33·37	33·86	33·54	33·54	33·72	16·48	16·26
MnO	0·12	0·15	0·14	0·15	0·16	0·08	0·08
FeO	5·76	5·74	5·87	5·86	5·90	2·26	2·15
K_2O	0·00	0·00	0·01	0·00	0·00	0·00	0·00
CaO	0·93	0·66	0·84	0·85	0·70	22·52	22·76
NiO	0·08	0·08	0·07	0·08	0·06	0·06	0·03
Cr_2O_3	0·65	0·51	0·58	0·53	0·51	1·38	1·22
TiO_2	0·07	0·05	0·06	0·05	0·04	0·13	0·12
Total	99·99	100·00	99·94	99·80	100·12	99·37	99·45

'Group' indicates textural group; c, core; r, rim.

(eXtended Range) high-resolution (HR-) ICP-MS system, coupled with a Geolas (Microlas) automated platform housing a ArF 193 nm Compex 102 laser from LambdaPhysik. Measurements were conducted in an ablation cell of *c.* 30 cm^3 in a He atmosphere, which enhances the sensitivity and reduces inter-element fractionation (Günther & Heinrich, 1999). The helium gas stream and particles from the sample were mixed with Ar before entering the plasma. Data were acquired in the fast E-scan mode at low resolution (M/DM = 300). Signals were measured in Time Resolved Acquisition (TRA) mode, devoting 2 min for the blank, and 1 min for cpx analysis. The laser was fired using an energy density of 15 J/cm^2 at a frequency of 5 Hz and using a spot size of 77 μm. Oxide level, measured using the ThO/Th ratio, was below 0·7%. ^{43}Ca was used as an internal standard and the concentrations were calibrated against the NIST 612 rhyolitic glass using the values given by Pearce *et al.* (1997). Data were

subsequently reduced using the GLITTER software (Van Achterbergh *et al.*, 2001) by carefully inspecting the time-resolved analysis to check for absence of heterogeneities (inclusions or fractures) in the analysed volume. Representative mineral analyses are reported in Tables 2 and 4.

Although fairly constant within samples, rare earth elements (REE) in cpx show extreme variations between the different samples, in the range 2–100 times chondritic abundances (Fig. 9). There is no significant correlation with modal and major-element compositions, but two compositional groups are clearly distinguished on the basis of REE abundances, particularly the light REE (LREE) contents.

The first group (samples 07RV3C, 07RV6, 07RV10B, 07RV12Bc, 07RV12Cw and 07RV13A—referred to as 'normal-type' clinopyroxenes in the following discussion) has REE concentrations below 10× chondrite and LREE (La–Ce) below 5× chondrite. This group shows nearly constant LREE concentrations (chondrite-normalized La content, $La_N = 2{\cdot}3$–3) and more variable heavy REE (HREE) concentrations ($Yb_N = 2{\cdot}5$–9). The most HREE-enriched clinopyroxenes display the 'MORB-type' (mid-ocean ridge basalt type) REE pattern that is typical of whole-rock and clinopyroxene compositions in the vast majority of orogenic lherzolites and several suites of spinel-bearing mantle xenoliths worldwide (McDonough & Frey, 1989*a*). HREE-depleted clinopyroxenes show convex-upward ('hump-shaped') REE patterns, a signature that is commonly ascribed to metasomatic enrichment of relatively refractory (HREE-depleted) peridotites (Bodinier & Godard, 2003; Bodinier *et al.*, 2008). Variations of HREE at nearly constant LREE content have been previously observed in orogenic peridotites, both in whole-rocks and clinopyroxenes (Fabriès *et al.*, 1989; McDonough & Frey, 1989*a*; Downes *et al.*, 1991). In most cases, however, these variations are coupled with modal changes from lherzolites (high HREE) to harzburgites (low HREE). Such a relationship is not observed in our dataset; the most HREE-enriched clinopyroxenes are from two lherzolites (samples 07RV6 and 07RV13A), but very similar REE contents were obtained for clinopyroxenes from the harzburgite 07RV10B. Moreover, the most HREE-depleted clinopyroxenes are from lherzolites (samples 07RV3C and 07RV12Cw).

The second group (samples 07RV17, 07RV13B, 07RV13C and 07RV13D—referred to as 'enriched-type' clinopyroxenes subsequently) has REE concentrations generally above 10× chondrite and LREE (La–Ce) above 25× chondrite; that is, more than 10 times higher than the LREE content of 'normal-type' clinopyroxenes. The 'enriched-type' clinopyroxene patterns nevertheless resemble the former group in terms of their relatively narrow range of LREE variation ($La_N = 26$–57), compared with HREE ($Yb_N = 10{\cdot}5$–100). This group also shows a subtle, but significant positive Eu anomaly. The selective enrichment of LREE and middle REE (MREE) observed in the harzburgites 07RV13D and 07RV13B has been frequently reported from mantle xenoliths, where it is generally ascribed to metasomatism by volatile-rich (e.g. carbonated) small-volume melts (e.g. Ionov *et al.*, 2002). However, the overall REE enrichment observed in samples 07RV13C and 07RV17 and the selective LREE enrichment are rare in orogenic peridotites. A noticeable exception is the Lherz massif (French Pyrenees) where both types of enrichment have been observed and interpreted as marking melt percolation fronts both at small scale, in the vicinity of alkaline veins (Bodinier *et al.*, 1990, 2004), and at larger scale, at the transition between harzburgites and lherzolites (Le Roux *et al.*, 2007).

Clinopyroxenes in sample 07RV1, a clinopyroxene-poor lherzolite from the coarse-granular domain analysed for comparison, show the MORB-type REE pattern typical of 'normal-type' clinopyroxenes (Fig. 9). This sample is, however, more depleted in LREE than any of the clinopyroxenes from the study area ($La_N = 1{\cdot}3$, compared with $2{\cdot}3$–3 for the 'normal-type' clinopyroxenes).

DISCUSSION

Melt–rock interactions

The present study highlights that, in the study area, the Ronda spinel tectonite domain is predominantly composed of lherzolites containing elongated bodies of harzburgite, metres to tens of metres wide, and centimetre-scale websterite bands (Fig. 2). Metre-scale lherzolite–harzburgite intercalations similar to those observed in the Ronda spinel tectonites have been described in other orogenic peridotite massifs, notably in Horoman and Lherz. These alternations were ascribed to compaction–decompaction of partially molten peridotites (Obata & Nagahara, 1987), partial melting followed by convective mingling of fertile and residual components (Toramaru *et al.*, 2001), focused melt flow (Bodinier *et al.*, 1988), mingling of asthenospheric and lithospheric mantle components (Bodinier & Godard, 2003), or refertilization of a refractory lithosphere by basaltic magmas (Saal *et al.*, 2001). The last hypothesis has been corroborated by a recent joint petrostructural and geochemical study of the Lherz massif, which confirms that igneous refertilization via reactive melt percolation is a very effective process to produce metre- to hectometre-scale compositional heterogeneity in the lithospheric mantle (Le Roux *et al.*, 2007).

Whereas partial melting and olivine-forming reactions consume pyroxenes and spinel and produce melt (±olivine), the refertilization reactions are characterized by olivine dissolution and pyroxene (±spinel) crystallization. Petrographic evidence for refertilization reactions is

Table 4: REE average contents (in ppm) in clinopyroxenes from the most representative samples

	Group 1											
Sample:	07RV3C		07RV6		07RV-10B		07RV-12Bc		07RV-12Cw		07RV-13A	
	n = 5	SD	*n* = 10	SD	*n* = 5	SD	*n* = 7	SD	*n* = 9	SD	*n* = 10	SD
La	0·92	0·04	1·10	0·06	0·92	0·02	0·84	0·07	0·86	0·10	1·07	0·03
Ce	3·63	0·25	4·06	0·18	2·94	0·06	3·62	0·25	3·53	0·39	4·05	0·10
Pr	0·64	0·04	0·76	0·05	0·51	0·01	0·72	0·05	0·66	0·07	0·75	0·02
Nd	3·62	0·17	4·70	0·34	2·99	0·09	4·45	0·28	3·80	0·42	4·57	0·10
Sm	1·12	0·03	1·81	0·06	1·26	0·05	1·76	0·12	1·37	0·17	1·84	0·04
Eu	0·45	0·02	0·76	0·03	0·54	0·01	0·74	0·06	0·56	0·07	0·76	0·02
Gd	1·31	0·04	2·77	0·14	2·20	0·07	2·54	0·15	1·93	0·20	2·76	0·05
Tb	0·20	0·01	0·51	0·02	0·42	0·01	0·44	0·03	0·33	0·03	0·50	0·01
Dy	1·34	0·04	3·65	0·22	3·25	0·08	3·06	0·14	2·26	0·17	3·69	0·09
Ho	0·25	0·01	0·80	0·06	0·71	0·02	0·61	0·03	0·45	0·03	0·80	0·02
Er	0·68	0·02	2·34	0·08	2·08	0·08	1·68	0·07	1·19	0·08	2·31	0·08
Tm	0·10	0·00	0·34	0·02	0·30	0·01	0·23	0·01	0·16	0·01	0·33	0·01
Yb	0·63	0·02	2·24	0·15	1·96	0·05	1·47	0·08	1·01	0·06	2·23	0·07
Lu	0·09	0·00	0·32	0·02	0·27	0·01	0·20	0·01	0·14	0·01	0·32	0·01

	Group 2									
Sample:	07RV13B		07RV13C		07RV13D		07RV17		07RV1	
	n = 3	SD	*n* = 7	SD	*n* = 4	SD	*n* = 6	SD	*n* = 6	SD
La	11·39	1·04	21·27	1·14	9·88	0·33	18·33	0·94	0·49	0·06
Ce	37·71	2·32	69·84	4·33	30·28	2·83	58·64	3·32	1·91	0·19
Pr	7·30	0·30	11·13	0·89	5·82	0·15	10·13	0·53	0·37	0·04
Nd	45·35	1·72	62·35	6·22	38·71	2·07	61·93	3·10	2·35	0·30
Sm	14·18	0·54	20·09	2·58	12·39	0·76	24·03	1·73	1·11	0·12
Eu	5·24	0·20	8·32	1·04	4·40	0·21	10·70	0·57	0·46	0·06
Gd	12·00	0·38	21·58	3·74	9·05	0·80	32·44	1·38	1·89	0·25
Tb	1·61	0·06	3·71	0·58	1·12	0·07	6·27	0·35	0·36	0·05
Dy	8·71	0·22	24·54	3·59	5·51	0·33	42·75	1·56	2·76	0·36
Ho	1·44	0·04	5·02	0·52	0·90	0·08	9·13	0·33	0·60	0·08
Er	3·48	0·12	13·86	1·19	2·29	0·12	25·78	0·97	1·76	0·25
Tm	0·53	0·03	1·98	0·17	0·38	0·02	3·67	0·14	0·24	0·03
Yb	3·47	0·13	13·52	1·14	2·87	0·15	24·83	0·77	1·65	0·22
Lu	0·59	0·01	1·98	0·14	0·48	0·05	3·58	0·14	0·23	0·03

n, number of analysed clinopyroxenes. SD, standard deviation.

common in the studied peridotites, in the form of undeformed interstitial opx and cpx in harzburgites and cpx-poor lherzolites and/or cpx–opx–sp aggregates in lherzolites (Fig. 5).

Geochemical data also display characteristics that are not consistent with simple evolution as a result of partial melting and are more readily explained by reactive porous melt flow, as follows.

(1) The concentration of minor elements in whole-rocks, such as Ti, shows a dispersed linear correlation with fertility markers, such as Mg contents (Fig. 8) or the modal proportion of cpx (Fig. 10).

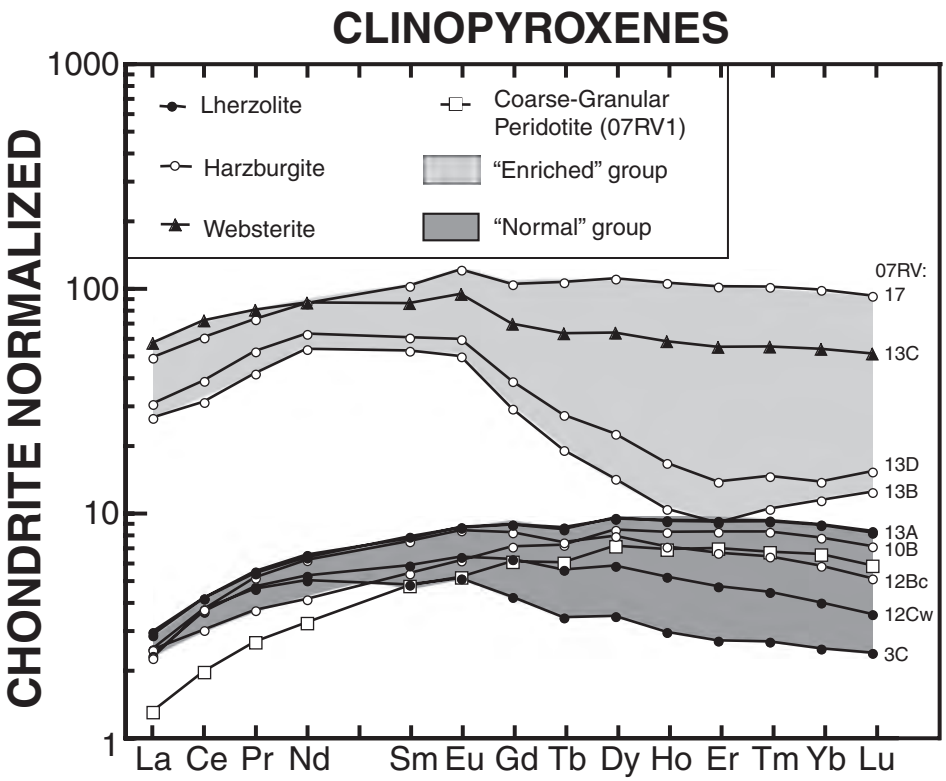

Fig. 9. Chondrite-normalized REE patterns (Sun & McDonough, 1989) of clinopyroxene in nine representative peridotites and one websterite from the spinel tectonite domain and in a peridotite from the coarse-granular domain at the eastern limit of the study area.

(2) HREE contents in cpx are highly variable, in contrast to nearly constant LREE concentrations (Fig. 9).
(3) Some peridotites (group 2—Fig. 9) show abnormally REE-enriched cpx compositions.

We propose that percolation of melt and melt–rock reactions may account for these geochemical particularities. Numerical simulation of Ti and REE variations involving a wide range of melt–rock interactions indicates that the following processes were active in the study area, with decreasing order of importance from (1) to (3):

(1) melt percolation associated with refertilization reactions; that is, melt–rock reactions at decreasing melt mass that involve olivine dissolution and pyroxene (±spinel) precipitation;
(2) further percolation of variably reacted melt without significant mineralogical reactions;
(3) percolative fractional crystallization of interstitial pyroxenes reflecting the final solidification of evolved, small melt fractions after the main refertilization reaction.

Igneous refertilization

The predominance of the igneous refertilization process in the studied peridotites is illustrated by the dispersed linear correlation between Ti contents and cpx modal proportions (Fig. 10). To compare the effects of melt-consuming, refertilization reactions with those of partial melting, we first modelled the variation in Ti content and cpx modal proportion using batch and fractional melting models (Gast, 1968; Shaw, 1970). As shown in Fig. 10a, partial melting models yield curved trajectories for the Ti vs cpx co-variation that do not fit the dispersed linear correlation observed in our samples.

To simulate igneous refertilization, the Plate Model of Vernières *et al.* (1997) was used in a configuration where a percolation column made of discrete reaction cells is affected by a pyroxene-forming, melt-consuming reaction. The reaction is monitored by the parameter R that stands for the mass ratio of newly crystallized minerals to infiltrated melt (see Bodinier *et al.*, 2008, for further details). Minor- and trace-element variations in solid and melt are controlled by the combined chromatographic effects of melt transport (Navon & Stolper, 1987) and the source–sink effects of fractional melt crystallization (Godard *et al.*, 1995; Bodinier *et al.*, 2008). We consider a low-Ti, highly refractory harzburgite from the study area (sample 07RV13E) as the protolith and the theoretical melt in equilibrium with the cpx from the coarse-granular peridotite 07RV1 as the infiltrated melt composition. This model

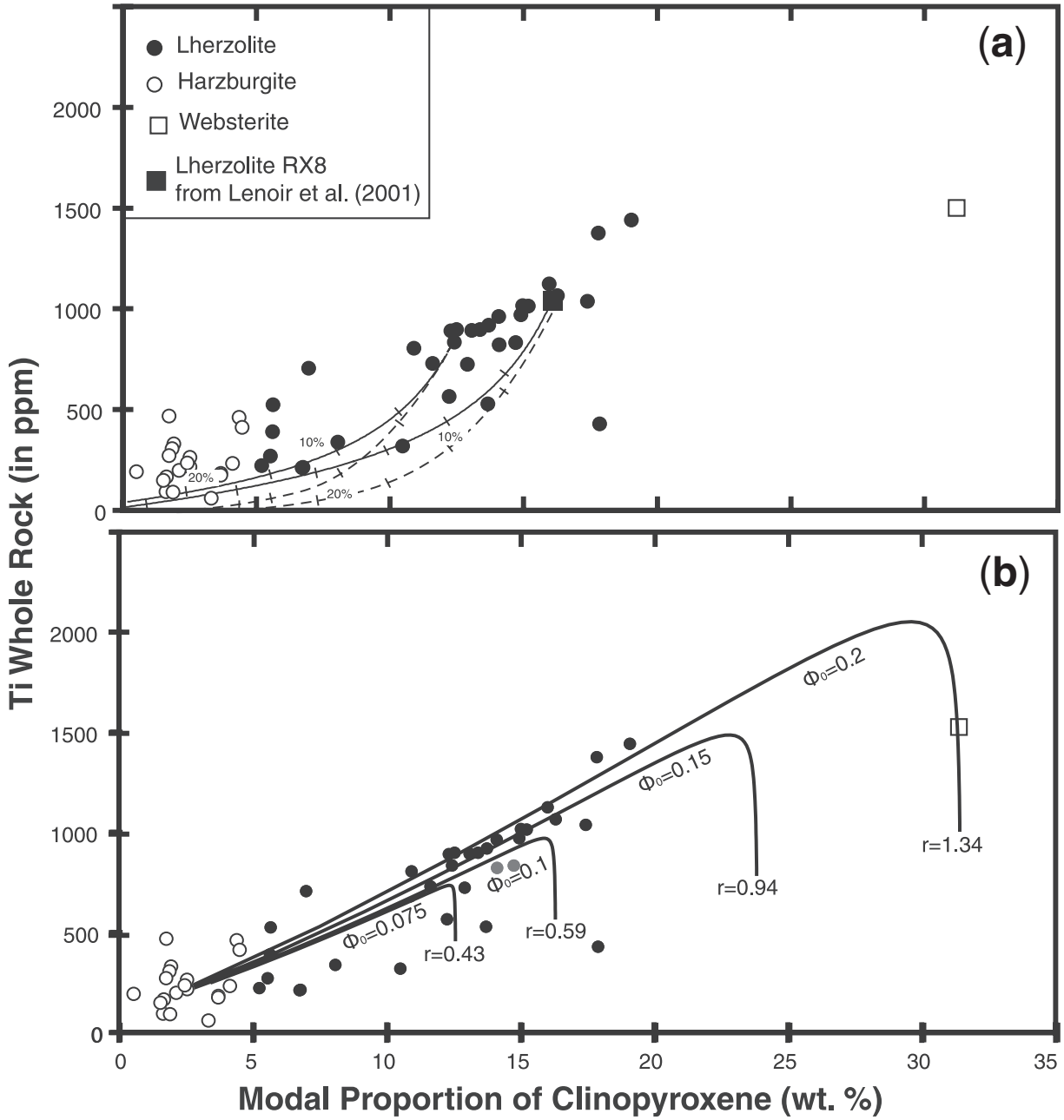

Fig. 10. Ti content in whole-rocks vs Cpx modal proportion for the studied samples, compared with: (a) batch (continuous lines) and fractional (dashed lines) partial melting models calculated with two lherzolite sources [samples 07RV13C from this study and RX8 from Lenoir *et al.* (2001)], and (b) igneous refertilization models calculated with the 'Plate Model' of Vernières *et al.* (1997) and four different initial porosity values (Φ_0), from 0·075 to 0·2. The results of the refertilization models are shown for the entire, 40-reaction cells columns used in the experiments. Cpx modal proportions and melt/rock ratios (r) increase from top to base of the columns; the maximum r values reached at base of each column are given. The refertilization reaction is given in the text; the melting reaction was fixed after Niu (1997). Mineral/melt partition coefficients (K_d) are from Wood & Blundy (2003).

assumes that the melt responsible for refertilization of the spinel tectonite domain was infiltrated from the nearby partial melting domain represented by the granular peridotites. This assumption is consistent with the suggestion by Lenoir *et al.* (2001) that the spinel tectonites were extensively refertilized up to a few hundred metres ahead of the melting front. We cannot exclude the possibility that partial melting of the garnet pyroxenite layers, as observed by Garrido & Bodinier (1999), also contributed to igneous refertilization in the spinel tectonite domain. Silica-rich

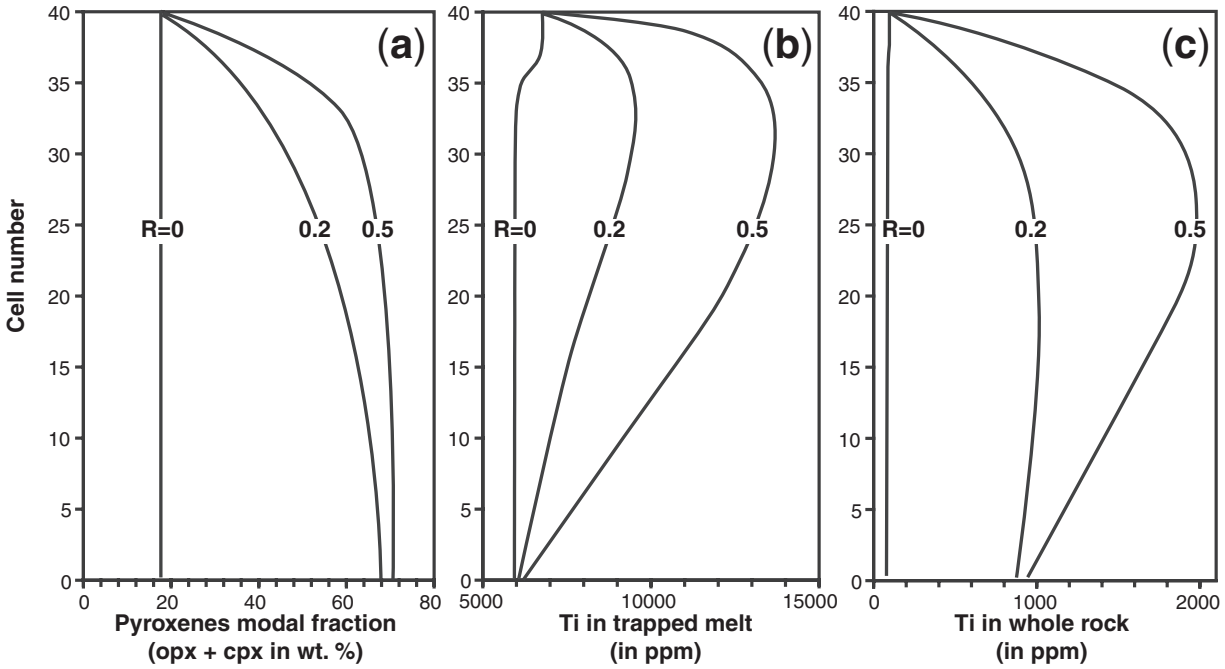

Fig. 11. Sketch illustrating the variations of (a) pyroxene modal proportion in the peridotite, (b) Ti content in the percolating melt and (c) Ti content in whole-rock peridotite along the 40-reaction cells column used for simulating igneous refertilization for R (mass ratio of precipitated pyroxene to infiltrated melt) = 0, 0·2 and 0·5 (see text for further explanation).

melt issued from the pyroxenite layers is indeed expected to react with the host peridotites and precipitate pyroxene (Yaxley & Green, 1998). The actual Ti content in the infiltrated melt is therefore poorly constrained. It should be noticed, however, that the infiltrated melt composition has virtually no effect on the results in the case of moderately incompatible elements such as Ti, compared with the drastic effects of the refertilization reaction.

The effect of igneous refertilization on the evolution of the Ti content in the melt and in the peridotites is illustrated in Fig. 11 that compares two models involving a refertilization reaction with different R values and a pure percolation process ($R = 0$). Percolation produces only subtle Ti variations associated with a chromatographic front (noticeable on melt composition at cells 35–37 in Fig. 11b). In contrast, the reactive process leads to substantial Ti enrichment in the percolating melt, which reaches a maximum immediately upstream of the chromatographic front (up to two times the original melt composition for $R = 0{\cdot}5$, cells 25–35 in Fig. 11b). Ti enrichment in the percolating melt is decoupled from the modal enrichment in pyroxene in the peridotite that is higher in the lower part of the column (cells 0–20 in Fig. 11a). The Ti content in whole-rocks is controlled by both the degree of Ti enrichment in the melt and the amount of pyroxene added to the peridotite by the reaction. The highest Ti contents in the peridotite are attained between the chromatographic front and the base of the column (cells 20–30 in Fig. 11c).

Because of field evidence for heterogeneous melt percolation (alternation of lherzolites, harzburgites and olivine websterite bands), we ran the refertilization model for different initial porosities Φ_0 (0·075–0·2). For $R = 0{\cdot}51$ and a ratio of precipitated cpx to opx consistent with that observed in the fertile lherzolites and websterites, the refertilization reaction is as follows (note that spinel is neglected in the modelling because of its low proportion in peridotites):

$$0{\cdot}74\ \mathrm{Liq}_1 + 0{\cdot}26\ \mathrm{ol} \rightarrow 0{\cdot}62\ \mathrm{Liq}_2 + 0{\cdot}18\ \mathrm{opx} + 0{\cdot}20\ \mathrm{cpx}. \quad (1)$$

In a Ti in whole-rock vs cpx modal contents diagram (Fig. 10c), these models yield convex-upward trajectories including: (1) a predominant, nearly linear segment that fits reasonably well the Ti-cpx co-variation observed in the studied peridotites and (2) a subordinate segment involving Ti decrease at nearly constant cpx content that may account for some of the data scatter. Models with high initial porosity values ($\Phi_0 = 0{\cdot}15$–$0{\cdot}2$, Fig. 10b) reproduce the whole observed range of Ti contents and modal compositions, from the Ti-poor depleted harzburgites to the Ti-rich lherzolites and olivine websterite. Simulations using lower initial porosities ($\Phi_0 = 0{\cdot}075$–$0{\cdot}1$) yield similar trends, but produce less fertile compositions; these

lower-porosity models may explain the variations in Ti content at a given cpx proportion observed in the harzburgites and cpx-poor lherzolites.

Further melt percolation

The igneous refertilization model based on reaction (1) can also reproduce the compositional range observed for other moderately incompatible elements such as HREE (e.g. HREE in cpx in Fig. 12a). However, this model fails to reproduce the variations observed for more incompatible elements such as the LREE. The analysed cpx have a narrow range of LREE contents, compared with HREE (e.g. samples 07RV3C, 07RV12Cw and 07RV10B from the 'normal-type' samples; Fig. 9), whereas the refertilization models show extreme LREE variations; LREE range from 5 to 560 times the chondritic values in the refertilization model with $\Phi_0 = 0{\cdot}15$ (Fig. 12a).

Variable HREE concentrations at nearly constant LREE content in whole-rocks and/or cpx such as those observed in the present study have been reported in several orogenic peridotites and in some mantle xenoliths suites (see reviews by McDonough & Frey, 1989*a*; Bodinier & Godard, 2003). In whole-rock, this feature may be partly accounted for by entrapment of small-volume melts as micro-inclusions in minerals (Bedini & Bodinier, 1999; Garrido *et al.*, 2000; Bodinier & Godard, 2003). However, melt inclusions cannot explain the HREE variations in cpx, which are better explained by chromatographic effects associated with porous melt flow (Godard *et al.*, 1995; Bodinier & Godard, 2003). According to the chromatographic theory (Navon & Stolper, 1987), mantle rocks subjected to porous melt flow are traversed by LREE chromatographic fronts that move almost as fast as the melt itself because of the strongly incompatible behaviour of the LREE. In contrast, because HREE are less incompatible, their chromatographic fronts are slower and require much higher melt/rock ratios to rise significantly through the porous-flow domain. The HREE and LREE contents are therefore strongly decoupled from each other. The HREE contents in percolating melt and peridotite minerals are governed by the composition of the initial peridotite and its subsequent variations as a result of melt–rock reaction, whereas the LREE contents are controlled by the percolating melt and remain roughly constant, in both melt and minerals (Godard *et al.*, 1995; Vernières *et al.*, 1997; Bodinier *et al.*, 2004).

To investigate this effect, we used the Plate Model of Vernières *et al.* (1997) to simulate a process whereby the virtual peridotites obtained with the refertilization model based on reaction (1) (Fig. 12a) were further percolated without additional reaction, either by an unreacted melt (equilibrium melt calculated from cpx of the coarse-grained peridotite 07RV1) or by a reacted melt (weighted average of melt compositions obtained with the refertilization model illustrated in Fig. 12a). Both simulations satisfactorily reproduce the HREE variations at nearly constant LREE contents observed in cpx from the 'normal-type' samples ('hump-shaped' patterns of Fig. 12b). We note that the percolation of unreacted melt yields LREE contents in cpx slightly lower that the observed values whereas the percolation of reacted melt results in slightly higher LREE and MREE contents. Although inferences on the precise composition of the percolating melt are hampered by the uncertainty in the mineral/melt partition coefficient values, these results suggest that the actual LREE content of the melt that percolated thought the study area was somewhere in the range defined by the two extreme compositions used for modelling.

Final crystallization of interstitial melt

Igneous refertilization involving reaction (1) or similar reactions at decreasing melt mass can generate extreme enrichments in LREE and other highly incompatible elements in evolved small melt fractions and equilibrium minerals (Fig. 12; Bedini *et al.*, 1997; Ionov *et al.*, 2002; Bodinier *et al.*, 2004; Le Roux *et al.*, 2007); however, this reaction cannot produce the overall REE enrichment in cpx locally observed in the study area ('enriched-type' samples from the lherzolite–harzburgite contact 07RV13 and 07RV17, Fig. 9). Reaction (1) leads to enrichment of moderately incompatible elements such as Ti in the melt that does not exceed a factor two (Fig. 11b) and may even result in a depletion of the less incompatible HREE. This is shown, for instance, by comparing the reacted and the infiltrated melt compositions for Ho to Lu in Fig. 12a. An enrichment factor of about 15 relative to the melt in equilibrium with coarse-granular peridotites or the normal-type peridotites from the study area is, however, required to account for the HREE composition measured in cpx from samples 07RV13 and 07RV17.

Modelling experiments conducted to investigate the HREE behaviour upon reactive porous flow indicate that olivine dissolution is the predominant factor responsible for the depletion (or limited enrichment) of moderately incompatible elements in reacted melt and equilibrium minerals. In fact, the observation of undeformed aggregates of secondary pyroxenes (Fig. 5) suggests that interstitial crystallization of cpx + opx without concomitant dissolution of olivine has occurred, at least in a late stage of the porous flow event. To simulate this late process, equivalent to the 'percolative fractional crystallization' of Harte *et al.* (1993), we used the Plate Model in a configuration where crystallization of interstitial cpx and opx from the percolating melt was not accompanied by dissolution of olivine. A best fit of the cpx REE composition for the 'enriched-type' samples was obtained with the reaction scheme

$$1\ \mathrm{Liq}_1 \rightarrow 0{\cdot}83\ \mathrm{Liq}_2 + 0{\cdot}078\ \mathrm{opx} + 0{\cdot}092\ \mathrm{cpx} \qquad (2)$$

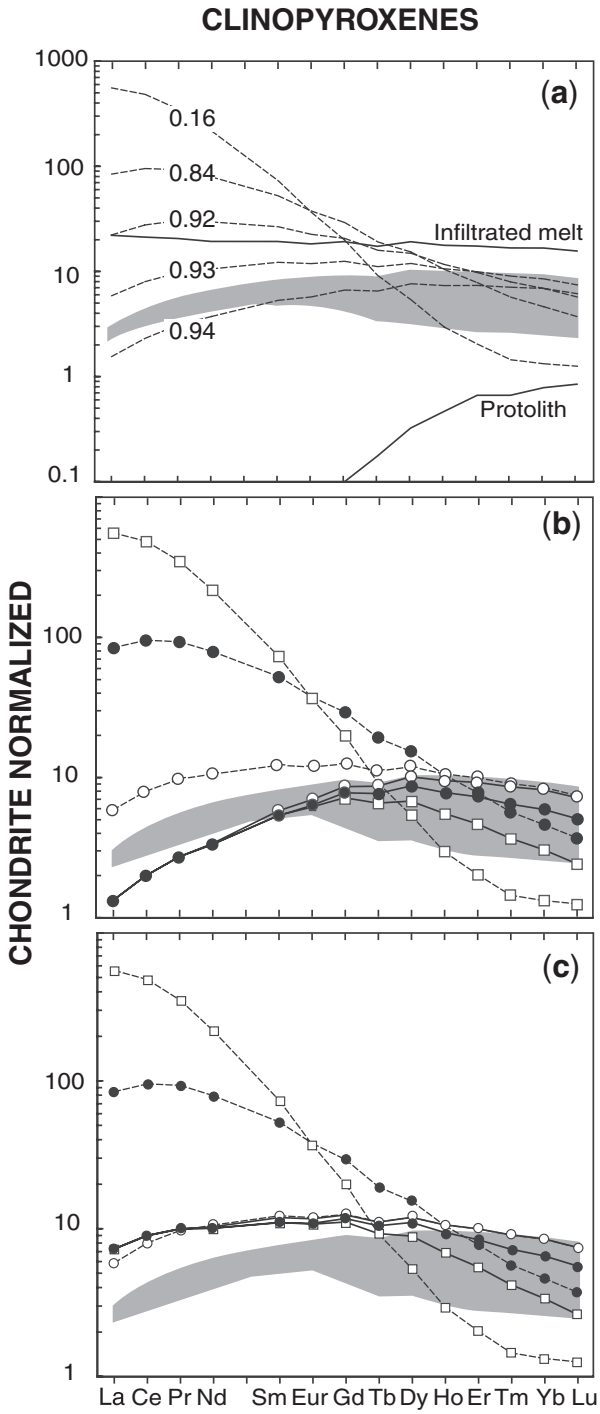

Fig. 12. (a) Results of an igneous refertilization model calculated for REE with the 'Plate Model' of Vernières *et al.* (1997). The model involves a 40-reaction cells peridotite column infiltrated by the theoretical melt in equilibrium with the cpx from the coarse-granular peridotite (sample 07RV1). The initial peridotite composition (protolith) is that of a residual peridotite obtained after 20% incremental melting of the lherzolite 07RV13E. The initial porosity value (Φ_0) is 0·15. The dashed lines show the results obtained for cells 1, 9, 17, 25, and 40, which have melt/rock ratios of 0·94, 0·93, 0·92, 0·84 and 0·16, respectively. (b, c) Results of porous flow models (40-reaction cells column) whereby three peridotite compositions obtained with the igneous refertilization model (cells 1, 25, and 40: dashed lines) are further percolated, either by (b) the same melt as used for the refertilization model or (c) the weighted average composition of reacted melts calculated with the refertilization model. The symbols allow comparison of the results (continuous lines) with the initial peridotite compositions. Olivine and opx melt/mineral K_d values are from Kelemen *et al.* (1993); the cpx K_d values are from Hart & Dunn (1993). The grey field shows the chondrite-normalized REE patterns of the 'normal-type' clinopyroxenes (Fig. 9).

where R, the mass ratio of crystallized minerals to infiltrated melt, is 0·2 (Fig. 12a). The infiltrated melt composition is the same as that employed for the refertilization model using reaction (1). Because this process is considered to have occurred in a late stage of the porous flow event, after the main refertilization, the protolith composition was fixed from the average of the 'normal-type' cpx REE compositions. The results reported in Fig. 13 represent the compositions obtained in four experiments run with distinct initial porosity values. The variation from overall REE enrichment in samples 07RV17 and 07RV13C to selective LREE enrichment in samples 07RV13B and 07RV13D is accounted for by the decreasing values of the initial porosity Φ_0, from 0·2 to 0·05. After reaction, porosity values in the range 0·003–0·0009 are observed in the cells yielding the REE compositions shown in Fig. 13.

Interactions between reactive magma transport and deformation

The similar kinematics, the continuity of the deformation structures, and the progressive variation in recrystallized grain size from $<200\,\mu m$ in the westernmost mylonites to 1–15 mm in the coarse-grained spinel tectonites close to the melting front (Fig. 3) suggests continuous deformation under decreasing stress conditions. Decrease in deviatoric stress may result from deformation under increasing temperature. A strong thermal gradient across the spinel peridotite domain is corroborated by the partial melting of garnet pyroxenites and their replacement by spinel pyroxenites within 800 m from the front. It is also in agreement with the temperature conditions inferred from the mineral assemblages in the coarse-grained peridotites of the asthenospheric domain (1250°C, Lenoir *et al.*, 2001) and those estimated for the final stages of the deformation in the garnet–spinel mylonites (850–950°C, Garrido *et al.*, 2006).

In addition, structural data at macroscopic and microscopic scales point to syn- to late-tectonic reactive melt transport in the spinel tectonite domain. Lithological contacts at all scales, from the recrystallization front to the centimetre-scale websterite bands, are parallel to the deformation structures (foliation and lineation), but diffuse. A close analysis of the centimetre-scale olivine websterite bands that often mark the harzburgite–lherzolite contacts allows us, in particular, to constrain the relations between

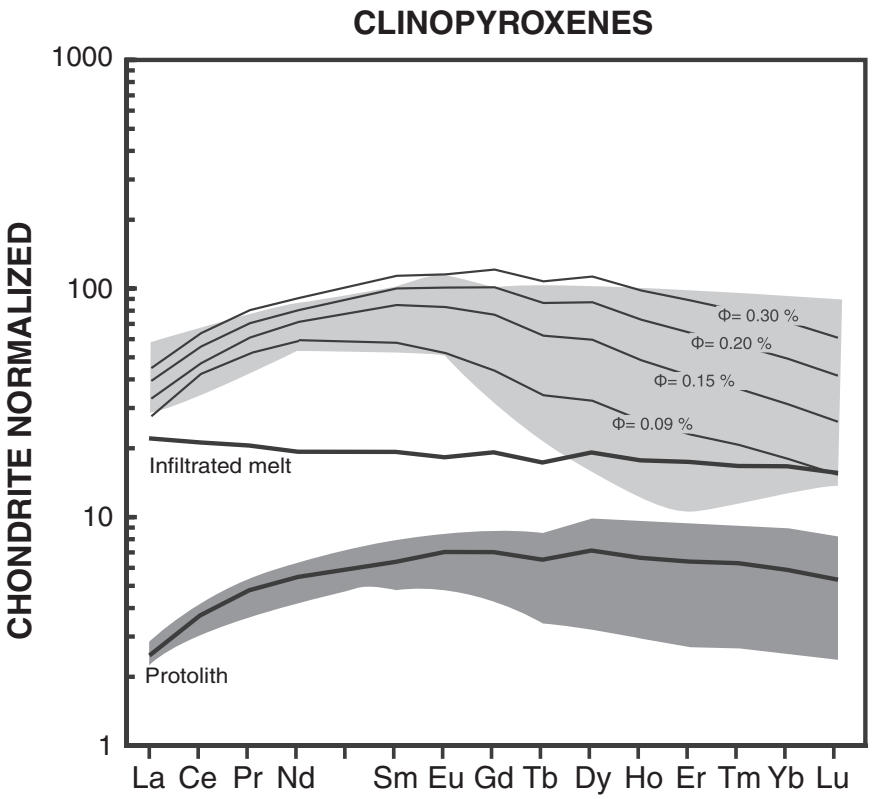

Fig. 13. Results of a 'percolative fractional crystallization' model calculated for REE with the 'Plate Model' of Vernières *et al.* (1997). The simulation involves interstitial precipitation of pyroxene through four 40-reaction cells peridotite columns. The composition of the percolated peridotite (protolith) was fixed from the average REE composition of 'normal-type' cpx. The infiltrated melt has the composition of theoretical melt in equilibrium with cpx from the coarse-granular peridotite 07RV1. The results are shown for cell 18 in the four columns, distinguished only by their initial porosity values, Φ_0, ranging from 0·2 to 0·05. They are labelled according to the porosity values (in %) observed in cell 18 after reaction. The mineral/melt K_d values are the same as for the igneous refertilization and porous flow models (Fig. 12). The upper and lower grey arrays show the chondrite-normalized REE patterns of the 'enriched-' and 'normal-type' clinopyroxenes, respectively (Fig. 9). Chondrite normalizing values after Sun & McDonough (1989).

deformation and melt percolation. As in Lherz, these thin olivine websterite bands are interpreted as marking melt segregation horizons (Le Roux *et al.*, 2007, 2008; Bodinier *et al.*, 2008). They are parallel to the peridotite foliation, but have highly convoluted limits at the millimetre scale (Fig. 4). Pyroxenes in these bands show variable deformation degrees; deformed olivine and pyroxenes coexist with undeformed pyroxenes and spinel. Similarly, in the lherzolites and harzburgites, corroded opx systematically displays clear intracrystalline deformation features, such as undulose extinction and kink bands, but secondary cpx and spinels, although forming aggregates aligned in the foliation, often preserve clear interstitial shapes and show no internal deformation (Fig. 4). In the garnet–spinel mylonites, opx and cpx do not show microstructural evidence of melt–rock reactions or partial melting. They are elongated parallel to the lineation, display undulose extinction and kink bands, and have a clear CPO.

Analysis of olivine CPO in lherzolites and harzburgites also supports the suggestion that deformation occurred in the presence of melt. Harzbugites have a rather constant olivine CPO intensity, whereas the olivine CPO in the lherzolites has variable strength, being either stronger or weaker than in the harzburgites (Fig. 7). Variations in the CPO intensity may result from either a gradient in strain or a change in the contribution of diffusion to deformation. High instantaneous melt fractions favour diffusion-accommodated deformation and lead to a decrease in CPO intensity (Hirth & Kohlstedt, 1995*a*, 1995*b*; Holtzman *et al.*, 2003). In contrast, at very low melt fractions, melt is essentially confined at triple junctions and cannot act as an interconnected fast diffusion path. It may nevertheless reduce the contact area between grains, leading to a local increase in stress (Hirth & Kohlstedt, 1995*a*). Higher stress may enhance dislocation creep and CPO development. Therefore, the observed variation in J-index in the lherzolites may result from deformation in presence of different instantaneous melt fractions.

Together these observations support the idea that deformation in the coarse-grained spinel tectonites took place

in the presence of melt. In this context, one may speculate that the parallelism between lithological contacts, websterite layers, and the foliation may result from deformation-controlled melt transport related to an enhanced permeability parallel to the foliation, as observed experimentally in rock-analogue systems by Rosenberg & Handy (2000) and Takei (2005). A strong feedback between melt transport and deformation has indeed often been suggested based on field observations and microstructural studies for both crustal and mantle shear zones (e.g. Tommasi *et al.*, 1994; Kelemen & Dick, 1995; Brown & Solar, 1998; Rosenberg, 2004; Le Roux *et al.*, 2008). In addition, although an effect of the thermal gradient cannot be excluded, stress-driven melt-segregation may also have played a role in the formation of the websteritic layers (Holtzman *et al.*, 2003; Le Roux *et al.*, 2008).

Constraints on the Ronda peridotite tectono-metamorphic history

Structural and petrographic observations from the field to the thin-section scale are consistent with deformation under increasing temperature conditions and syn- to late-tectonic reactive melt transport. The inferred thermal gradient (Fig. 14) is in agreement with the contrast in P–T conditions recorded by the coarse-grained peridotites at the partial melting front (*c.* 1250°C and 1·4 GPa, Lenoir *et al.*, 2001) and those estimated for the final stages of the deformation in the garnet–spinel mylonites (850–950°C and 1·9 GPa, Garrido *et al.*, 2006). Based on these observations, we suggest that reactive melt transport in the spinel tectonites is linked to the formation of the melting front. This interpretation is corroborated by the analysis of the REE and Ti compositions of the spinel tectonites, which are well explained by refertilization models in which the percolating melt has a composition in equilibrium with the coarse-granular peridotites (Figs 10, 12 and 13).

The consistency of the deformation structures (foliation and lineation) from the mylonites to the melting front implies that the spinel tectonites and the mylonites have recorded similar kinematics and thus shared the same deformation, although under significantly different stress conditions. Propagation of the melting front led to an enhancement of the thermal gradient, melt percolation, and local partial melting in the close vicinity above the melting front. This situation may have resulted in a progressive transfer of the deformation from the mylonites towards the hotter, melt-bearing domains just above the melting front and, further, to the partially molten domain. Absence of deformation in the last melt–rock reaction products suggests nevertheless that deformation ceased before cooling of the domain, leading to re-equilibration of the microstructures in the coarse-granular peridotites under static conditions (Vauchez & Garrido, 2001).

In summary, the Ronda massif records a continuous history of exhumation of a section of the lithospheric mantle. The initial stages of this exhumation were accommodated by the garnet–spinel mylonites that recorded the progressive exhumation of the Ronda peridotites from ca. 100 km to ca. 60 km depth (Garrido *et al.*, 2006). This was followed by the propagation of an asthenospherization front through partial melting of the lithospheric mantle, forming the coarse-grained peridotites, in response to an enhanced heat flow at the base of the lithosphere (Lenoir *et al.*, 2001). We propose that the thermo-mechanical evolution recorded in the spinel tectonite domain is the 'missing bridge' between these two events. Continued exhumation and lithospheric thinning in the presence of a strong transient thermal gradient maintained by the large-scale partial melting in the asthenospheric domain may indeed account for the decrease in equilibrium pressure from 1·9 GPa in the last stages of deformation in the mylonites to 1·4 GPa in the coarse-grained peridotites of the asthenospheric domain (Fig. 14).

Although the present-day orientation of the foliations and lineations in the Ronda massif may have been modified by rigid-body rotations during the late stages of exhumation, hindering the direct interpretation of these structures in terms of mantle kinematics, analysis of the CPO in these peridotites allows constraints to be made on the deformation regime (Tommasi *et al.*, 1999). In all studied spinel peridotites and mylonites, ol [100] and opx [001] axes show a systematic dispersion within the foliation plane with weak maxima at $<10°$ to the lineation marked by the olivine and pyroxene elongation (Fig. 6). This pattern is typical of transpression, since an association of simple shear and shortening normal to the shear plane is necessary to produce both the dispersion of the glide directions in the flattening plane and the weak obliquity between their maxima and the lineation (Tommasi *et al.*, 1999). Olivine and orthopyroxene CPO displaying the same deformation regime are observed in mylonites in the northern part of the massif (Precigout *et al.*, 2007) and in a larger scale study that compared the olivine CPO in the spinel tectonite and in the coarse-grained domain (Vauchez & Garrido, 2001). This suggests that the present observations do not record a local variation in strain regime (i.e. at the scale of the studied zone) but the general strain regime that affected the lithospheric mantle during the exhumation of the Ronda peridotites.

CONCLUSIONS

Our observations show that the spinel tectonite domain in the Ronda peridotite massif records deformation and syn- to late-tectonic melt percolation in a narrow zone, *c.* 1·5 km wide, at the base of the mantle lithosphere. Heat transfer from a neighbouring large-scale partial melting domain (or 'asthenospherized' mantle) results in an extremely high thermal gradient in this domain, which controls

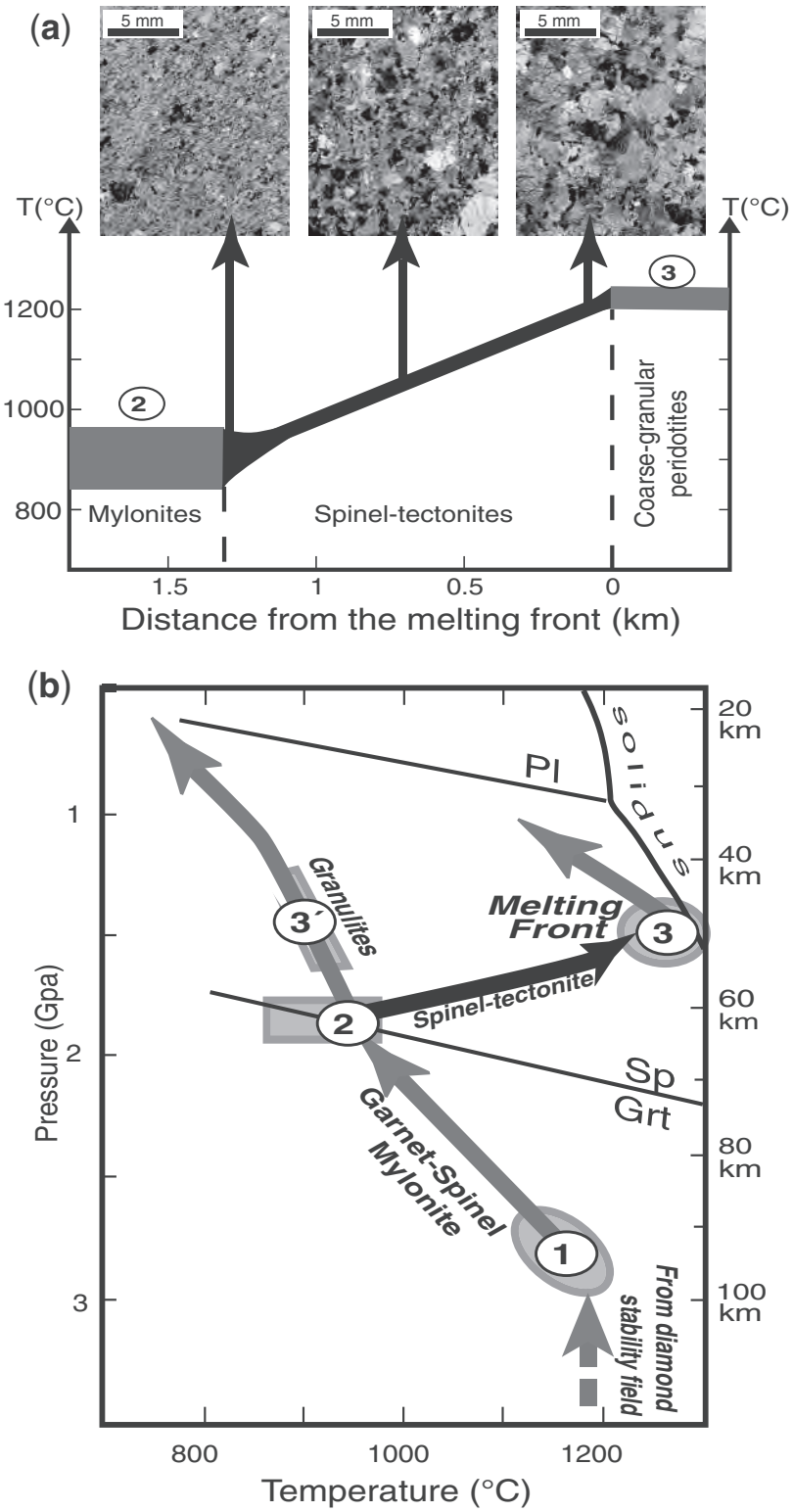

Fig. 14. (a) Evolution of the temperature and grain size in the spinel tectonite domain as a function of the distance from the melting front. (b) *P–T–t* paths for (1) the garnet–spinel mylonites (Garrido *et al.*, 2006) and (3′) neighbouring granulites *et al.* (Morishita *et al.*, 2001), (2) the spinel tectonites (this work), and (3) the coarse-grained peridotites (Lenoir *et al.*, 2001).

both the deformation distribution and the melt migration ahead of the partial melting front.

The observed co-variations of minor elements (Na, Ti, Cr) in whole-rocks with cpx proportions indicate that melt transport was accompanied by a near-solidus peritectic refertilization reaction involving precipitation of pyroxenes and spinel from percolating melts, combined with olivine dissolution. Field evidence, consistent with previous work on Ronda mafic layers, suggests that *in situ* partial melting of pre-existing aluminous pyroxenites probably also contributed to the reactive melt fraction. REE patterns in cpx reveal that a second-order melt process was locally superimposed on the predominant refertilization process: circulation and interstitial crystallization of small residual melt fractions. This is consistent with the observation of undeformed interstitial pyroxenes and spinel.

Structural observations highlight the interactions between melt transport and deformation. The parallelism between deformation structures and diffuse lithological contacts at all scales (from kilometre to millimetre) suggests that deformation controlled magma transport. On the other hand, the variation in olivine CPO intensities implies that the presence of melt results in a higher contribution of diffusion to deformation, leading to a slower CPO evolution.

The consistency of the deformation structures (orientation of the foliation and lineation) from the mylonites to the melting front implies that the spinel tectonites and the mylonites have recorded similar kinematics and thus shared the same deformation, although under significantly different stress conditions. In addition, the olivine and opx CPO in the mylonites and the spinel tectonites highlights that transpression played a fundamental role in the exhumation of the Ronda peridotites. Finally, the present study highlights that reactive melt transport in the lithospheric mantle ahead of the partial melting domain played a fundamental role in the thinning of the Alboran lithosphere, as it enhanced its fertility, facilitating the propagation of the transient lithosphere–asthenosphere boundary represented by the partial melting front.

ACKNOWLEDGEMENTS

We thank C. Nevado and D. Delmas, who supplied high-quality polished thin section for EBDS measurement, electron probe microbeam and ICP-MS LA analysis. We are indebted to C. Merlet and O. Bruguier for assistance during electron probe microbeam and ICP-MS LA analysis, respectively. D. Mainprice is thanked for providing software for analysing and plotting CPO data. We acknowledge Dr Othmar Müntener, Dr Nina Simon and Dr Günter Suhr for their constructive reviews. This work has been supported by the France–Spain integrated action PICASSO. Carlos J. Garrido acknowledges funding from the Spanish MICINN (Grants CGL2006-04440/BTE, CGL2007-61205, PCI2006-A9 0580 and HF-2008-0073), CSIC (grant 200830I014) and the 'Junta de Andalucía' (research group RNM-131).

REFERENCES

Bedini, R. M. & Bodinier, J. L. (1999). Distribution of incompatible trace elements between the constituents of spinel peridotite xenoliths: ICP-MS data from the East African Rift. *Geochimica et Cosmochimica Acta* **63**(22), 3883–3900.

Bedini, R.-M., Bodinier, J.-L., Dautria, J. M. & Morten, L. (1997). Evolution of LILE-enriched small melts fractions in the lithospheric mantle: a case study from the East African Rift. *Earth and Planetary Science Letters* **153**, 67–83.

Ben Ismail, W. & Mainprice, D. (1998). An olivine fabric database: an overview of upper mantle fabrics and seismic anisotropy. *Tectonophysics* **296**, 145–158.

Bodinier, J. L. & Godard, M. (2003). Orogenic, ophiolitic, and abyssal peridotites. In: Carlson, R. W. (ed.) *Geochemistry of the Mantle and Core. Treatise on Geochemistry 2.* Amsterdam: Elsevier, pp. 103–170.

Bodinier, J. L., Dupuy, C. & Dostal, J. (1988). Geochemistry and petrogenesis of Eastern Pyrenean peridotites. *Geochimica et Cosmochimica Acta* **52**(12), 2893–2907.

Bodinier, J. L., Vasseur, G., Vernières, J., Dupuy, C. & Fabriès, J. (1990). Mechanisms of mantle metasomatism—geochemical evidence from the Lherz orogenic peridotite. *Journal of Petrology* **31**(3), 597–628.

Bodinier, J. L., Menzies, M. A., Shimizu, N., Frey, F. A. & McPherson, E. (2004). Silicate, hydrous and carbonate metasomatism at Lherz, France: Contemporaneous derivatives of silicate melt–harzburgite reaction. *Journal of Petrology* **45**(2), 299–320.

Bodinier, J. L., Garrido, C. J., Chanefo, I., Bruguier, O. & Gervilla, F. (2008). Origin of pyroxenite-peridotite veined mantle by refertilization reactions: evidence from the Ronda peridotite (S. Spain). *Journal of Petrology* **49**, 999–1025.

Brown, M. & Solar, G. S. (1998). Shear-zone systems and melts: feedback relations and self- organization in orogenic belts. *Journal of Structural Geology* **20**(2–3), 211–227.

Bunge, H. J. (1982). *Texture Analysis in Materials Sciences*. London: Butterworth.

Darot, M. (1973). Méthode d'analyse structurale et cinématique. Application à l'étude du massif ultrabasique de la Sierra Bermeja. Nantes.

Dijkstra, A. H., Barth, M. G., Drury, M. R., Mason, P. R. D. & Vissers, R. L. M. (2003). Diffuse porous melt flow and melt–rock reaction in the mantle lithosphere at a slow-spreading ridge: A structural petrology and LA-ICP-MS study of the Othris Peridotite Massif (Greece). *Geochemistry, Geophysics, Geosystems* **4**, 24, doi:10.1029/2001GC000278.

Downes, H., Bodinier, J. L., Thirwall, M. F., Lorand, J. P. & Fabriès, J. (1991). REE and Sr–Nd isotopic geochemistry of eastern Pyrenean peridotite massifs: sub-continental lithospheric mantle modified by continental magmatism. *Journal of Petrology (Special Lherzolites Issue)* 97–115.

Fabriès, J., Bodinier, J. L., Dupuy, C., Lorand, J. P. & Benkerrou, C. (1989). Evidence for modal metasomatism in the orogenic spinel lherzolite body from Caussou (northeastern Pyrenees, France). *Journal of Petrology* **30**(1), 199–228.

Frey, F. A., Suen, C. J. & Stockman, H. W. (1985). The Ronda high-temperature peridotite—geochemistry and petrogenesis. *Geochimica et Cosmochimica Acta* **49**(11), 2469–2491.

Garrido, C. J. & Bodinier, J. L. (1999). Diversity of mafic rocks in the Ronda peridotite: Evidence for pervasive melt–rock reaction during heating of subcontinental lithosphere by upwelling asthenosphere. *Journal of Petrology* **40**(5), 729–754.

Garrido, C. J., Bodinier, J. L. & Alard, O. (2000). Incompatible trace element partitioning and residence in anhydrous spinel peridotites and websterites from the Ronda orogenic peridotite. *Earth and Planetary Science Letters* **181**(3), 341–358.

Garrido, C. J., Sautter, V., Gueydan, F., Booth-Rea, G. & Gervilla, F. (2006). Unequivocal garnet and garnet–spinel lherzolite assemblages in the Ronda Peridotite (S. Spain): implications for exhumation of sub-continental mantle in the Alborán basin. *Geophysical Research Abstracts* **8**(10263).

Gast, P. W. (1968). Trace element fractionation and the origin of tholeiitic and alkaline magma types. *Geochimica et Cosmochimica Acta* **32**, 1057–1089.

Godard, M., Bodinier, J. L. & Vasseur, G. (1995). Effects of mineralogical reactions on trace element redistributions in mantle rocks during percolation processes: A chromatographic approach. *Earth and Planetary Science Letters* **133**(3–4), 449–461.

Günther, D. & Heinrich, C. A. (1999). Enhanced sensitivity in LA-ICP-MS using helium–argon mixtures as aerosol carrier. *Journal of Analytical Atomic Spectrometry* **14**, 1369–1374.

Hart, S. R. & Dunn, T. (1993). Experimental cpx/melt partitioning of 24 trace elements. *Contributions to Mineralogy and Petrology* **113**, 1–8.

Hirth, G. & Kohlstedt, D. L. (1995*a*). Experimental constraints on the dynamics of the partially molten upper mantle 2. Deformation in the dislocation creep regime. *Journal of Geophysical Research* **100**(B8), 15441–15449.

Hirth, G. & Kohlstedt, D. L. (1995*b*). Experimental constraints on the dynamics of the partially molten upper-mantle—deformation in the diffusion creep regime. *Journal of Geophysical Research—Solid Earth* **100**(B2), 1981–2001.

Holtzman, B. K., Groebner, N. J., Zimmerman, M. E., Ginsberg, S. B. & Kohlstedt, D. L. (2003). Stress-driven melt segregation in partially molten rocks. *Geochemistry, Geophysics, Geosystems* **4**, article number 8607.

Ionov, D. A., Bodinier, J. L., Mukasa, S. B. & Zanetti, A. (2002). Mechanisms and sources of mantle metasomatism: Major and trace element compositions of peridotite xenoliths from Spitsbergen in the context of numerical modelling. *Journal of Petrology* **43**(12), 2219–2259.

Kaczmarek, M.-A. & Müntener, O. (2008). Juxtaposition of melt impregnation and high-temperature shear zones in the upper mantle; field and petrological constraints from the Lanzo Peridotite (Northern Italy). *Journal of Petrology* **49**, 2187–2220.

Kelemen, P. B. & Dick, H. J. B. (1995). Focused melt flow and localized deformation in the upper mantle—juxtaposition of replacive dunite and ductile shear zones in the Josephine Peridotite, SW Oregon. *Journal of Geophysical Research—Solid Earth* **100**(B1), 423–438.

Kelemen, P. B., Dick, H. J. B. & Quick, J. E. (1992). Formation of harzburgite by pervasive melt rock reaction in the upper mantle. *Nature* **358**(6388), 635–641.

Kelemen, P. B., Shimizu, N. & Dunn, T. (1993). Relative depletion of niobium in some arc magmas and the continental crust—partitioning of K, Nb, La and Ce during melt/rock reaction in the upper mantle. *Earth and Planetary Science Letters* **120**(3–4), 111–134.

Kendall, J. M., Stuart, G. W., Ebinger, C. J., Bastow, I. D. & Keir, D. (2005). Magma-assisted rifting in Ethiopia. *Nature* **433**, 146–149.

Kohlstedt, D. L., Evans, B. & Mackwell, S. J. (1995). Strength of the lithosphere—constraints imposed by laboratory experiments. *Journal of Geophysical Research—Solid Earth* **100**(B9), 17587–17602.

Le Roux, V., Bodinier, J.-L., Tommasi, A., Alard, O., Dautria, J.-M., Vauchez, A. & Riches, A. J. V. (2007). The Lherz spinel lherzolite: Refertilized rather than pristine mantle. *Earth and Planetary Science Letters* **259**, 599–612.

Le Roux, V., Tommasi, A. & Vauchez, A. (2008). Feedback between melt percolation and deformation in an exhumed lithosphere–asthenosphere boundary. *Earth and Planetary Science Letters* **274**, 401–413.

Lenoir, X., Garrido, C. J., Bodinier, J. L., Dautria, J. M. & Gervilla, F. (2001). The recrystallization front of the Ronda peridotite: Evidence for melting and thermal erosion of subcontinental lithospheric mantle beneath the Alboran basin. *Journal of Petrology* **42**(1), 141–158.

McDonough, W. F. & Frey, F. A. (1989*a*). Rare earth elements in upper mantle rocks. In: Lipin, B. R. & McKay, G. A. (eds) *Geochemistry and Mineralogy of Rare Earth Elements. Mineralogical Society of America, Reviews in Mineralogy* **21**, 99–145.

McDonough, W. F. & Sun, S.-S. (1995). The composition of the Earth. *Chemical Geology* **120**, 223–253.

Morishita, T., Arai, S. & Gervilla, F. (2001). High-pressure aluminous mafic rocks from the Ronda peridotite massif, southern Spain: significance of sapphirine- and corundum-bearing mineral assemblages. *Lithos* **57**(2–3), 143–161.

Muntener, O., Piccardo, G. B., Polino, R. & Zanetti, A. (2005). Revisiting the Lanzo peridotite (NW Italy): 'Asthenospherization' of ancient mantle lithosphere. *Ofioliti* **30**(2), 111–124.

Navon, O. & Stolper, E. (1987). Geochemical consequence of melt percolation: the upper mantle as a chromatographic column. *Journal of Geology* **95**, 285–307.

Niu, Y. (1997). Mantle melting and melt extraction processes beneath ocean ridges: evidence from abyssal peridotites. *Journal of Petrology* **38**, 1047–1074.

Obata, M. (1980). The Ronda peridotite—garnet-lherzolite, spinel-lherzolite, and plagioclase-lherzolite facies and the P–T trajectories of a high-temperature mantle intrusion. *Journal of Petrology* **21**(3), 533–572.

Obata, M. & Nagahara, N. (1987). Layering of alpine-type peridotite and the segregation of partial melt in the upper mantle. *Journal of Geophysical Research* **92**, 3467–3474.

Pearce, N. J. G., Perkins, W. T., Westgate, J. A., Gorton, M. P., Jackson, S. E., Neal, C. R. & Chenery, S. P. (1997). A compilation of new and published major and trace element data for NIST SRM 610 and NIST SRM 612 glass reference materials. *Geostandards Newsletter-the Journal of Geostandards and Geoanalysis* **21**(1), 115–144.

Precigout, J., Gueydan, F., Gapais, D., Garrido, C. J. & Essaifi, A. (2007). Strain localisation in the subcontinental mantle—a ductile alternative to the brittle mantle. *Tectonophysics* **445**, 318–336.

Rosenberg, C. (2004). Shear-zone systems and melts: feedback relations and self-organization in orogenic belts. *Tectonics* **23** (TC3002).

Rosenberg, C. & Handy, M. R. (2000). Syntectonic melt pathways during simple shearing of an anatectic rock analogue (norcamphor-benzamide). *Journal of Geophysical Research* **105**, 3135–3149.

Saal, A. E., Takazawa, E., Frey, F. A., Shimizu, N. & Hart, S. R. (2001). Re–Os isotopes in the Horoman peridotite: Evidence for refertilization? *Journal of Petrology* **42**(1), 25–37.

Shaw, D. M. (1970). Trace element fractionation during anatexis. *Geochimica et Cosmochimica Acta* **34**, 237–243.

Sun, S.-S. & McDonough, W. F. (1989). Chemical and isotopic systematics of oceanic basalts: implications for mantle composition and processes. In: Saunders, A. D. & Norry, M. J. (eds) *Magmatism in the Ocean Basins. Geological Society, London, Special Publications* **42**, 313–345.

Takei, Y. (2005). Deformation-induced grain boundary wetting and its effects on the acoustic and rheological properties of partially molten rock analogue. *Journal of Geophysical Research—Solid Earth* **110**(B12), doi:10.1029/2005JB003801.

Tarantola, A. & Valette, B. (1982). Generalized non-linear inverse problems solved using least-squares criterion. *Reviews of Geophysics and Space Physics* **20**, 219–232.

Thoraval, C., Tommasi, A. & Doin, M. (2006). Plume–lithosphere interaction beneath a fast moving plate. *Geophysical Research Letters* **33**(1), L01301, doi:10.1029/2005GL024047.

Tommasi, A., Vauchez, A., Fernandes, L. A. D. & Porcher, C. C. (1994). Magma-assisted strain localization in an orogen-parallel transcurrent shear zone of southern Brazil. *Tectonics* **13**(2), 421–437.

Tommasi, A., Tikoff, B. & Vauchez, A. (1999). Upper mantle tectonics: three-dimensional deformation, olivine crystallographic fabrics and seismic properties. *Earth and Planetary Science Letters* **168**(1–2), 173–186.

Tommasi, A., Mainprice, D., Canova, G. & Chastel, Y. (2000). Viscoplastic self-consistent and equilibrium-based modeling of olivine lattice preferred orientations: Implications for the upper mantle seismic anisotropy. *Journal of Geophysical Research—Solid Earth* **105**(B4), 7893–7908.

Toramaru, A., Takazawa, E., Morishita, T. & Matsukage, K. (2001). Model of layering formation in a mantle peridotite (Horoman, Hokkaido, Japan). *Earth and Planetary Science Letters* **185**(3–4), 299–313.

Van Achterbergh, E., Ryan, C. G., Jackson, S. E. & Griffin, W. L. (2001). Data reduction software for LA-ICP-MS. In: Sylvester, P. J. (ed.) *Laser-Ablation-ICPMS in the Earth Sciences. Principles and Applications.* Mineralogical Association of Canada Short Course Volume **29**, 239–243.

Van der Wal, D. (1993). Deformation processes in mantle peridotites. Ph.D. thesis, University of Utrecht.

Van der Wal, D. & Bodinier, J. L. (1996). Origin of the recrystallisation front in the Ronda peridotite by km-scale pervasive porous melt flow. *Contributions to Mineralogy and Petrology* **122**(4), 387–405.

Van der Wal, D. & Vissers, R. L. M. (1996). Structural petrology of the Ronda peridotite, SW Spain: Deformation history. *Journal of Petrology* **37**(1), 23–43.

Vauchez, A. & Garrido, C. J. (2001). Seismic properties of an asthenospherized lithospheric mantle: constraints from lattice preferred orientations in peridotite from the Ronda massif. *Earth and Planetary Science Letters* **192**(2), 235–249.

Vernières, J., Godard, M. & Bodinier, J. L. (1997). A plate model for the simulation of trace element fractionation during partial melting and magma transport in the Earth's upper mantle. *Journal of Geophysical Research—Solid Earth* **102**(B11), 24771–24784.

Wood, B. J. & Blundy, J. D. (2003). Trace elements partitioning under crustal and uppermost mantle conditions: the infuences of ionic radius, cation charge, pressure and temperature. In: Carlson, R. W. (ed.) *Treatise on Geochemistry.* Amsterdam: Elsevier, pp. 395–425.

Yaxley, G. M. & Green, D. H. (1998). Reactions between eclogite and peridotite: mantle refertilization by subduction of oceanic crust. *Contributions to Mineralogy and Petrology* **139**, 326–338.

Chapitre 3

Effets des interactions fluides-roche sur la déformation et les propriétés sismiques du coin mantellique : exemple de la subduction du Kamchatka

Ce chapitre présente une étude pétro-structurale sur 23 xénolites de péridotites à spinelle extraites de la base de la lithosphère par le volcan Avacha qui est toujours en activité au sud-est de la péninsule du Kamchatka. Les échantillons ont été récoltés dans des tufs datés à l'Holocène, ce qui signifie que ces péridotites échantillonnent le manteau actuel au-dessus d'une zone de subduction active.

La première partie intitulée "les interactions entre déformation et percolation réactive de fluides dans le manteau supra-subduction" a fait l'objet d'un article publié dans *Journal of Petrology* (Soustelle et al., 2010). Ce travail traite des interactions entre déformation et percolation réactive de magma ou de fluides dans le coin mantellique. Il est basé sur des observations microstructurales et des mesures d'OPR et de teneurs en eau des minéraux de ces péridotites. Les xénolites étudiées sont des harzburgites à spinelle montrant une texture porphyroclastique à gros grain. Les olivines ont des microstructures caractéristiques d'une déformation par fluage dislocation avec une forte contribution des processus de diffusion. Ces microstructures sont cohérentes avec une déformation sous de faibles contraintes déviatoriques (< 13 MPa), ce qui est confirmé par différents paléopiézomètres de l'olivine. L'analyse des OPR montre que les systèmes de glissement dominant de l'olivine et de l'orthopyroxène sont, respectivement {0kl}[100] et (100)[001]. De nombreux échantillons montrent des bandes millimétriques enrichies en orthopyroxène orientées parallèlement à la foliation, ainsi que de gros cristaux d'orthopyroxène allongés selon la linéation contenant de petites olivines en inclusions sur leur bordure. Ceci indique la cristallisation d'orthopyroxenes

aux dépens de l'olivine en réponse à la percolation d'un fluide ou d'un magma riche en silice durant la déformation. On distingue deux groupes de xénolites: (1) les harzburgites enrichies en orthopyroxène montrant de faible mais homogène intensité d'OPR, et (2) les harzburgites "normales" où l'intensité des OPR de l'olivine est forte mais variable. L'enrichissement en orthopyroxène mène donc à une décroissance de la taille des cristaux d'olivines et de l'intensité de leur OPR, mais les systèmes de glissement dominants des deux minéraux ne sont pas affectés. De plus, la moitié des échantillons contiennent des agrégats d'orthopyroxène aciculaires communément associés à une "matrice" à grain très fin qui est composée de grains d'olivine arrondis ne montrant aucune structure de déformation intracristalline, d'orthopyroxènes, de spinelles et d'amphibole. Cette "matrice" se localise de façon diffuse aux joints de grains, forme des lentilles millimétriques de forme irrégulière ou des petites veines organisées en réseau anastomosé recoupant les gros cristaux ainsi que leurs structures de déformation. Ces orthopyroxènes aciculaires et la "matrice" à grain fin sont interprétés comme résultant du transport réactif de fluide riche en eau sous des conditions statiques, probablement alors que les échantillons faisaient déjà partie de la lithosphère. Les analyses par spectroscopie infrarouge montrent que les olivines contiennent de 1 à 8 ppm en poids d'H_2O. Ces concentrations d'eau sont similaires à celles observées dans d'autre xénolites de péridotites à spinelles de zones de subduction (e.g., Demouchy, 2004; Peslier & Luhr, 2006; Falus et al., 2008). Elles résultent probablement de la faible solubilité d'H_2O dans l'olivine à basse pression (2- 0,5 GPa) et dans les conditions oxydantes du coin mantellique, mais il n'est pas exclu qu'elles aient été un peu abaissées par déshydratation durant l'exhumation des xénolites (Demouchy et al., 2006). Les orthopyroxènes ont des concentrations en eau très variables (25-506 ppm en poids d'H_2O) qui pourraient refléter les interactions spatialement hétérogènes avec les fluides ou les magmas, ainsi qu'un déséquilibre compositionnel. Ces péridotites enregistrent des processus de percolation évoluant d'un flux poreux diffus à de la fracturation suggérant une histoire en refroidissement. Cette observation confirme la déformation sous des conditions de haute température enregistrée par les échantillons alors, que les températures d'équilibre estimées à partir de la thermométrie sur pyroxènes sont de l'ordre de 800-900°C. Ces xénolites ont donc été déformées dans l'asthénosphère puis ont été accrétées à la lithosphère probablement suite à un refroidissement du coin mantellique. Durant toute leur histoire, ces péridotites ont été percolées par des fluides riches en silice ou des magmas enrichis en eau. Cette interaction avec des fluides a favorisé les processus de diffusion durant la déformation ductile.

Cependant la direction de glissement dominante dans l'olivine n'évolue pas de [100] à [001] contrairement aux études expérimentales.

La deuxième partie intitulée "Implication sur les propriétés sismiques du coin mantellique" correspond à un article paru dans *Geophysical Research Letters* (Soustelle & Tommasi, 2010), qui analyse l'impact de la percolation réactionnelle durant la déformation sur les propriétés sismiques des xénolites de péridotites de l'Avacha. La présence de fluide ou de magma n'a pas affecté la direction de glissement dominante dans l'olivine, car tous les échantillons montrent une OPR de l'olivine de type axiale-[100]. Ceci implique que la direction de polarisation des ondes S rapides, dans la partie supérieure du coin mantellique de la subduction du Kamchatka, est parallèle à la direction d'écoulement du manteau. Cependant, la percolation réactive de fluide riche en silice a entrainé un enrichissement en orthopyroxène associé à une décroissance de l'intensité des OPR de l'olivine, ce qui a pour conséquence une réduction non négligeable de l'anisotropie. Si cette réduction n'est pas prise en compte, elle pourrait induire une sous-estimation de la couche anisotrope d'au maximum 26%. L'enrichissement en orthopyroxène est aussi invoqué par certains auteurs (c.f., Wagner et al., 2006) pour expliquer les faibles rapports Vp/Vs (< 1,7) observés localement dans le coin mantellique des zones de subduction comme le Japon ou les Andes (Zhang et al., 2004; Wagner et al., 2005). Nous avons donc calculé les variations de rapport Vp/Vs impliquée par un enrichissement en orthopyroxène similaire à celui observé dans nos échantillons. Les résultats montrent que la réduction de rapport n'est pas assez importante pour expliquer des rapports Vp/Vs inférieur à 1,7. Cependant, ce travail montre que part la prise en compte de l'anisotropie des ces péridotites, en considèrant la géométrie de la déformation et les directions de propagation des ondes P et S dans le coin mantellique, il devient possible d'obtenir des rapports Vp/Vs < 1,7.

3.1. Les interactions entre déformation et percolation réactive de fluides dans le manteau en supra-subduction

Soustelle, V., Tommasi, A., Demouchy S., Ionov, D. *(2010)*. Deformation and fluid-rock interactions in supra-subduction mantle: Microstructures and water contents in peridotites xenoliths from the Avacha volcano, Kamchatka, ***Journal of Petrology***, 51(1-2), 363-394.

3.2. Implication sur les propriétés sismiques du coin mantellique

Soustelle, V., Tommasi, A. *(2010)*. Seismic properties of the supra-subduction mantle: Constraints from peridotite xenoliths from the Avacha volcano, southern Kamchatka, ***Geophysical Research Letters***, 37, L13307.

JOURNAL OF PETROLOGY | VOLUME 51 | NUMBERS 1 & 2 | PAGES 363–394 | 2010 | doi:10.1093/petrology/egp085

Deformation and Fluid–Rock Interaction in the Supra-subduction Mantle: Microstructures and Water Contents in Peridotite Xenoliths from the Avacha Volcano, Kamchatka

V. SOUSTELLE[1]*, A. TOMMASI[1], S. DEMOUCHY[1] AND D. A. IONOV[2]

[1]GÉOSCIENCES MONTPELLIER, UNIVERSITÉ MONTPELLIER II & CNRS, CC 60, PLACE E. BATAILLON, 34095 MONTPELLIER CEDEX 5, FRANCE

[2]UNIVERSITE DE LYON, UNIVERSITÉ JEAN MONNET, F42023 SAINT-ETIENNE & LABORATOIRE MAGMAS ET VOLCANS, UMR 6524, CNRS, FRANCE

RECEIVED MARCH 17, 2009; ACCEPTED NOVEMBER 11, 2009

The mantle above a subducting slab is the site of complex interactions between deformation, partial melting, fluid migration and magma transport. To constrain these interactions and their effects on olivine deformation, we analyze microstructures, crystal preferred orientations, and water contents of peridotite xenoliths entrained by andesites of the Avacha volcano, southern Kamchatka arc. These xenoliths are refractory spinel harzburgites that have coarse-grained microstructures with widely spaced subgrain boundaries and sinuous grain boundaries in olivine, consistent with deformation by dislocation creep under low deviatoric stress (≤13 MPa) and with a significant contribution from diffusional processes. Analysis of crystal preferred orientations (CPO) indicates dominant activation of high-temperature, low-stress {0kl}[100] slip systems in olivine and of (100)[001] in orthopyroxene. In most samples, coarse opx crystals, elongated parallel to the lineation, enclose small olivine grains in crystallographic continuity with neighbouring crystals, indicating crystallization of orthopyroxene at the expense of olivine as a result of reactive percolation of Si-rich fluids coeval with the high-temperature deformation. Secondary crystallization of interstitial orthopyroxene led locally to development of opx-rich lenses parallel to the foliation, characterized by a decrease in olivine grain size and dispersion of the olivine CPO without changing the dominant slip systems. Half of the samples also show acicular orthopyroxene aggregates with which is associated a fine-grained matrix composed of rounded strain-free olivine, orthopyroxene, spinel, and rare amphibole crystals. This matrix occurs pervasively along grain boundaries or forms millimeter-scale irregular lenses and anastomosing veinlets that crosscut the coarse crystals and their ductile deformation structures. Both acicular orthopyroxene and the fine-grained matrix are interpreted as resulting from reactive transport of H_2O-rich fluids under static conditions, probably in the lithospheric mantle. Infrared analyses show that olivine contains 1–8·6 ppm by weight of water. These low water contents are similar to those observed in spinel peridotites from other subduction zones and probably record both the low solubility of water in olivine at low pressure and dehydration during exhumation of the xenoliths. Water contents in orthopyroxene are highly variable (25–506 ppm H_2O), probably recording spatially heterogeneous interaction with fluids or melts and compositional disequilibrium in the studied samples. Change in the dominant percolation mechanism from porous flow to fracturing suggests cooling, consistent with the low temperatures estimated from pyroxene thermometry (≤ 800–900°C). The Avacha xenoliths therefore record pervasive deformation of a region of the mantle under asthenospheric conditions, followed by its accretion to the base of the lithosphere, probably as a result of cooling of the mantle wedge. Percolation of Si-rich fluids or hydrous melts is recorded at all stages; this probably enhanced diffusion and lowered deviatoric stresses during ductile deformation, but did not change the dominant slip direction in olivine from [100] to [001].

*Corresponding author. Telephone: +33-(0)467143941. Fax: +33-(0)467143603. E-mail: vsoustel@gm.univ-montp2.fr

KEY WORDS: *xenolith; harzburgite; olivine; orthopyroxene; subduction; Kamchatka; microstructure; CPO; melt or fluid percolation; water; lithosphere; mantle wedge*

INTRODUCTION

The dynamics of subduction are the result of a complex force balance in which the rheology of the mantle wedge plays an essential role. The supra-subduction mantle is also the site of a series of petrological processes, ranging from dehydration of subducted material to partial melting in the wedge. Because both the presence of small melt fractions and the incorporation of water in olivine strongly reduce the strength of upper mantle rocks (Blacic, 1972; Mackwell *et al.*, 1985; Karato *et al.*, 1986; Hirth & Kohlstedt, 1995; Mei & Kohlstedt, 2000*a*, 2000*b*; Mei *et al.*, 2002; Zimmerman & Kohlstedt, 2004), the mantle wedge rheology depends on interactions between these petrological processes, migration of the resulting fluids and melts, and deformation of the solid peridotite matrix. Numerical models show that changes in mantle wedge rheology as a result of the presence of melt or water may enhance small-scale thermal convection in the wedge, leading to the erosion of the overriding arc and back-arc lithosphere (Honda *et al.*, 2002; Arcay *et al.*, 2006; Cagnioncle *et al.*, 2007; Currie *et al.*, 2008), or induce the development of partially molten diapirs in the mantle wedge (Gerya & Yuen, 2003).

Experimental studies show that incorporation of water in nominally anhydrous minerals (Hier-Majumder *et al.*, 2004; Demouchy *et al.*, 2007; Costa & Chakraborty, 2008), such as olivine, or the presence of interconnected small melt fractions also enhance diffusion, favouring recovery of dislocations (Karato *et al.*, 1993), recrystallization (Avé-Lallemant & Carter, 1970; Jung & Karato, 2001*b*), and grain growth (Karato, 1989). This is consistent with recent studies of mantle xenoliths and peridotite massifs, which suggest that melt percolation under both dynamic and static conditions may significantly modify the microstructure of mantle rocks (e.g. Vauchez & Garrido, 2001; Tommasi *et al.*, 2006, 2008; Le Roux *et al.*, 2008; Soustelle *et al.*, 2009). Reactive melt transport may also change the modal mineralogy (Le Roux *et al.*, 2007) and produce Fe- or pyroxene-enrichment, changing the density and reducing the seismic velocities of mantle rocks (Lee, 2003; Tommasi *et al.*, 2004). Finally, the presence of trace amounts of water may also result in a change of the dominant glide direction in olivine and consequently modify the crystal preferred orientations (CPO) formed during deformation by dislocation creep (Jung & Karato, 2001*a*), with direct implications for the interpretation of upper mantle seismic anisotropy in terms of flow geometry.

The actual fluids or melt content and distribution in the mantle wedge above a subduction zone and their effect on mantle wedge deformation are, nevertheless, still poorly constrained. Direct samples of the mantle wedge are brought up to the surface by subduction-related calc-alkaline volcanism; however, these samples are extremely rare. Moreover, previous studies of subduction zone mantle xenoliths have focused on geochemical and petrological processes rather than on their deformation histories (e.g. Arai & Kida, 2000; Grégoire *et al.*, 2001; McInnes *et al.*, 2001; Arai *et al.*, 2003; Ishimaru *et al.*, 2007; Ionov & Seitz, 2008). Here we present a detailed microstructural study, including an analysis of dislocation structures, as well as measurements of crystal preferred orientations and water concentrations in olivine and orthopyroxene from 23 spinel harzburgite xenoliths from the Avacha volcano in the southeastern Kamchatka subduction zone. These data are used to investigate the relationship between deformation, fluid or melt percolation and hydration in the supra-subduction mantle.

GEOLOGICAL SETTING

All the studied xenoliths were collected from Holocene tuffs of the active Avacha (Avachinsky) volcano (53°15′N, 158°51′E; summit elevation 2741 m) located near the southeastern coast of the Kamchatka peninsula, 200 km NE of the Kurile–Kamchatka trench (Fig. 1). The Kamchatka peninsula is located in the northwestern corner of the Pacific and has been the site of continuing subduction since the Oligocene (Avdeiko *et al.*, 2002). The peninsula is composed of three volcanic fronts (Fig. 1): the older (Oligocene) Sredinny range in the west and two younger volcanic fronts in the east, of which only the easternmost is currently active (Tatsumi *et al.*, 1994). The present tectonic situation results from the collision of two volcanic arcs 5–7 Myr ago as a result of the closure of the Vetlovka basin, which separated two opposed subduction systems that were active between the middle Eocene and the Late Miocene (Konstantinovskaia, 2001). This collision resulted in an eastward displacement of the active volcanic front and the formation of the Eastern Kamchatka volcanic front, which has been active since 5 Ma (Konstantinovskaia, 2001) in response to the fast subduction (~8 cm/year) of the old Pacific plate (~80 Myr old).

Avacha is one of the most active volcanoes in the central part of the eastern volcanic front. The depths of the Moho and of the upper surface of the subducting slab beneath it are about 37 km and 120 km, respectively (Gorbatov *et al.*, 1997; Levin *et al.*, 2002). Seismic tomography shows low P-wave velocities in the mantle wedge beneath the eastern arc, which is consistent with melt generation and the locus of volcanic activity (Gorbatov *et al.*, 1999; Manea *et al.*, 2005). Seismic anisotropy measurements using local shear waves show trench-normal fast polarizations in the fore-arc and arc domains in southeastern Kamchatka (i.e. below the Avacha volcano) but trench-parallel polarizations in the back-arc (Levin *et al.*, 2004). This observation

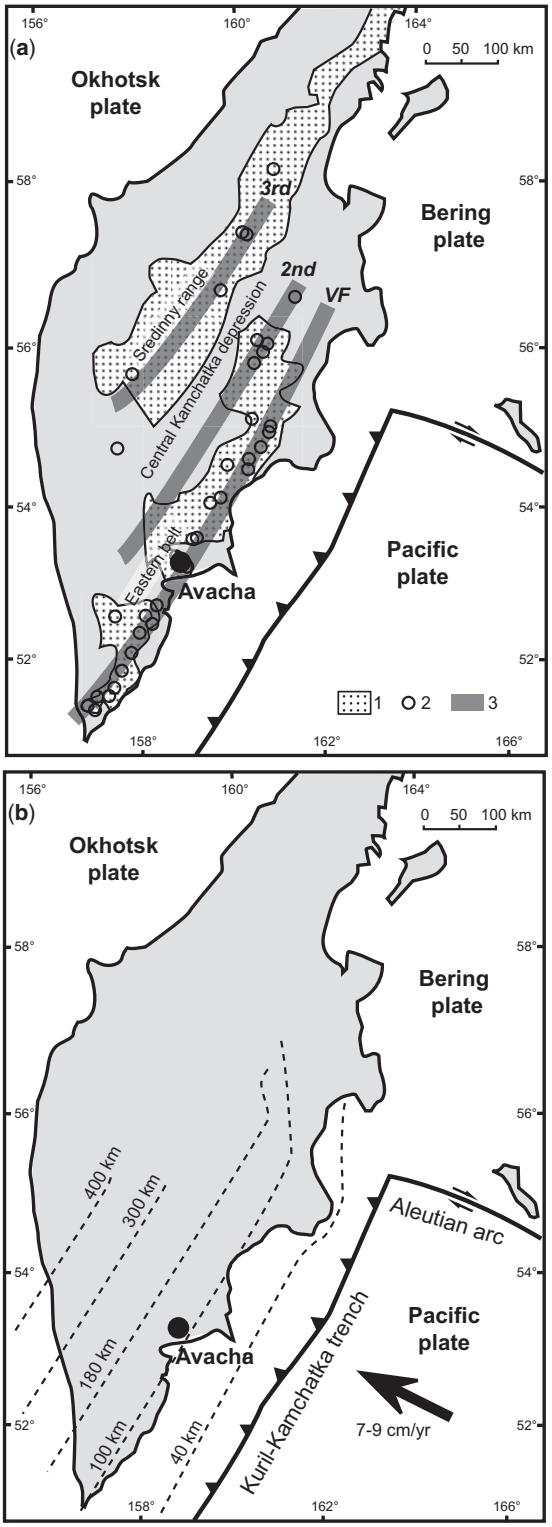

Fig. 1. (a) Simplified geological map of the Kamchatka peninsula showing the two ancient volcanic ranges (contours from Konstantinovskaia, 2001) and the active volcanic front (VF) (Tatsumi *et al.*, 1994); circles mark major active and extinct volcanos; Avacha is indicated by a full circle. (1) Volcanic ranges, (2) active and major extinct volcanoes, (3) active and former volcanic fronts. (b) Contours of the Wadati–Benioff zone beneath southern Kamchatka (Gorbatov *et al.*, 1997; Ishimaru *et al.*, 2007).

suggests that two-dimensional corner flow in the mantle wedge does not extend inland beyond the volcanic arc (Levin *et al.*, 2004). Beyond this, the anisotropy is interpreted as recording asthenospheric flow around and beneath the disrupted slab edge at the Aleutian junction (Peyton *et al.*, 2001).

The Avacha volcano formed in the late Pleistocene, and the last eruptions occurred in 2001. Large Holocene eruptions have produced ash-falls and pyroclastic flows, with compositions varying from low-K andesite to basaltic andesite, dated using ^{14}C from 7200 to 3700 years BP (Braitseva *et al.*, 1998). The xenoliths studied here are angular blocks (10–40 cm in size) collected in volcanic ash on the western slope of the volcano (Ionov, 2009).

MODAL COMPOSITIONS AND GEOCHEMICAL DATA

All studied xenoliths are fresh peridotites with no secondary alteration. The majority (AV1 to AV17) are homogeneous at the hand-specimen scale, but some samples (AV18 to AV23) are crosscut by millimeter-scale pyroxene-rich veins or pockets. These peridotites have been the subject of a detailed petrological and geochemical study (Ionov, 2010), including petrographic descriptions and major and trace element analyses of whole-rocks and minerals. These data are summarized below. The compositions of the pyroxene-rich veins have been discussed in Bénard & Ionov (2009).

The Avacha peridotites are spinel harzburgites composed of 67–79% olivine (ol), 18–30% orthopyroxene (opx), ≤1% spinel (sp), 1–3% clinopyroxene (cpx), and ≤1% amphibole (amph); the mass proportions of minerals were calculated from whole-rock and mineral major oxide compositions. Cpx and amphibole are always interstitial. Coarse-grained orthopyroxenes show widespread unmixing and core–rim zoning in Ca and Al, indicating cooling from sub-magmatic temperatures to 900–1000°C. Late-stage acicular or fine-grained interstitial orthopyroxene exhibits a broad range in Ca contents, possibly as a result of cooling to ≤800–900°C followed by heating shortly before the eruption. The Avacha peridotites are highly refractory, with ≥44% MgO and very low Al_2O_3 and CaO (0·4–0·9%), TiO_2 (≤0·01%), Na_2O (≤0·03%), K_2O and P_2O_5 (below detection) contents in whole-rocks, high Mg-number $[Mg/(Mg + Fe)_{at}]$ in olivine (0·907–0·918), high Cr-number $[Cr/(Cr + Al)_{at}]$ in spinel (0·53–0·65), and very low Al_2O_3 (≤2·1%) in orthopyroxene and Na_2O (0·1–0·3%) in clinopyroxene. These compositions are consistent with up to 30–40% of melt extraction at ≤1–2 GPa, leaving no clinopyroxene in the peridotitic residue.

Compared with refractory peridotite xenoliths in continental basalts, the Avacha harzburgites tend to have

higher orthopyroxene (and SiO_2) and lower clinopyroxene contents. These features may indicate either fluid fluxing during melting in the mantle wedge or post-melting enrichment in SiO_2 as a result of reactive percolation by Si-rich fluids leading to crystallization of orthopyroxene at the expense of olivine. This silica enrichment is restricted to peridotites with abundant coarse orthopyroxenes and is not related to late-stage processes.

Abundances of rare earth elements (REE) in the Avacha peridotites are very low (≥10 times lower than in primitive mantle). All the studied xenoliths show depletion in the light and middle relative to the heavy REE, suggesting that partial melting was not followed by subsequent metasomatism by basaltic magma or low melting degree products.

MICROSTRUCTURAL OBSERVATIONS

Most of the studied xenoliths have coarse-grained porphyroclastic microstructures characterized by olivine and orthopyroxene crystals up to 5 mm wide (Fig. 2). These coarse porphyroclastic samples display a well-developed lineation marked by spinel trails and by the elongation of coarse olivine crystals that show aspect ratios ranging from 1:4 to 1:2 (Fig. 2a and b). Some coarse porphyroclastic xenoliths also show aligned discontinuous opx-rich lenses, up to 1 cm thick, which are characterized by finer olivine grain sizes (<0·5 mm on average, Fig. 2a). Both coarse- and fine-grained olivine crystals have curvilinear grain boundaries that locally evolve into more polygonal shapes, forming 120° triple junctions (Fig. 2b and c). They usually display undulose extinction and widely spaced subgrain boundaries. In the coarse grains, the latter tend to be normal to the crystal elongation (Fig. 2b). An exception is sample AV3, where subgrain boundaries are parallel to the elongation of the olivine crystals. Both the orientation of the subgrains and the crystal elongation in this sample are, however, normal to the lineation marked by the spinel trails, suggesting that the elongation of the olivine crystals in this sample is a 'false' lineation formed by rotation recrystallization along (100) subgrain boundaries. Although rare, this phenomenon has previously been described in both peridotites and quartzites (Bouchez *et al.*, 1984; Tommasi *et al.*, 2001). Finally, neighbouring olivine crystals intercalated with orthopyroxene in opx-rich lenses often show similar crystallographic orientations and intracrystalline deformation features suggesting that they were originally part of a single coarse olivine crystal that was partially replaced by orthopyroxene (Figs 2e and 3). Inclusion trails crosscutting several olivine crystals are common. They may represent healed fractures.

The coarse porphyroclastic peridotites display two types of orthopyroxene. 'Coarse' orthopyroxene occurs as isolated grains or in aggregates (Fig. 2a). Grain sizes vary from 0·2 to 5 mm, but millimeter-sized grains dominate. The coarser opx crystals (>1 mm wide) often have a turbid aspect as a result of the presence of a large amount of minute fluid inclusions (Fig. 4a). Exsolution lamellae of clinopyroxene and spinel, undulose extinction, and kink bands are common in the central parts of these large orthopyroxene crystals (Fig. 4a and c). Both isolated grains and aggregates have irregular shapes indenting and sometimes enclosing olivine crystals (Fig. 4a and c). Within an aggregate, orthopyroxene grain boundaries are straight and tend to form 120° triple junctions. Olivine relicts within large orthopyroxene crystals often show the same extinction angle as neighbouring coarse olivine crystals, suggesting that they were derived from a single coarse olivine crystal that was progressively replaced by orthopyroxene (Fig. 4a). Smaller isolated orthopyroxene crystals, ≤0·5 mm wide, (referred to as 'interstitial' orthopyroxenes in the following discussion) are locally observed in olivine triple junctions and along two-crystal boundaries (Fig. 4b). These smaller orthopyroxene crystals usually do not show intracrystalline deformation features.

The second type of orthopyroxene (referred to as 'acicular' orthopyroxene subsequently) is characterized by aggregates of fine-grained prismatic to acicular grains, <50 μm in width and <100 μm long, with a similar crystallographic orientation; these are probably inherited from precursor coarse orthopyroxene (Fig. 4d). Acicular orthopyroxene aggregates are 1–5 mm wide and often surround coarse orthopyroxenes and olivine crystals with 'corroded' shapes (Fig. 4c). These acicular orthopyroxene aggregates are probably equivalent to the 'recrystallized orthopyroxenes' described by Arai *et al.* (2003) from a different suite of Avacha peridotite xenoliths. Acicular orthopyroxenes are usually associated with a fine-grained ol–opx–spinel matrix made up of equant olivine and orthopyroxene crystals <50 μm in size (Figs 2f, h and 4c–e) with minor amounts of interstitial clinopyroxene, amphibole, oxides (Ionov & Seitz, 2008), and glass. This matrix occurs in all samples, but in variable proportions. In most samples, it occurs as thin films along olivine and orthopyroxene grain boundaries (Fig. 2e and g). However, it may also locally form large (>1 mm) irregularly shaped pockets (Fig. 2d, f and h). Larger matrix volumes are usually observed along the opx-rich lenses parallel to the foliation or around acicular orthopyroxenes. The fine-grained matrix also fills thin anastomosing veinlets (50–500 μm wide) that crosscut coarse olivine crystals and their internal deformation features (subgrain boundaries) without any evidence of displacement (Fig. 4d). These veinlets often enclose small (<300 μm) strain-free polygonal olivine grains with strong misorientations relative to the coarse

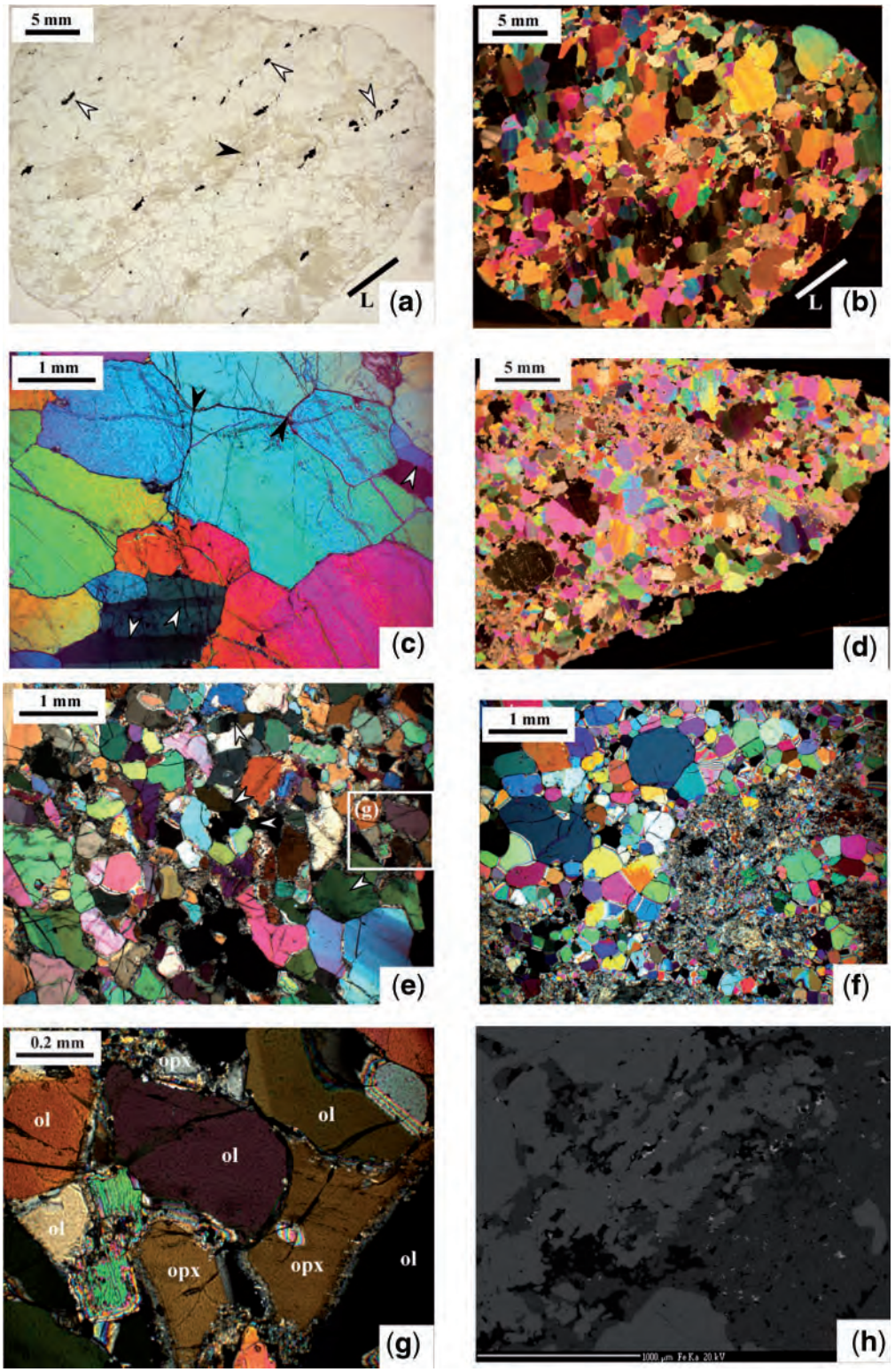

Fig. 2. Photomicrographs in plane-polarized light (a) and cross-polarized light (b–g) illustrating the typical microstructures in the Avacha peridotite xenoliths. (a) Coarse-grained peridotite AV12 showing a lineation (L) marked by the alignment of spinel (white arrows) and orthopyroxene (opx) aggregates (black arrow). (b) Same sample in cross-polarized light showing elongation of coarse olivine crystals parallel to the lineation and olivine grain refinement within opx-rich bands. (c) Subgrain boundaries (white arrow) and 120° triple junctions (black arrow) in olivine in sample AV12. (d) Fine-grained ol–opx–oxides ± amph ± cpx ± glass matrix along grain boundaries and in a millimeter-scale band in sample AV5. (e) Detail of an opx-rich band in coarse porphyroclastic peridotite AV15 showing pervasive distribution of the fine-grained matrix along grain boundaries; white arrows highlight subgrain boundaries and polygonal grain boundaries in olivine. (f) Strain-free polygonal olivine and thick pocket of ol–opx–oxides ± amph ± cpx ± glass matrix in equigranular peridotite AV16. (g) Detail of (e) showing interstitial orthopyroxene and thin films of the fine-grained matrix along grain boundaries. (h) Fe distribution map in the fine-grained matrix of sample AV5; scale bar represents 1 mm. Olivine (light gray) is abundant in the matrix; it forms subhedral grains that appear to be in textural equilibrium with orthopyroxene (medium gray), cpx (dark gray), and amphibole (darkest gray).

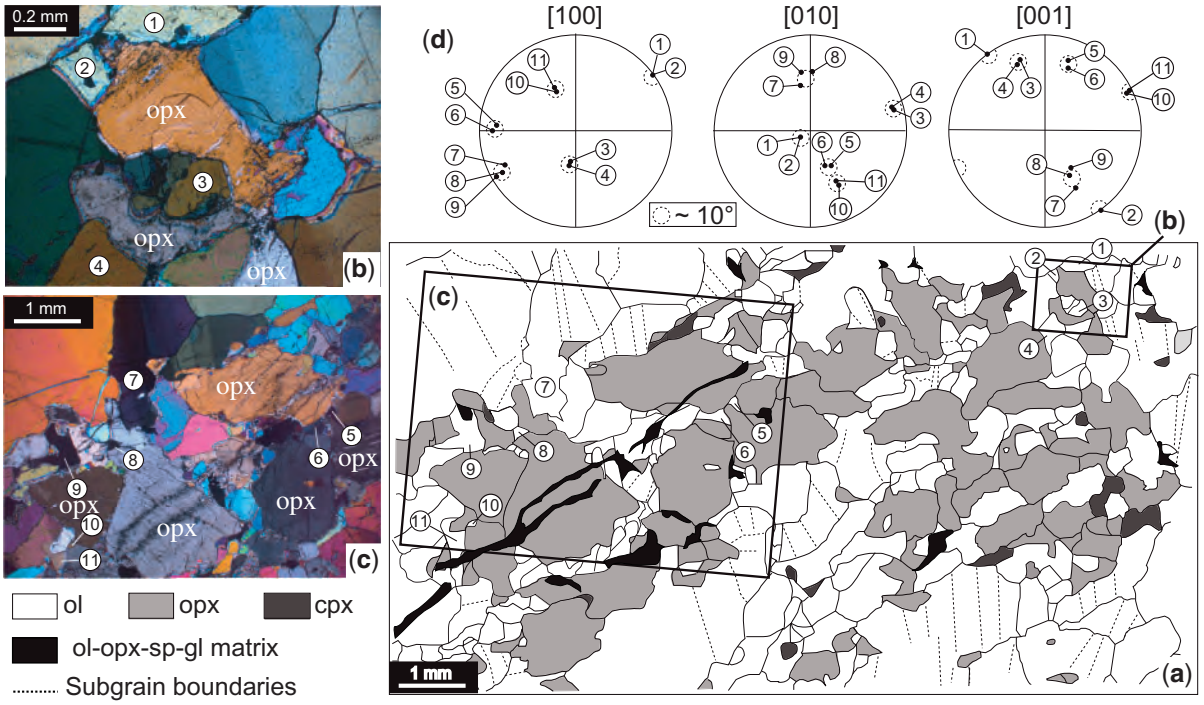

Fig. 3. Microstructure and crystallographic relations in opx-rich lenses. (a) Sketch of an opx-rich lens in sample AV12; black rectangles mark the location of cross-polarized light photomicrographs (b) and (c), which show the interstitial shapes of orthopyroxene (opx). In (c) a late vein-like structure filled by the fine-grained matrix is also observed. (d) Equal-area lower-hemisphere stereographic projections of the orientation of the [100], [010] and [001] axes of olivine crystals 1–11 in the thin-section reference frame (EBSD measurements) highlighting the crystallographic continuity between neighbouring olivine crystals separated by interstitial orthopyroxene.

host crystals (Fig. 4e). When the veinlets crosscut an orthopyroxene, they tend to lose their vein-like structure, forming diffuse reaction zones characterized by the crystallization of acicular orthopyroxene (Fig. 4d).

A single sample (AV16) has a fine-grained equigranular microstructure (Fig. 2f). The olivine crystals have polygonal shapes and are on average <0·5 mm wide. They are entirely free of intra-crystalline deformation features and often show 120° triple junctions (Fig. 2f) that may contain an isotropic phase that probably corresponds to glass. All the orthopyroxenes are acicular. This sample is particularly rich in the ol–opx–oxides ± amph ± cpx ± glass matrix, which occurs as large millimeter-scale irregular pockets (Fig. 2f).

Lastly, the coarse-grained porphyroclastic peridotites AV20 and AV21 are crosscut by linear millimeter-scale orthopyroxenite veins. These veins have a magmatic texture, characterized by equigranular strain-free orthopyroxenes (100–500 μm) with irregular shapes.

CRYSTAL PREFERRED ORIENTATIONS

Analytical procedure

Olivine and orthopyroxene crystal preferred orientations (CPO) were determined by indexation of electron-backscattered diffraction patterns (EBSD) at the SEM-EBSD facility at Geosciences Montpellier. The EBSD patterns were generated by interaction of a vertical incident electron beam with a carefully polished thin section tilted at 70° in a scanning electron microscope (JEOL JSM 5600). The diffraction pattern was projected onto a phosphor screen and recorded by a digital CCD camera. The image was then processed and indexed in terms of crystal orientation using the CHANNEL5 software from Oxford Instruments HKL.

For each sample, we obtained crystallographic orientation maps covering almost entirely the thin section (usually 35 mm long and 20 mm wide) with sampling steps of 100, 75, or 50 μm, depending on the grain size (Fig. 5). Indexation rates in the raw maps range from 50 to 80%. In general, indexation rates are lower for orthopyroxene than for olivine. Acicular orthopyroxenes, because of the fine grain size of the crystals composing the aggregates and poor polishing, were particularly poorly indexed. Very low indexation rates (<20%) were also obtained for the fine-grained ol–opx–oxides ± amph ± cpx ± glass matrix.

Post-acquisition data treatment allowed us to increase further the indexation rate by (1) filling the non-indexed pixels that have up to eight identical neighbours with this orientation, (2) repeating this operation

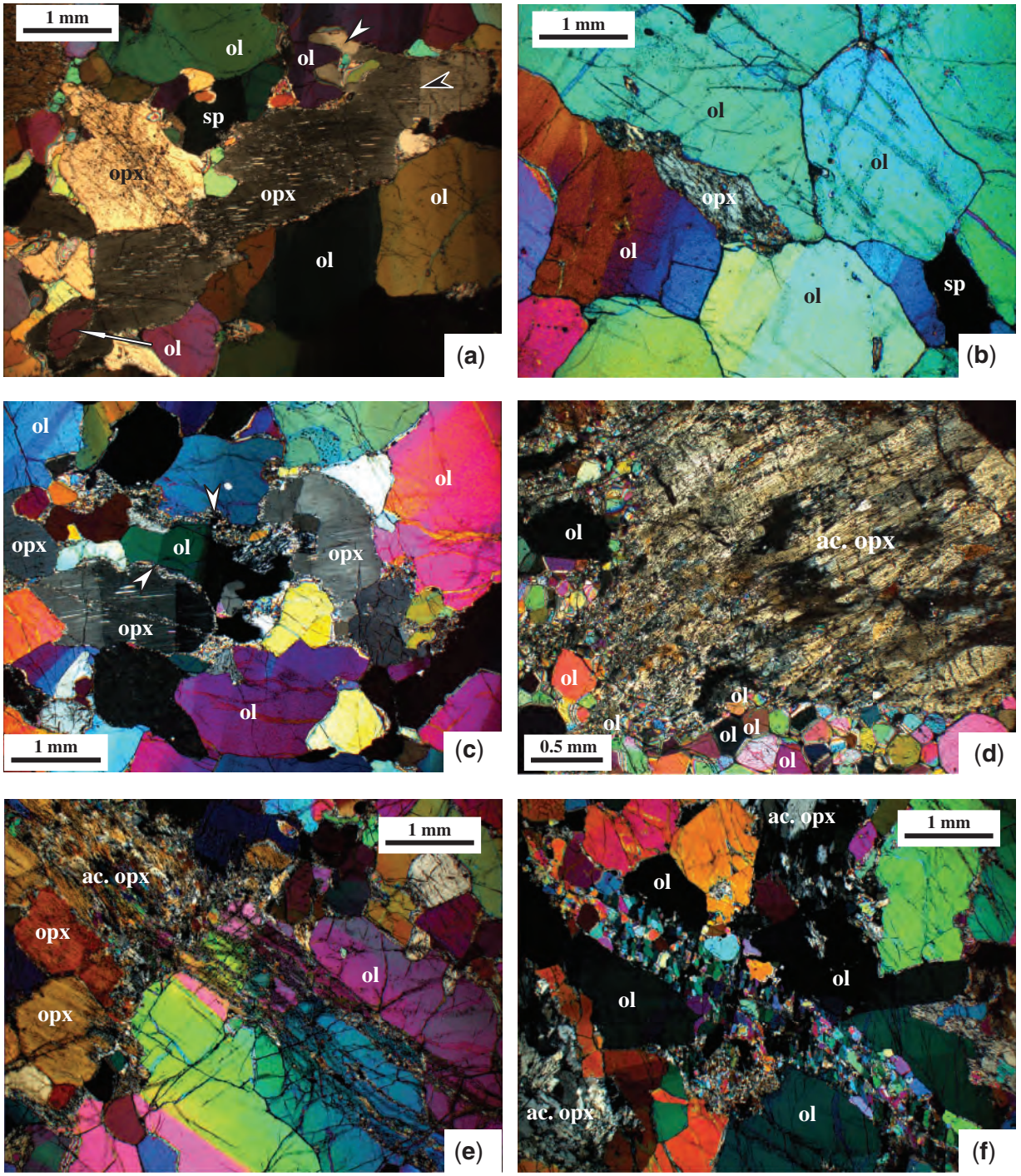

Fig. 4. Photomicrographs in cross-polarized light of typical orthopyroxene morphologies and microstructures. (a) Coarse orthopyroxene (opx) elongated parallel to the lineation with well-developed kink bands (black arrow) that fills corrosion embayments in neighbouring olivine (ol) crystals and encloses olivine relicts (long white arrow); deformation-free orthopyroxene overgrowth is marked by a short white arrow. (b) Interstitial orthopyroxene in an olivine triple junction. (c) Detail of an opx-rich band, showing corroded olivine crystals surrounded by orthopyroxene with well-developed kink bands subparallel to subgrains in neighbouring olivine as well as crystallization of the fine-grained ol–opx–oxides ± amph ± cpx ± glass matrix in films along grain boundaries and in intergranular pockets (white arrows). (d) Acicular orthopyroxene (ac opx) surrounded by polygonal olivine crystals in equigranular peridotite AV16. (e) Anastomosing veinlets filled with the fine-grained ol–opx–oxides ± amph ± cpx ± glass matrix in continuity with an acicular orthopyroxene in coarse porphyroclastic peridotite AV20. (f) Small polygonal strain-free olivine grains within anastomosing veinlets crosscuting intracrystalline deformation features in coarse olivine crystals in sample AV1.

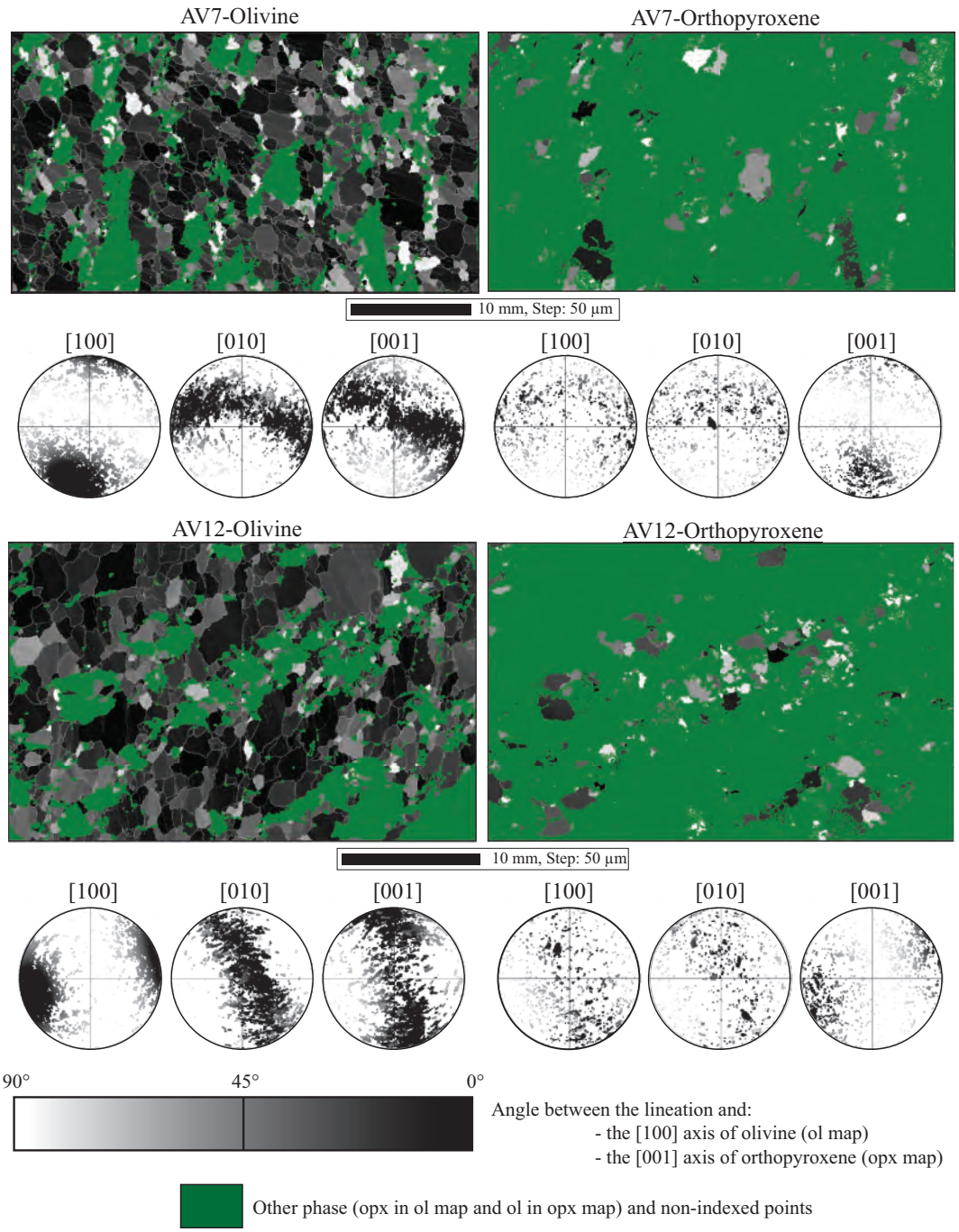

Fig. 5. Crystallographic orientation map and equal-area lower hemisphere stereographic projections in the thin-section reference frame of [100], [010], and [001] axes of olivine and orthopyroxene. Data are from samples AV7 and AV12. Greyscale in the maps indicates the angle between the orientation of the [100] olivine axis or the [001] orthopyroxene axis and the lineation indicated by the elongation of coarse olivine crystals.

using respectively seven, six, and five identical neighbours, (3) identifying the grains (i.e. continuous domains characterized by an internal misorientation <15°), and (4) within each olivine crystal, searching and correcting for systematic indexation errors caused by the olivine hexagonal pseudo-symmetry, which results in similar diffraction patterns for orientations differing by a rotation of 60° around [100]. At each step, the resulting orientation maps were verified by the operator to avoid over-extrapolation of the data.

Because the foliation and lineation could not be determined macroscopically in most samples, most thin-sections were cut in random orientations, rather than parallel to the lineation and normal to the foliation. To allow a straightforward comparison between the CPO of the different samples, all the CPO measurements were rotated to have the maximum concentrations of olivine [100] and [010] axes parallel to the east–west and north–south directions, respectively. When the lineation is clearly marked by the elongation of olivine or alignment of spinels, the latter is indicated in the pole figures (Fig. 6). Well-developed foliations are never observed in the studied Avacha peridotites, but when opx-rich bands are present, their average orientation is also plotted. To avoid over-representation of large crystals, CPO are plotted as one measurement per grain (average orientation of the crystal).

Results

The studied peridotites show strong olivine CPO (Figs 5 and 6). An exception is the fine-grained peridotite AV16, which has an almost random olivine CPO. Olivine CPO shows well-developed axial [100] patterns characterized by a strong point concentration of [100] axes. When observed, the mineral lineation is always sub-parallel to the maximum concentration of the olivine [100] axes (Fig. 6). [010] and [001] axes show girdle distributions normal to the [100] maximum, with two weak maxima roughly normal to each other. The [010] maximum is usually stronger than the [001] one, but this relation is reversed in samples AV10, AV11, AV18 and AV23 (Fig. 6).

The CPO strength or intensity can be defined by two dimensionless indices, as follows.

(1) The J index, which is the volume-averaged integral of the squared orientation densities (Bunge, 1982). It has a value of unity for a random CPO and tends to infinity for a single crystal, but most natural peridotites show J-index values between two and 20, with a peak around eight (Ben Ismail & Mainprice, 1998; Tommasi *et al.*, 2000). The J index of all samples was calculated for both the full orientation dataset from the EBSD maps and the mean orientation for each grain using the SuperJ7x program by D. Mainprice with a 10 degree Gaussian half-width, data at 1 degree bins, and truncation of the orientation distribution function (ODF) at degree 22.

(2) The M index (misorientation index), which corresponds to the difference between the observed distribution of uncorrelated misorientation angles and that predicted for a random fabric (Skemer *et al.*, 2005). It has a value of zero for a random CPO and unity for a single crystal.

J and M indices show a good linear correlation ($R^2 = 0{\cdot}88$, Fig. 7), indicating that both indices correctly represent the CPO strength of the studied samples. Because most published CPO data for natural peridotites and experimental aggregates have their strength expressed as J indices, we chose to use this index in the following discussion as it is widely used not only in geology, but also in material sciences.

In the studied peridotites, the J index ranges between 9·5 and 2. This variation in J index is correlated with the olivine grain size distribution (Fig. 8a). The lowest J index is observed in the fine-grained equigranular peridotite AV16. In the coarse porphyroclastic samples, two behaviours can be discriminated: samples with >10% vol. of fine-grained olivine (<0·5 mm) show weak olivine CPO (J<5), whereas the remaining samples have J indices between 5 and 10. These two groups may also be distinguished on the basis of their modal composition: weak olivine CPOs are associated with an enrichment in orthopyroxene (Fig. 8b). Within a group, no clear correlation between J index and fine-grained olivine or orthopyroxene contents can be established. Analysis of the J indices calculated for different grain size populations in a sample (Fig. 9) shows, however, that fine (<0·5 mm) and intermediate-size grains (0·5–1 mm) have lower J indices (i.e. more dispersed orientations) than coarse olivine crystals in a sample. The fine-grained population has therefore a strong influence on the estimation of the sample J index if the latter is calculated using one measurement per grain, as fine grains are more numerous on a given analysed surface. Comparison of J indices calculated using one measurement per grain and using the full orientation dataset from the EBSD map that take into account the surface of the crystals shows that the former method underestimates the intensity of the CPO (Fig. 10). This observation highlights the problem of estimating the CPO intensity in samples exhibiting strong grain-size heterogeneity. The use of one average orientation per grain overestimates the contribution of the fine grains, whereas by using the EBSD map data a higher weight is given to coarse grains. The choice depends on the type of study performed. Use of one measurement per grain allows relation of the CPO to the microstructure, as in the present study, whereas surface-weighted CPO should be preferred when calculating CPO-induced anisotropy of physical properties.

The symmetry of the olivine CPO may be defined by the relative proportion of point, girdle and random components for each axis distribution (Fig. 11). This diagram is constructed using the eigenvectors of the orientation matrix for each crystallographic axis (Vollmer, 1990). The weak CPO of the equigranular peridotite AV16 is expressed by a dominant random component in all three axes distribution. In contrast, coarse-grained porphyroclastic peridotites show a variation in the [100] and [010]

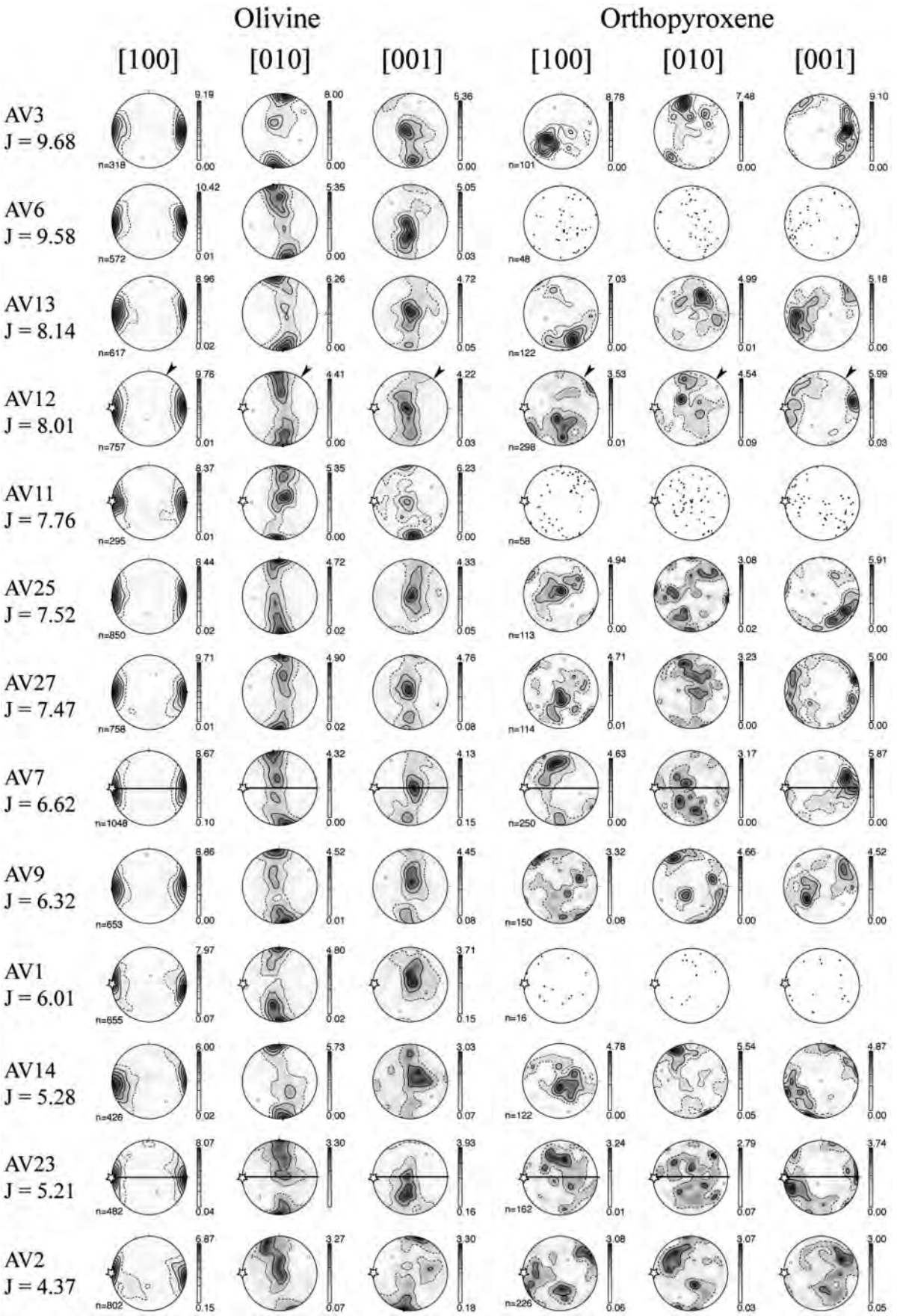

Fig. 6. Olivine and orthopyroxene crystal preferred orientations. Lower hemisphere, equal-area stereographic projections, contours at one multiple of uniform distribution. All data were rotated to have the olivine [100] maximum in the east–west horizontal direction and the [010] maximum close to the north–south horizontal direction. N, number of measured grains. Orthopyroxenes were not contoured when fewer than 100 grains were measured. Lineation, when observed, is marked by a star. Compositional banding, when observed, is indicated by a continuous line; when parallel to the projection plane, it is marked by a black arrow showing the circle of the pole figure.

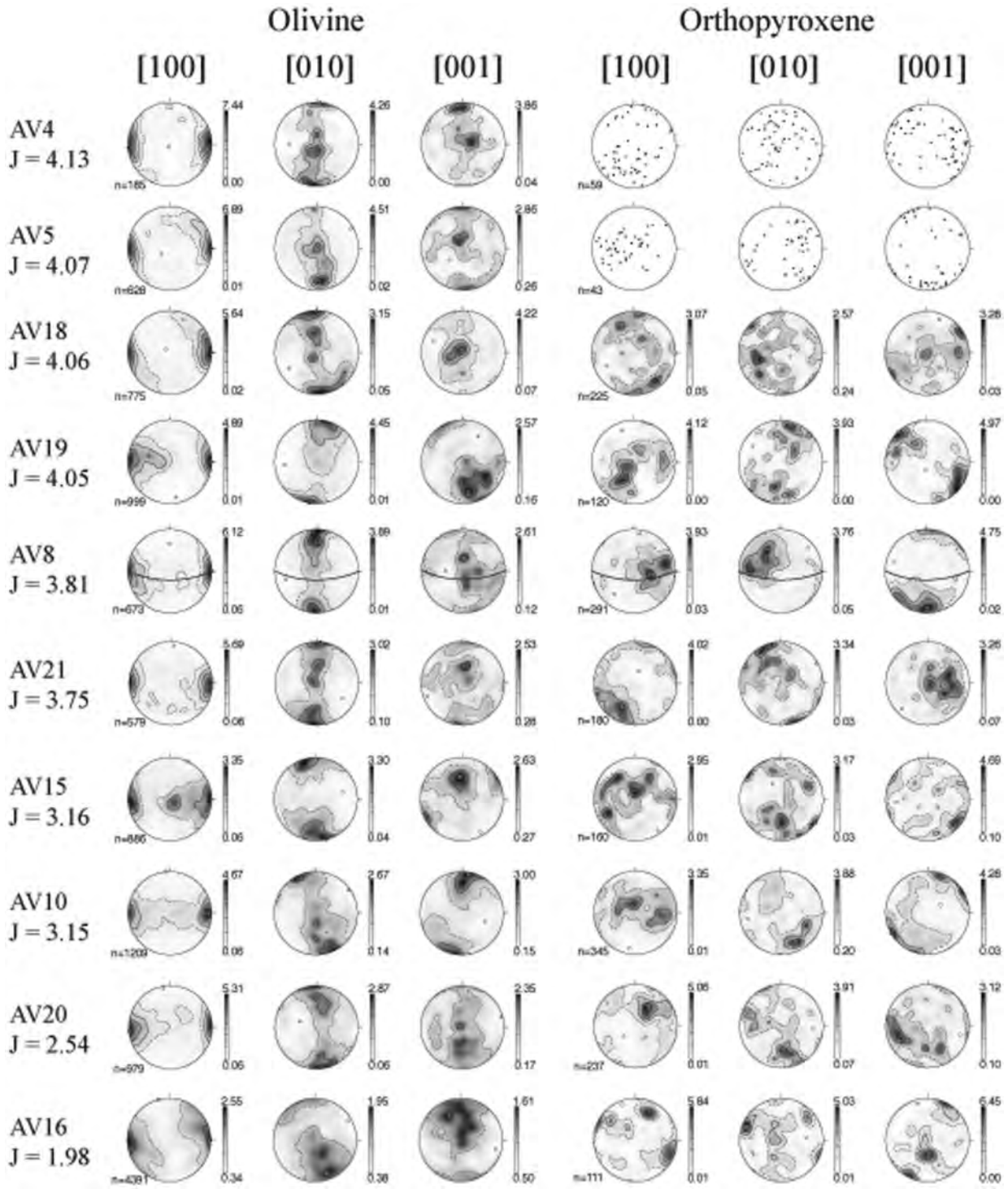

Fig. 6. Continued.

distributions symmetry with increasing proportion of fine-grained olivine crystals (Fig. 11). This evolution is correlated with a decrease in the J index. The [100] distribution evolves from point symmetry towards a weak girdle (points plot at the transition between the random and the girdle fields). The [010] distribution evolves from girdle symmetry to random. Except for AV2, which has a stronger concentration of [001] than of [010], all samples show a

higher dispersion of [001], characterized by a dominant random component. Together, these observations show that the olivine CPO evolves from a strong axial [100] pattern to a weak orthorhombic pattern with increase in the volume of fine grains.

In most studied peridotites, orthopyroxene CPO is more dispersed than the olivine CPO (Fig. 6). The multiple maxima observed in some pole figures result from the poor indexation of orthopyroxene during the automatic mapping. Because of bad polishing or reaction rims, many large orthopyroxene crystals were incompletely indexed and were recorded in the maps as multiple isolated patches with a similar orientation. This leads to an over-representation of the weight of this orientation and hence to a maximum in the pole figure when the latter is plotted as one measurement per grain. The same problem occurs with the acicular orthopyroxene aggregates, which form large areas with similar orientations that are very poorly indexed because of their fine-grained nature. The real orthopyroxene CPO patterns are thus partially obscured by these indexation problems, but the major features remain visible. The [001] distribution is usually characterized by a single or double maximum with, in some samples, a tendency to form a weak girdle normal to [100]. Ten samples have a maximum concentration of the orthopyroxene [001] axes close to the olivine [100] axes maximum (AV3, AV4, AV6, AV7, AV9, AV11, AV12, AV13, AV18, AV23), but with a systematic angular shift (<30°) (Fig. 6). Another 10 xenoliths have the orthopyroxene [001] maximum that differs by more than 45° from the olivine [100] one (AV2, AV5, AV11, AV15, AV16, AV19, AV20, AV21, AV25, AV27). A few samples (AV8, AV10, AV14) exhibit a double maxima of orthopyroxene [001] axes with one direction at 30–40° to the olivine [100] maximum and the other almost normal to it. Orthopyroxene [100] axes are usually more dispersed than [001] one and their orientation varies greatly from sample to sample. In samples AV3, AV14 and AV15 the maximum concentration of orthopyroxene [100] axes is close to the olivine [001] axes maximum, whereas in AV4, AV7, AV9, AV12, AV13, AV18, AV21 and AV23 it is close to the maximum concentration of the olivine [010] axes. Orthopyroxene [010] axes are generally more dispersed than [001] and [100], except in samples AV9 and AV14. where the orthopyroxene [010] maximum is at a low angle to the olivine [010] maximum.

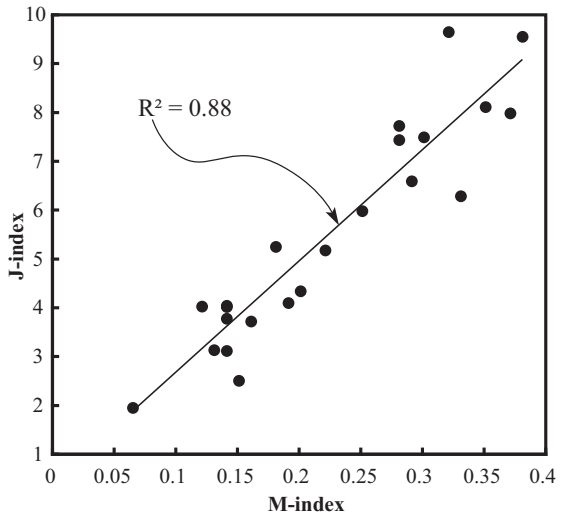

Fig. 7. Strength of olivine crystal preferred orientation in the studied samples characterized by the J and the M indices (see text for definitions). The high correlation coefficient (R^2) indicates that these two measures of the CPO strength are consistent.

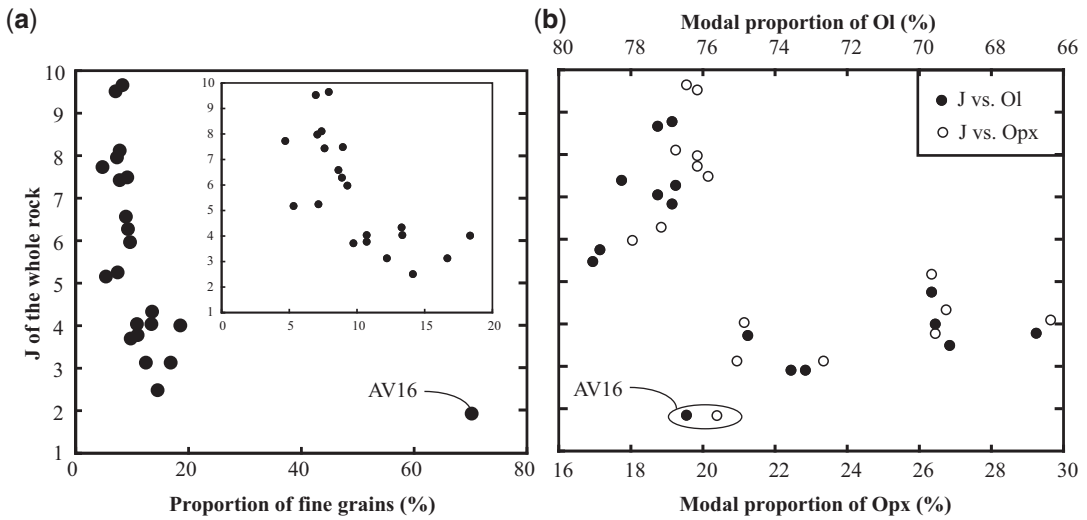

Fig. 8. J index for olivine calculated using one orientation datum per grain versus (a) the proportion (vol. %) of fine-grained olivine (ø < 0·5 mm) and (b) the modal proportion of olivine and orthopyroxene in each sample.

Deformation mechanisms and dominant slip systems in olivine and orthopyroxene

The well-developed olivine and orthopyroxene CPO imply that the coarse-grained Kamchatka peridotites deformed mainly by dislocation creep. Under pressure and temperature conditions appropriate to the upper mantle, the dominant slip system in orthopyroxene is (100)[001] (Doukhan *et al.*, 1986). Olivine deforms essentially by slip on the $\{0kl\}[100]$ and $\{hk0\}[001]$ systems; the relative strength of these systems depends on the temperature, pressure, deviatoric stress, and water fugacity conditions that prevail during deformation (Durham *et al.*, 1977; Mackwell *et al.*, 1985; Bai *et al.*, 1991; Jung & Karato, 2001*a*; Couvy *et al.*, 2004; Jung *et al.*, 2006; Raterron *et al.*, 2007).

The correlation between shape and crystal preferred orientation is a reliable tool to constrain the dominant slip systems in olivine and orthopyroxene, as these minerals display few slip systems with highly variable strengths. This results in alignment of the dominant slip direction with the shear (or maximum stretching) direction and of the normal to the slip plane with the normal to the shear plane (or foliation) in simple shear (or pure shear) deformation (Zhang & Karato, 1995; Tommasi *et al.*, 1999;

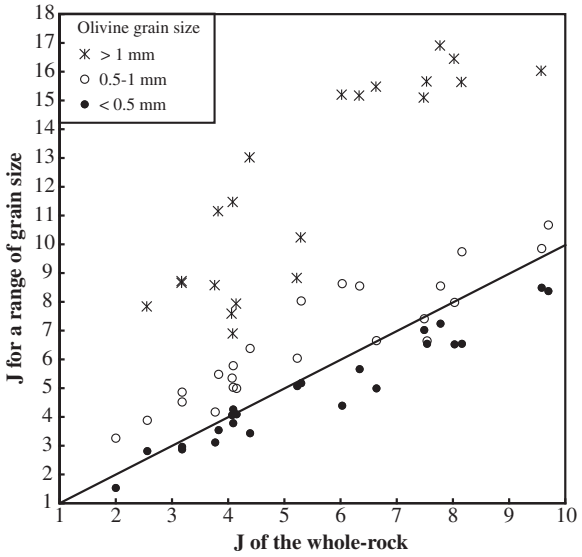

Fig. 9. J index for various olivine grain size populations vs J index of the whole-rock. Stars, coarse grains (ø > 1 mm); open circles, intermediate grains (ø between 1 and 0·5 mm); black circles, fine grains (ø < 0·5 mm).

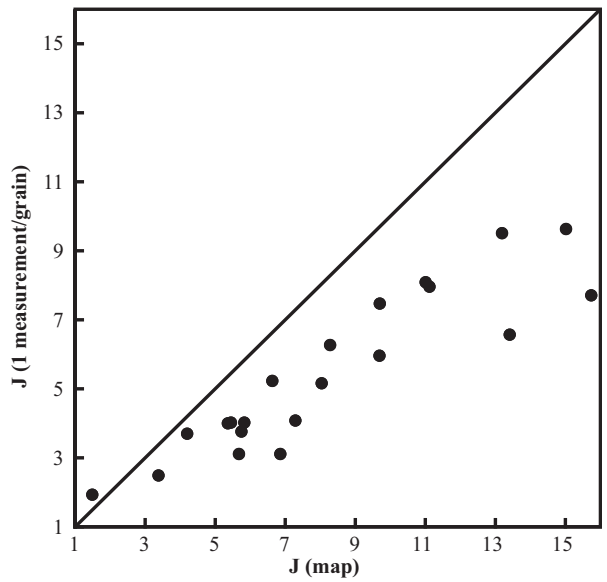

Fig. 10. Comparison of the olivine J index calculated using the raw crystallographic data from the EBSD maps with that for one orientation datum per grain.

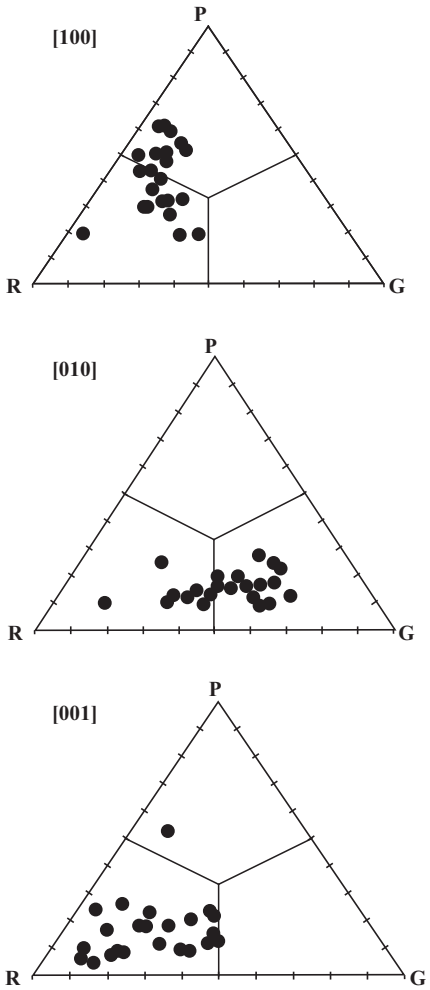

Fig. 11. Olivine CPO symmetry expressed as the proportion of point (P), girdle (G) and random (R) components calculated from the eigenvalues (λ_1, λ_2, λ_3) of the normalized orientation matrix for the three principal crystallographic axes: [100], [010] and [001]. $P = \lambda_1 - \lambda_3$, $G = 2(\lambda_2 - \lambda_3)$, $R = 3\lambda_3$.

Bystricky *et al.*, 2000). In xenoliths, however, the foliation and the lineation cannot always be easily identified and other observations are needed to constrain the dominant slip system. In this case, information on the active slip systems may be derived from the analysis of the following factors.

(1) The relative concentrations of the three main crystallographic axes in agreement with polycrystal plasticity modelling of CPO evolution that shows that the slip direction and the normal to the plane of the dominant slip system tend to orient faster than the remaining crystallographic axes (e.g. Tommasi *et al.*, 2000).
(2) The relations between the olivine and orthopyroxene CPO.
(3) The rotation axes accommodating low-angle (<15°) misorientations within a crystal, because variations in crystallographic orientation within a grain or across a low-angle grain boundary (subgrain boundary), as well as the orientation of subgrain boundaries, are directly related to the dislocations forming the boundary (Frank & Read, 1950; Amelinckx & Dekeyser, 1959). Misorientation axes data should nevertheless be used with caution, as the dislocations stacked in the subgrain boundaries may not be representative of the most mobile and, hence, most active slip systems.

In all coarse-porphyroclastic xenoliths, olivine displays a well-developed axial [100] pattern (Fig. 6) characterized by a strong point concentration of [100] axes subparallel to the lineation, when the latter can be observed, and systematically normal to the average orientation of the subgrain boundaries. This indicates that [100] is the dominant slip direction for olivine. This interpretation is corroborated by the predominance of (100) subgrain boundaries in the crystallographic orientation maps (Fig. 5).

Dominant [001] slip in orthopyroxene is in agreement with the observations that in most coarse-grained peridotites, orthopyroxene [001] axes are more concentrated than [100] or [010] and that in half of the studied xenoliths the orthopyroxene [001] maximum is at a low angle to both the lineation and the olivine [100] axes (Fig. 6). The poor orientation of orthopyroxene [100] and [010] axes hinders a clear determination of the slip plane, but there is a predominance of [010] rotation axes for low-angle misorientations (5–15°) in orthopyroxene crystals that is consistent with subgrain boundaries formed essentially by (100)[001] edge dislocations (Fig. 12).

Obliquity between the olivine and the orthopyroxene CPO is common in naturally deformed peridotites (e.g. Tommasi *et al.*, 2004, 2006; Le Roux *et al.*, 2008). It is usually interpreted as resulting from lower finite strains in stronger orthopyroxene crystals (Mackwell, 1991) at a given macroscopic strain. Many Avacha peridotites, however, display an obliquity between the olivine and orthopyroxene CPO that is too strong (>20°) to result from variations in finite strain between the two minerals. We propose that this obliquity results from late to post-kinematic crystallization of part of the orthopyroxenes. This process may also explain the higher dispersion of the orthopyroxene CPO relative to the olivine CPO.

The girdle distribution of olivine [010] and [001] axes suggests activation of multiple $\{0kl\}$ slip planes. The foliation is poorly developed in the studied peridotites. To determine the dominant slip plane, we therefore analyzed: (1) the relative concentrations of olivine [010] and [001] axes, represented by the ratio between the maximum

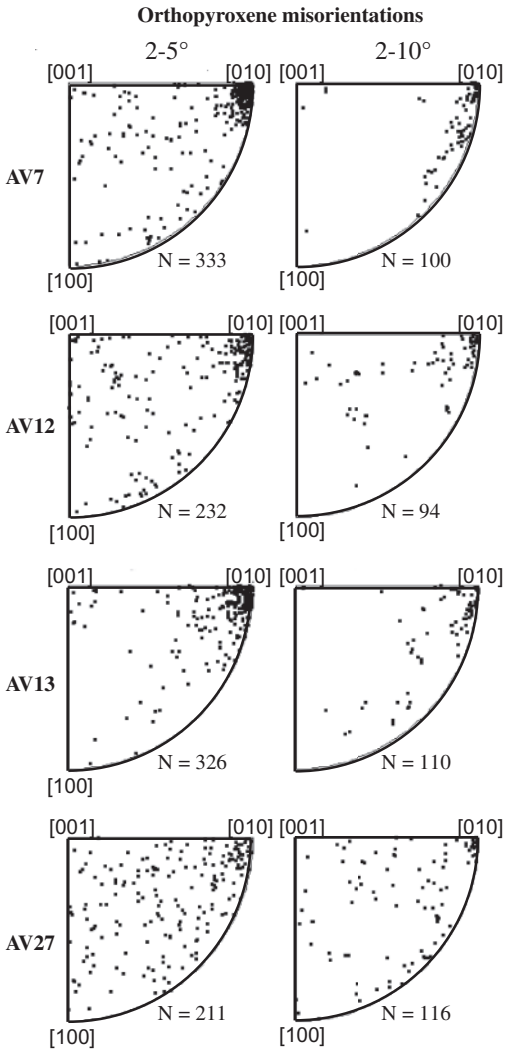

Fig. 12. Rotation axes accommodating misorientations ≤10° within orthopyroxene crystals in an EBSD map. Inverse pole figures in the crystal reference frame. N, number of measurements. Predominance of [010] rotation axes is consistent with dominant activation of the [001](100) slip system.

concentration of these two axes; (2) the rotation axes (in the crystal frame) accommodating low-angle misorientations (<10°) within olivine crystals; (3) the relative orientations of orthopyroxene [100] and olivine [010] and [001] axes for the nine samples where the slip directions of orthopyroxene and olivine were subparallel.

Analysis of Figure 13 highlights that these three independent criteria do not always provide consistent information. Most samples show a stronger concentration of [010], suggesting dominant slip on the (010) plane. However, [010] and [001] have similar concentrations in samples AV2, AV9, AV25, and AV27, suggesting equal activation of the two planes. Finally, in samples AV10, AV11, and AV18 the stronger concentration of [001] implies dominant glide on (001). On the other hand, comparison between olivine and orthopyroxene CPO highlights that sample AV18, similarly to AV7, AV12, AV13, and AV23, has the olivine [010] maximum subparallel to the orthopyroxene [100] maximum, implying dominant glide on the (010) plane. In contrast, in samples AV3, AV19, AV25, and AV27, the comparison between olivine and orthopyroxene CPO favours dominant glide on the (001) plane.

Analysis of lattice rotations across all low-angle boundaries in olivine within a map (Fig. 13) highlights that the rotation axes are mainly normal to [100], with two maxima parallel to [001] and [010]. Predominance of rotation axes close to [010] indicates a higher density of [100](001) edge dislocations in the subgrain boundaries, even in those samples where the analysis of the two other criteria clearly indicates dominant slip on [100](010).

We also compared the olivine and orthopyroxene CPO with the orientation of the opx-rich lenses when the latter were present (Fig. 5). The opx-rich lenses always contain the olivine [100] and the orthopyroxene [001] maximum concentrations. They are normal to the olivine [010] maximum concentration in sample AV7 and to the [001] maximum in AV12, suggesting dominant slip of [100] dislocations on the (010) plane in the former and on the (001) plane in the latter. However, both samples show girdle distributions of [010] and [001], suggesting that multiple $\{0kl\}$ planes were activated. In conclusion, all the observations converge towards activation of multiple [100]$\{0kl\}$ slip systems in olivine, with predominance of (010) or (001) planes depending on the sample.

DISLOCATION STRUCTURES

Sample preparation and analytical procedures

To observe the dislocation structures, sections of three coarse porphyroclastic peridotites and of the equigranular peridotite were decorated using the method described by Kohlstedt *et al.* (1976*b*). This method consists in annealing a polished sample slab for 30 min in air at 900°C (oxidizing conditions). A standard 30 μm thin section is prepared with the previously polished face in contact with the glass slide. Observations were made using both an optical microscope in natural light and a scanning electron microscope (SEM). Electron backscattered images were obtained using a FEI Quanta 200 SEM at the acceleration voltage of 15 kV and currents up to 2 μA in a low-vacuum chamber. Under these conditions, the interaction thickness is *c.* 450 nm. Slabs of the porphyroclastic peridotites were cut based on their CPO in order to have, for the majority of the crystals composing the rock, two of the main olivine crystallographic axes: [100] and [010] or [100] and [001] in the plane of the section. The orientation of the analyzed crystals was checked by EBSD.

Observations

Coarse olivine crystals in the porphyroclastic peridotites display low dislocation densities ranging from $0{\cdot}5 \times 10^{11}$ to $4 \times 10^{11}\,m^{-2}$ (Table 1). This allows easy observation of the dislocation structures both in transmitted light (Fig. 14) and by electron back-scattered imaging (Fig. 15). Some rare crystals yield much higher dislocation densities that cannot be characterized by optical observation. A large variety of dislocation structures is observed. In crystals cut parallel to (010), the most pre-eminent features are straight dislocation walls normal to [100] that crosscut the whole crystal (black arrows in Fig. 14a, b and e). They represent subgrain boundaries that are spaced at 10–55 μm. Free dislocations with lines roughly parallel to [100] branch from these (100) subgrain boundaries (Fig. 14a, b and e). These dislocations are classically interpreted as screw dislocations with a [100] Burgers vector (Nicolas & Poirier, 1976). However, some of these dislocation lines have festoon shapes (white arrow in Fig. 14b) suggesting pinning by defects while moving in the [001] direction; they might represent edge dislocations with a [001] Burgers vector. A second family of dislocation walls, which is in a plane oblique to the thin-section plane but containing [100] (i.e. parallel to a $\{0kl\}$ plane) is also locally observed (white arrows in Fig. 14a). Finally, the presence of open dislocation loops (Fig. 14b) suggests activation of cross-slip.

Olivine crystals in the fine-grained equigranular peridotite AV16 are almost devoid of dislocations (Fig. 14c). Rare dislocations are observed around inclusions. Extremely low dislocation densities also characterize small olivine crystals (<500 μm) within a 5 mm wide vein filled by the fine-grained ol–opx–oxides ± amph ± cpx ± glass matrix that crosscuts the porphyroclastic peridotite AV1 (Fig. 14d and f). In contrast, the dislocation densities and structures of coarse olivine crystals outside the vein are similar to those in other porphyroclastic peridotites (Fig. 14e). A steep transition between the two dislocation structures takes place at the vein wall. However, the dislocation

Sample	Correlation between ol & opx CPO	Relative concentration of olivine [010] & [001] axes	Rotation axes
AV1	Not enough Opx measured in thin section	1.29	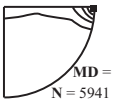
AV2	[001]opx not // [100]ol	0.99	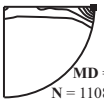
AV3	[100]ol // [001]opx [001]ol // [100]opx	1.49	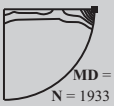
AV4	[100]ol // [001]opx [010]ol // [100]opx	1.10	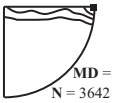
AV5	Not enough Opx measured in thin section	1.57	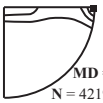
AV6	Not enough Opx measured in thin section	1.06	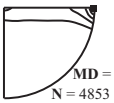
AV7	[100]ol // [001]opx [010]ol // [100]opx	1.04	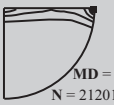
AV8	[001]opx not // [100]ol	1.50	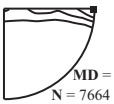
AV9	[001]opx not // [100]ol	1.01	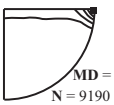
AV10	[001]opx not // [100]ol	0.89	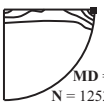
AV11	[001]opx not // [100]ol	0.86	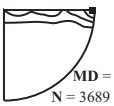
AV12	[100]ol // [001]opx [001]ol // [100]opx	1.04	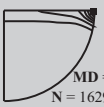
AV13	[100]ol // [001]opx [010]ol // [100]opx	1.32	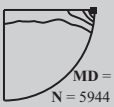

Sample	Correlation between ol & opx CPO	Relative concentration of olivine [010] & [001] axes	Rotation axes
AV14	[001]opx not // [100]ol	1.89	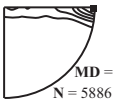
AV15	[001]opx not // [100]ol	1.25	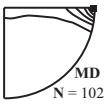
AV16	[001]opx not // [100]ol	1.21	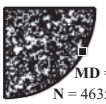
AV18	[100]ol // [001]opx [010]ol // [100]opx	0.74	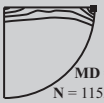
AV19	[001]opx not // [100]ol	1.73	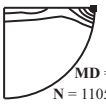
AV20	[001]opx not // [100]ol	1.22	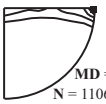
AV21	[001]opx not // [100]ol	1.19	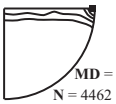
AV23	[100]ol // [001]opx [010]ol // [100]opx	0.83	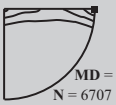
AV25	[001]opx not // [100]ol	1.09	
AV27	[100]ol // [001]opx [001]ol // [100]opx	1.02	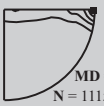

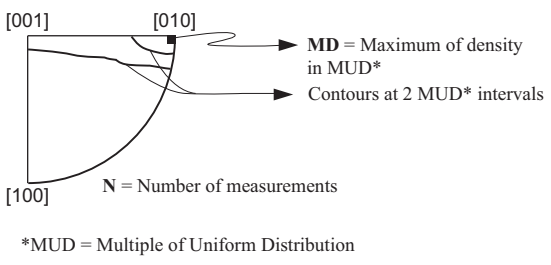

Fig. 13. Comparison of various parameters used for identifying the dominant slip plane in olivine: (1) correlation between olivine and orthopyroxene CPO, (2) relative concentrations of olivine [010] and [001] axes, and (3) rotation axes accommodating misorientations ≤10° within olivine crystals. Samples highlighted in grey have correlated olivine and orthopyroxene CPO; that is, the angle between the maximum concentration of [100] olivine axes and [001] orthopyroxene is <20°. For these samples, the comparison between orthopyroxene and olivine CPO may be used to identify the dominant slip plane in olivine. Relative concentrations of olivine [010] and [001] axes are quantified by the ratio of the density maxima of the [010] and [001] axes. Rotation axes are represented as inverse pole figures in the crystal reference frame; for sample AV16 they are represented as points instead of as density contours at two multiples of a uniform distribution because they are almost random.

Table 1: Deviatoric stresses estimated from free dislocation density

Sample	Number of analyzed grains	Dislocation density ($\times 10^{11}$ m^{-2})	Standard deviation ($\times 10^{11}$ m^{-2})	Average stress (MPa)	Minimum stress (MPa)	Maximum stress (MPa)
AV1	4	3·37	0·45	58·05	54·04	61·81
AV3	4	1·67	0·91	40·87	27·57	50·79
AV23	3	2·06	0·99	45·39	32·71	55·23

density in the coarse olivine crystals in contact with the vein tends to be lower than that in grains several millimeters away from it (Fig. 14g). The observed decrease in the dislocation density suggests that diffusional processes were enhanced within and around these veins.

FTIR ANALYSES OF WATER CONTENTS IN OLIVINES AND ORTHOPYROXENES

Analytical procedure

Unpolarized Fourier Transform infra-red (FTIR) spectroscopy measurements were performed using a Bruker Vertex70 spectrometer coupled with a Bruker Hyperion microscope at the Laboratoire Magmas et Volcans (LMV) in Clermont-Ferrand (France) and using a Bruker IFS66v coupled with a Bruker IR microscope at the Laboratoire des Colloïdes, Verres et Nanomateriaux (LCVN) in Montpellier (France). Both microscopes were equipped with all-reflecting Cassegranian optics, a condenser, and a 15×objective. Analyses were made at room pressure and temperature. Mid-IR measurements were performed using a Globar light source, a KBr beam splitter, a high-sensitivity DTGS (deuterated triglycine sulfate) at the LMV and a high-sensitivity MCT (DTGS) at the LCVN, both cooled by liquid nitrogen. Spectra were acquired with a resolution of 4 cm^{-1} and at least 100 scans were accumulated for each spectrum (Table 2). As these were open-air analyses, a background correction had to be performed on each measurement to remove the contribution of the vapour phase. This was done by always performing two analyses, one without and another with the sample; the difference between the two yields the spectrum used for the determination of the water contents in the minerals. This background correction and the baseline correction were carried out using the OPUS software.

Unpolarized FTIR absorption spectra of olivines and orthopyroxenes were obtained on doubly polished sections with a thickness of ~500 μm. Thinner sections, 250–150 μm thick, were used for measuring water contents in fine-grained olivines in the equigranular peridotite AV16 and in the coarse porphyroclastic samples AV10 and AV15 (Table 2). The detection limit at the lowest sample thickness is 1 ppm. The sections were left in an acetone bath for at least 12 h to remove any residual glue. Measurements were performed in selected crack- and inclusion-free grains (optical observation) using a square or circular aperture at LMV and LCVN, respectively, with a diameter between 90 and 105 μm as a function of the analyzed grain size (Table 2). Measurements in orthopyroxenes were hindered by the large amount of inclusions in the coarse crystals and by the fine-grained texture of the acicular aggregates. Most measurements were performed at the grains' core, which should be least affected by late, extraction-related water loss (Demouchy *et al.*, 2006).

The water concentration in the analyzed minerals was calculated by integrating the absorption bands according to the calibration of Paterson (1982):

$$C_{\mathrm{OH}} = \frac{X_i}{150\zeta}\int \frac{K(\bar{\nu})}{(3780-\bar{\nu})}\,\mathrm{d}\bar{\nu} \qquad (1)$$

where C_{OH} is the hydroxyl concentration (in H/10^6 Si or ppm wt H_2O), ζ is an orientation factor (1/3 for unpolarized measurements), and $K(\bar{\nu})$ is the absorption coefficient in cm^{-1} for a given wavenumber $\bar{\nu}$. X_i is a density factor; its value for olivine and orthopyroxene is 2695 and 2769 wt ppm H_2O, respectively [see Bolfan-Casanova *et al.* (2000) for calculation method]. The calibration of Paterson (1982) underestimates the water concentration in olivine compared with the calibration proposed by Bell *et al.* (2003). However, the Bell *et al.* (2003) calibration may be applied only to olivine spectra dominated by high wavenumber (3650–3450 cm^{-1}) OH absorption bands. This is not the case for olivine in the studied Avacha peridotites, whose spectra are dominated by low wavenumber absorption bands (Fig. 16). Moreover, the calibration of Paterson (1982) has the advantage of allowing direct comparison of water contents in olivine and pyroxenes (Bolfan-Casanova *et al.*, 2000). Errors on the absolute water contents are, however, of±30% (Kohlstedt *et al.*, 1996).

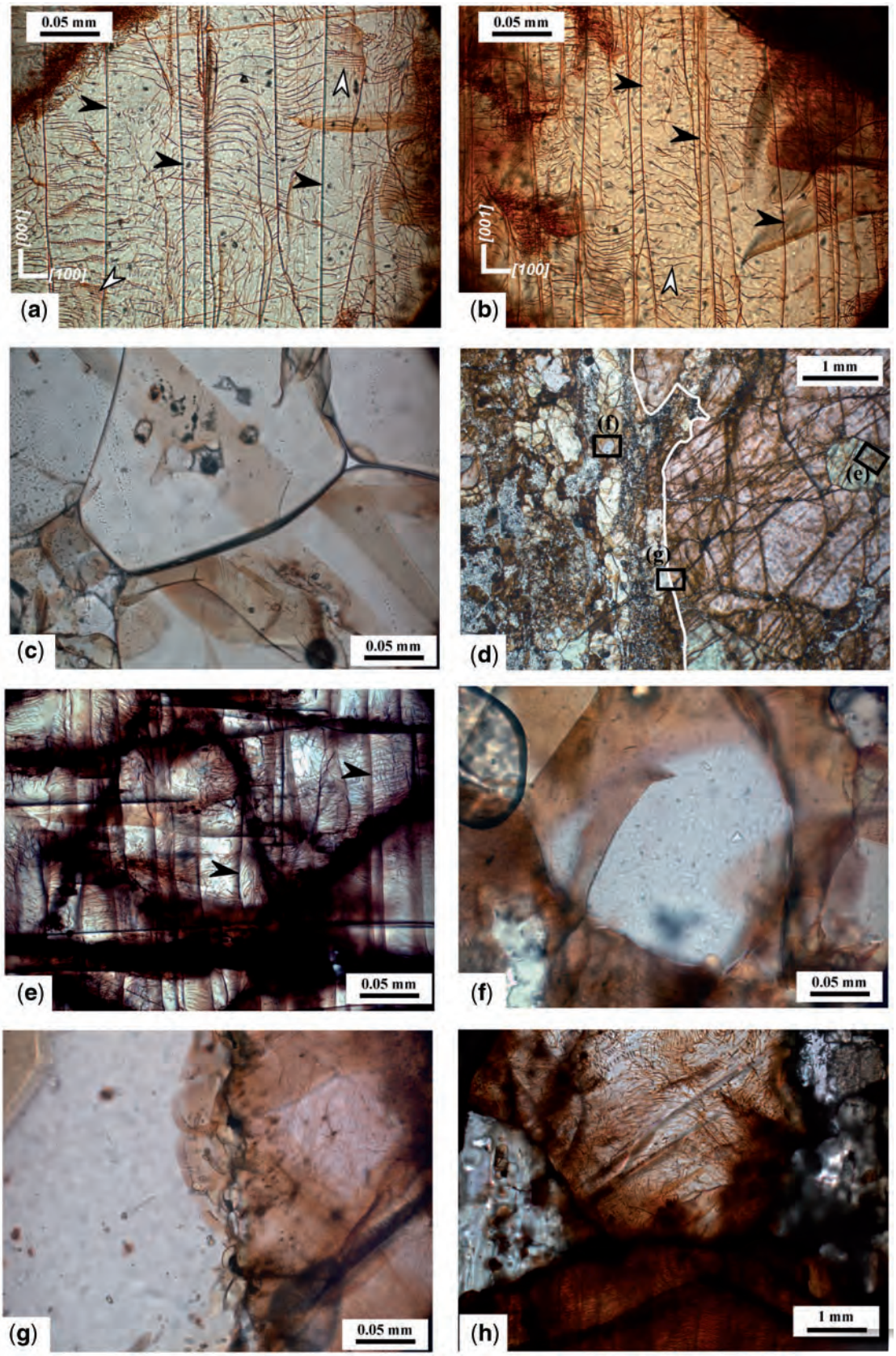

Fig. 14. Photomicrographs (plane-polarized light) of decorated dislocations in olivine. (a, b) Dislocation structures seen on two olivine crystal cut on planes close to (010); black arrows indicate the dominant (100) subgrain boundaries. In (a) the white arrow marks a subgrain boundary oblique to the section plane, which is formed by dislocations of two slip systems with perpendicular Burgers vectors, probably [100] and [001]. In (b) the white arrow shows festoon-like dislocation lines that may represent pinned edge dislocations with [001] Burgers vectors. (c) Small olivine crystals totally free of dislocations and displaying an open triple junction in fine-grained peridotite AV16. (d) Lower enhancement image of sample AV1 showing the change in dislocation structure and density between olivine crystals that form a coarse porphyroclastic microstructure and small polygonal olivine crystals in a vein filled by the fine-grained matrix; the white line marks the edge of the vein. Black rectangles show the location of photomicrographs (e–g). (h) Variations in dislocation densities between neighbouring olivine crystals with different orientations in coarse porphyroclastic peridotite AV20.

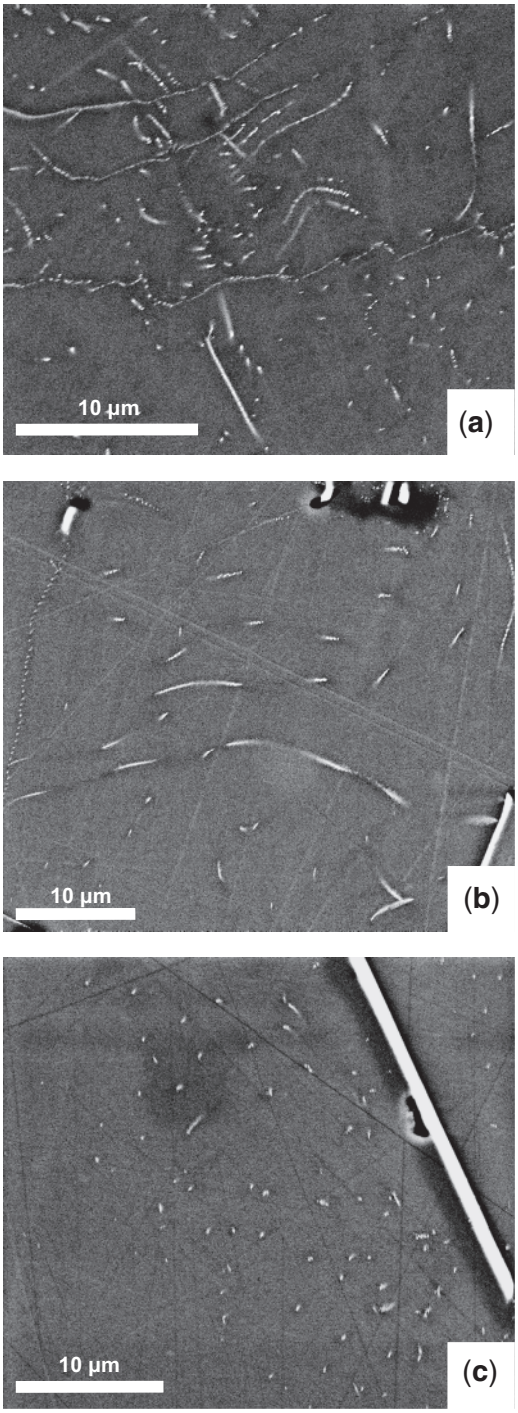

Fig. 15. Backscattered electron (BSE) image of dislocations (white lines or points as a function of the angle between the dislocation line and the observation surface) in olivine crystals from coarse porphyroclastic peridotites AV1 (a), AV23 (b), and AV3 (c). Densities estimated using the intercept length method are $3{\cdot}86 \times 10^{11}$, $1{\cdot}92 \times 10^{11}$, and $0{\cdot}55 \times 10^{11}\,m^{-2}$, respectively.

Results: IR spectra and water solubility

Figure 16 shows typical unpolarized FTIR spectra for olivines and orthopyroxenes in xenoliths AV1, AV3, AV10, AV15, AV16 and AV23. The olivine spectra are rather homogeneous. The major O–H absorption bands are at 3354 and 3328 cm^{-1}. In contrast, the band at 3574 cm^{-1}, where the maximum O–H absorbance is often observed in natural peridotites (Miller *et al.*, 1987; Bell *et al.*, 2004; Demouchy, 2004; Demouchy *et al.*, 2006; Peslier & Luhr, 2006; Grant *et al.*, 2007), displays only a minor peak. The observed spectra are nevertheless similar to those of olivines in peridotite xenoliths from Mexico, Kenya, and the Carpathians (Miller *et al.*, 1987; Falus *et al.*, 2008) and of olivine ($Mg_{1{\cdot}8}Fe_{0{\cdot}2}SiO_4$) in equilibrium with orthopyroxene in the experimental sample of Berry *et al.* (2005). Water contents in the studied samples range from 1 to 8·3 ppm H_2O by weight (Table 2). The water content varies as a function of the grain size: coarse (>1 mm), intermediate (0·5–1 mm) and fine (<0·5 mm) olivine crystals show on average 6·1, 3·4 and 2·4 ppm H_2O, respectively (Table 2). These values are in the same range as the water contents in olivine from spinel-peridotite xenoliths sampling the continental lithosphere above the western North America, Patagonia and Carpathian subduction zones (Demouchy, 2004; Peslier & Luhr, 2006; Falus *et al.*, 2008).

Orthopyroxene spectra are characterized by major O–H absorption bands at 3596, 3543, and 3520 cm^{-1} and by broader minor peaks around 3420, 3317 and 3070 cm^{-1} (Fig. 16b). This pattern is typical for orthopyroxene from mantle xenoliths (Peslier *et al.*, 2002; Grant *et al.*, 2007). Water contents are however very heterogeneous, varying from 25 to 506 ppm (Table 2). Although there is a clear variation in water contents from sample to sample, strong heterogeneity is also observed within samples (Table 2). Orthopyroxenes in coarse-grained porphyroclastic peridotite AV15 and in equigranular peridotite AV16 have abnormally low water contents (25–128 ppm) for subduction zone xenoliths (Peslier & Luhr, 2006; Falus *et al.*, 2008). AV10 has the most water-rich orthopyroxenes (218–506 ppm). The latter value (>500 ppm H_2O) represents an abnormally high water content for spinel peridotites; however, the spectra of the two orthopyroxenes are consistent and do not show evidence for contamination of the measurements by water-rich inclusions or amphibole lamellae (typical peak at 3900 cm^{-1}).

There is a weak positive correlation between the average water contents in olivine and orthopyroxene in each sample. Concentration ratios (R_c) calculated using the mean water contents in olivine and orthopyroxene in each sample are 18·6 in AV15, 20·9 in AV16, 39·5 in AV3, and 76 (Table 2) in AV10. These concentration ratios, although extremely variable, are within the range of published values of water partitioning coefficients between olivine

Table 2: Water contents in olivines and orthopyroxenes

Sample	Mineral	Laboratory	Number of accumulated scans	Aperture size (mm)	Section thickness (cm)	Water content* (wt ppm H_2O)	Water content* ($H/10^6$ Si)	Grain size (mm)	Peridotite type
AV1	ol-1	LMV	300	0·1	0·0552	5·1	78·438	>1	CG
AV1	ol-2	LMV	300	0·1	0·0552	8	123·04	>1	CG
AV3	ol-1	LMV	300	0·1	0·0580	2·3	35·374	0·5–1	CG
AV3	ol-2	LMV	300	0·1	0·0580	7·2	110·736	>1	CG
AV3	opx-1	LMV	300	0·1	0·0580	188	2891·44	—	CG
AV10	ol-1	LCVN	300	0·09	0·0252	7	107·66	>1	CG
AV10	ol-2	LCVN	300	0·09	0·0252	4	61·52	0·5–1	CG
AV10	ol-3	LCVN	300	0·09	0·0252	4	61·52	0·5–1	CG
AV10	ol-4	LCVN	300	0·09	0·0264	4	61·52	<0·5	CG
AV10	opx-1	LCVN	300	0·075	0·0252	218	3352·84	—	CG
AV10	opx-2	LCVN	300	0·09	0·0300	506	7782·28	—	CG
AV15	ol-1	LCVN	300	0·09	0·0184	4	61·52	>1	CG
AV15	ol-2	LCVN	300	0·09	0·0184	3	46·14	<0·5	CG
AV15	ol-3	LCVN	300	0·09	0·0184	3	46·14	<0·5	CG
AV15	ol-4	LCVN	300	0·09	0·0184	2	30·76	<0·5	CG
AV15	ol-5	LCVN	300	0·09	0·0184	2	30·76	<0·5	CG
AV15	ol-6	LCVN	300	0·09	0·0184	2	30·76	<0·5	CG
AV15	ol-7	LCVN	300	0·09	0·0184	4	61·52	>1	CG
AV15	ol-8	LCVN	300	0·09	0·0184	3	46·14	<0·5	CG
AV15	ol-9	LCVN	300	0·09	0·0184	3	46·14	<0·5	CG
AV15	ol-10	LCVN	300	0·09	0·0184	5	76·9	>1	CG
AV15	ol-11	LCVN	300	0·09	0·0184	5	76·9	>1	CG
AV15	opx-1	LCVN	300	0·09	0·0184	55	845·9	—	CG
AV15	opx-2	LCVN	300	0·09	0·0184	128	1968·64	—	CG
AV15	opx-3	LCVN	300	0·09	0·0184	35	538·3	—	CG
AV15	opx-4	LCVN	300	0·09	0·0184	25	384·5	—	CG
AV16	ol-1	LCVN	100	0·09	0·0163	3	46·14	<0·5	FG
AV16	ol-2	LCVN	100	0·09	0·0163	2	30·76	<0·5	FG
AV16	ol-3	LCVN	100	0·09	0·0163	3	46·14	<0·5	FG
AV16	ol-4	LCVN	200	0·105	0·0163	1	15·38	<0·5	FG
AV16	opx-1	LCVN	200	0·105	0·0163	47	722·86	—	FG
AV23	ol-1	LMV	300	0·1	0·0552	6·6	101·508	>1	CG
AV23	ol-2	LMV	300	0·1	0·0552	7·3	112·274	>1	CG
AV23	ol-3	LMV	300	0·1	0·0552	8·3	127·654	>1	CG

CG, coarse-grained peridotite; FG, fine-grained peridotite. LMV, Laboratoire Magmas et Volcans, Université Clermont-Ferrand. France. LCVN, Laboratoire des Colloïdes, Verres et Nanomatériaux, Université Montpellier 2, France. *Calibration of Paterson (1982). Water contents have±30% error.

and orthopyroxene ($D^{opx/ol}_{water}$) in spinel-lherzolites: 40·7 ± 19·8 (Grant *et al.*, 2007). Because the water contents in olivine vary as a function of grain size and because water contents in the orthopyroxenes are extremely heterogeneous, the R_c values calculated using single olivine–orthopyroxene pairs show an even greater dispersion, varying from five in AV15 (ol10–opx4) to 126·5 in AV10 (ol2–opx2). These extreme concentration ratios are not pertinent to equilibrium water partitioning between mantle minerals, but rather reflect the heterogeneity of water distribution in orthopyroxene and compositional disequilibrium in the studied samples.

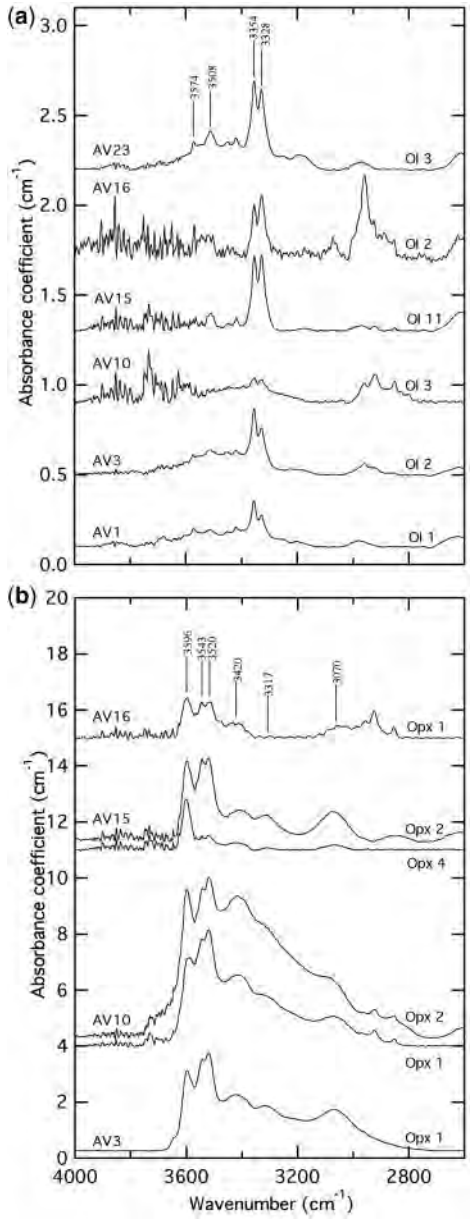

Fig. 16. Unpolarized IR spectra for the most representative olivine (a) and orthopyroxene (b) of each sample. As the water content in orthopyroxenes is highly heterogeneous, even within a single sample, we plotted the two spectra corresponding to the two extreme values measured for each sample (Table 3). Spectra are normalized to 1 cm^{-1}.

DEVIATORIC STRESS ESTIMATES

In deformation by dislocation creep, the density of dislocations (ρ) in a crystal depends on the applied stress (Poirier, 1985):

$$\rho = \alpha b^{-2}(\sigma/\mu)^2 \qquad (2)$$

where α is a non-dimensional constant of order unity, b is the Burgers vector, σ is the stress and μ the shear modulus.

Analysis of the microstructure of experimentally deformed olivine-rich rocks highlights that the applied differential stress is proportional to the free dislocations density (e.g. Kohlstedt & Goetze, 1974), to the average subgrain size (e.g. Raleigh & Kirby, 1970; Karato *et al.*, 1980), or to the average recrystallized grain size (e.g. Mercier *et al.*, 1977; Karato *et al.*, 1980; Van der Wal *et al.*, 1993). However, these microstructural parameters have different stabilities relatively to annealing or changes in stress. Free dislocation densities are easily reduced by post-kinematic annealing. They also readily re-equilibrate in response to changes in the stress field, in particular to a stress increase, even if the associated strain is very small. Subgrain and recrystallized grain sizes are more stable features that need long annealing times (or high temperatures) or significant finite strains to be modified. In the following discussion, we compare the stresses estimated using these three paleopiezometers for the Avacha peridotites.

Free dislocations density

To estimate the free dislocations density we used the method described by Hirsch *et al.* (1965), which consists of measuring the total dislocation lines length in a unit volume of the crystal. The total dislocation lines length in a crystal was estimated by the intersection analysis method (Ham, 1961) applied to the BSE images (Fig. 15). The density of dislocations Λ is defined as

$$\wedge = 2N/Lt \qquad (3)$$

where N is the number of intersections, L is the total length of lines composing the random network, and t is the thickness of the observation zone ($\approx$450 nm, which is the BSE interaction depth in the present case).

During plastic deformation, crystals are submitted to variable stresses according to their orientation and to heterogeneity in the deformation between neighbouring grains. These stress gradients may be high for low-symmetry minerals such as olivine that show a high plastic anisotropy (Bai *et al.*, 1991), leading to highly variable dislocation densities within a rock sample. Such variable dislocation densities are observed in the decorated sections of the coarse-grained Kamchatka peridotites (Fig. 14h). In the present study, we selected optically three or four representative olivine crystals (i.e. displaying an 'average' dislocation density) in coarse-grained porphyroclastic peridotites AV1, AV3 and AV23. Dislocation densities estimated using both optical and SEM observations in these crystals range from $0{\cdot}5 \times 10^{11}$ to 4×10^{11} m^{-2} (Table 1). Based on the stress vs dislocation density relation given by Kohlstedt *et al.* (1976*a*), these observed dislocation densities record deviatoric stresses ranging from 28 to 62 MPa.

As discussed above, a major inconvenience of this paleopiezometer is that the free dislocations density is not

stable against variations in stress or annealing (Poirier, 1985). The preservation of highly variable dislocation densities within a sample suggests limited annealing. One cannot exclude, however, an effect of a weak, low-temperature, high-stress deformation in the lithosphere or during extraction on the observed free dislocation density.

Subgrain size

Karato *et al.* (1980) obtained the following relationship between stress and the subgrain boundary spacing in olivine single crystals deformed under high-temperature conditions:

$$d_s = 280\sigma^{-0.67} \quad (4)$$

where d_s is the subgrain boundary spacing in μm and σ is the stress in MPa. The spacing between adjacent (100) subgrain boundaries measured in 25 olivines from four decorated coarse porphyroclastic peridotites varies between 10 and 150 μm (Fig. 14a and b), with an average at 32·5 μm (the median is at 30 μm). The mean values correspond to paleo-stresses of 43·5 MPa, and extreme values range from 130 to 2·5 MPa, respectively.

The average subgrain size should vary rapidly with increasing stress, but remain stable under decreasing stress conditions. This paleopiezometer should therefore be representative of the maximum stress experienced by a crystal (Poirier, 1985). As discussed above, during deformation, crystals are submitted to variable stresses according to their orientation and to the heterogeneity of deformation between neighbouring grains. This may partially explain the high variability in subgrain boundary spacing recorded in our samples. However, 50% of the measured subgrains are spaced by 20 to 40 μm. This implies that the mean value of the stress (43·5 MPa) obtained by this method could be representative of the maximum stress to which the studied samples were exposed.

Recrystallized grain size

All empirical relations between recrystallized grain sizes and deviatoric stresses follow a power law:

$$D_g = A\sigma^{-n} \quad (5)$$

where D_g is the recrystallized grain size, σ is the differential stress, and A and n are empirical constants obtained by fitting experimental data. In this study, we used (1) the calibration of Karato *et al.* (1980), which is based on single crystal deformation experiments, (2) the calibrations of Van der Wal *et al.* (1993), and (3) those of Zhang *et al.* (2000), which are derived from deformation experiments on olivine-rich polycrystals, and the calibration of Jung & Karato (2001*b*) derived from deformation experiments on hydrated olivine (Table 3).

Table 3: Parameters for equation (5)

Paleopiezometer	A	n
Karato *et al.* (1980)	8300	1·18
Van der Wal *et al.* (1993)	15000	1·33
Zhang *et al.* (2000)*	3544	1·23
Jung & Karato (2001b)*	67103	1·45

*Calculated by regression through their data.

Grain sizes in the coarse-grained porphyroclastic peridotites were estimated from the EBSD maps. Measured mean intercept lengths were multiplied by a geometric factor of 1·2 to convert the grain size in thin section to a three-dimensional grain diameter (Van der Wal *et al.*, 1993). An inconvenient aspect of this technique is that the minimum observed grain size is limited by the EBSD measurement step size. This leads to some bias in the estimation of the smaller grain sizes, even if all maps were obtained with measurement steps at least four times smaller than the initial (optical) estimation of the average grain size.

In coarse-grained porphyroclastic peridotites, such as the studied Kamchatka xenoliths, that show a continuous grain size distribution (Fig. 17), the main difficulty, however, is to discriminate between porphyroclasts and recrystallized grains. For all coarse-grained porphyroclastic xenoliths, more than 75% of the measured olivine grains are smaller than 750 μm, whereas 75% of the thin-section area is occupied by grains larger than 750 μm. We cannot discriminate the porphyroclasts from the recrystallized grains, but we assume that the majority of the latter have a grain size lower than 750 μm and choose to use the mean grain size in a sample as the recrystallized grain size. Average grain sizes range from 300 to 800 μm (Table 4). In this grain size range, the Van der Wal *et al.* (1993) and Zhang *et al.* (2000) calibrations give the maximum and minimum stress estimates for dry conditions, respectively (Table 4, Fig. 18). Recrystallized grain sizes of 307–797 μm correspond to stresses of 9–18 MPa or 3–11 MPa. Higher stresses (21–41 MPa) are estimated for deformation under hydrated conditions, consistent with data suggesting faster grain growth under hydrated conditions. However, this latter estimation should be used with caution, because water contents in the Kamchatka olivines (Table 2) are much lower than those in the Jung & Karato (2001*b*) samples (50 wt ppm or 800 H/10^6 Si).

The recrystallized grain size is the most stable paleopiezometer and could reflect the last high-temperature deformation episode. However, uncertainty in the determination of the equilibrium recrystallized grains size hinders its use. Moreover, in the studied Kamchatka xenoliths,

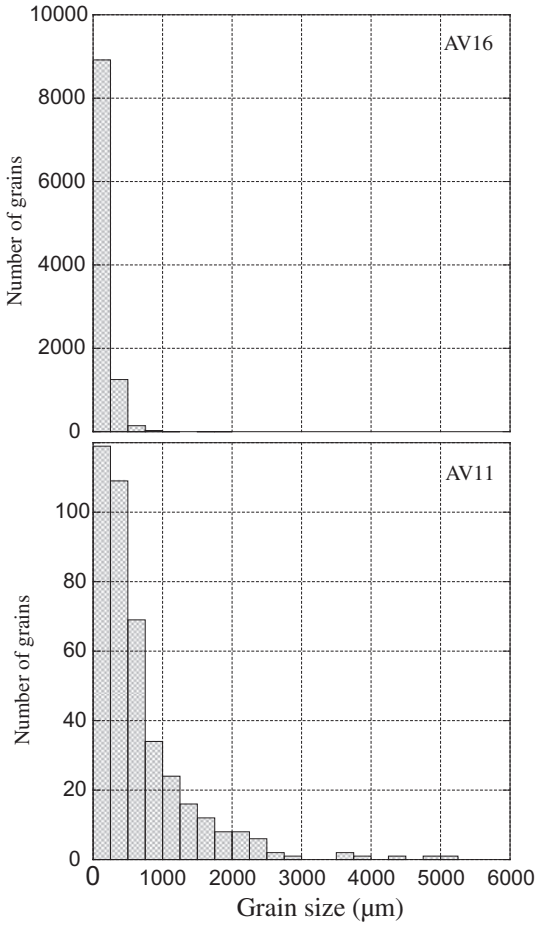

Fig. 17. Olivine grain size histograms for samples AV16 and AV11.

olivine grain sizes were also modified by reaction with percolating fluids that led to crystallization of orthopyroxene at the expense of olivine (Figs 3 and 4a) and, in the opx-rich bands, olivine grain growth may have been limited by interstitial orthopyroxene. Grain sizes in these bands are thus probably minimum values, leading to overestimation of stresses in the opx-rich samples.

DISCUSSION

Thermo-mechanical history of the Avacha spinel-harzburgites

Peridotite xenoliths from the Avacha volcano are highly refractory spinel harzburgites. Primary cpx is absent, and secondary cpx (≤3 vol. %) occurs only as interstitial crystals in the fine-grained matrix (Ionov, 2010). Modal and whole-rock chemical compositions suggest therefore that these xenoliths are the residues of high-degree (30–40%) partial melting at shallow depths (<1 to 2 GPa, Ionov, 2009). On the other hand, widespread unmixing and core–rim compositional gradients in coarse orthopyroxene crystals record slow cooling to temperatures <900°C (Ionov, 2010), indicating that these peridotites were part of the lithospheric mantle at the time of their extraction by the host andesitic magmas. The analysis of microstructures and crystal preferred orientations in the xenoliths implies that they underwent a complex history involving deformation and fluid and/or melt percolation at variable temperature conditions. Unravelling the chronology of the thermal, chemical and deformation events recorded by these peridotites is essential to determine if these events are related to the subduction process.

Except for one sample, the Avacha xenoliths exhibit coarse-grained porphyroclastic microstructures characterized by a lineation marked by coarse elongated olivine crystals with sinuous grain boundaries, widely spaced subgrain boundaries, low free dislocation densities, and well-developed olivine CPO. These microstructures are characteristic of deformation by dislocation creep under high-temperature, low deviatoric stress conditions, where dislocation glide is assisted by diffusional processes, such as climb and grain boundary migration. These deformation conditions are consistent with the measured olivine CPO that implies dominant activation of the high temperature, low-pressure $\{0kl\}[100]$ slip systems with dominant activation of the (010) and (001) planes. The activation of multiple $\{0kl\}$ slip planes may have been favoured by decreasing temperature conditions (Durham *et al.*, 1977) or by deformation under moderately hydrous conditions (Mackwell *et al.*, 1985; Katayama *et al.*, 2004). Hydrous conditions also enhance diffusion rates, lowering the viscosity of mantle rocks (Blacic, 1972; Mei & Kohlstedt, 2000*a*) and favouring recrystallization and grain growth (Karato, 1989; Jung & Karato, 2001*b*) and, hence, development of coarse-grained, well-recovered microstructures, like those observed in the studied xenoliths, at lower temperatures. Taken together, the microstructural observations and the CPO suggest that the major deformation episode recorded by these xenoliths took place under low-stress conditions like those that probably prevail in the asthenosphere or at the base of the lithosphere. Later deformation under higher stress, lower temperature conditions is consistent with the higher deviatoric stresses (28–62 MPa) estimated from dislocation densities. A cooling history is also consistent with the brittle character (veins) of the late fluid transport structures (Fig. 4e and f) in the Kamchatka xenoliths.

Comparison of the paleo-stresses estimated from free dislocation densities and recrystallized grain sizes with rheological profiles (Fig. 19) calculated using a geothermal gradient for a mature volcanic arc, such as Kamchatka, and empirical flow laws for dry and wet dunite (Chopra & Paterson, 1981, 1984) allow discussion of the rheological behaviour and strain rates and location in the supra-subduction mantle. For a regional surface heat flow

Table 4: Deviatoric stresses estimated from recrystallized grain sizes

Sample	Recrystallized grain size (μm)	Corrected (3D) recrystallized grain size (μm)	Stress (MPa)			
			Karato *et al.* (1980)	Van der Wal *et al.* (1993)	Zhang *et al.* (2000)	Jung & Karato (2001)
AV1	476·0	571·2	9·7	11·7	4·4	26·9
AV2	362·0	434·4	12·2	14·3	5·5	32·5
AV3	583·6	700·3	8·1	10·0	3·7	23·4
AV4	512·0	614·4	9·1	11·0	4·2	25·6
AV5	307·8	369·3	14·0	16·2	6·3	36·4
AV6	632·1	758·6	7·6	9·4	3·5	22·1
AV7	501·2	601·4	9·2	11·2	4·2	26·0
AV8	424·9	509·9	10·6	12·7	4·9	29·1
AV9	462·3	554·8	9·9	11·9	4·5	27·5
AV10	352·3	422·7	12·5	14·6	5·7	33·2
AV11	664·8	797·8	7·3	9·1	3·4	21·4
AV12	500·7	600·8	9·3	11·2	4·2	26·0
AV13	558·4	670·0	8·4	10·4	3·9	24·1
AV14	412·6	495·1	10·9	13·0	5·0	29·7
AV15	395·8	474·9	11·3	13·4	5·1	30·6
AV16	157·5	189·0	24·7	26·8	10·9	57·8
AV18	443·5	532·2	10·3	12·3	4·7	28·3
AV19	255·9	307·1	16·3	18·6	7·3	41·4
AV20	349·4	419·3	12·6	14·7	5·7	33·4
AV21	482·6	579·1	9·5	11·6	4·4	26·7
AV23	617·1	740·5	7·8	9·6	3·6	22·5
AV25	348·0	417·6	12·6	14·8	5·7	33·4
AV27	409·1	491·0	11·0	13·1	5·0	29·9

of 88 mW/m^2 (Currie & Hyndman, 2006), the base of the lithosphere, which we assume to be defined by the 1200°C isotherm, is located at *c.* 70 km. Furthermore, temperatures of 900°C, which correspond to the maximum estimates from two-pyroxene thermometry, are reached at *c.* 45 km depth.

For strain rates of 10^{-14} s^{-1} (10^{-15} s^{-1}) and a dry peridotite flow law, stresses equivalent to those estimated from the free dislocation density and recrystallized grain size are obtained for depth of 47–42 km (38–43 km) and 50–64 km (45–58 km), respectively. The last stages of deformation, which control in particular the free dislocation density, may thus have occurred in the upper part of the lithospheric mantle, from where the xenoliths were extracted. However, the recrystallized grain sizes record instead a deformation in the lower lithosphere, below 45–50 km. However, the reaction forming orthopyroxene at the expense of olivine may have modified the olivine

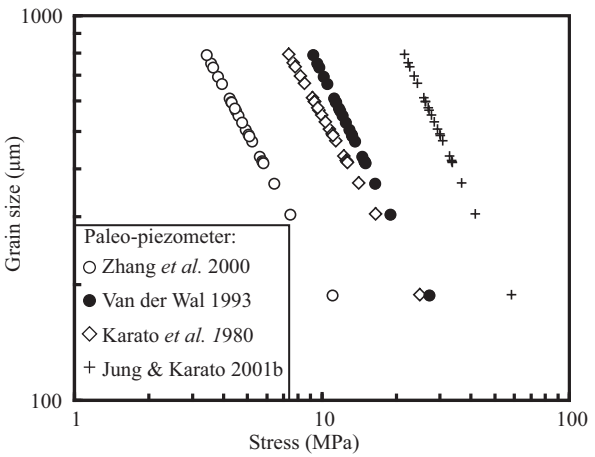

Fig. 18. Deviatoric stresses estimated using different paleopiezometers vs average olivine recrystallized grain size for all studied samples.

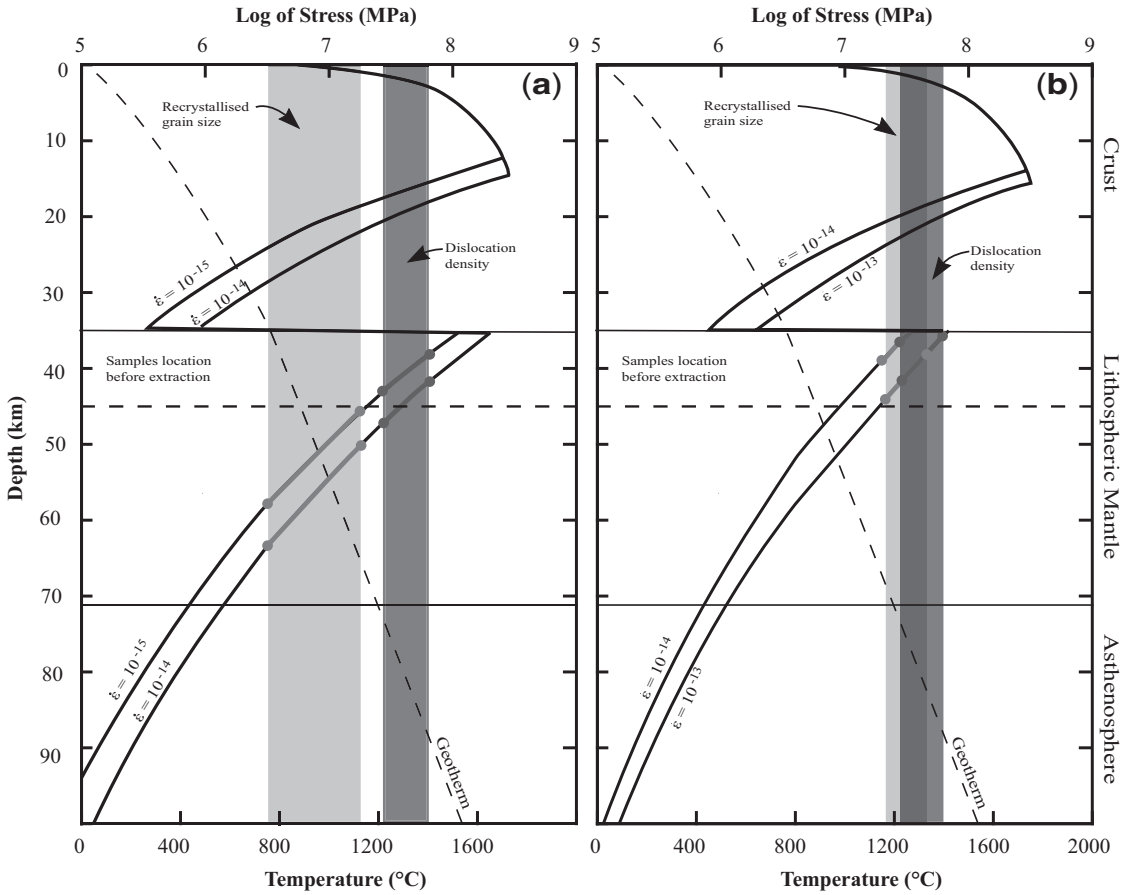

Fig. 19. Rheological profiles of the lithosphere beneath the Kamchatka active volcanic arc considering a dry (a) or a wet (b) mantle. We assumed a granodioritic crust with a thickness of 35 km (Zhuravlev & Antipov, 1993; Kharakhinov, 1996), a surface heat flow of 88 mW/m^2 (Currie & Hyndman, 2006), and a constant thermal conductivity of 2·51 and 3·35 W/m K for the granodiorite and peridotite layers, respectively (Philpotts, 1990). The brittle upper crust strength was estimated using Byerlee (1978) and the lower crust strength by using a dry granodiorite power law (Ranalli, 1995). The mantle strength was calculated using either the dry or the wet dunite flow laws of Chopra & Paterson (1981, 1984). $\dot{\varepsilon}$ is the strain rate given in s^{-1}. Light and dark grey bands indicate deviatoric stresses estimated from the average recrystallized grain sizes and free dislocation densities, respectively.

grain size distribution (Fig. 3), leading to an underestimation of the mean recrystallized grain size and an overestimation of the stresses.

The stresses estimated using the 'wet' paleopiezometer of Jung & Karato (2001*b*) are similar to those obtained from the free dislocation density. For a wet dunite flow law and a strain rate of 10^{-14} s^{-1}, these rather high stresses are attained only just below the Moho and in the crust (Fig. 19). Strain rates of 10^{-13} s^{-1} are needed to produce stresses of 20–60 MPa in a wet mantle. These results are consistent with the IR spectroscopy data which show that olivines in the studied samples have rather low water contents.

Evidence for fluid–melt percolation and consequences for the olivine microstructures and CPO

All coarse-grained Avacha xenoliths present clear microstructural evidence of reactive percolation of Si-rich fluids leading to crystallization of orthopyroxene at the expense of olivine. This evidence includes the following: (1) large orthopyroxenes elongated parallel to the lineation enclosing small olivine grains in crystallographic continuity with neighbouring olivine crystals (Fig. 4a); (2) corrosion embayments in olivine crystals filled by interstitial orthopyroxenes that may show kink bands subparallel to the olivine subgrain walls or be undeformed (Fig. 4c); (3) concentration of interstitial orthopyroxenes in lenses parallel to the foliation (Figs 2a,b, 3 and 5). The latter observations also indicate that the reactive fluid percolation is synkinematic to the main high-temperature deformation. Concentration of interstitial orthopyroxenes in lenses parallel to the foliation may, for example, result from deformation-controlled fluid segregation, similar to melt segregation in simple shear experiments using olivine–spinel–basalt aggregates, where melt-rich bands tends to form parallel to the shear plane (Holtzman *et al.*, 2003).

On the other hand, the absence of intra-crystalline deformation features in most interstitial orthopyroxenes (Fig. 2g and 3b) or in small crystals filling corrosion embayments in olivine (Figs 3b and 4c), as well as the stronger dispersion of the orthopyroxene CPO relative to the olivine CPO (Fig. 6), implies that reactive fluid percolation probably continued after the deformation slowed down. Finally, because it led to orthopyroxene crystallization, the fluid percolation must have occurred at temperatures below the hydrous orthopyroxene solidus, which is 1360°C and 1270°C at 1 GPa and 2 GPa (Kushiro *et al.*, 1968), respectively. This is consistent with a fluid percolation occurring during the main deformation at the base of the lithosphere and/or in the shallow asthenosphere (Fig. 19).

Although olivine CPO patterns are rather homogeneous in the studied peridotites, the intensity of the CPO decreases with increasing volume fraction of fine-grained olivine crystals. Within a sample, the J index is 2–4 times lower for fine-grained olivine crystals than for coarse ones (Fig. 9). These fine-grained olivine crystals, which dominantly occur in opx-rich bands parallel to the foliation (Fig. 2b and e), are either undeformed or display deformation microstructures similar to the coarse olivine grains, such as subgrains or undulose extinction. Dynamic recrystallization may explain both the grain size reduction and the dispersion of the CPO. However, crystallographic continuity between neighbouring olivine crystals separated by interstitial orthopyroxene (Fig. 3) suggests that they were originally part of a single coarse olivine crystal. We propose that the dominant mechanism for olivine grain size reduction in these bands is the reactive percolation of Si-rich fluids leading to olivine replacement by orthopyroxene. A similar phenomenon has been described by Dijkstra *et al.* (2002) in the Othris peridotite massif (Greece).

Concentration of fluids or melts within the bands may have favoured the activation of diffusional processes and grain boundary sliding resulting in weaker olivine CPO. Similar weakening of the olivine CPO in deformation experiments on olivine–melt aggregates (Holtzman *et al.*, 2003) and in peridotite massifs where deformation occurred in the presence of small melt fractions (Dijkstra *et al.*, 2002; Le Roux *et al.*, 2008; Soustelle *et al.*, 2009) has also been attributed to an increased contribution of diffusion to deformation. Fluid concentration in these bands probably also resulted in a viscosity decrease (Holtzman & Kohlstedt, 2007) and, because the bands are aligned, in anisotropic mechanical behaviour where shearing parallel to the foliation is favoured.

Superimposed on the high-temperature deformation microstructures, the studied peridotites show a wide range of features related to melt or fluid transport in the lithospheric mantle. These features include the formation of the acicular orthopyroxene aggregates (Fig. 4d), probably at the expense of pre-existing coarse orthopyroxene crystals, and the crystallization of a fine-grained ol–opx–oxides ± cpx ± amph ± glass matrix (Fig. 2g) at the expense of orthopyroxene and olivine. The fine-grained matrix occurs as a pervasive film along grain boundaries (Figs 2e, g and 4c), in millimeter-scale lenses flattened parallel the foliation (Fig. 2d), or forming irregular pockets in equigranular peridotite AV16 (Fig. 2f). It corrodes olivine and orthopyroxene and crosscuts their internal deformation microstructures (Fig. 4c), implying post-deformation crystallization. In general, a higher concentration of the fine-grained matrix along grain boundaries is observed in the opx-rich bands. We propose that it records the higher permeability of these bands caused by their finer grain size (Wark & Watson, 2000; Le Roux *et al.*, 2008). The fine-grained matrix is also observed along anastamosing veinlets that crosscut large deformed olivine crystals (Fig. 4e). Acicular orthopyroxenes similar to those observed in the studied peridotites have been generally attributed to metasomatism by aqueous fluids with a small amount of dissolved silicates (Arai & Kida, 2000; Grégoire *et al.*, 2001, 2007; McInnes *et al.*, 2001; Arai *et al.*, 2003; Ishimaru *et al.*, 2007; Facer & Downes, 2008). However, the fine-grained matrix crystallizes at the expense of both olivine and orthopyroxene. Moreover, the acicular orthopyroxenes are not the sole reaction product; the fine-grained matrix also contains less common amphibole and clinopyroxene. Together these observations suggest that their formation is due instead to a reaction between harzburgite and a hydrous silicate melt.

The late-stage melt percolation likely took place under static lithospheric conditions and has no major influence on the olivine CPO unless it results in crystallization of large volumes of the fine-grained ol–opx–oxides ± amph ± cpx ± glass matrix. It may also have contributed to the partial annealing of the deformation structures in the olivine in these bands. The fine-grained ol–opx–oxides ± amph ± cpx ± glass matrix, which occurs in post-deformation veinlets crosscutting olivine crystals (Fig. 4d and e), often encloses polygonal olivine crystals free of dislocations and deformation microstructures (Figs 4f and 14c, f), which probably result from neo-crystallization of olivine. The fine-grained peridotite AV16 that is essentially composed of strain-free polygonal olivine crystals probably represents a highly fractured domain or the wall-rock of a major dyke. Its weak CPO ($J = 1{\cdot}98$) implies nevertheless that at least some of these strain-free polygonal olivines were inherited from coarser grains with a pre-existing and probably stronger CPO.

The observed microstructures suggest an evolution of the fluid transport process. It started by pervasive porous flow of Si-rich aqueous fluids synchronous with or following the high-temperature deformation (crystallization of

interstitial and coarse orthopyroxene at the expense of olivine). This was followed by porous flow of hydrous melts under static conditions (formation of the ol–opx–oxides ± amph ± cpx ± glass matrix) that later evolved to melt transport localized in a network of connected veins formed by fluid-assisted fracturing. This variation in melt transport processes is consistent with the cooling history inferred from the orthopyroxene thermometry and from the deformation microstructures. It corroborates the inference of a continuous cooling history before extraction of the xenoliths from shallow lithospheric levels.

Hydration of the supra-subduction zone wedge mantle

Measurements of water concentrations in olivine and coarse orthopyroxene in the studied peridotites yield values between 1 and 8·6 ppm of H_2O by weight and 25 and 506 ppm of H_2O, respectively (Table 2). These are respectively lower and higher than the theoretical H_2O saturation values for olivine and orthopyroxene in spinel peridotites equilibrated between 1 and 2 GPa (16 and 290 ppm H_2O, Keppler & Bolfan-Casanova, 2006). Olivines in the studied peridotites are clearly water undersaturated; their water concentrations are 2–8 times lower than the theoretical calculated saturation value. Orthopyroxenes, on the other hand, have heterogeneous water contents ranging from 10 times lower to 1·7 times higher than the saturation value. Consequently, the orthopyroxene/olivine water concentration ratios in the studied xenoliths vary from 5 to 126. The extreme values differ significantly from the orthopyroxene/olivine water concentration ratio derived from the theoretical saturation values (~18, Keppler & Bolfan-Casanova, 2006), from orthopyroxene/olivine water concentration ratios measured in natural spinel peridotites (40·7 ± 18·9, Grant *et al.*, 2007; Falus *et al.*, 2008), or from partition coefficients ($D^{opx/ol}_{water}$) determined experimentally for peridotites equilibrated in the spinel field (7–10, Aubaud *et al.*, 2004). This suggests that olivines and orthopyroxenes in the Avacha peridotites are not in equilibrium with respect to their water contents.

Orthopyroxenes in the Avacha peridotites, except for coarse peridotite AV10, have lower water contents (25–218 ppm H_2O by weight) than the theoretical saturation value (290 ppm H_2O, Keppler & Bolfan-Casanova, 2006). The measured water contents in the three most hydrated pyroxenes (Table 2) are nevertheless in the same range as those observed in water saturation experiments on pure and natural enstatite at pressures of 1 and 2·5 GPa: 114 ± 10 and 238 ± 7 ppm H_2O by weight (Paterson calibration), respectively (Rauch & Keppler, 2002). If we calculate water concentration ratios between these pyroxenes and the coarser, more water-enriched olivines in each sample we obtain values of 27 in AV3, 31 in AV10 and 26 in AV15. These values are consistent with the concentration ratios obtained in saturation experiments, suggesting that these three orthopyroxenes and the coarser olivine are in equilibrium and display water concentrations that could represent the original (pre-exhumation) water contents in our samples. The lowest water contents (25–55 ppm H_2O by weight) were measured in a coarse orthopyroxene from sample AV15 and in one acicular orthopyroxene from sample AV16. These two orthopyroxenes are texturally different, but both samples display wide fine-grained zones, which probably result from interaction with a percolating melt. Peslier *et al.* (2002) proposed that an increase in oxygen fugacity linked to percolation of metasomatic fluids or melts may account for observed low water concentrations in orthopyroxenes from subduction-related mantle xenoliths. Oxygen fugacity in Kamchatka peridotite xenoliths is between 0 and 2 ΔFMQ (fayalite–magnetite–quartz buffer) with a peak around +1 ΔFMQ (Arai *et al.*, 2003; Ionov *et al.*, 2007; Ionov, 2010), which corresponds to the values measured by Peslier *et al.* (2002). The high oxygen fugacity of the Kamchatka samples is also consistent with the fact that the major O–H absorption bands of the olivine IR spectrum are at 3354 and 3328 cm^{-1} (Fig. 11, Berry *et al.*, 2005). Finally, extremely high water contents (>500 ppm H_2O by weight) were observed in one orthopyroxene from sample AV10. Such concentrations have been previously observed only under high-pressure conditions or in Al-rich orthopyroxene (Rauch & Keppler, 2002; Keppler & Bolfan-Casanova, 2006), yet the orthopyroxenes in our samples are equilibrated at low pressures (1–2 GPa) and have low Al_2O_3 contents (≤2 wt %). Although the absorbance spectrum is coherent (Fig. 16), we cannot completely discard the possibility of an analytical problem concerning this measurement. However, independently of this extreme value, the broad variations in orthopyroxene water contents, both within and between samples in the Kamchatka xenoliths, suggest that the H_2O concentration in minerals, particularly in orthopyroxene, is controlled by localized melt or fluid percolation, as a result of melt segregation during porous flow or in fractures.

Despite the fact that water concentrations in the Avacha olivines are within the range observed in other spinel-peridotite xenoliths from supra-subduction zone settings (Demouchy, 2004; Peslier & Luhr, 2006; Falus *et al.*, 2008), they are relatively low. A probable explanation is loss of water by diffusion to the host magma during the transport of the xenoliths (Demouchy *et al.*, 2006; Peslier & Luhr, 2006). The observation that small olivines have the lowest water concentrations is consistent with dehydration. Measurements in a coarse olivine crystal yielded a broad range of values within a single grain; however, the variation is within the uncertainty of the measurements (±30%) as the water contents are very low. Moreover, core–rim measurements in crystal ol7 of sample AV15

gave water contents of 5 and 2·5 ppm H_2O by weight, respectively, corroborating potential dehydration during the ascent of the xenolith in the magma. The orthopyroxene, in contrast, has not experienced dehydration during the ascent of the xenoliths. Hence, we can use the water concentration in orthopyroxenes AV3opx1, AV10opx1 and AV15opx3 (Table 2), which have water contents in the range of those observed in water saturation experiments on pure and natural enstatite, and $D^{opx/ol}_{water}$ consistent with the data of Aubaud *et al.* (2004) to calculate a hypothetical concentration of water in olivine before the inferred dehydration. This yields values of 13–28 ppm H_2O by weight, which are consistent with the theoretical saturation value (16 ppm H_2O).

Experiments predict that incorporation of water in olivine results in activation of different slip systems (e.g. Jung & Karato, 2001*a*). Jung *et al.* (2006) show that the transition from dominant glide on (010)[100] to (001)[100] under high-temperature and moderate-stress conditions occurs at ~15 wt ppm H_2O. The low measured water contents in olivine (1–8·6 wt ppm H_2O) and stresses estimated from the various paleopiezometers (3–60 MPa) imply a dominant activation of the (010)[100] system. However, if dehydration occurred during the ascent of the xenoliths to the surface, olivine would have higher water contents, corresponding to the transition between dominant glide on the [100](010) and [100](001) systems. This is consistent with the CPO data, which imply that olivine deformed by [100] glide on both (010) and (001) planes.

Implications for the dynamics of the supra-subduction zone mantle

The analysis of the textures and deformation microstructures of the Avacha xenoliths allows us partially to reconstruct their thermo-mechanical history even if the precise timing of the different episodes cannot be established. The first recorded event is high-degree partial melting at shallow mantle depths (1–2 GPa, Ionov, 2009). This was followed by deformation under high-temperature, low-stress conditions, contemporaneous with porous flow of a hydrous melt or fluid. Cooling and integration of the samples into the lithosphere mark the end of the major deformation and result in a change of the melt–fluid transport process to fracturing. Finally, two samples (AV20 and AV21) were crosscut by orthopyroxenite veins of probably magmatic origin. This evolution can be compared with the long and complex history of the Kamchatka subduction zone.

High degrees of partial melting at shallow depths are observed only at mid-ocean ridges or in the mantle wedge above subduction zones. Based on the modal (absence of primary cpx and high orthopyroxene contents relative to olivine) and chemical compositions (Al–Fe relations) of the Avacha peridotites, Ionov (2009) proposed that they are probably residues of hydrous melting in the mantle wedge. Numerical simulations by Arcay *et al.* (2007*a*, 2007*b*) show that influx of water and the resulting viscosity reduction in the mantle wedge may induce an upwelling of the lithosphere–asthenosphere boundary, allowing partial melting at depths shallower than 50 km. The Avacha peridotites may represent the residues of such a shallow partial melting process that were subsequently carried away by wedge convection, experiencing high-temperature, low-stress deformation and porous flow of hydrous fluids or melts at the base of the lithosphere and/or in the shallow asthenosphere.

The cooling recorded consistently by the change in deformation and fluid transport mechanisms and by the thermometry (Ionov, 2010) suggests that the Avacha peridotites were subsequently accreted to the lithosphere. To account for this evolution, we need to invoke a process producing a decrease in temperature in the mantle wedge and, hence, the deepening of the isotherms, leading to accretion of the shallow asthenospheric mantle to the lithosphere. Numerical models show that a decrease in the velocity of plate convergence reduces the convective vigour in the wedge, leading to a decrease in temperature in the mantle wedge and thickening of the upper plate (Arcay *et al.*, 2007*b*).

The present Kamchatka peninsula was formed by the collision of two volcanic arcs in response to the closure, between the late Miocene and the Quaternary, of a back-arc basin that separated two opposed subduction zones (Konstantinovskaia, 2001). A decrease in the convergence velocity associated with the collision of the two arcs may thus account for a decrease in the mantle wedge temperatures, leading to accretion of shallow asthenospheric mantle to the base of the lithosphere of the upper plate and cooling of the latter. This collision resulted in the eastward displacement of the volcanic front; calc-alkaline magmas from this new volcanic front fractured the lithosphere and carried to the surface the Avacha xenoliths that record both an asthenospheric and a lithospheric history.

CONCLUSION

Our observations show that although the spinel harburgite xenoliths from the Avacha volcano were extracted from the upper part of the lithospheric mantle (≥45 km), they record a thermo-mechanical history that started with partial melting and deformation under asthenospheric conditions, followed by accretion to the base of the lithosphere and subsequent cooling. Percolation of hydrous fluids or melts began in the asthenosphere and continued under lithospheric conditions. This succession of events, which suggests cooling of the supra-subduction zone mantle, is

consistent with the evolution of the Kamchatka arc since the late Miocene.

Percolation of small-fraction fluids or hydrated melts is recorded at all stages of the long history of the Avacha xenoliths. Analysis of the microstructures suggests that early ingress of Si-rich aqueous fluids was contemporaneous with deformation under high-temperature, low-stress conditions and took place essentially by reactive porous flow. Deformation-induced fluid segregation is probably responsible for the development of irregular compositional banding parallel to the foliation; higher degrees of interaction with fluids led to opx-enrichment and olivine grain size reduction by crystallization of orthopyroxene at the expense of olivine and to a local decrease in viscosity which, because the bands are aligned, result in anisotropic mechanical behaviour.

Olivine CPO shows clear axial [100] patterns that record deformation by dislocation creep with dominant activation of the high-temperature, low-stress, low-pressure $\{0kl\}[100]$ slip systems. This interpretation is consistent with the elongation of olivine crystals in the [100] directions and with the well-developed (100) tilt boundaries observed in the decorated sections and in EBSD maps. Olivine CPO within the opx-rich bands is similar, but more dispersed than the CPO in the neighbouring coarse domains. This suggests that the concentration of fluids in these bands does not result in a change in dominant olivine slip direction, but enhances the contribution of diffusional processes to the deformation.

Subsequent cooling and accretion to the lithosphere led to a continuous transition from reactive porous flow to the development of a network of interconnected veins and probably also to a change in the fluid composition towards hydrated melts. This later percolation produced crystallization of acicular orthopyroxene aggregates and of a fine-grained matrix composed of ol–opx–oxides ± amph ± cpx ± glass at the expense of both orthopyroxene and olivine. Finally, the xenoliths were crosscut by veins and carried up to the surface by calc-alkaline magmas.

In spite of the microstructural evidence for interaction with hydrous fluids or melts at all stages of their supra-subduction zone evolution, the water contents in olivine are low (1–8·6 wt ppm). These values are nevertheless similar to those observed in spinel peridotites from various subduction zone settings. If these xenoliths have been dehydrated during their ascent, the maximum water content expected would be 13–28 wt ppm H_2O. This could explain the activation of both (010) and (001) slip planes in olivine. On the other hand, water contents in orthopyroxene are strongly variable (25–506 wt ppm H_2O), probably recording spatially heterogeneous interaction with fluids or melts and compositional disequilibrium.

ACKNOWLEDGEMENTS

We thank C. Nevado and D. Delmas, who supplied high-quality polished thin sections for EBDS measurement. FTIR analyses were performed at Université Montpellier 2 (France) with the help of David Maurin at the Laboratoire Colloids, Verre et Nanomateriaux, and at Université Blaise Pascal, Clermont-Ferrand (France) with the help of Nathalie Bolfan-Casanova at the Laboratoire Magmas et Volcans. D. Mainprice is thanked for discussions on the interpretation of dislocation structures, and for providing software for analysing and plotting CPO data. We acknowledge Arjan Dijkstra, Phil Skemer and Jessica Warren for their constructive reviews. This study was partially funded by the program SEDIT of the Institut National des Sciences de l'Univers (INSU-CNRS), France, in the frame of the project 'Deformation in the supra-subduction mantle' coordinated by A.T. V.S. benefited from a PhD scholarship from the Ministère de la Recherche et de l'Enseignement Supérieur.

REFERENCES

Amelinckx, S. & Dekeyser, W. (1959). The structure and properties of grain boundaries. *Solid State Physics* **8**, 325–499.

Arai, S. & Kida, M. (2000). Origin of fine-grained peridotite xenoliths from Iraya volcano of Batan Island, Philippines: deserpentinization or metasomatism at the wedge mantle beneath an incipient arc? *Island Arc* **9**(4), 458–471.

Arai, S., Ishimaru, S. & Okrugin, V. (2003). Metasomatized harzburgite xenoliths from Avacha volcano as fragments of mantle wedge of the Kamchatka arc: Implication for the metasomatic agent. *Island Arc* **12**(2), 233–246.

Arcay, D., Doin, M.-P., Tric, E., Bousquet, R. & de Capitani, C. (2006). Overriding plate thinning in subduction zones: Localized convection induced by slab dehydration. *Geochemistry, Geophysics, Geosystems* **7**(2), doi:10.1029/2005GC001061.

Arcay, D., Doin, M.-P., Tric, E. & Bousquet, R. (2007*a*). Influence of the precollisional stage on subduction dynamics and the buriest crust thermal state: Insights from the numerical simulations. *Tectonophysics* **441**, 27–45.

Arcay, D., Tric, E. & Doin, M.-P. (2007*b*). Slab surface temperatutre in subduction zone: Influnce of the interplate decoupling depth and upper mantle plate thinnig processes. *Earth and Planetary Science Letters* **255**, 324–338.

Aubaud, C., Hauri, E. H. & Hirschmann, M. M. (2004). Hydrogen partition coefficient between nominally anhydrous minerals and basaltic melts. *Geophysical Research Letters* **31**, L20611.

Avdeiko, G. P., Popruzhenko, S. V. & Palueva, A. A. (2002). The tectonic evolution and volcano-tectonic zonation of the Kuril–Kamchatka island-arc system. *Geotectonics* **36**(4), 312–327.

Avé-Lallemant, H. G. & Carter, N. L. (1970). Syntectonic recrystallization of olivine and modes of flow in the upper mantle. *Geological Society of America Bulletin* **81**, 2003–2020.

Bai, Q., Mackwell, S. J. & Kohlstedt, D. L. (1991). High-temperature creep of olivine single-crystals. 1. Mechanical results for buffered samples. *Journal of Geophysical Research—Solid Earth and Planets* **96**(B2), 2441–2463.

Bell, D., Rossman, G. & Moore, R. (2004). Abundance and partitioning of OH in a high-pressure magmatic system: Megacrysts from

the Monastery kimberlite, South Africa. *Journal of Petrology* **45**(8), 1539–1564.

Bell, D. R., Rossman, G. R., Maldener, J., Endisch, D. & Rauch, F. (2003). Hydroxide in olivine: A quantitative determination of the absolute amount and calibration of the IR spectrum. *Journal of Geophysical Research—Solid Earth* **108**(B2), 2015.

Bénard, A. & Ionov, D. A. (2009). Veined peridotite xenoliths from the Avacha volcano, Kamchatka: Fluid types and fluid–rock interaction in supra-subduction mantle. *Geochimica et Cosmochimica Acta* **73**, [13(S1)], A108.

Ben Ismail, W. & Mainprice, D. (1998). An olivine fabric database: an overview of upper mantle fabrics and seismic anisotropy. *Tectonophysics* **296**, 145–158.

Berry, A. J., Hermann, J., O'Neill, H. S. C. & Foran, G. J. (2005). Fingerprinting the water site in mantle olivine. *Geology* **33**(11), 869–872.

Blacic, J. D. (1972). Effect of water on the experimental deformation of olivine. In: Heard, H. C., Borg, I. Y., Carter, N. L. & Rayleigh, C. B. (eds) *Flow and Fracture of Rocks*. American Geophysical Union: Washington, pp. 109–115.

Bolfan-Casanova, N., Keppler, H. & Rubie, D. C. (2000). Water partitioning between nominally anhydrous minerals in the MgO–SiO_2–H_2O system up to 24 GPa: implications for the distribution of water in the Earth's mantle. *Earth and Planetary Science Letters* **182**(3–4), 209–221.

Bouchez, J. L., Mainprice, D. H., Trepied, L. & Doukhan, J.-C. (1984). Secondary lineation in a high-T quartzite (Galicia, Spain): an explanation for an abnormal fabric. *Journal of Structural Geology* **6**(1/2), 159–165.

Braitseva, O. A., Bazanova, L. I., Melekestev, I. V. & Sulerzhitskiy, L. D. (1998). Large Holocene eruptions of Avacha volcano, Kamchatka (7250–3700 ^{14}C years B.P.). *Volcanology and Seismology* **20**, 1–27.

Bunge, H. J. (1982). *Texture Analysis in Materials Sciences*. London: Butterworth.

Byerlee, J. (1978). Friction of rocks. *Pure and Applied Geophysics* **116**(4–5), 615–626.

Bystricky, M., Kunze, K., Burlini, L. & Burg, J. P. (2000). High shear strain of olivine aggregates; rheological and seismic consequences. *Science* **290**(5496), 1564–1567.

Cagnioncle, A.-M., Parmentier, E. M. & Elkins-Tanton, L. T. (2007). Effect of solid flow above a subducting slab on water distribution and melting at convergent plate boundaries. *Journal of Geophysical Research* **112**, B09402.

Chopra, P. N. & Paterson, M. S. (1981). The experimental deformation of dunite. *Tectonophysics* **78**(1–4), 453–473.

Chopra, P. N. & Paterson, M. S. (1984). The role of water in the deformation of dunite. *Journal of Geophysical Research* **89**, 7861–7876.

Costa, F. & Chakraborty, S. (2008). The effect of water on Si and O diffusion rates in olivine and implications for transport properties and processes in the upper mantle. *Physics of the Earth and Planetary Interiors* **166**, 11–29.

Couvy, H., Frost, D. J., Heidelbach, F., Nyilas, K., Ungar, T., Mackwell, S. & Cordier, P. (2004). Shear deformation experiments of forsterite at 11 GPa–1400°C in the multianvil apparatus. *European Journal of Mineralogy* **16**(6), 877–889.

Currie, C. A. & Hyndman, R. D. (2006). The thermal structure of subduction zone back arcs. *Journal of Geophysical Research* **111**(B8), B08404.

Currie, C. A., Huismans, R. S. & Beaumont, C. (2008). Thinning of continental backarc lithosphere by flow-induced gravitational instability. *Earth and Planetary Science Letters* **269**, 436–447.

Demouchy, S. (2004). Water in the Earth's interior: Thermodynamics and kinetics of hydrogen incorporation in olivine and wadsleyite. Universität Bayreuth.

Demouchy, S., Jacobsen, S. D., Gaillard, F. & Stern, C. R. (2006). Rapid magma ascent recorded by water diffusion profiles in mantle olivine. *Geology* **34**(6), 429–432.

Demouchy, S., Mackwell, S. J. & Kohlstedt, D. L. (2007). Influence of hydrogen on Fe–Mg interdiffusion in (Mg,Fe)O and implications for Earth's lower mantle. *Contributions to Mineralogy and Petrology* **154**, 279–289.

Dijkstra, A. H., Drury, M. R., Vissers, R. L. M. & Newman, J. (2002). On the role of melt–rock reaction in mantle shear zone formation in the Othris Peridotite Massif (Greece). *Journal of Structural Geology* **24**(9), 1431–1450.

Doukhan, J.-C., Doukhan, N., Naze, L. & Van Duysen, J.-C. (1986). Défauts de réseau et plasticité cristalline dans les pyroxenes: Une revue. *Bulletin de Minéralogie* **109**, 377–374.

Durham, W. B., Goetze, C. & Blake, B. (1977). Plastic-flow of oriented single-crystals of olivine. 2. Observations and interpretation of dislocation-structures. *Journal of Geophysical Research* **82**(36), 5755–5570.

Facer, J. & Downes, H. (2008). , Hydrous fluid metasomatism in spinel dunite xenoliths from the Bearpaw Mountains, Montana, USA. *9th International Kimberlite Conference*. Frankfurt. Extented abstract No. 9IKC-A-00116.

Falus, G., Tommasi, A., Ingrin, J. & Szabo, C. (2008). Deformation and seismic anisotropy of the lithospheric mantle in the southeastern Carpathians inferred from the study of mantle xenoliths. *Earth and Planetary Science Letters* **272**, 50–64.

Frank, F. C. & Read, W. T. J. (1950). Multiplication processes for slow moving dislocations. *Physical Review* **79**, 722–723.

Gerya, T. V. & Yuen, D. A. (2003). Rayleigh–Taylor instabilities from hydration and melting propel 'cold plumes' at subduction zones. *Earth and Planetary Science Letters* **212**, 47–62.

Gorbatov, A., Kostoglodov, V., Suarez, G. & Gordeev, E. (1997). Seismicity and structure of the Kamchatka subduction zone. *Journal of Geophysical Research* **102**(B8), 17883–17898.

Gorbatov, A., Dominguez, J., Suarez, G., Kostoglodov, V., Zhao, D. & Gordeev, E. (1999). Tomographic imaging of the P-wave velocity structure beneath the Kamchatka peninsula. *Geophysical Journal International* **137**, 269–279.

Grant, K., Ingrin, J., Lorand, J. & Dumas, P. (2007). Water partitioning between mantle minerals from peridotite xenoliths. *Contributions to Mineralogy and Petrology* **154**(1), 15–34.

Grégoire, M., McInnes, B. I. A. & O'Reilly, S. Y. (2001). Hydrous metasomatism of oceanic sub-arc mantle, Lihir, Papua New Guinea; Part 2. Trace element characteristics of slab-derived fluids. *Lithos* **59**(3), 91–108.

Grégoire, M., Jego, S., Maury, R. C., Polve, M., Payote, B., Tamayo, R. A., Jr & Yumul, G.P., Jr (2007). Metasomatic interactions between slab-derived melts and depleted mantle: Insights from xenoliths within Monglo adakite (Luzon arc, Philippines). *Lithos* **103**(3–4), 415–430.

Ham, R. K. (1961). The detemination of dislocation densities in thin films. *Philosophical Magazine* **6**(69), 1183–1184.

Hier-Majumder, S., Anderson, I. M. & Kohlstedt, D. L. (2004). Influence of proton on Fe–Mg interdiffusion in olivine. *Journal of Geophysical Research* **B2**, B02202.

Hirsch, P. B., Howie, A., Nicholson, B. B. & Pashley, D. W. (1965). *Electron Microscopy of Thin Crystals*. London: Butterworth.

Hirth, G. & Kohlstedt, D. L. (1995). Experimental constraints on the dynamics of the partially molten upper-mantle. 2. Deformation in the dislocation creep regime. *Journal of Geophysical Research—Solid Earth* **100**(B8), 15441–15449.

Holtzman, B. K. & Kohlstedt, D. L. (2007). Stress-driven melt segregation and strain partitioning in partially molten rocks: Effects of stress and strain. *Journal of Petrology* **48**, 2379–2406.

Holtzman, B. K., Groebner, N. J., Zimmerman, M. E., Ginsberg, S. B. & Kohlstedt, D. L. (2003). Stress-driven melt segregation in partially molten rocks. *Geochemistry, Geophysics, Geosystems* **4**, article number 8607.

Honda, S., Saito, M. & Nakakuki, T. (2002). Possible existence of small-scale convection under the backarc. *Geophysical Research Letters* **29**(21), 2043, doi:10.1029/2002GL015853.

Ionov, D. A. (2010). Petrology of Mantle Wedge Lithosphere: New Data on Supra-Subduction Zone Peridotite Xenoliths from the Andesitic Avacha Volcano, Kamchatka. *Journal of Petrology* **51**, 327–361.

Ionov, D. A. & Seitz, H.-M. (2008). Lithium abundances and isotopic compositions in mantle xenoliths from subduction and intra-plate settings: Mantle sources vs. eruption histories. *Earth and Planetary Science Letters* **266**(3–4), 316–331.

Ionov, D. A., Bruegmann, G., Seitz, H.-M., Lahaye, Y. & Woodland, A. B. (2007). Peridotite xenoliths from the andesitic Avacha volcano, Kamchatka—any signatures of subduction metasomatism? Abstracts, 17th Goldschmidt Conference, Cologne. *Geochimica et Cosmochimica Acta* , 71[15(S1)], A430.

Ishimaru, S., Arai, S., Ishida, Y., Shirasaka, M. & Okrugin, V. (2007). Melting and multi-stage metasomatism in the mantle wedge beneath a frontal arc inferred from highly depleted peridotite xenoliths from the Avacha volcano, Southern Kamchatka. *Journal of Petrology* **48**(2), 395–433.

Jung, H. & Karato, S. (2001*a*). Water-induced fabric transitions in olivine. *Science* **293**(5534), 1460–1463.

Jung, H. & Karato, S. I. (2001*b*). Effects of water on dynamically recrystallized grain-size of olivine. *Journal of Structural Geology* **23**(9), 1337–1344.

Jung, H., Katayama, I., Jiang, Z., Hiraga, I. & Karato, S. (2006). Effect of water and stress on the lattice-preferred orientation of olivine. *Tectonophysics* **421**(1–2), 1–22.

Karato, S. (1989). Grain growth kinetics in olivine aggregates. *Tectonophysics* **168**, 255–273.

Karato, S., Toriumi, M. & Fujii, T. (1980). Dynamic recrystallization of olivine single crystals during high temperature creep. *Geophysical Research Letters* **7**(9), 649–652.

Karato, S. I., Paterson, M. S. & Fitz Gerald, J. D. (1986). Rheology of synthetic olivine aggregates—influence of grain-size and water. *Journal of Geophysical Research—Solid Earth and Planets* **91**(B8), 8151–8176.

Karato, S., Rubie, D. C. & Yan, H. (1993). Dislocation recovery in olivine under deep upper mantle conditions—Implications for creep and diffusion. *Journal of Geophysical Research* **20**(5), 315–322.

Katayama, I., Jung, H. & Karato, S. I. (2004). New type of olivine fabric from deformation experiments at modest water content and low stress. *Geology* **32**(12), 1045–1048.

Keppler, H. & Bolfan-Casanova, N. (2006). Thermodynamics of water solubility and partitionning. In: Keppler, H. & Smyth, J. R. (eds) *Water in Nominally Anhydrous Minerals*. Geochemical Society, Mineralogical Society of America: Washington, pp. 193–230.

Kharakhinov, V. V. (1996). Tectonics and history of sedimentary basins development. In: Rodnikov, A. G., Tuezov, I. K. & Kharakhinov, V. V. (eds) *Structure and Dynamics of the Lithosphere and Asthenosphere of the Okhotsk Sea Region*. Moscow: Russian Academy of Science: Moscow, pp. 256–305.

Kohlstedt, D. L. & Goetze, C. (1974). Low-stress high-temperature creep in olivine single-crystals. *Journal of Geophysical Research* **79**(14), 2045–2051.

Kohlstedt, D. L., Goetze, C. & Durham, W. B. (1976*a*). Experimental deformation of single crystal olivine with application to flow in the mantle. In: Strens, R. G. J. (ed.) *The Physics and Chemistry of Minerals and Rocks*. Chichester: John Wiley, pp. 39–45.

Kohlstedt, D. L., Goetze, C., Durham, W. B. & Vandersande, J. (1976*b*). New technique for decorating dislocations in olivine. *Science* **191**(4231), 1045–1046.

Kohlstedt, D. L., Keppler, H. & Rubie, D. C. (1996). Solubility of water in the alpha, beta and gamma phases of $(Mg,Fe)_2SiO_4$. *Contributions to Mineralogy and Petrology* **123**(4), 345–357.

Konstantinovskaia, E. A. (2001). Arc–continent collision and subduction reversal in the Cenozoic evolution of the Northwest Pacifc: an example from Kamchatka (NE Russia). *Tectonophysics* **333**(1–2), 75–94.

Kushiro, I., Yoder, H. S. J. & Nishikawa, N. (1968). Effect of water on the melting of enstatite. *Geological Society of America Bulletin* **79**(12), 1685–1692.

Lee, C. A. (2003). Compositional variation of density and seismic velocities in natural peridotites at STP conditions: Implications for seismic imaging of compositional heterogeneities in the upper mantle. *Journal of Geophysical Research* **108**(B9), 2444.

Le Roux, V., Bodinier, J.-L., Tommasi, A., Alard, O., Dautria, J.-M., Vauchez, A. & Riches, A. J. V. (2007). The Lherz spinel lherzolite: Refertilized rather than pristine mantle. *Earth and Planetary Science Letters* **259**, 599–612.

Le Roux, V., Tommasi, A. & Vauchez, A. (2008). Feedback between melt percolation and deformation in an exhumed lithosphere–asthenosphere boundary. *Earth and Planetary Science Letters* **274**, 401–413.

Levin, V., Park, J., Brandon, M., Lees, J., Peyton, V., Gordeev, E. & Ozerov, A. (2002). Crust and upper mantle of Kamchatka teleseismic reciever functions. *Tectonophysics* **358**, 233–253.

Levin, V., Droznin, D., Park, J. & Gordeev, E. (2004). Detailed mapping of seismic anisotropy with local shear waves in southeastern Kamchatka. *Geophysical Journal International* **158**, 1009–1023.

Mackwell, S. J. (1991). High-temperature rheology of enstatite: implications for creep in the mantle. *Geophysical Research Letters* **18**(11), 2027–2030.

Mackwell, S. J., Kohlstedt, D. L. & Paterson, M. S. (1985). The role of water in the deformation of olivine single-crystals. *Journal of Geophysical Research—Solid Earth and Planets* **90**(NB13), 1319–1333.

Manea, V. C., Manea, M., Kostoglodov, V. & Sewell, G. (2005). Thermal models, magma transport and velocity anomaly estimation beneath southen Kamchatka. In: Foulger, G., Natland, J. & Presnall, D. (eds) *Plates, Plumes and Paradigms. Geological Society of America, Special Papers*.

McInnes, B. I. A., Gregoire, M., Binns, R. A., Herzig, P. M. & Hannington, M. D. (2001). Hydrous metasomatism of oceanic subarc mantle, Lihir, Papua New Guinea: petrology and geochemistry of fluid-metasomatised mantle wedge xenoliths. *Earth and Planetary Science Letters* **188**(1–2), 169–183.

Mei, S. & Kohlstedt, D. L. (2000*a*). Influence of water on plastic deformation of olivine aggregates 1. Diffusion creep regime. *Journal of Geophysical Research—Solid Earth* **105**(B9), 21457–21469.

Mei, S. & Kohlstedt, D. L. (2000*b*). Influence of water on plastic deformation of olivine aggregates 2. Dislocation creep regime. *Journal of Geophysical Research—Solid Earth* **105**(B9), 21471–21481.

Mei, S., Bai, W., Hiraga, T. & Kohlstedt, D. L. (2002). Influence of melt on the creep behavior of olivine–basalt aggregates under hydrous conditions. *Earth and Planetary Science Letters* **201**(3–4), 491–507.

Mercier, J. C. C., Anderson, D. A. & Carter, N. L. (1977). Stress in lithosphere—inferences from steady-state flow of rocks. *Pure and Applied Geophysics* **115**(1–2), 199–226.

Miller, G. H., Rossman, G. R. & Harlow, G. E. (1987). The natural occurence of hydroxide in olivine. *Physics and Chemistry of Minerals* **14**(5), 461–472.

Nicolas, A. & Poirier, J. P. (1976). *Crystalline Plasticity and Solid State Flow in Metamorphic Rocks*. London: John Wiley.

Paterson, M. S. (1982). The determination of hydroxyl by infrared absorption in quartz, silicate-glasses and similar materials. *Bulletin de Minéralogie* **105**(1), 20–29.

Peslier, A. & Luhr, J. (2006). Hydrogen loss from olivines in mantle xenoliths from Simcoe (USA) and Mexico: Mafic alkalic magma ascent rates and water budget of the sub-continental lithosphere. *Earth and Planetary Science Letters* **242**(3–4), 302–319.

Peslier, A. H., Luhr, J. F. & Post, J. (2002). Low water contents in pyroxenes from spinel-peridotites of the oxidized, sub-arc mantle wedge. *Earth and Planetary Science Letters* **201**(1R), 69–86.

Peyton, V., Levin, V., Park, J., Brandon, M., Lees, J., Gordeev, E. Ozerov & A., (2001). Mantle flow at a slab edge: seismic anisotropy in the Kamchatka region. *Geophysical Research Letters* **28**(2), 379–382.

Philpotts, A. R. (1990). *Principles of Igneous and Metamorphic Rocks*. Englewood Cliffs, NJ: Prentice Hall.

Poirier, J. P. (1985). *Creep of Crystals. High-temperature Deformation Processes in Metals, Ceramics and Minerals*. Cambridge: Cambridge University Press.

Raleigh, C. B. & Kirby, S. H. (1970). Creep in the upper mantle. *Mineralogical Society of America, Special Papers* **3**, 113–121.

Ranalli, G. (1995). *Rheology of the Earth*, 2nd edn edn. London: Chapman & Hall.

Raterron, P., Chen, J., Li, L., Weidner, D. & Cordier, P. (2007). Pressure-induced slip-system transition in forsterite: Single-crystal rheological properties at mantle pressure and temperature. *American Mineralogist* **92**(8–9), 1436–1445.

Rauch, M. & Keppler, H. (2002). Water solubility in orthopyroxene. *Contributions to Mineralogy and Petrology* **143**(5), 525–536.

Skemer, P., Katayama, I., Zhenting, J. & Karato, S. (2005). The misorientation index: Development of a new method for calculating the strength of lattice-preferred orientation. *Tectonophysics* **411**, 157–167.

Soustelle, V., Tommasi, A., Bodinier, J.-L., Garrido, C. J. & Vauchez, A. (2009). Deformation and reactive melt transport in the mantle lithosphere above a large-scale partial melting domain: the Ronda peridotite massif, S Spain. *Journal of Petrology* **50**(7), 1335–1266.

Tatsumi, Y., Furukawa, Y., Kogiso, T., Yamanaka, Y., Yokoyama, T. & Fedotov, S. A. (1994). A 3rd volcanic chain in Kamchatka—thermal anomaly at transform convergence plate boundary. *Geophysical Research Letters* **21**(7), 537–540.

Tommasi, A., Tikoff, B. & Vauchez, A. (1999). Upper mantle tectonics: three-dimensional deformation, olivine crystallographic fabrics and seismic properties. *Earth and Planetary Science Letters* **168**(1–2), 173–186.

Tommasi, A., Mainprice, D., Canova, G. & Chastel, Y. (2000). Viscoplastic self-consistent and equilibrium-based modeling of olivine lattice preferred orientations: Implications for the upper mantle seismic anisotropy. *Journal of Geophysical Research—Solid Earth* **105**(B4), 7893–7908.

Tommasi, A., Gibert, B., Seipold, U. & Mainprice, D. (2001). Anisotropy of thermal diffusivity in the upper mantle. *Nature* **411**(6839), 783–786.

Tommasi, A., Godard, M., Coromina, G., Dautria, J. M. & Barsczus, H. (2004). Seismic anisotropy and compositionally induced velocity anomalies in the lithosphere above mantle plumes: a petrological and microstructural study of mantle xenoliths from French Polynesia. *Earth and Planetary Science Letters* **227**(3–4), 539–556.

Tommasi, A., Vauchez, A., Godard, M. & Belley, F. (2006). Deformation and melt transport in a highly depleted peridotite massif from the Canadian Cordillera: Implications to seismic anisotropy above subduction zones. *Earth and Planetary Science Letters* **252**, 245–259.

Tommasi, A., Vauchez, A. & Ionov, D. A. (2008). Deformation, static recrystallization, and reactive melt transport in shallow subcontinental mantle xenoliths (Tok Cenozoic volcanic field, SE Siberia). *Earth and Planetary Science Letters* **272**, 65–77.

Van der Wal, D., Chopra, P., Drury, M. & Gerald, J. F. (1993). Relationships between dynamically recrystallized grain-size and deformation conditions in experimentally deformed olivine rocks. *Geophysical Research Letters* **20**(14), 1479–1482.

Vauchez, A. & Garrido, C. J. (2001). Seismic properties of an asthenospherized lithospheric mantle: constraints from lattice preferred orientations in peridotite from the Ronda massif. *Earth and Planetary Science Letters* **192**(2), 235–249.

Vollmer, F. W. (1990). An application of eigenvalue methods to structural domain analysis. *Geological Society of America Bulletin* **102**, 786–791.

Wark, D. A. & Watson, B. E. (2000). Effect of grain size on the distribution and transport of deep-seated fluids and melts. *Geophysical Research Letters* **27**(14), 2029–2032.

Zhang, S. & Karato, S.-I. (1995). Lattice preferred orientation of olivine aggregates deformed in simple shear. *Nature* **375**, 774–777.

Zhang, S., Karato, S.-I., Fitz Gerald, J., Faul, U. H. & Zhou, Y. (2000). Simple shear deformation of olivine aggregates. *Tectonophysics* **316**, 133–152.

Zhuravlev, A. V. & Antipov, M. P. (1993). The Okhotsk sea area of Cenozoic submergence. In: Sokolov, B. S. (ed.) *Seismostratigraphic Researches in Eurasia*. Moscow: Nauka, pp. 160–183.

Zimmerman, M. E. & Kohlstedt, D. L. (2004). Rheological properties of partially molten lherzolite. *Journal of Petrology* **45**(2), 275–298.

GEOPHYSICAL RESEARCH LETTERS, VOL. 37, L13307, doi:10.1029/2010GL043450, 2010

Seismic properties of the supra-subduction mantle: Constraints from peridotite xenoliths from the Avacha volcano, southern Kamchatka

Vincent Soustelle[1] and Andréa Tommasi[1]

Received 30 March 2010; revised 13 May 2010; accepted 7 June 2010; published 10 July 2010.

[1] This work presents seismic properties derived from a detailed microstructural study of supra-subduction mantle xenoliths extracted by the active Avacha volcano in the southern Kamchatka arc. These peridotites underwent low-stress deformation and syn- to late-kinematic reactive percolation of hydrous melts or fluids leading to local orthopyroxene enrichment and dispersion of the olivine CPO in the shallow mantle wedge. All samples show an axial [100] olivine CPO implying fast S-wave polarization parallel to the flow direction in the mantle. Orthopyroxene-enrichment by reactive fluids/melts percolation lowers the Vp/Vs ratio, but cannot explain the Vp/Vs ratios <1.7 mapped in the Japan and Andes forearc mantle. These low Vp/Vs ratios may however be explained by considering the intrinsic anisotropy of the peridotites. **Citation:** Soustelle, V., and A. Tommasi (2010), Seismic properties of the supra-subduction mantle: Constraints from peridotite xenoliths from the Avacha volcano, southern Kamchatka, *Geophys. Res. Lett.*, *37*, L13307, doi:10.1029/2010GL043450.

1. Introduction

[2] Seismic data are invaluable tools to probe the thermal structure, flow patterns, and fluid distribution in subduction zones. Seismic anisotropy in the upper mantle depends primarily on the orientation of olivine crystals; splitting measurements using local S-waves may thus record flow directions in the wedge. However, the presence of water and melt may modify the plastic deformation of olivine and hence the relation between seismic anisotropy and mantle flow [*Jung and Karato*, 2001; *Holtzman et al.*, 2003]. In Kamchatka, fast shear-wave polarization directions vary both along the subduction and with increasing distance to the trench [*Levin et al.*, 2004]. Variable polarization directions and delay times are also observed in other subduction zones, as the Kurils-Japan-Izu Bonin system [e.g., *Nakajima and Hasegawa*, 2004]. It is fundamental to know if these variations reflect variations in the mantle flow pattern, a change in the dominant olivine intracrystalline deformation mechanism, or result from serpentinization-related processes [*Faccenda et al.*, 2008; *Boudier et al.*, 2010].

[3] The Vp/Vs ratio allows constraining the composition of the mantle wedge. High Vp/Vs ratios may denote the presence of fluids or melts [*Takei*, 2002]. Low Vp/Vs ratios were attributed to changes in mineralogical composition. However, highly unusual mantle compositions (involving quartz) were invoked to explain Vp/Vs ratios <1.7 [*Wagner et al.*, 2006, and references therein]. Moreover, the effect of intrinsic anisotropy of mantle rocks on the Vp/Vs ratio is never considered.

[4] We computed the seismic properties of mantle xenoliths from an active subduction zone. They were extracted by the Avacha volcano in southeastern Kamchatka volcanic arc. Their study allows us to determine the active deformation mechanisms in olivine in the presence of hydrous fluids or melts and, hence, to constrain the relation between seismic anisotropy and flow directions in the shallow mantle wedge. It also allows quantification of the effect of the reactive fluids/melts percolation on the seismic properties.

2. Microstructures, Compositions, and Crystal Preferred Orientations

[5] The 23 studied mantle xenoliths come from Holocene andesitic tuffs of the active Avacha volcano located on the southeastern coast of the Kamchatka peninsula. The depths of the Moho and of the top of the subducting slab beneath the Avacha volcano are ca. 35 km and 120 km, respectively [*Gorbatov et al.*, 1997; *Levin et al.*, 2002]. Low P-wave velocities beneath the active volcanic arc are consistent with partial melting in the wedge [*Gorbatov et al.*, 1999]. Splitting measurements on local shear waves in southeastern Kamchatka yield trench-normal and trench-parallel polarization of fast S-waves in the fore-arc and the back-arc, respectively [*Levin et al.*, 2004].

[6] These Avacha peridotite xenoliths were the subject of detailed petrological [*Ionov*, 2010] and microstructural [*Soustelle et al.*, 2010] studies. They are highly refractory harzburgites (>3% clinopyroxene) formed by high degrees of melting (28–35%) at relatively low pressures (1–2 GPa). They display a coarse-grained porphyroclastic texture with a well-developed lineation marked by spinel trails and large elongated olivine crystals (1–5 mm long). Olivine crystals have curvilinear grain boundaries that locally evolve into polygonal shapes with 120° triple junctions, widely-spaced (100) subgrain boundaries, and low free dislocation densities. These microstructures are characteristic of diffusion-assisted dislocation creep, suggesting deformation under low-stress, high-temperature conditions. Two-pyroxenes equilibrium temperatures around 800–900°C [*Ionov*, 2010] imply that the low-stress "asthenospheric" deformation was followed by cooling and addition to the overriding plate lithosphere from where the xenoliths were extracted.

[7] One third of the studied xenoliths are slightly enriched in Si and show rather high orthopyroxene modal contents (18–30%). In some samples, orthopyroxene tends to con-

[1]Géosciences Montpellier, Université Montpellier II, CNRS, Montpellier, France.

0094-8276/10/2010GL043450

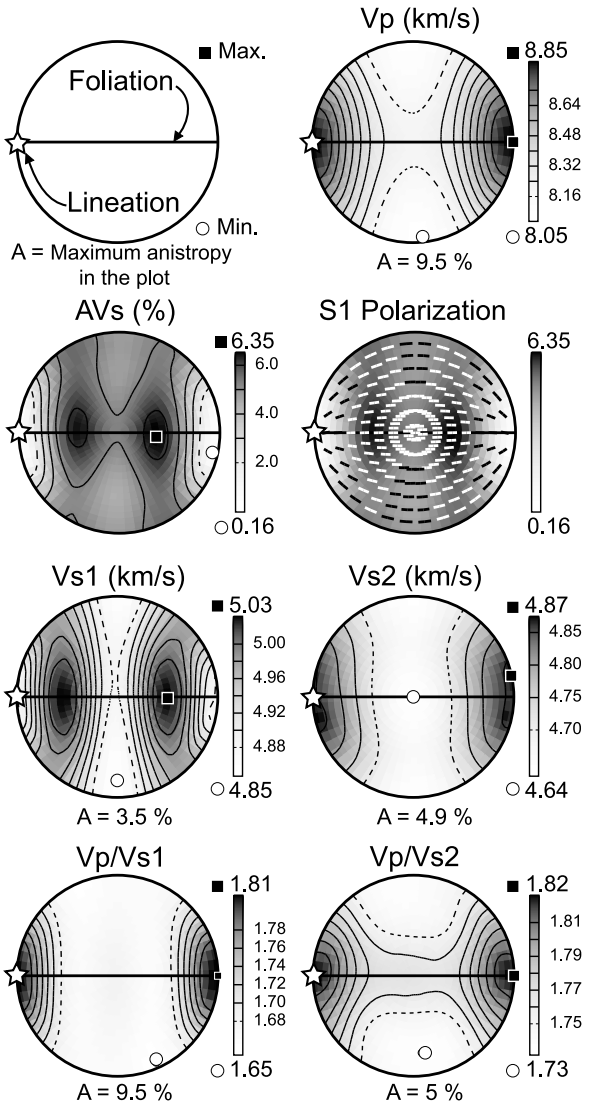

Figure 1. Seismic properties of an average sample obtained by summation of the CPO of 23 peridotite xenoliths. From left to right and top to bottom, schematic representation of the foliation/lineation reference frame used in this study, variation as a function of the propagation direction of the compressive waves velocities (Vp in km/s), of the intensity of the shear wave polarization anisotropy (AVs = 200* $(Vs_1 - Vs_2)/(Vs_1 + Vs_2)$ in %), of the polarization of the fast shear wave S_1 (grey scale represents the intensity of AVs, as in the previous plot), of the two quasi-shear waves (Vs_1 and Vs_2) velocities, and of the Vp/Vs_1 and Vp/Vs_2 ratios. Equal area, lower hemisphere stereographic projections.

centrate in lenses parallel to the foliation. Based on the analysis of the microstructures, *Soustelle et al.* [2010] proposed that orthopyroxene enrichment resulted from syn- to late kinematic reactive percolation of a Si-rich melt/fluid leading to orthopyroxene crystallization at the expense of olivine.

[8] Olivine CPO obtained by electron backscattered diffraction (EBSD) [*Soustelle et al.*, 2010] show well-developed axial-[100] patterns characterized by alignment of [100] parallel to the lineation, and girdle distributions of [010] and [001] normal to it, pointing to dominant [100] slip on multiple {0kl} planes, mainly (010) and (001). Activation of [100] slip on multiple planes is consistent with the maximum water contents in olivine (13–28 wt ppm H_2O) estimated from IR spectroscopy measurements [*Soustelle et al.*, 2010] and with deformation at moderate pressures, in the spinel stability field [*Mainprice et al.*, 2005]. The highly variable orthopyroxene CPO, which may either be correlated or not with the olivine CPO, and the decrease of the intensity of the olivine CPO in opx-rich samples corroborate the syn- to late kinematic character of the reactive fluid transport [*Soustelle et al.*, 2010].

3. Seismic Properties

[9] The three-dimensional distributions of seismic velocities have been computed by averaging the individual grain elastic constants tensor as a function of the crystallographic orientation given by the EBSD measurements and modal composition [*Mainprice and Humbert*, 1994]. We used Voigt-Reuss-Hill averaging and single-crystal elastic constants tensors of olivine and orthopyroxene at ambient conditions [*Duffy and Vaughan*, 1988; *Abramson et al.*, 1997].

[10] As seismic waves sample the anisotropy at length scales ranging from a few to a thousand of kilometers, we calculate seismic properties for an average harzburgite sample obtained by summation of the CPO of the 23 individual samples. For summation, all individual CPO were rotated as to have the lineation and the pole of the foliation in the E-W and N-S directions, respectively. 3D-seismic properties of the average sample (Figure 1) are very similar to those of individual xenoliths (not shown here). P- and S_2-waves propagation is fastest parallel to the lineation and slowest in the plane normal to the lineation. S_1-wave velocity is minimum for propagation directions both parallel and normal to the lineation and maximum at ~45° to the lineation in the foliation plane. S-wave splitting is minimum for waves propagating at low angle to the lineation and highest for waves propagating at high angles (≥30°) to the lineation in the foliation plane. S-waves propagating normal to the foliation also sample a high birefringence direction. For all propagation directions, the fast S-wave is polarized parallel to the lineation. This anisotropy pattern is typical of peridotites which olivine CPO has an orthorhombic or axial [100] symmetry [*Tommasi et al.*, 2004; *Vauchez et al.*, 2005]. It is also in good agreement with the seismic properties calculated for another Avacha volcano xenolith collection by *Michibayashi et al.* [2009]. Moreover, Vp/Vs_1 and Vp/Vs_2 ratios are minimum for propagation directions at high angle (>30°) to the lineation and the foliation, respectively. Both ratios are maximum parallel to the lineation.

[11] In Avacha xenoliths, syn- to late kinematic reactive percolation resulted in crystallization of orthopyroxene at the expense of olivine. To quantify the effect of this process, we analyze the evolution of the P-wave azimuthal anisotropy and S-wave polarization anisotropy (splitting) as a function of the orthopyroxene modal content in the studied samples (Figure 2). Two groups may be discriminated: (1) Harzburgites with "normal" opx contents (<21%) display P-wave anisotropy and S-waves splitting maxima ranging from 14 to 10% and 9.5 to 6%, respectively. (2) Harzburgites enriched in opx (>21%) show lower and less variable

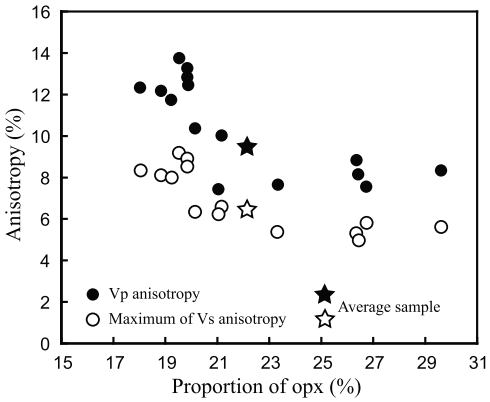

Figure 2. P- and maximum S-wave anisotropy as a function of the orthopyroxene content in 15 Avacha peridotite xenoliths for which the modal composition has been accurately determined.

P-wave anisotropy and S-waves splitting maxima of 6.5−9% and 5.5−6.5%, respectively.

4. Discussion

4.1. Seismic Anisotropy and Flow Directions in the Mantle Wedge Beneath Kamchatka

[12] The determination of the dominant deformation mechanisms in olivine is fundamental to deduce flow patterns in the mantle from S-waves anisotropy data. Through the analysis of the CPO and microstructures of the Avacha xenoliths, *Soustelle et al.* [2010] showed that even if the samples were percolated by hydrous melts/fluids, olivine had moderate water contents and deformed essentially by [100] slip assisted by diffusional processes. The resulting axial [100] olivine CPO patterns in the Kamchatka peridotite xenoliths imply that for all propagation directions the fast S-wave is polarized parallel to the lineation or the flow direction (Figure 1). The presence of hydrous melts or fluids has therefore no impact on the fast S-waves polarization directions in the shallow mantle wedge and S-waves splitting data can be used to map the horizontal component of the mantle flow. The present study thus corroborates the interpretation of *Levin et al.* [2004] that ascribed the trench-normal fast polarizations beneath the southern part of the Kamchatka arc to a local corner flow. The corner flow probably does not extend inland beyond the arc, since stations in the back-arc domain show trench-parallel fast polarizations.

4.2. Effect of Reactive Melt/Fluid Percolation on Seismic Anisotropy

[13] Syn-deformation reactive melt/fluid percolation lead to orthopyroxene enrichment, dispersion of the olivine CPO, and decrease in seismic anisotropy in 1/3 of the Avacha xenoliths (Figure 2). The average S-wave anisotropy maximum in "normal" harzburgites is 8%, whereas the average over the entire suite, including the opx-enriched harzburgites, is 6.35%. Reactive transport of hydrous fluids or melts during mantle deformation may thus decrease anisotropy by up to 20%. Splitting measurements in southern Kamchatka using local shear waves yield delay times between 0 and 1.5 s with a peak at 0.5 s [*Levin et al.*, 2004]. If we assume that the "normal" harzburgites represent the typical upper mantle wedge, delay times of 0.5, 1, and 1.5 s for a mean Vs = 4.5 km.s^{-1} are produced by 28, 56, and 84 km long paths along the foliation at high angle to the lineation (other propagation directions relative to the structural reference frame sample lower intrinsic anisotropies and require thicker anisotropic layers to produce the same delay times, cf. Figure 1). Minimum anisotropic paths needed to produce the same delay times are however 35, 71, and 106 km long if the average sample birefringence is considered. Thus if large volumes of the wedge mantle were modified by reactive fluid percolation leading to an anisotropy decrease similar to the one observed in the Kamchatka orthopyroxene-rich harzburgites, 26% longer anisotropic paths or an additional contribution from the slab or the crust of the upper plate are required to produce the observed delay times.

4.3. Significance of Low Vp/Vs Ratios in the Mantle Wedge

[14] Vp/Vs ratios mapped by seismic tomography models in subduction zones are highly variable, ranging from 1.6 to 1.95 [*Zhang et al.*, 2004; *Wagner et al.*, 2005]. The average Vp/Vs in the shallow upper mantle is 1.73–1.75. High Vp/Vs (>1.8) are characteristic of processes leading to a stronger decrease in S-waves velocities relatively to P-waves; they are traditionally interpreted as recording the presence of melts, fluids [*Takei*, 2002], or serpentine [*Christensen*, 1996] in the mantle wedge.

[15] The processes producing low Vp/Vs ratios (<1.7) in subduction zones are, in contrast, poorly constrained. Such low Vp/Vs ratios are nevertheless observed in tens of km wide domains in the fore-arc mantle from Japan, Andes and Alaska subduction zones [*Zhang et al.*, 2004; *Rossi et al.*, 2006; *Wagner et al.*, 2006]. Different models were proposed to explain these observations, like the presence of quartz [*Rossi et al.*, 2006; *Wagner et al.*, 2006] or orthopyroxene enrichment [*Zhang et al.*, 2004; *Wagner et al.*, 2006].

[16] Based on the analysis of the microstructures and modal compositions of the Avacha xenoliths, *Soustelle et al.* [2010] proposed that reactive percolation leads to local enrichment in orthopyroxene in the mantle wedge. To quantify if the observed orthopyroxene enrichment may account for the observed low Vp/Vs ratios, we calculated the Vp/Vs ratios for the Avacha peridotites. Because body-wave tomographic models, from which Vp/Vs ratios are extracted, usually neglect seismic anisotropy, we first calculated the seismic properties of isotropic aggregates with the same modal composition as the studied samples. S-wave velocities are almost insensitive to the orthopyroxene enrichment, whereas P-waves velocities strongly decrease with increasing orthopyroxene contents, leading to a decrease of the Vp/Vs ratio (Figure 3a). The variation in Vp/Vs ratio produced by an orthopyroxene enrichment similar to the one observed in the Avacha peridotite xenoliths is similar to the one induced by an increase in pressure by 1 GPa or a decrease in temperature by ~300°C (Figure 3b). The minimum Vp/Vs ratio obtained for the most opx-enriched composition sampled by the Avacha peridotites (30% opx) is 1.72. This ratio is higher than those observed in tens of km wide domains of the fore-arc mantle from the Japan and Andes subduction zones (1.65–1.7 [*Zhang et al.*, 2004; *Wagner et al.*, 2006]). To explain these ratios, large areas of

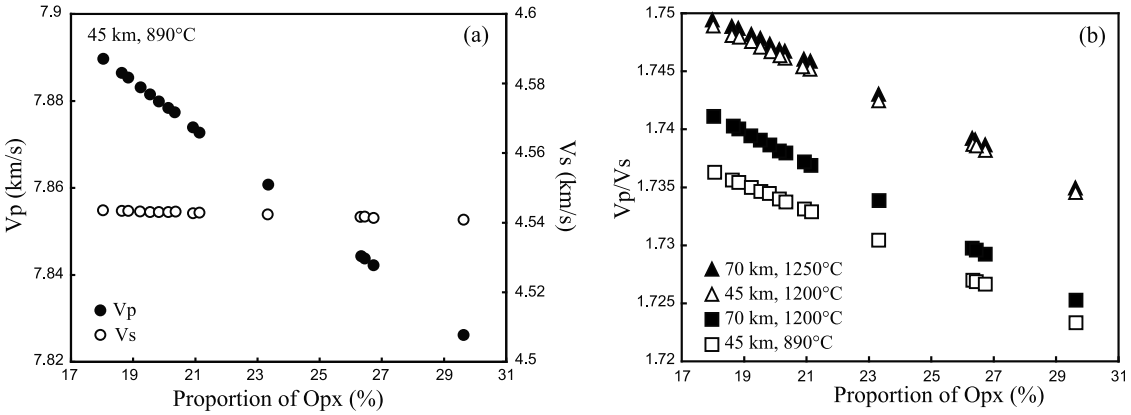

Figure 3. (a) P- and S-waves velocities, and (b) Vp/Vs ratios for different depths and temperatures in an isotropic harzburgite (random olivine CPO) with variable orthopyroxene modal contents.

the mantle wedge should have an orthopyroxenite composition (>90% opx), which is unrealistic. Indeed, orthopyroxenites are only observed as thin dykes, a few cm to tens of cm wide, in both xenoliths and peridotite massifs [e.g., *Tommasi et al.*, 2006; *Soustelle et al.*, 2010].

[17] Low Vp/Vs ratios in the upper mantle way however be understood by considering the anisotropy of seismic properties of deformed peridotites. The average Avacha peridotite sample displays indeed a strong variation of the Vp/Vs_1 and Vp/Vs_2 ratios as a function of the propagation direction: the Vp/Vs_1 ratio is <1.7 for all propagation directions at angles >30° to the lineation (Figure 1).

[18] How are "isotropic" Vp/Vs ratios measured in an anisotropic mantle? Vp/Vs ratios are determined by picking the first S-wave arrival on the transverse component [e.g., *Wagner et al.*, 2005], which usually corresponds to the S1 wave. Only in the special case where the initial polarization, which depends essentially on the focal mechanism, is along the S2 direction there will be no energy in the S1 direction. Deformation in mantle wedge is usually defined as a combination of corner and trench-parallel flow, resulting from entrainment by the downgoing slab and geometrical complexities of the plates' boundary geometry or oblique convergence, respectively. The latter induces horizontal lineations in the fore-arc mantle, whereas corner-flow produces lineations that range between horizontal and shallow to steeply-deeping depending on the proximity to the slab and on the slab dip. This implies that most seismic rays produced by local earthquakes cross the mantle wedge at high angle to the lineation [*Kneller and van Keken*, 2008]. Thus, the measured "isotropic" Vp/Vs ratio is most often the Vp/Vs_1 ratio, which is <1.7 in all domains of the mantle wedge with a horizontal to shallowly-deeping lineation, unless fluids, melts or serpentinization are present.

5. Conclusion

[19] Peridotite xenoliths sampling the sub-arc mantle in the Kamchatka subduction zone show high-temperature, low-stress deformation microstructures and axial [100] olivine CPO, pointing to deformation by dislocation creep with dominant activation of [100] glide, consistent with the measured moderate water contents in olivine. Thus if anisotropy in the mantle wedge results essentially from olivine deformation, the fast S-waves polarization will be parallel to the flow direction. Synkinematic porous flow of melts or fluids may favor diffusion leading to weaker olivine CPO and locally lower the anisotropy.

[20] More important, reactive percolation of Si-rich fluids or hydrous melts in the wedge results in crystallization of orthopyroxene at the expenses of olivine. Opx-enrichment induces a limited decrease in the Vp/Vs ratio, but cannot explain the Vp/Vs ratios <1.7 observed in many subduction wedges. The latter may nevertheless be accounted for by considering the intrinsic anisotropy of deformed peridotites.

[21] **Acknowledgments.** V.S. and A.T. thank D. Mainprice for providing softwares for calculating seismic properties of anisotropic rocks, C. Tiberi for discussions on measurements of Vp/Vs ratios, Martha Savage and an anonymous referee for their constructive reviews. This study was partially funded by the program SEDIT of the Institut National des Sciences de l'Univers (INSU-CNRS), France, in the frame of the project "Deformation in the supra-subduction mantle" coordinated by A.T. V.S. benefited from a PhD scholarship from the Ministere de la Recherche et de l'Enseignement Superieur, France.

References

Abramson, E. H., J. M. Brown, L. J. Slutsky, and J. Zaug (1997), The elastic constants of San Carlos olivine to 17 GPa, *J. Geophys. Res.*, *102*, 12,253–12,263, doi:10.1029/97JB00682.

Boudier, F., A. Baronnet, and D. Mainprice (2010), Serpentine mineral replacements of natural olivine and their seismic implications: Oceanic lizardite versus subduction-related antigorite, *J. Petrol.*, *51*, 495–512, doi:10.1093/petrology/egp049.

Christensen, S. I. (1996), Poisson's ratio and crustal seismology, *J. Geophys. Res.*, *101*, 3139–3156, doi:10.1029/95JB03446.

Duffy, T. S., and M. T. Vaughan (1988), Elasticity of enstatite and its relationships to crystal structure, *J. Geophys. Res.*, *93*, 383–391, doi:10.1029/JB093iB01p00383.

Faccenda, M., L. Burlini, and D. Mainprice (2008), Fault-induced seismic anisotropy by hydration in subduction oceanic plates, *Nature*, *455*, 1097–1100, doi:10.1038/nature07376.

Gorbatov, A., V. Kostoglodov, G. Suárez, and E. Gordeev (1997), Seismicity and structure of the Kamchatka subduction zone, *J. Geophys. Res.*, *102*, 17,883–17,898, doi:10.1029/96JB03491.

Gorbatov, A., J. Dominguez, G. Suarez, V. Kostoglodov, D. Zhao, and E. Gordeev (1999), Tomographic imaging of the P-wave velocity structure beneath the Kamchatka peninsula, *Geophys. J. Int.*, *137*, 269–279, doi:10.1046/j.1365-246X.1999.00801.x.

Holtzman, B. K., D. L. Kohlstedt, M. E. Zimmerman, F. Heidelbach, T. Hiraga, and J. Hustoft (2003), Melt segregation and strain partitioning: Implications for seismic anisotropy and mantle flow, Science, 301, 1227–1230, doi:10.1126/science.1087132.

Ionov, D. A. (2010), Petrology of mantle wedge lithosphere: New data on supra-subduction zone peridotite xenoliths from the andesitic Avacha volcano, Kamchatka, *J. Petrol.*, *51*, 327–361, doi:10.1093/petrology/egp090.

Jung, H., and S. Karato (2001), Water-induced fabric transitions in olivine, *Science*, *293*, 1460–1463, doi:10.1126/science.1062235.

Kneller, E. A., and P. E. van Keken (2008), The effects of three-dimensional slab geometry on deformation in the mantle wedge: Implications for shear wave anisotropy, *Geochem. Geophys. Geosyst.*, *9*, Q01003, doi:10.1029/2007GC001677.

Levin, V., J. Park, M. Brandon, J. Lees, V. Peyton, E. Gordeev, and A. Ozerov (2002), Crust and upper mantle of Kamchatka from teleseismic receiver functions, *Tectonophysics*, *358*, 233–265, doi:10.1016/S0040-1951(02)00426-2.

Levin, V., D. Droznin, J. Park, and E. Gordeev (2004), Detailed mapping of seismic anisotropy with local shear waves in southeastern Kamchatka, *Geophys. J. Int.*, *158*, 1009–1023, doi:10.1111/j.1365-246X.2004.02352.x.

Mainprice, D., and M. Humbert (1994), Methods of calculating petrophysical properties from lattice preferred orientation data, *Surv. Geophys.*, *15*, 575–592, doi:10.1007/BF00690175.

Mainprice, D., A. Tommasi, H. Couvy, P. Cordier, and D. J. Frost (2005), Pressure sensitivity of olivine slip systems and seismic anisotropy of Earth's upper mantle, *Nature*, *433*, 731–733, doi:10.1038/nature03266.

Michibayashi, K., T. Oohara, T. Satsukawa, S. Ishimaru, S. Arai, and V. Okrugin (2009), Rock seismic anisotropy of the low-velocity zone beneath the volcanic front in the mantle wedge, *Geophys. Res. Lett.*, *36*, L12305, doi:10.1029/2009GL038527.

Nakajima, J., and A. Hasegawa (2004), Shear-wave polarization anisotropy and subduction-induced flow in the mantle wedge of northeastern Japan, *Earth Planet. Sci. Lett.*, *225*, 365–377, doi:10.1016/j.epsl.2004.06.011.

Rossi, G., G. A. Abers, S. Rondenay, and D. H. Christensen (2006), Unusual mantle Poisson's ratio, subduction, and crustal structure in central Alaska, *J. Geophys. Res.*, *111*, B09311, doi:10.1029/2005JB003956.

Soustelle, V., A. Tommasi, S. Demouchy, and D. A. Ionov (2010), Deformation and fluid-rock interaction in the supra-subduction mantle: Microstructures and water contents in peridotite xenoliths from the Avacha Volcano, Kamchatka, *J. Petrol.*, *51*, 363–394, doi:10.1093/petrology/egp085.

Takei, Y. (2002), Effect of pore geometry on V_P/V_S: From equilibrium geometry to crack, *J. Geophys. Res.*, *107*(B2), 2043, doi:10.1029/2001JB000522.

Tommasi, A., M. Godard, G. Coromina, J. M. Dautria, and H. Barsczus (2004), Seismic anisotropy and compositionally induced velocity anomalies in the lithosphere above mantle plumes: A petrological and microstructural study of mantle xenoliths from French Polynesia, *Earth Planet. Sci. Lett.*, *227*, 539–556, doi:10.1016/j.epsl.2004.09.019.

Tommasi, A., A. Vauchez, M. Godard, and F. Belley (2006), Deformation and melt transport in a highly depleted peridotite massif from the Canadian Cordillera: Implications to seismic anisotropy above subduction zones, *Earth Planet. Sci. Lett.*, *252*, 245–259, doi:10.1016/j.epsl.2006.09.042.

Vauchez, A., F. Dineur, and R. Rudnick (2005), Microstructure, texture and seismic anisotropy of the lithospheric mantle above a mantle plume: Insights from the Labait volcano xenoliths (Tanzania), *Earth Planet. Sci. Lett.*, *232*, 295–314, doi:10.1016/j.epsl.2005.01.024.

Wagner, L. S., S. Beck, and G. Zandt (2005), Upper mantle structure in the south central Chilean subduction zone (30° to 36°S), *J. Geophys. Res.*, *110*, B01308, doi:10.1029/2004JB003238.

Wagner, L. S., S. Beck, G. Zandt, and M. N. Ducea (2006), Depleted lithosphere, cold, trapped asthenosphere, and frozen melt puddles above the flat slab in central Chile and Argentina, *Earth Planet. Sci. Lett.*, *245*, 289–301, doi:10.1016/j.epsl.2006.02.014.

Zhang, H., C. H. Thurber, D. Shelly, S. Ide, G. C. Beroza, and A. Hasegawa (2004), High-resolution subducting-slab structure beneath northern Honshu, Japan, revealed by double-difference tomography, *Geology*, *32*, 361–364, doi:10.1130/G20261.2.

V. Soustelle and A. Tommasi, Géosciences Montpellier, Université Montpellier II, CNRS, CC 60, Place E. Bataillon, F-34095 Montpellier CEDEX 5, France. (vsoustel@gm.univ-montp2.fr)

Chapitre 4

Effets des interactions fluides-roche sur la déformation et les propriétés sismiques du coin mantellique : exemple de la subduction de Papouasie-Nouvelle-Guinée

Ce chapitre présente une étude pétrostructurale sur 8 xénolites de manteau extraites de la lithosphère océanique par deux volcans sous-marin (TUBAF et EDISON) situés près de l'ile de Lihir dans l'archipel de Bismarsk au NE de la Papouasie-Nouvelle-Guinée. Le volcanisme à l'origine de ces deux monts sous-marins à débuté il y a environ 3,6 Ma; il résulte de la tectonique extensive affectant la région (McInnes, 1992; Rytuba et al., 1993). Cependant, ces deux volcans se situent au-dessus d'une ancienne subduction où la plaque Pacifique plongeait sous la microplaque Bismarck. Cette subduction s'est arrêtée il y a 15 Ma lors de la collision du plateau océanique de Ontong-Java avec la fosse Manus-Kilinailau (Coleman & Kroenke, 1981). Les xénolites de manteau supérieur extraites par les volcans TUBAF et EDISON permettent donc d'étudier les processus d'interaction entre déformation et percolation de fluide, ainsi que leur effets sur les propriétés sismiques du coin mantellique de la subduction de Papouasie-Nouvelle-Guinée.

Ce chapitre est constitué d'un article en phase finale de préparation qui sera soumis à *Tectonophysics.* Ce travail se base sur les observations microstructurales, les mesures d'OPR et de teneurs en eau des minéraux de ces péridotites ainsi que le calcul des propriétés sismiques de ces xénolites de manteau. L'étude des textures des différentes phase minérales et des microstructures de déformation suggère que ces échantillons ont subi une déformation de

haute température, basse contrainte, probablement dans le coin mantellique alors que la subduction était encore active. Cet événement fut synchrone à la percolation d'un fluide riche en SiO_2 et en Ca qui a entrainé la précipitation d'orthopyroxène et, en moindre mesure, de clinopyroxène au dépens de l'olivine. Les OPR de l'olivine sont cohérentes avec cette déformation de haute température, basse contrainte. En effet, leur analyse montre que le système de glissement dominant est {0kl}[100]. Ce type d'OPR implique que la direction rapide de polarisation des ondes S est parallèle à la linéation et donc parallèle à la direction de fluage du manteau. Ces échantillons montrent aussi une anti-corrélation entre intensité de l'OPR de l'olivine et la proportion modale de pyroxène. Ce qui signifie que, comme pour les xénolites de l'Avacha, Kamchatka (cf. chapitre 4.1 et Soustelle et al., 2010), la percolation réactive syn-cinématique de fluides provoque une dispersion de l'OPR de l'olivine sans pour autant affecter les systèmes de glissement. Les échantillons étudiés ont des rapports Vp/Vs quasiment identiques à ceux des xénolites de péridotite de l'Avacha (cf. chapitre 4.2 et Soustelle & Tommasi, 2010), ce qui tend à confirmer l'hypothèse faite au chapitre 4.2 que les faibles rapports Vp/Vs (<1,7) observés dans certains domaines d'avant-arc pourraient être expliqués simplement par l'anisotropie intrinsèque du manteau en supra-subduction.

Postérieurement à l'événement de déformation de haute température basse contrainte, les échantillons étudiés ont subit un métasomatisme en conditions statiques alors que les échantillons étaient dans la lithosphère. Cet épisode a entrainé la formation d'orthopyroxène fibreux et de veines composées de pyroxène, d'amphibole et de phlogopite sécantes sur les minéraux préexistants et leurs microstructures.

Les analyses par spectroscopie infrarouge à transformée de Fourrier montrent que les olivines contiennent de 1 à 4 ppm en poids d'H_2O. Ces concentrations d'eau sont similaires à celles observées dans d'autres xénolites de péridotites à spinelle de zones de subduction (e.g., Demouchy, 2004; Peslier & Luhr, 2006; Falus et al., 2008; Soustelle et al., 2010). Elles résultent de la faible solubilité d'H_2O dans l'olivine dans les conditions oxydantes et de basse pression du coin mantellique (cf. chapitre 4.1 et (Soustelle et al., 2010). Il est aussi possible que les olivines aient été déshydratées durant l'exhumation vers la surface des xénolites (Demouchy et al., 2006). Les orthopyroxènes et clinopyroxènes ont des concentrations en eau très hétérogènes (respectivement 39-431 et 77-382 ppm en poids d'H_2O) qui pourraient résulter des interactions spatialement hétérogènes avec les fluides, ainsi que d'un déséquilibre compositionnel.

Comme montré dans le chapitre précédent et contrairement aux études expérimentales, les interactions entre percolation de fluides et déformation dans le manteau au dessus d'une

subduction n'ont pas provoqué de changement de direction de glissement dominante dans l'olivine. Ces directions n'évoluent pas de [100] à [001] en fonction de la présence de fluide/magma.

Effect of fluid-rock interactions on deformation and seismic properties of the oceanic sub-arc mantle: Microstructural study of mantle xenoliths from seamounts near Lihir Island, Papua-New-Guinea.

Vincent Soustelle*[1], Andrea Tommasi [1], Sylvie Demouchy and Leander Franz [2]

[1] Géosciences Montpellier, Université Montpellier II & CNRS, CC60, Place E. Bataillon, 34095 Montpellier cedex 5, France.

[2] Mineralogisch-Petrographisches Institut, Universität Basel, Bernoullistrasse 30, 4056 Basel, Switzerland.

* Corresponding author: vsoustel@gm.univ-montp2.fr

INTRODUCTION

Seismic anisotropy and tomography are important tools to investigate the thermal structures, flow pattern, and fluid or melt distribution in subduction zones. They strongly depend on the intrinsic physical properties of the mantle wedge rocks. For example, the seismic anisotropy in the upper mantle results primarily from the orientation of olivine crystals, and the density of the peridotites is affected by mineralogical changes. The supra-subduction mantle is the site of a series of petrological processes, ranging from dehydration of subducted slab to partial melting and metasomatism in the wedge. All of them may affect the mineralogical composition of the rock, the mantle rheology and the mantle flow pattern, and the deformation mechanism. Indeed, the presence of small melt fractions and/or water in olivine strongly reduces the strength of mantle rocks (Blacic, 1972; Hirth and Kohlstedt, 1995a; Hirth and Kohlstedt, 1995b; Karato et al., 1986; Mackwell et al., 1985; Mei et al., 2002; Mei and Kohlstedt, 2000a; Mei and Kohlstedt, 2000b; Zimmerman and Kohlstedt, 2004), and may modify the mechanisms of plastic deformation in olivine and then the relation between seismic anisotropy and mantle flow (Holtzman et al., 2003b; Jung and Karato, 2001). Recent studies have also highlighted the role of interactions between deformation and reactive melt percolation in the upper mantle (Le Roux et al., 2008;; Soustelle et al., 2009; Soustelle et al., 2010; Soustelle and Tommasi, 2010), which lead to mineralogical change such as pyroxene enrichment, to the decrease of crystal preferred orientation (CPO) intensity of olivine, and finally to a reduction of the mantle rocks intrinsic anisotropy.

The actual fluid or melt content and distribution in the mantle wedge above a subduction zone and their effect on deformation are, nevertheless, still poorly constrained. Direct samples from mantle wedge are generally extracted by subduction-related calc-alkaline volcanism, but these samples are extremely rare. Moreover, most of the previous studies on subduction zone mantle xenoliths have focused on geochemical and petrological processes (e.g., Arai and Kida, 2000; Bénard and Ionov, 2009; Grégoire et al., 2001; Ionov, 2010; Ionov and Seitz, 2008; Ishimaru et al., 2007; McInnes et al., 2001) rather than on their deformation history and the implications for seismic properties of the mantle wedge. At the present time, three studies give information on this topic (Michibayashi et al., 2009; Soustelle and Tommasi, 2010b; Soustelle et al., 2010a), but they are all focused on mantle xenoliths from the Avacha volcano, in southern Kamchatka subduction zone. Here, we present a detailed microstructural studies, as well as measurement of olivine, orthopyroxene and clinopyroxene CPO and water contents on 8 mantle xenoliths sampled from two seamounts near the Lihir Island above a stalled Tertiary subduction zone in the Bismarck Archipelago, NE of Papua-

New-Guinea. We also computed seismic properties of these mantle xenoliths. These data are used to investigate the relationship between deformation, fluids and melt percolation, and hydration in the sub-arc mantle wedge in order to understand how they impact the observed seismic data.

GEOLOGICAL SETTINGS

All the studied mantle xenoliths, hosted in trachybasalts, were collected from the top of two volcanoes, TUBAF (3°15.25'S, 152°32.50'E, 1280 m below sea level-BSL) and EDISON (3°19.05'S, 152°34.90'E, 1450 m BSL) seamounts, close southward to Lihir Island in the Bismarck archipelago located NE of Papua-New-Guinea (Fig. 1).

The geodynamical context involves a southwestward subduction of the Pacific plate beneath the Bismarck microplate along the Manus-Kilinailau trench, and an associated voluminous calc-alkaline arc volcanism during the Oligocene and Miocene. About 15 my ago, the subduction ceased due to a collision of the Ontong-Java plateau with the trench (Coleman and Kroenke, 1981) implying plate rotation and regional stress changes, which involved subduction reversal with the formation of the currently active NNW- to NNE-dipping New Britain trench. Today the Solomon microplate is subducted below the Bismarck microplate, where a back-arc spreading contemporaneous to this subduction occurs in the Manus basin and separates it in a North and a South Bismarck microplate (Fig. 1).

TUBAF and EDISON seamounts belong to the Tabar-Lihir-Tanga-Feni (TLTF) volcanic island chain located NE to the New Ireland Island (Fig. 1). The volcanic activity started 3.6 my ago (McInnes, 1992; Rytuba et al., 1993), and the most recent eruption on land occurred on Feni Island around 2.3 ky ago (Licence et al., 1987). The high-K calc-alkaline volcanism can be linked with lithospheric thinning of New Ireland, which is induced by the opening of the Manus back-arc basin (e.g., Taylor, 1979). McInnes & Cameron (1994) show that the melt generation was triggered by strong metasomatic influence from the Pacific plate subducted beneath the Bismarck microplate.

SYNTHESIS OF THE PREVIOUS PETROLOGICAL AND GEOCHEMICAL STUDIES

The 8 studied mantle xenoliths come from a larger collection that has been the subject of a detailed petrological and geochemical study (Franz et al., 2002), which includes petrographic description, major and trace elements whole rock analyses and mineral electron microprobe analyses. These data are summarized below.

The studied mantle rocks include two dunites (54-2A, 55-2B), three harzburgites (55-2A, 56-2A, 56-2T) and two lherzolites (54-2D, 56-2H) composed of 93-96%, 72-85% and 67-83% olivine (ol), 0%, 16-26% and 9-24% orthopyroxenes (opx), 3-5%, 1-3% and 6-15 clinopyroxenes (cpx), respectively, plus <1 to 2% of spinel (sp) and < 1% of phlogopite (phl) and amphibole (amph) in modally metasomatized samples, The peridotites often show modal metasomatism with distinct veining and may contain two types of opx and cpx, i.e. primary and the metasomatic ones. The primary opx and cpx are granular crystals, whereas the metasomatic opx and cpx are aggregates of minute needle-like and rounded crystals, respectively. Furthermore, there is one olivine clinopyroxenite (33-2A), which is crosscut by hornblende-phlogopite veins (5 mm wide).

The small modal amount of primary clinopyroxene in the peridotites illustrates the strong depletion of the lithospheric mantle of the Bismarck microplate (cf. Franz et al. 2002). A series of harzburgites xenoliths from the same location displaying similar features as our samples, have many characteristics of solid residues resulting from high degree of partial melting (Grégoire et al., 2001; McInnes et al., 2001): They have similar refractory modal compositions with the bulk rock analyses showing a depletion in Al_2O_3, CaO, Na_2O, and an enrichment in Ni and Co. Grégoire et al. (Grégoire et al., 2001) show that the degree of partial melting was likely between 15 and 25%.

Based on retrograde zoning and on exsolution lamellae of spinel in olivine, Franz & Wirth (Franz and Wirth, 2000) proved that the thermal history of the studied xenoliths possibly started a mid-ocean ridge or back-arc basin spreading centre, where the formation of the mantle lithosphere occurred by uprise of asthenospheric material. Similarly, ortho- and clinopyroxene show distinct mineral chemical zoning and exsolution lamellae typical for lithospheric cooling, which probably occurred during the transport of the mantle lithosphere away from the ridge (Franz et al. 2002).

Geothermometry on primary pyroxenes from spinel peridotites (rim composition) using the T BKN calibration of Brey and Köhler (1990) yields equilibrium temperatures of 665-860°C. Intersecting the K_D-lines of this geothermometer with the recent geothermal gradient of the region (i.e. 60 mW/m^2; cf. (Pollack and Chapman, 1977)) results in pressures of 13-18 kbar (~43-60 km), i.e. in the spinel-peridotite stability field (Franz et al., 2002). According to its peculiar mineralogy and texture, and its geochemistry, the olivine pyroxenite (sample 33-2A) is interpreted as a magmatic cumulate. A PT-estimate using a combination of the olivine-spinel geothermometer (T BBG) of Ballhaus et al. (1991) and the Ca-in-olivine

geobarometer of Köhler and Brey (1990) points to a shallow lithospheric origin at elevated temperatures (i.e. 950±30°C at 1.3 ± 4 kbar) for this sample.

Peridotite xenoliths experienced a relatively high temperature metasomatism after the lithospheric cooling in the mantle. Most peridotites are veined or show a growth of metasomatic minerals (i.e. secondary opx, cpx, spl, phl, and amph) on grain boundaries. The T BBG geothermometer of Ballhaus et al. (1991) calculates temperatures of 750-950°C for spinel and olivine in the metasomatic veins. Oxygen barometry on these veins reveals a high oxygen fugacity ($Dlog(fO_2)^{FMQ}$ values of 0.4-4.3), which is typical for metasomatism by hydrous fluids derived from the dehydrated subducted slab (Franz et al., 2002; McInnes et al., 2001). Metasomatism also occurred in a shallow lithospheric level as evident by metasomatic plagioclase-lherzolites and olivine clinopyroxenites (e.g. sample 33-2a). PT conditions for the metasomatic overprint of these samples were estimated at 680-780°C and 2-3 kbar using different thermobarometers (Franz et al., 2002).

Most of the mineralogical arguments point to a hydrous fluid phase with variable amount of dissolved alkali cations as the metasomatic agent in xenoliths with modal metasomatism (Franz et al., 2002; Gregoire et al., 2001). Remarkably, xenoliths without any visible metasomatic features also record a distinct metasomatic alteration as evident by their elevated light rare earth element (LREE) patters. This cryptic metasomatism probably also occurred in the supra-subduction zone setting during the subduction of the Pacific Plate underneath the Bismarck microplate (Franz et al., 2002).

MICROSTRUCTURAL OBSERVATIONS

Olivines in the spinel peridotite xenoliths display a coarse-grained porphyroclastic texture characterized by a mean ol grain-size of 1-1.4 mm with crystal up to 8 mm, and of 600-850 µm with larger grain up to 5 mm for the dunites and the lherzolites/harzburgites, respectively (Table 1). All these samples show high variation in grain size, indeed the standard deviation for olivine grain size is 800-1100 µm for the dunites, and 300-650 µm for the harzburgites/lherzolites. An exception concerns 54-2D, which shows a standard deviation of 325 µm for a mean olivine grain size of 607 µm (Table 1), and almost displays an equigranular texture. The mean grain size in roughly positively correlated with the proportion of pyroxene (table 1), except for the sample 56-2A which only contains ol and metasomatic fibrous opx crystals (cf. below).

These coarse porphyroclastic peridotites display lineation marked by spinel trails (Fig. 2a and b), however no mineral species show a lineation of elongation. The thin sections of the

samples 56-2T and 56-2H, which include or are at low angle to the lineation, show 0.5 to 1.5 cm wide pyroxene rich bands and olivine orthopyroxenite, respectively, roughly orientated parallel to the spinel trails (Fig. 2a and b). The 55-2A thin section is orientated normal to both the lineation and the foliation that is marked by a weak spinel alignment, which is however less well-developed when observed parallel to the lineation (Fig. 2c). In this sample, the pyroxenes are not distributed randomly, but rather concentrated in bands or lenses elongated more or less along the foliation trend. In other samples, relationships between deformation structures and pyroxenes repartition are not visible because: they are dunites (54-2A, 55-2B), olivine clinopyroxenites (33-2A), they have not enough spinel to determine a clear lineation or foliation trend (56-2A), or the thin section planes are at high angle with both the lineation and foliation (54-2D), which precludes such observations. Inside or at the vicinity of these pyroxenite bands or pyroxene-rich lenses, the olivine grain size is finer (≤ 0.3 mm, Fig. 2d) than in pyroxene-poor part of the sample. In dunites, harzburgites and lherzolites, both coarse- and fine-grained olivine crystals have curvilinear grain boundaries that locally evolve into more polygonal shape, forming 120° triple junction (Fig. 2e). The coarse-grained olivine crystals display wavy extinction, most of them show one family of widely spaced subgrain boundaries (0.2-0.5 mm, Fig. 2d), and few olivine crystals display a second family parallel to the first one and characterized by a narrow spacing (~50 μ m). The fine-grained olivine crystals are generally free of deformation microstructures, but rare ones display microstructures similar to those of the coarse-grained types. Many of these fine-grained olivine crystals in or at the vicinity of the pyroxene-rich bands and lenses are isolated from each other by pyroxenes, and often show similar orientation and deformation features with their neighbours. Similar textures are observed in harzburgite xenoliths from the Avacha volcano in Kamchatka, where Soustelle et al. (2010) demonstrated these fine-grained olivine crystals were generally part of the same coarse crystal partially replaced by opx.

The coarse porphyroclastic peridotites display three types of orthopyroxenes and clinopyroxenes:

(1) The first type (referred to as primary opx or cpx subsequently), described as primary pyroxenes by Franz et al. (2002), are coarse crystals (> 0.5 mm) displaying a turbid aspect as the resulting from a large amount of minute inclusions (Fig. 3a). Orthopyroxene bears clinopyroxene exsolutions while clinopyroxene yields orthopyroxene exsolutions; furthermore, both pyroxenes contain minor spinel exsolutions (Franz et al., 2002). In their central part, they often show deformation microstructures such as wavy extinction (Fig. 3a) and kink-bands (for the opx only, Fig. 3b). Remote from the pyroxene rich

lenses, the cpx mainly occurs as small corroded crystals displaying a lot of exsolution lamellae (Fig 3c). Both isolated grains and aggregates have irregular shapes indenting and/or enclosing olivine crystals. Within an aggregate, pyroxenes may sometimes display straight grain boundaries and tend to form 120° triple junction.

(2) Within or at the vicinity of the pyroxene-rich bands and lenses occurs small (< 0.5 mm) opx and rare cpx (referred to as secondary opx or cpx subsequently), which display interstitial shapes; they indeed occur at grain boundaries and/or at triple junction and generally corrode the neighbouring olivines and primary opx (Fig. 3b & d). They have clear aspect and are free of deformation features and exsolutions.

(3) The third type (referred to as tertiary opx or cpx subsequently) corresponds to the secondary metasomatic orthopyroxenes and recrystallized clinopyroxenes of Franz et al. (2002). They are formed by aggregates of fine-grained prismatic (< 200 µm) to acicular (< 50µm wide and <200 µm long) grains. The tertiary pyroxenes occur in metasomatic opx veins (Fig. 3e) and cpx-ol-phlogopite (Fig. 3f) veins (Franz et al., 2002), which crosscut all the minerals and their microstructures and sometimes form a connected network. When these veins crosscut a primary or secondary opx or cpx, they often tend to loose their vein-like structures forming diffuse reaction zones characterized by the recrystallization of the primary and secondary pyroxenes to tertiary ortho- or clinopyroxene. In pyroxene-rich area of the studied lherzolites and harzburgites, the mineralogical assemblages forming the metasomatic veins may occur as thin films along grain boundaries corroding the surrounding crystals. All these observations clearly show that the metasomatic event, which is responsible for the formation of the tertiary pyroxenes, took place after the deformation event that affect the coarse olivine and the primary pyroxene and also after the crystallization of the secondary ortho- and clinopyroxene.

The olivine clinopyroxenite sample (33-2A) is mainly composed of primary cpx that display a large range of grain size with a mean value of 680 µm and a standard deviation of 530 µm, and the biggest crystal is 4120 µm long (Tab. 1). Numerous lamellae of hornblende and spinel are found in primary clinopyroxene. Olivine occurs only as small grains (mean size of 450 µm) with interstitial shape, and most of them are free of deformation microstructures. Two linear millimetre-scale phlogopite-hornblende veins crosscut this sample. They are characterized by equigranular (~500 µm) strain-free crystals with irregular shapes.

CRYSTAL PREFERRED ORIENTATION

Analytical procedure

Minerals crystal preferred orientations (CPO) were determined by indexation of electron-backscattered diffraction patterns (EBSD) at the SEM-EBSD facility at Geosciences Montpellier. EBSD patterns are generated by interaction of a vertical incident electron beam with a carefully polished thin section tilted at 70° in a scanning electron microscope JEOL JSM 5600. The diffraction pattern is projected onto a phosphor screen and recorded by a digital CCD camera. The image is then processed and indexed in terms of crystal orientation using the CHANNEL5 software from Oxford Instruments HKL.

For each sample, we obtained crystallographic orientation maps covering almost entirely the thin section (usually 35mm long and 20 mm wide) with sampling steps of 100, 75, or 50 µm, depending on the grain size. Indexation rates in the raw maps range from 50 to 80 %. In general, indexation rates are lower for the pyroxenes than for olivine. Tertiary pyroxenes, due to the fine-grain size of the individual crystals composing the aggregates, are poorly indexed. Very low indexation rates were also obtained in the metasomatic veins.

Post-acquisition data treatment allowed to further increase the indexation rate by (i) filling the non-indexed pixels that have up to 8 identical neighbours with this orientation, (ii) repeating this operation using respectively 7, 6, and 5 identical neighbours, (iii) identifying the grains, i.e., continuous domains characterized by an internal misorientation <10°, and (iv) within each olivine crystal, searching and correcting for systematic indexation errors due to the olivine hexagonal pseudo-symmetry, which results in similar diffraction patterns for orientations differing by a rotation of 60° around [100]. At each step, the operator verified the resulting orientation maps to avoid over-extrapolation of the data.

Because of the xenoliths size and geometry, the thin-sections are not systematically parallel to the lineation and normal to the foliation, but all CPO were rotated to have the maximum concentrations of olivine [100] and [010] axes parallel to the E-W and N-S directions, respectively. This allows a straightforward comparison between the different samples CPO as well as to the other studies. In order to avoid overrepresentation of large crystals, CPO are plotted as one measurement per grain (average orientation of the crystal).

Results

The studied mantle xenoliths display strong to medium olivine CPO (Fig. 4). The samples 55-2B, 54-2A, 55-2A, 54-2D and 56-2H show well-developed axial [100] patterns characterized by a strong point concentration of the [100] axes. [010] and [001] axes display a girdle distribution normal to the [100] maximum, with the two maxima roughly normal to

each other. The [010] maximum is usually stronger than the [001] ones. The samples 56-2A, 56-2T and 33-2A display an orthorhombic olivine CPO pattern characterized by strong point concentration of the three axes. The concentration of the [100] axes is stronger than the one of the [010] axes, and the [001] axes are rather dispersed. All of them show a maximum concentration normal to each other. When observed, for the both kind of pattern, the mineral lineation is always sub-parallel to the maximum concentration of the [100] axes.

In this study, the J-index is used to quantify the CPO strength (see, Soustelle et al., 2010, for explanation and details). It is the volume-averaged integral of the squared orientation densities (Bunge, 1982). It has a value of unity for a random CPO and tends to infinity for single crystal, but most of natural peridotites show J-index values between 2 and 20 with a peak around 8 (Ben Ismail and Mainprice, 1998; Tommasi et al., 2000). In the studied peridotites the J-index ranges from around 3.25 to 10.2. The J-index is the lowest in the olivine clinopyroxenite 33-2A, between 3.3 and 4.2 in the lherzolites and harzburgites, around 8 for the harzburgite 56-2A displaying similar textures as the dunites 55-2B and 54-2A, and 9.25 and 10.2 for the both dunites. The J-index linearly decreases with the increasing proportion of opx and cpx up to 25% and then there is a plateau between J index value of 3 and 4 (Fig. 5). This implies that its evolution is also correlated with the olivine grain size decrease, which is negatively correlated with the pyroxene modal proportion (Tab. 1). This correlation is rather close to what was observed in peridotite xenoliths from the Avacha volcano, Kamchatka (Soustelle et al., 2010). However, the Avacha xenoliths do not display a linear correlation but two families of samples, one poor in pyroxene (< 21%) with relatively high J index (5-10), and one displaying opposite characteristic (>21% opx and J index between 3 and 5). The reason why these two groups are not observed in the studied xenolith may result from the fact that mechanisms that affected our samples were different, or from the limited number of samples.

In studied peridotite, opx and cpx display more dispersed CPO than olivine. Even when there are enough grains to make contouring, this is difficult to distinguish a clear pattern because of the occurrence of more than one maximum in one pole figure. This problem is due to bad polishing or reaction rims inducing an incomplete indexation of the pyroxenes, which were recorded as multiple patches with a similar orientation. This leads to an over-representation of this orientation and hence to a maximum in the pole figure when this one is plotted as one grain by measurement. Generally, both opx and cpx CPO do not show clear patterns consistent with the olivine CPO. An exception, however, is the opx CPO of the sample 55-2A, which shows one maximum with a relatively high concentration of the

[100] and [001] axes doing low angle with the olivine of [010] and [100] maxima, respectively.

WATER IN MINERALS

Analytical procedure

Unpolarized Fourier Transform infrared (FTIR) spectroscopy measurements were performed using a Bruker IFS66v coupled with a Bruker IR microscope type A590 and a Bruker Hyperion microscope at Laboratoire des Colloïdes, Verre et Nanomateriaux (LCVN) in Montpellier (France). Both microscopes were equipped with all-reflecting Cassegranian optics, a condenser, and an x15 objective. Analyses were made at room pressure and temperature. Mid-infrared measurements were performed using a Globar light source, a KBr beam splitter, and a high sensitivity MCT (Deuterated triglycine sulfate) cooled by liquid nitrogen. Spectra were acquired with a resolution of 4 cm^{-1} and 300 scans were accumulated for each spectrum, except for 56-2H minerals (100 scan).

Unpolarized FTIR absorption spectra of ol and opx were obtained on doubly polished sections with a thickness of 280 to 353 µm (Table 2). The sections have been left in an acetone bath for at least 12 hours in order to remove any residual glue. We selected optically crack- and inclusion-free grains, and used a circular and squared aperture with the Bruker IFS66v coupled with a Bruker type A590 and the Bruker Hyperion microscope, respectively. The circular and squared apertures had diameter and a length side of 105 µm and ~100 µm, respectively (Table 1). Measurements in opx and cpx were aggravated by the large amount of inclusions in the coarse crystals and by the fine-grained texture of the opx acicular aggregates.

The water concentration in the analyzed minerals was calculated by integrating the absorption bands according to the calibration of Paterson (1982):

$$C_{OH} = \frac{X_i}{150\zeta} \int \frac{K(\bar{\nu})}{(3780 - \bar{\nu})} d\bar{\nu}$$

where $\mathbf{C}_{OH}$ is the hydroxyl concentration (in $H/10^6$ Si or ppm wt H_2O), ζ is an orientation factor (1/3 for unpolarized measurements), and $K(\bar{\nu})$ is the absorption coefficient in cm^{-1} for a given wavenumber $\bar{\nu}$. X_i is a density factor; its value for studied ol, opx and cpx is 2695 and 2769 and 2705 wt ppm H_2O, respectively (see Bolfan-Casanova et al., 2000, for calculation method). The range of integration for ol, opx and cpx are 3200-3400 cm^{-1}, 3000-3630 cm^{-1} and 3100-3670 cm^{-1}, respectively. The Paterson calibration underestimates the water concentration in olivine compared to the calibration given by Bell et al. (2003). However, the Bell (2003) calibration may only be applied for olivine spectra dominated by high

wavenumbers (3650-3450 cm^{-1}) of OH absorption bands. This is not the case for olivine in the studied peridotites, which spectra present dominantly low wave-number absorption bands (Fig. 6). Moreover, the Paterson calibration allows direct comparison of water contents in olivine and pyroxenes (Bolfan-Casanova et al., 2000). Errors on the absolute water contents are however of ± 30% (Kohlstedt et al., 1996).

IR spectra and water solubility

Figure 6 displays the mean spectra for olivine, orthopyroxène and clinopyroxene. These are typical unpolarized FTIR spectra for olivine, orthopyroxene and clinopyroxene in xenoliths 33-2A, 54-2A, 54-2D, 55-2A, 56-2A. The spectra obtained from the Bruker Hyperion sysrtem display a high noise between 3500 to 4000 cm^{-1}, whereas those acquired with the Bruker type A590 coupled are clean.

Clean FTIR spectra for olivine show no absorption bands in the wavenumber range where occurs the noise for measurement performed with the Bruker Hyperion. all the olivine crystals display the same pattern for lower wavenumbers. Moreover, as there is no difference in term of IR spectra for coarse- or fine-grained olivine crystals from the same sample and no textural change between olivines from different xenoliths, we assume that the major O-H absorption bands are at 3355 and 3328 cm^{-1}, and that the family of peaks occurring between 3650 and 3450 cm^{-1} are not observed, and particularly the band at 3574 cm^{-1} where the maximum O-H absorbance often occurs in natural peridotites (Bell et al., 2004; Demouchy, 2004; Demouchy et al., 2006; Grant et al., 2007; Miller et al., 1987; Peslier and Luhr, 2006). The observed spectra are similar to those of olivine in peridotites xenoliths from the Kamchatka subduction zone (Soustelle et al., 2010a). The water contents are very low, between 1 and 4 ppm H_2O, and did not depend of grain size or texture. Opx spectra are characterized by major O-H absorption bands at 3600, 3548, 3520 and 3407 cm^{-1} and by a minor peak at 3060 cm^{-1} (Fig 6). This pattern is typical for opx from mantle xenoliths (Grant et al., 2007; Peslier et al., 2002; Soustelle et al., 2010a). Water contents are heterogeneous: 39, 249 and 431 ppm for samples 56-2T, 56-2H and 56-2A. This variation seems to be related to the different generation of orthopyroxenes: the low values are observed in orthopyroxene layer parallel to the lineation in 56-2T; the high water content is measured in fibrous tertiary opx; and the intermediate concentration (probably over-estimated) correspond to primary orthopyroxene. The water contents >400 ppm H_2O are abnormally for spinel peridotites. As the spectra do not show evidences of contamination by water-rich inclusions, amphibole lamellae or epoxy, these high contents seem to be linked with the fibrous opx (Soustelle et al.,

2010). Cpx display major O-H absorption bands at 3648, 3456 and 3355 cm^{-1} (Fig. 6). These peaks are classical in natural diopside (Skogby, 2006), the peak between 3530 and 3540 is never observed in studied samples. The mean water contents in primary fine-grained cpx measured in 54-2D are 77.5 ppm H_2O. Cpx texture from other sample have not been identified because of the thin section thickness (300 µ m) used for the analyses. Unfortunately, the studied samples experienced a thermal equilibration in a range of temperature (665-860°C) lower than other peridotite xenoliths where the water contents in minerals were measured (e.g., Demouchy et al., 2006; Falus et al., 2008; Grant et al., 2007; Peslier and Luhr, 2006; Peslier et al., 2002; Soustelle et al., 2010). It is not possible to compare our results with those data because water solubility in minerals depends of P, T and water fugacity (Keppler and Bolfan-Casanova, 2006).

Concentration ratios between minerals (R_c) have been calculated using mean water contents for each sample. $R_c^{cpx/ol}$ are 38.5, 111 and 180 in 54-2D, 55-2A and 56-2H, respectively. $R_c^{opx/ol}$ are 431.5, 124.5 and 19.5 in 56-2A, 56-2H and 56-2T, respectively. $R_c^{opx/cpx}$ is 1.53 in 56-2H. In sample 56-2H, the only orthopyroxene studied does not have a clean spectrum, that's why its values of $R_c^{opx/cpx}$ and $R_c^{opx/ol}$ have to be considered carefully. The concentration ratios between minerals are highly variable from one sample to another, which result from the heterogeneity of pyroxene water contents compared to the constant concentrations in olivine, and probably reflect disequilibrium between these minerals.

SEISMIC PROPERTIES

The three-dimensional distributions of seismic velocities have been computed by averaging the individual grain elastic constants tensor as a function of the crystallographic orientation given by the EBSD measurements and modal composition (Mainprice and Humbert, 1994). We used Voigt-Reuss-Hill averaging and single-crystal elastic constants tensors of olivine, orthopyroxene and clinopyroxene at ambient conditions (Abramson et al., 1997; Collins and Brown, 1998; Duffy and Vaughan, 1988).

As seismic waves sample the anisotropy at length scales ranging from a few to a thousand of kilometers, we calculate seismic properties for an average peridotite sample obtained by summation of the CPO of the 7 individual samples. The olivine clinopyroxenite is not used because it seems unrealistic that one eighth of the mantle wedge may have a pyroxenite composition. Indeed, pyroxenites usually occur as centimeter to tens of centimeter wide layers in both xenoliths and peridotite massifs (Franz et al., 2002; Soustelle et al., 2009; Tommasi et al., 2006). 3D-seismic properties of the average sample (Fig. 7) are very similar to those of

individual xenoliths (not shown here). This pattern is typical of peridotites with olivine CPO with an orthorhombic or axial [100] symmetry (Tommasi et al., 2004; Vauchez et al., 2005). P- and S_2-waves propagation is fastest parallel to the lineation and slowest in the plane normal to the lineation. S_1-wave velocity is minimum for propagation directions both parallel and normal to the lineation and maximum at ~ 45° to the lineation in the foliation plane. S-wave splitting is minimum for waves propagating at low angle to the lineation and highest for waves propagating at high angles (≥ 30°) to the lineation in the foliation plane. S-waves propagating normal to the foliation also sample a high birefringence direction. For all propagation directions, the fast S-wave is polarized parallel to the lineation. The Vp/Vs_1 and Vp/Vs_2 ratios are minimum for propagation directions at high angle (>30°) to the lineation and the foliation, respectively. Both ratios are maximum parallel to the lineation. These anisotropy patterns are in good agreement with the seismic properties calculated on xenoliths from the Avacha volcano in Kamchatka, which also sample the supra-subduction mantle (Michibayashi et al., 2009; Soustelle and Tommasi, 2010).

The study of the olivine CPO shows that there is an anti-correlated relationship between the J-index and the modal proportion of pyroxene. The J-index represents the strength of the CPO and, as olivine is the dominant mineral in the mantle, it is consistent with the intrinsic anisotropy of the studied peridotites. There is a negative correlation between the pyroxene content and the Vp and maximum Vs anisotropy (Fig. 8).

DISCUSSION

Synkinematic reactive melt percolation

The first event which affected the studied samples is a high degree partial melting (15-20%) at a mid-ocean ridge or a back-arc spreading centre (Franz et al., 2002; Grégoire et al., 2001). This is supported by the textures of the primary pyroxene. Indeed, they display corroded grain boundaries when they are in contact with olivine (Fig 3a-c), particularly the fine-grained primary clinopyroxene crystals that may be relics of coarser grains after partial melting, which is also consistent with their very low water contents (Table 2). This xenolith suite is however not entirely composed by refractory pyroxene-poor peridotites, indeed lherzolites can have up to 31% of pyroxenes and harzburgites 26% of opx. This implies that an enrichment in pyroxene, and particularly in opx occurred subsequently to the partial melting event. Previous studies on peridotites xenoliths from Lihir (Franz et al., 2002; Grégoire et al., 2001; McInnes et al., 2001) have proposed that a late and relatively hot (900-

950°C) metasomatic event occurred in the mantle and lead to the formation of the millimeter-scale metasomatic veins and of fibrous tertiary pyroxenes. Nevertheless, the proportion of the tertiary pyroxenes is not sufficient to explain the high pyroxene contents in studied samples. All the harzburgites and lherzolite however display many secondary opx and some secondary cpx that display interstitial shape with no exsolution and deformation feature. The metasomatic vein crosscuts these pyroxenes, and some of them may have been recrystallized to tertiary opx or cpx. These observations suggest that the event that produced these secondary pyroxenes happened after the cooling subsequent to the partial melting and before the late hot metasomatic event.

In the studied xenolith peridotite collection, we note that the olivine grain size decrease is roughly correlated with the increase in modal pyroxene content (Table 1). This could be explained by studying the mean olivine grain size in function of the Zener parameter in each sample (Fig. 9). As we do not have a lot of samples, the peridotite xenoliths from the Avacha, which display similar texture and microstructures, have been added. They indeed have many textural and microstructural features that are similar to our samples, and they come from a comparable geodynamical context (Soustelle et al., 2010). The Zener parameter allows to distinguish two mechanisms, which explain the observed grain size evolution of the dominant phase in a polymineralic rock during deformation at relatively high temperature (Herwegh and Berger, 2004). In case of a positive correlation in the Z vs. grain size diagram, the secondary phase controls the grain growth of the primary phase and the dominant mechanism for deformation is granular flow (grain boundaries sliding combined with mass transfer; cf. Herwegh and Berger (2004). In case of a plateau, the modal content of the secondary phase is not enough or that it is constituted by coarse isolated crystals; then the dislocation creep regime becomes the main deformation mechanism, and the grain size of the main phase is controlled by the competition between grain growth and recrystallization. Figure 9 shows that the olivine grain size is roughly positively correlated with the Zener parameter. This may imply that the secondary phase (cpx+opx) controls the microstructures and the deformation mechanisms, and then could account for the relationship between olivine grain size and pyroxene contents as well as for the J index decrease with the increase of the cpx and opx contents. However, there are some observations that are not in a good agreement with this explanation. First, the coefficient of correlation in figure 9 is quite weak ($R^2 = 0.76$). Secondly, the assumptions behind the above analyses work for a random repartition of the secondary phase, which is only the case for the sample 54-2D. Finally, the secondary phase has to be present during the deformation, but in those peridotites only the primary pyroxenes

display deformation features, the tertiary ones are clearly posterior. The secondary pyroxenes have interstitial shape and generally isolate small olivine crystal from bigger grains that show similar orientation (Fig. 3b). Such were also observed in peridotite xenoliths from Avacha and in refertillized spinel peridotites from the Ronda massif (Soustelle et al., 2009; Soustelle et al., 2010a), where they were ascribed to the crystallization of pyroxene at the expenses of olivine. We then may assume that secondary crystals result from the reactive percolation of a Si-rich fluid or melt slightly enriched in Ca and Al.

In many of the studied samples, there is evidence for a synkinematic crystallization of the secondary cpx and opx. Most of the pyroxenes, and particularly the secondary ones, are concentrated in bands (56-2, 56-2T) and lenses (55-2A, Fig. 10) aligned and elongated, respectively, according to the deformation structures. Such texture has been regularly observed in melt-rock deformation experiments (e.g., Holtzman et al., 2003a; King et al., 2010), and also in peridotite massifs (e.g., Le Roux et al., 2008; Soustelle et al., 2009) and mantle xenoliths (Soustelle et al., 2010) where synkinematic melt or fluid percolation took place. Soustelle et al. (2010a) demonstrated that synkinematic reactive percolation may lead to the formation of fine olivine crystals. They correspond to isolated part of coarser grain due to the olivine corrosion by the pyroxene precipitation, and they are slightly disorientated compared to the "father" crystal. This phenomenon leads to a decrease of the J index in the entire rock. Figure 11 shows the ratio between the J index of the coarse (> 1mm) and the whole olivines of one sample in function of the proportion of fine olivine crystals (<1 mm). In case of a high ratio, the J index obtained for all olivine in a thin section is relatively low and given by fine grains, whereas a low ratio goes along with very few disoriented fine olivine crystals. We observed a positive correlation, which implies that the precipitation of pyroxenes at the expense of olivines also induced disorientation of the newly formed fine olivine crystals and led to a the decrease of the J index.

This synkinematic reactive percolation event took place after the cooling subsequent to the partial melting and before the late relatively hot static metasomatic event. As demonstrated before, the metasomatism is responsible for the formation of the metasomatic veins that crosscut all the other minerals as well as their deformation structures. It is nonetheless complex to determine in which condition the crystallization of the secondary pyroxenes took place. The observation of deformation microstructures such as widely spaced subgrain boundaries and olivine crystals with polygonal shape highlight a deformation by dislocation creep with an important part of diffusion processes, i.e. a strain under relatively high temperature and low stress. Such features could have been preserved from the early

history of these samples at the spreading centre, but may also have taken place during a later deformation event. The presence of a melt or a fluid during deformation confirms the temperature conditions. Hence, these samples, after the partial melting have been dragged away from their spreading centre accreted at the base of the lithosphere, then cooled until the occurrence of the subduction. As McInnes et al. (1999) pointed out, the Bismarck microplate once formed a part of the Pacific Plate and delaminated from it any time in the past. The Pacific plate was then subducted below its former segment. A possibility to explain our observations, is that these peridotites was located at the base of the upper lithosphere during the subduction, and they may have been integrated to the mantle wedge, and thus undergone its dynamics as well as melt and/or fluid percolation. Afterward, the collision of Ontong-Java plateau (Coleman and Kroenke, 1981) induced a decrease of the convergence velocity leading to the cooling of the mantle wedge and the thickening of the upper plate (Arcay et al., 2007), and thus the accretion and cooling of the studied peridotite xenoliths. Afterward, they have been affected by the late and relatively hot metasomatic stage. Except for the partial melting, these samples have undergone a similar history as the harzburgite xenoliths from the Avacha volcano (Soustelle et al., 2010).

Hydration of the sub-arc mantle

Measurement of water contents in olivine, opx and cpx yield values of 1-4, 38-431 and 77-382 ppm H_2O by weight (Table 2). Franz et al. (2002) determined that the studied peridotites have been equilibrated between 665 and 860°C at a depth of 43-60 km. Keppler & Bolfan-Casanova (2006) have established the following equation of water solubility:

$$C_{water} = A f_{H_2O}^{n} \exp\left(-\frac{\Delta H^{1bar} + \Delta V^{s} P}{RT}\right)$$

where C_{water} is the water solubility in ppm, A is a constant in ppm/bar^n, f_{H_2O} is the water fugacity in bar, n is an exponent related to the dissolution mechanism of OH, ΔH^{1bar} is the reaction enthalpy at 1 bar in J.mol^{-1}, ΔV^{s} is the volume change of the solids in m^3.mol^{-1}, P is the pressure in Pa, R is the gas constant, and T the temperature in K. We did the calculation for the both couples of pressure and temperature corresponding to equilibrium conditions (665°C-43 km and 860°C-60 km). f_{H_2O} has been determined with the database of Holland & Powel (1998), and for A, n, ΔH^{1bar}, ΔV^{s} we used the values of Zhao et al. (2004), Mierdel & Keppler (2004) and Gavrilenko (2008) for ol, opx and cpx, respectively. The water solubility

in olivine, opx and cpx for the equilibrium conditions are then 5-35, 90-193 and 188-327 ppm H_2O by weight, respectively.

The olivines from the studied peridotites are therefore undersaturated. This may result from water loss by diffusion to the magma during the xenoliths extraction (Demouchy et al., 2006; Peslier and Luhr, 2006). The opx measured water contents are either lower or higher than the theoretical saturation. An Al enrichment could explain the higher values (Rauch and Keppler, 2002), however all the opx display between 0.1 and 2 weight % of Al_2O_3 (Franz et al., 2002). The opx1 from sample 56-2H, which have 249 ppm H_2O, is easily explained by the fact that its spectrum show a contamination by the epoxy, and this considerably change the water concentration calculation. The opx1 in sample 56-2A has an extremely high water content (431 ppm) for these equilibrium conditions, however it is a fibrous tertiary opx, which is in fact an aggregate of minutes needle or rounded opx (Fig. 3g), it is therefore possible that the spectrum is also polluted by grain boundaries. The lower opx water contents values (38-39 ppm) measured in opx1 and 2 in the sample 56-2T may result from two processes: (1) those opx are residue of partial melting, but they are located in the orthopyroxenite band, or (2) they may have equilibrated under high oxygen fugacity (Peslier et al., 2002), which is consistent with the $Dlog(fO_2)^{FMQ}$ values for the studied samples ranging from 0.4 to 4.3 (Franz et al., 2002), and with the fact that the major O-H absorption bands in olivine IR spectrum are at 3355 and 3328 cm^{-1} (Berry et al., 2005; Mosenfelder et al., 2006). The cpx water contents are in good agreement with the theoretical saturation, and by considering the 30% error induced by calibration of Paterson. Only the sample 54-2D has cpx with very low concentration of H_2O (77-78 ppm), which may be explained by the fact that the analyzed crystals are primary fine cpx (Fig 3c), as almost all the cpx in this sample, and they are likely residue of the partial melting event. However, if it is either because of the partial melting or late metasomatism under high oxygen fugacity, the broad variations in pyroxene water contents in the Lihir peridotite xenoliths suggest that the H_2O concentration in opx and cpx may have been controlled by localized melt or fluid percolation. Similar variations and observations also occurred in xenolith from the Avacha volcano (Soustelle et al., 2010a).

Incorporation of water in olivine can result in activation of different slip systems (e.g., Jung and Karato, 2001). Unfortunately, microstructures in olivine from studied peridotites show that the main deformation stage took place under relatively high temperature and low stress, which is not consistent with the equilibrium conditions recorded. As this is not possible to have an accurate idea of the temperature, that is therefore not possible to have an idea of

the water content in olivine during the deformation either by calculating the theoretical saturation or by comparison with the literature.

Consequences to olivine CPO and seismic properties

The determination of the dominant deformation mechanisms is fundamental to deduce the flow patterns in the mantle from S-waves anisotropy data. All the studied peridotites display a strong concentration of the olivine [100] axes relatively to the [010] and [001] axes, moreover when a mineral lineation is observed, it is generally parallel to this [100] axes maximum (Fig. 4). This strongly suggests a [100] slip system. Except for 56-2A, the [010] and [001] axes display a girdle distribution normal to the [100] maximum, with the two maxima roughly normal to each other, however the maximum concentration of the [010] axes is always stronger than for the [001] axes. In sample 55-2A, the direction of the spinel and pyroxene-rich lenses alignment that mark the foliation is normal to the maximum concentration of the [010] axes. The opx in this sample display a weak CPO, where the [100] and [001] axes show a maximum concentration at low angle with the ol [010] and [100] axes, respectively. Under pressure and temperature appropriate to the upper mantle conditions, the dominant slip system in opx is (100)[001] (Doukhan et al., 1986). This implies that the dominant slip plane for this sample and, by analogy, in the studied peridotites the dominant slip plane in ol is [010]. However, as the [010] and [001] axes display a girdle distribution and as the textures and microstructures are similar to those of the peridotite xenolith from the Avacha volcano (Soustelle et al., 2010), hence we assume that there is the activation of multiple {0kl} ol slip planes with [010] as the dominant one. This slip system is characteristic for deformation under high temperature, low stress, low pressure, and low water contents in olivine (Bai et al., 1991; Couvy et al., 2004; Durham and Goetze, 1977; Jung and Karato, 2001; Jung et al., 2006; Mackwell et al., 1985; Raterron et al., 2007).

This study demonstrates that the deformation responsible for this CPO probably occurred in the upper mantle wedge, and that the olivine CPO display an [100] axial. This implies that for all propagation directions that fast S-wave is polarized parallel to the lineation and therefore to the mantle flow direction (Fig. 6). Then, as observed for peridotite xenolith from Avacha volcano (Soustelle and Tommasi, 2010b), the presence of fluids or melt during the deformation does not have an influence on the fast S-wave polarization directions in the shallow mantle wedge. Reactive percolation however affects the intensity of the anisotropy. It indeed induces a pyroxene enrichment, which is negatively correlated with the Vp and maximum Vs anisotropy (Fig. 7). The calculation of the anisotropy evolution produced just

by addition of randomly orientated pyroxene does not yield a decrease enough important to explain our data. This constitutes another argument for synkinematic reactive melt or fluid percolation leading to olivine grain size decrease and disorientation of the newly created crystals. If we assume that the "normal" composition of the mantle wedge have less than 21 % of pyroxene as suggested by Soustelle et al. (2010) and Soustelle and Tommasi (2010), the maximum Vs anisotropy would be around 8.3%, whereas the average over the entire suite, including the pyroxene enriched samples, is 5.7%. Reactive transport of melt or fluid during mantle deformation event in the mantle wedge can thus decrease the anisotropy by around 30%. This difference is higher than what Soustelle et al. (2010b) found (20%), but it remains the same order of value.

Another important result is the Vp/Vs ratios that display exactly the same pattern and values for all the propagation direction as those calculated for peridotite xenoliths from Avacha volcano (Soustelle and Tommasi, 2010). This ratio is very important because it allows constraining the composition of the mantle wedge. The high Vp/Vs ratio may indicate the presence of fluids or melts (Takei, 2002), whereas low Vp/Vs ratios (<1.7) are classically attributed to change in mineralogical composition. Soustelle and Tommasi (2010) however demonstrate that this may be explain by the intrinsic anisotropy of the rocks from mantle wedge. As the observed Vp/Vs ratios are similar in the Lihir sub-arc mantle, which is located in comparable geodynamical context as the Avacha volcano, this strengthens this theory.

CONCLUSION

Previous studies on mantle xenoliths from Lihir show that they experienced a complex history (Franz et al., 2002). It started by partial melting at a spreading centre; afterward they cooled during the transport away from the ridge. They formed part of the lithospheric oceanic mantle of the Bismarck microplate at a depth of 43-60 km at temperatures of 665-860°C. On the basis of microstructural observations, this study shows that these samples underwent an episode of reactive percolation of an Si-rich melt or fluid locally enriched in Ca synchronous to a relatively high temperature low stress deformation prior to their transport to the seafloor by Quaternary basalt eruptions. This probably happened in the shallow mantle wedge when the subduction of the Pacific plate underneath the Bismarck microplate was still active. As strain features recorded by all the samples correspond to this event, we assume that the observed CPO and the calculated seismic anisotropy directly result from this event.

The synkinematic reactive percolation that happened in the mantle wedge lead to pyroxene enrichment, which is mainly localised in band or lenses elongated parallel to the

deformation structures, the lineation or the foliation. This observation is characteristic of a deformation induced fluid segregation as observed in melt-rock experiment (e.g., Holtzman et al., 2003b; King et al., 2010) and peridotites massifs and xenoliths (e.g., Le Roux et al., 2008; Soustelle et al., 2009; Soustelle et al., 2010). During this event, pyroxenes crystallized at the expense of coarse olivine crystals, increasing the proportion of fine disorientated olivine crystals and to the decrease of the intensity of olivine CPO. This suggest that the presence of fluids or melt during deformation does not results in a change of dominant slip direction, but probably enhance the contribution of diffusion processes to the deformation.

Olivine CPO displays for most of the samples an axial [100] pattern that records deformation by dislocation creep with dominant activation of the high temperature, low stress, low pressure {0kl}[100]. Therefore, if anisotropy in the mantle wedge results essentially from olivine deformation, the fast S-wave polarization will be parallel to the lineation and thus to the flow direction. The synkinematic reactive percolation of melts or fluids may locally induce an important decrease of anisotropy. As for the sample from the Avacha volcano (Soustelle and Tommasi, 2010), these ones also display intrinsic seismic properties able to explain the very low Vp/Vs ratio often observed above subduction zones.

The mantle xenoliths from the Lihir Island display similar microstructures, CPO and seismic properties to those from the Avacha volcano (Michibayashi et al., 2009; Soustelle and Tommasi, 2010; Soustelle et al., 2010). Both collections moreover sample the sub-arc mantle above a subduction zone. This similarity would then mean that this synkinematic reactive melt or fluid percolation is a common process in the mantle wedge dynamics.

REFERENCES

Abramson, E.H., Brown, J.M., Slutsky, L.J. and Zaug, J., 1997. The elastic constant s of the San Carlos olivine up to 17 GPa. Journal of geophysical Research, 102: 12,252-12,263.

Arai, S. and Kida, M., 2000. Origin of fine-grained peridotite xenoliths from Iraya volcano of Batan Island, Philippines: deserpentinization or metasomatism at the wedge mantle beneath an incipient arc? Island Arc, 9(4): 458-471.

Arcay, D., Tric, E. and Doin, M.-P., 2007. Slab suface temperatutre in subduction zone: Influnce of the interplate decoupling depth and upper mantle plate thinnig processes. Earth and Planetary Science Letters, 255: 324-338.

Bai, Q., Mackwell, S.J. and Kohlstedt, D.L., 1991. High-Temperature Creep of Olivine Single-Crystals .1. Mechanical Results for Buffered Samples. Journal of Geophysical Research-Solid Earth and Planets, 96(B2): 2441-2463.

Ballhaus, C., Berry, R.F. and Green, D.H., 1991. High pressure experimental calibration of the olivine-orthopyroxene-spinel oxygen geobarometer: implications for the oxidation state of the upper mantle. Contribution to Mineralogy and Petrology, 107: 27-40.

Bell, D., Rossman, G. and Moore, R., 2004. Abundance and partitioning of OH in a high-pressure magmatic system: Megacrysts from the Monastery kimberlite, South Africa. Journal of petrology, 45(8): 1539-1564.

Bell, D.R., Rossman, G.R., Maldener, J., Endisch, D. and Rauch, F., 2003. Hydroxide in olivine: A quantitative determination of the absolute amount and calibration of the IR spectrum. Journal of Geophysical Research-Solid Earth, 108(B2): 2105-2113.

Ben Ismail, W. and Mainprice, D., 1998. An olivine fabric database: an overview of upper mantle fabrics and seismic anisotropy. Tectonophysics, 296: 145-158.

Bénard, A. and Ionov, D.A., 2009. Veined peridotite xenoliths from the Avacha volcano, Kamchatka: Fluid types and fluid-rock interaction in supra-subduction mantle. Geochimica Et Cosmochimica Acta, 73(13(S1)): A108.

Berry, A.J., Hermann, J., O'Neill, H.S.C. and Foran, G.J., 2005. Fingerprinting the water site in mantle olivine. Geology, 33(11): 869-872.

Blacic, J.D., 1972. Effect of water on the experimental deformation of olivine. In: H.C. Heard, I.Y. Borg, N.L. Carter and C.B. Rayleigh (Editors), Flow and Fracture of Rocks. Geophysical Monograph. American Geophysical Union, Washington, pp. 109-115.

Bolfan-Casanova, N., Keppler, H. and Rubie, D.C., 2000. Water partitioning between nominally anhydrous minerals in the MgO-SiO2-H2O system up to 24 GPa: implications for the distribution of water in the Earth's mantle. Earth and Planetary Science Letters, 182(3-4): 209-221.

Brey, G.P., Kohler, T. and Nickel, K.G., 1990. Geothermobarometry in four-phase lherzolites .1. Experimental Results from 10 to 60 Kb. Journal of Petrology, 31(6): 1313-1352.

Bunge, H.J., 1982. Texture analysis in materials sciences. Buttleworth, London, 593 pp.

Coleman, P.J. and Kroenke, L.W., 1981. Subduction without volcanism in the Solomon Island arc. Geo-Marine Letters, 1: 129-134.

Collins, M.D. and Brown, J.M., 1998. Elasticity of an upper mantle clinopyroxene. Physics and chemistry of minerals, 26(1): 7-13.

Couvy, H. et al., 2004. Shear deformation experiments of forsterite at 11GPa-1400 degrees C in the multianvil apparatus. European Journal of Mineralogy, 16(6): 877-889.

Demouchy, S., 2004. Water in the Earth's interior: Thermodynamics and kinetics of hydrogen incorporation in olivine and wadsleyite, Universität Bayreuth, Bayreuth, 165 pp.

Demouchy, S., Jacobsen, S.D., Gaillard, F. and Stern, C.R., 2006. Rapid magma ascent recorded by water diffusion profiles in mantle olivine. Geology, 34(6): 429-432.

Doukhan, J.-C., Doukhan, N., Naze, L. and Van Duysen, J.-C., 1986. Défauts de réseau et plasticité cristalline dans les pyroxenes: Une revue. Bulletin de minéralogie, 109: 377-374.

Duffy, T.S. and Vaughan, M.T., 1988. Elasticity of enstatite and its relationships to crystal structure Journal of geophysical Research, 93: 383-391.

Durham, W.B. and Goetze, C., 1977. Plastic-flow of oriented single-crystals of olivine. 1. Mechanical data. Journal of geophysical Research, 82(36): 5737-5753.

Falus, G., Tommasi, A., Ingrin, J. and Szabo, C., 2008. Deformation and seismic anisotropy of the lithospheric mantle in the southeastern Carpathians inferred from the study of mantle xenoliths. Earth and Planetary Science Letters, 272: 50-64.

Franz, L., Becker, K.-P., Kramer, W. and Herzig, M., 2002. Metasomatic mantle xenoliths from the Bismarck microplate (Papua New Guinea)- Thermal evolution, geochemistry and extent of slab-induced metasomatism. Journal of petrology, 43(2): 315-343.

Franz, L. and Wirth, R., 2000. Spinel inclusion in olivine of peridotite xenoliths from TUBAF seamount (Bismark Archipelago/Papua New Guinea): Evidence for the thermal and tectonic evolution of the oceanic lithosphère. Contribution to Mineralogy and Petrology, 140: 283-295.

Gavrilenko, P., 2008. Water solubility in diopside, Bayreuth, 133 pp.

Grant, K., Ingrin, J., Lorand, J. and Dumas, P., 2007. Water partitioning between mantle minerals from peridotite xenoliths. Contributions to Mineralogy and Petrology, 154(1): 15-34.

Gregoire, M., McInnes, B.I.A. and O'Reilly, S.Y., 2001. Hydrous metasomatism of oceanic sub-arc mantle, Lihir, Papua New Guinea - Part 2. Trace element characteristics of slab- derived fluids. Lithos, 59(3): 91-108.

Grégoire, M., McInnes, B.I.A. and O'Reilly, S.Y., 2001. Hydrous metasomatism of oceanic sub-arc mantle, Lihir, Papua New Guinea; Part 2. Trace element characteristics of slab-derived fluids. Lithos, 59(3): 91-108.

Herwegh, M. and Berger, A., 2004. Deformation mechanisms in second phase affected microstructures and their enery balance. Journal of structural geology, 26: 1483-1498.

Hirth, G. and Kohlstedt, D.L., 1995a. Experimental Constraints on the Dynamics of the Partially Molten Upper-Mantle - Deformation in the Diffusion Creep Regime. Journal of Geophysical Research-Solid Earth, 100(B2): 1981-2001.

Hirth, G. and Kohlstedt, D.L., 1995b. Experimental Constraints on the Dynamics of the Partially Molten Upper-Mantle .2. Deformation in the Dislocation Creep Regime. Journal of Geophysical Research-Solid Earth, 100(B8): 15441-15449.

Holland, T.J.B. and Powell, R., 1998. An internally consistent thermodynamic data set for phases of petrological interest. Journal of Metamorphic Geology, 16(3): 309-343.

Holtzman, B.K., Groebner, N.J., Zimmerman, M.E., Ginsberg, S.B. and Kohlstedt, D.L., 2003a. Stress-driven melt segregation in partially molten rocks. Geochemistry Geophysics Geosystems, 4: art. no.-8607.

Holtzman, B.K. et al., 2003b. Melt segregation and strain partitioning: Implications for seismic anisotropy and mantle flow. Science, 301(5637): 1227-1230.

Ionov, D.A., 2010. Petrology of Mantle Wedge Lithosphere: New Data on Supra-Subduction Zone Peridotite Xenoliths from the Andesitic Avacha Volcano, Kamchatka. Journal of Petrology, 51(1-2): 327-361.

Ionov, D.A. and Seitz, H.-M., 2008. Lithium abundances and isotopic compositions in mantle xenoliths from subduction and intra-plate settings: Mantle sources vs. eruption histories. Earth and Planetary Science Letters, 266(3-4): 316-331.

Ishimaru, S., Arai, S., Ishida, Y., Shirasaka, M. and Okrugin, V., 2007. Melting and multi-stage metasomatism in the mantle wedge beneath a frontal arc inferred from highly

depleted peridotite xenoliths from the Avacha volcano, Southern Kamchatka. Journal of Petrology, 48(2): 395-433.

Jung, H. and Karato, S., 2001. Water-induced fabric transitions in olivine. Science, 293(5534): 1460-1463.

Jung, H., Katayama, I., Jiang, Z., Hiraga, I. and Karato, S., 2006. Effect of water and stress on the lattice-preferred orientation of olivine. Tectonophysics, 421(1-2): 1-22.

Karato, S.I., Paterson, M.S. and Fitz Gerald, J.D., 1986. Rheology of Synthetic Olivine Aggregates - Influence of Grain-Size and Water. Journal of Geophysical Research-Solid Earth and Planets, 91(B8): 8151-8176.

Keppler, H. and Bolfan-Casanova, N., 2006. Thermodynamics of water solubility and partitionning. In: H. Keppler and J.R. Smyth (Editors), Water in Nominally Anhydrous Minerals. Reviews in mineralogy and geochemistry. Geochemical society and Mineralogical society of America, Bayreuth Boulder, pp. 193-230.

King, D.S.H., Zimmerman, M.E. and Kohlstedt , D.L., 2010. Stress-driven melt segregation in partially molten olivine-rich rocks deformed in torsion Journal of Petrology, 51: 21-42.

Köhler, T. and Brey, G.P., 1990. Calcium exchange between olivine and clinopyroxenes calibrated as a geothermometer for natural peridotites from 2 to 60 kb with applications. Geochemica et Cosmochemica Acta, 54: 2375-2388.

Kohlstedt, D.L., Keppler, H. and Rubie, D.C., 1996. Solubility of water in the alpha, beta and gamma phases of (Mg,Fe)(2)SiO4. Contributions to Mineralogy and Petrology, 123(4): 345-357.

Le Roux, V., Tommasi, A. and Vauchez, A., 2008. Feedback between melt percolation and deformation in an exhumed lithosphere–asthenosphere boundary. Earth and Planetary Science Letters, 274: 401-413.

Licence, P.S., Terril, J.E. and Fergusson, L.J., 1987. Epithermal gold mineralisation, Amnittle Island, Papua New Guinea, Proceedings of the Pacific Rim Conference '87, Melbourne: Australian Institute of Mining and Metallurgy, pp. 273-278.

Mackwell, S.J., Kohlstedt, D.L. and Paterson, M.S., 1985. The Role of Water in the Deformation of Olivine Single-Crystals. Journal of Geophysical Research-Solid Earth and Planets, 90(NB13): 1319-1333.

Mainprice, D. and Humbert, M., 1994. Methods of calculating petrophysical properties from lattice preferred orientation data. Surveys in Geophysics, 15: 575-592.

McInnes, B.I.A., 1992. A glimpse of ephemeral subduction zone processes from Simberi island, Papua New Guinea, University of Ottawa, 235 pp.

McInnes, B.I.A. and Cameron, E.M., 1994. Carbonated, alkaline metasomatic melts from a sub-arc environement: mantle wedge from the Tabar-Lihir-Feni arc, Papua New Guinea Earth and Planetary Science Letters, 122: 125-141.

McInnes, B.I.A., Gregoire, M., Binns, R.A., Herzig, P.M. and Hannington, M.D., 2001. Hydrous metasomatism of oceanic sub-arc mantle, Lihir, Papua New Guinea: petrology and geochemistry of fluid-metasomatised mantle wedge xenoliths. Earth and Planetary Science Letters, 188(1-2): 169-183.

McInnes, B.I.A., McBride, J.S., Evans, N.J., Lambert, D.D. and Andrew, A.S., 1999. Osmium isotope constraints on ore metal recycling in subduction zones. Science, 286: 512-517.

Mei, S., Bai, W., Hiraga, T. and Kohlstedt, D.L., 2002. Influence of melt on the creep behavior of olivine-basalt aggregates under hydrous conditions. Earth and Planetary Science Letters, 201(3-4): 491-507.

Mei, S. and Kohlstedt, D.L., 2000a. Influence of water on plastic deformation of olivine aggregates 1. Diffusion creep regime. Journal of Geophysical Research-Solid Earth, 105(B9): 21457-21469.

Mei, S. and Kohlstedt, D.L., 2000b. Influence of water on plastic deformation of olivine aggregates 2. Dislocation creep regime. Journal of Geophysical Research-Solid Earth, 105(B9): 21471-21481.

Michibayashi, K. et al., 2009. Rock seismic anisotropy of the low-velocity zone beneath the volcanic front in the mantle wedge Geophysical Research Letters, 36: L12305, doi:10.1029/2009GL038527.

Mierdel, K. and Keppler, H., 2004. Temperature dependence of water solubility in enstatite. Contribution to Mineralogy and Petrology, 148(305-311).

Miller, G.H., Rossman, G.R. and Harlow, G.E., 1987. The natural occurence of hydroxyde in olivine. Physics and chemistry of minerals, 14(5): 461-472.

Mosenfelder, J.L., Sharp, T.G., Asimow, P.D. and Rossman, G.R., 2006. Hydrogen incorporation in natural mantle olivines. In: S. Jacobsen and S. Lee (Editors), Earth's deep water cycle. Geophysical Monograph. American Geophysical Union, pp. 45-56.

Paterson, M.S., 1982. The determination of hydrxyl by infrared abbsorption in quartz, silicate-glasses and similar materials Bulletin de minéralogie, 105(1): 20-29.

Peslier, A. and Luhr, J., 2006. Hydrogen loss from olivines in mantle xenoliths from Simcoe (USA) and Mexico: Mafic alkalic magma ascent rates and water budget of the sub-continental lithosphere. Earth and Planetary Science Letters, 242(3-4): 302-319.

Peslier, A.H., Luhr, J.F. and Post, J., 2002. Low water contents in pyroxenes from spinel-peridotites of the oxidized, sub-arc mantle wedge. Earth and Planetary Science Letters, 201(1): 69-86.

Pollack, H.N. and Chapman, D.S., 1977. On the regional variation of heat flow, geotherms, and lithospheric thickness Tectonophysics, 38: 279-296.

Raterron, P., Chen, J., Li', L., Weidner, D. and Cordier, P., 2007. Pressure-induced slip-system transition in forsterite: Single-crystal rheological properties at mantle pressure and temperature. American Mineralogist, 92(8-9): 1436-1445.

Rauch, M. and Keppler, H., 2002. Water solubility in orthopyroxene. Contributions to Mineralogy and Petrology, 143(5): 525-536.

Rytuba, J.J., McKee, E.H. and Cox, D., 1993. Geochronology and geochemistry of the Ladolam gold deposit, Lihir island, and gold deposits and volcanoes of Tabar and Tatau, Papua New Guinea. US Geological Survey Bulletin, 2039: 119-126.

Skogby, H., 2006. Water in natural mantle minerals I: Pyroxenes. In: H. Keppler and J.R. Smyth (Editors), Water in Nominally Anhydrous Minerals. Reviews in mineralogy and geochemistry. Geochemical society and Mineralogical society of America, Bayreuth Boulder, pp. 155-167.

Soustelle, V. and Tommasi, A., 2010. Seismic properties of the supra-subduction mantle: Constraints from peridotite xenoliths from the Avacha volcano, southern Kamchatka. Geophysical Research Letters 37: L13307.

Soustelle, V., Tommasi, A., Bodinier, J.-L., Garrido, C.J. and Vauchez, A., 2009. Deformation and reactive melt transport in the mantle lithosphere above a large-scale partial melting domain: the Ronda peridotite massif, S Spain. Journal of Petrology, 50(7): 1235-1266.

Soustelle, V., Tommasi, A., Demouchy, S. and Ionov, D.A., 2010. Deformation and Fluid-Rock Interaction in the Supra-subduction Mantle: Microstructures and Water Contents in Peridotite Xenoliths from the Avacha Volcano, Kamchatka. Journal of Petrology, 51(1-2): 363-394.

Takei, Y., 2002. Effect of pore geometry on Vp/Vs: from equilibrium geometry to crack. Journal of geophysical Research, 107(B2): 2043.

Taylor, B., 1979. Bismarck sea: evolution of a back-arc basin. Geology, 7: 171-174.

Tommasi, A., Godard, M., Coromina, G., Dautria, J.M. and Barsczus, H., 2004. Seismic anisotropy and compositionally induced velocity anomalies in the lithosphere above mantle plumes: a petrological and microstructural study of mantle xenoliths from French Polynesia. Earth and Planetary Science Letters, 227(3-4): 539-556.

Tommasi, A., Mainprice, D., Canova, G. and Chastel, Y., 2000. Viscoplastic self-consistent and equilibrium-based modeling of olivine lattice preferred orientations: Implications for the upper mantle seismic anisotropy. Journal of Geophysical Research-Solid Earth, 105(B4): 7893-7908.

Tommasi, A., Vauchez, A., Godard, M. and Belley, F., 2006. Deformation and melt transport in a highly depleted peridotite massif from the Canadian Cordillera: Implications to seismic anisotropy above subduction zones Earth and Planetary Science Letters, 252: 245-259.

Van der Wal, D., Chopra, P., Drury, M. and Gerald, J.F., 1993. Relationships between Dynamically Recrystallized Grain-Size and Deformation Conditions in Experimentally Deformed Olivine Rocks. Geophysical Research Letters, 20(14): 1479-1482.

Vauchez, A., Dineur, F. and Rudnick, R., 2005. Microstructure, texture and seismic anisotropy of the lithospheric mantle above a mantle plume: Insights from the Labait volcano xenoliths (Tanzania). Earth and Planetary Science Letters, 232: 295-314.

Zhao, Y.H., Ginsberg, S.B. and Kohlstedt, D.L., 2004. Solubility of hydrogen in olivine: dependence on temperature and iron content. Contribution to Mineralogy and Petrology, 147: 155-161.

Zimmerman, M.E. and Kohlstedt, D.L., 2004. Rheological Properties of Partially Molten Lherzolite Journal of Petrology, 45(2): 275-298.

FIGURE CAPTIONS

Figure 1: Map of the Bismarck Archipelago with the TUBAF and EDISON seamounts location; insert show the position of this Archipelago compared to Papua-New-Guinea (modified after Franz et al., 2002)

Figure 2: Photomicrograph in plane polarized light (a, b, c) and cross-polarized light (d, e, f) illustrating typical structures and microstructures in the Lihir peridotites xenoliths. (a, b and c) Parallelism between deformation structures (L and S are lineation and the foliation, respectively) and pyroxenes distribution (olivines, pyroxenes and spinels are in white, grey and black, respectively) in sample 54-2A (a), 56-2T (b) and 55-2A (c). (d) Zone of fine olivine crystals and fine interstitial secondary opx (see text) close at the contact with the orthopyroxenite crosscutting 56-2T. (e) Subgrain boundaries (black arrows) and 120° triple junction (white arrows) in sample 54-2A. (f) The two families of subgrain boundaries, the larger (white arrows) and the narrow (black arrows) ones in sample 56-2A.

Figure 3: Photomicrograph in cross-polarized light illustrating the opx and cpx textures. (a) Exsolution-bearing coarse primary opx and cpx displaying a turbid aspect and wavy extinction in a pyroxene-rich vein in the sample 56-2H. (b) Coarse primary opx displaying kink-bands and highly indented grain boundaries next to several smaller ,undeformed secondary opx and cpx in sample 55-2A. (c) Fine corroded secondary cpx in sample 54-2D. (d) Secondary opx crystallized on olivine grain boundaries in sample 55-2A. (e) Primary cpx crosscut by metasomatic veins containing tertiary opx in sample 54-2D. (f) Metasomatic veins crosscutting olivine crystals and their microstructures, and forming aggregate of cpx-ol-phlogopite at the contact with a primary cpx; sample 54-2D. (g) Details of a fine-grained acicular and prismatic opx aggregate forming the tertiary opx in sample 56-2A. (h) Detail of (f) showing the recrystallized cpx aggregates forming the tertiary cpx.

Figure 4: Olivine, orthopyroxene and clinopyroxene crystal preferred orientation. Lower hemisphere, equal area stereographic projections, contours at one multiple of uniform distribution. All the data were rotated to have the olivine [100] maximum in the E-W horizontal direction and the [010] maximum close to the N-S horizontal direction. Lineation and foliation, when observed, are indicated by a star and a continuous line, respectively.

Figure 5: J index for olivine calculated using one orientation datum per grain versus the modal proportion of pyroxene in each sample. White and black circle are peridotites and clinopyroxenites from this study, respectively, and the small grey square are data of peridotite xenoliths from Avacha volcano, Kamchatka (Soustelle et al., 2010).

Figure 6: Mean unpolarized IR spectra for olivine, orthopyroxenes and clinopyroxenes. The spectrum for opx in the sample 56-2A is just one measurement of a tertiary opx. Spectra are normalized to 1 cm^{-1}.

Figure 7: Seismic properties of a mean sample obtained by the summation of the CPO of the 7 studied peridotite xenoliths. From left to right and top to bottom, schematic representation of the lineation and foliation reference frame used in this study, variation as a function of the propagation direction of the compressive waves velocities (Vp in $km.s^{-1}$), of the shear wave polarization anisotropy ($AVs = 200*(Vs_1-Vs_2)/(Vs_1+Vs_2)$ in %), of the polarization of the fast shear wave S_1 (grey scale represent the intensity of AVs, as in the previous plot), of the two quasi-shear waves (Vs_1 and Vs_2) velocities, and of the Vp/Vs1 and Vp/Vs2 ratios. Equal area, lower hemisphere stereographic projections.

Figure 8: P- and maximum S-wave anisotropy as a function of the pyroxenes modal proportion. The black and dashed line represent the evolution of the P- and maximum S-wave anisotropy when an increase of randomly orientated pyroxene (opx, cpx or the both do not change the result) is imposed to the most refractory sample 55-2B, respectively. Small triangle and circle have the same meaning as the big ones but for data from peridotite xenoliths from Avacha volcano, Kamchatka (Soustelle et al., 2010).

Figure 9: Zener parameter (Z) in function of the mean olivine grain size. Z is the ratio between the mean size and the modal proportion of the secondary phases (cpx+opx). White and black circle are peridotites and clinopyroxenites from this study, respectively, and the small grey square are data of peridotite xenoliths from Avacha volcano, Kamchatka (Soustelle et al., 2010). The log regression (R^2) has been calculated for the both sample collection.

Figure 10: Ratio between coarse (>1 mm) and whole olivines J index (Jgg/J) in function of the proportion of fine olivine crystals (<1 mm). The arrow for the sample 56-2A is explained by the fact that this sample has a texture similar to the other dunites but it display an

abnormally high contents of fibrous tertiary opx, which corrode olivine and then give wrong values for fine olivine proportion. The regression has been calculated without 56-2A.

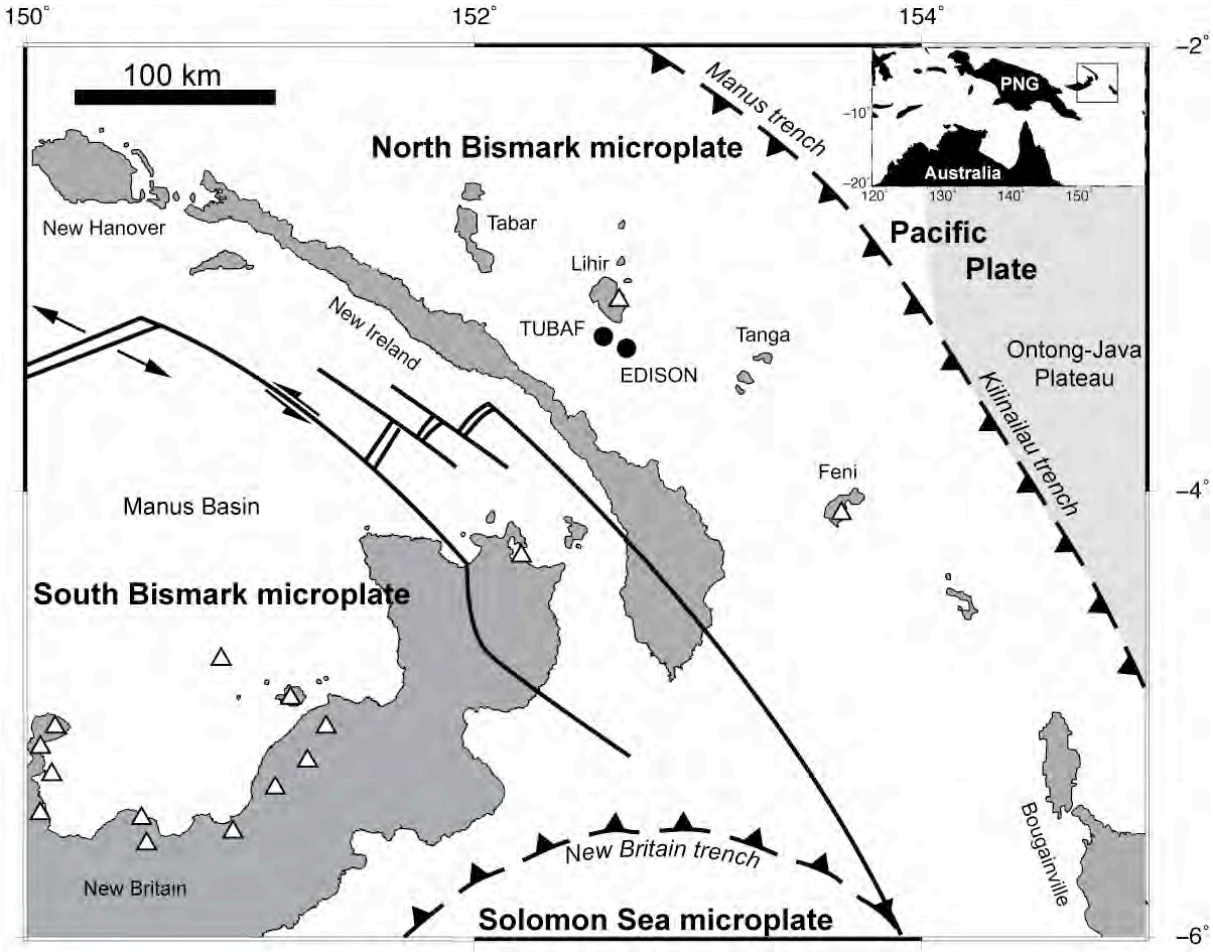
150°
152°
154°
−2°
−4°
−6°
100 km
Manus trench
North Bismark microplate
PNG
Australia
−10°
−20°
120°
130°
140°
150°
New Hanover
Tabar
Lihir
Pacific
Plate
TUBAF
EDISON
Tanga
New Ireland
Ontong-Java
Plateau
Kilinailau trench
Feni
Manus Basin
South Bismark microplate
New Britain trench
Bougainville
New Britain
Solomon Sea microplate

Figure 1

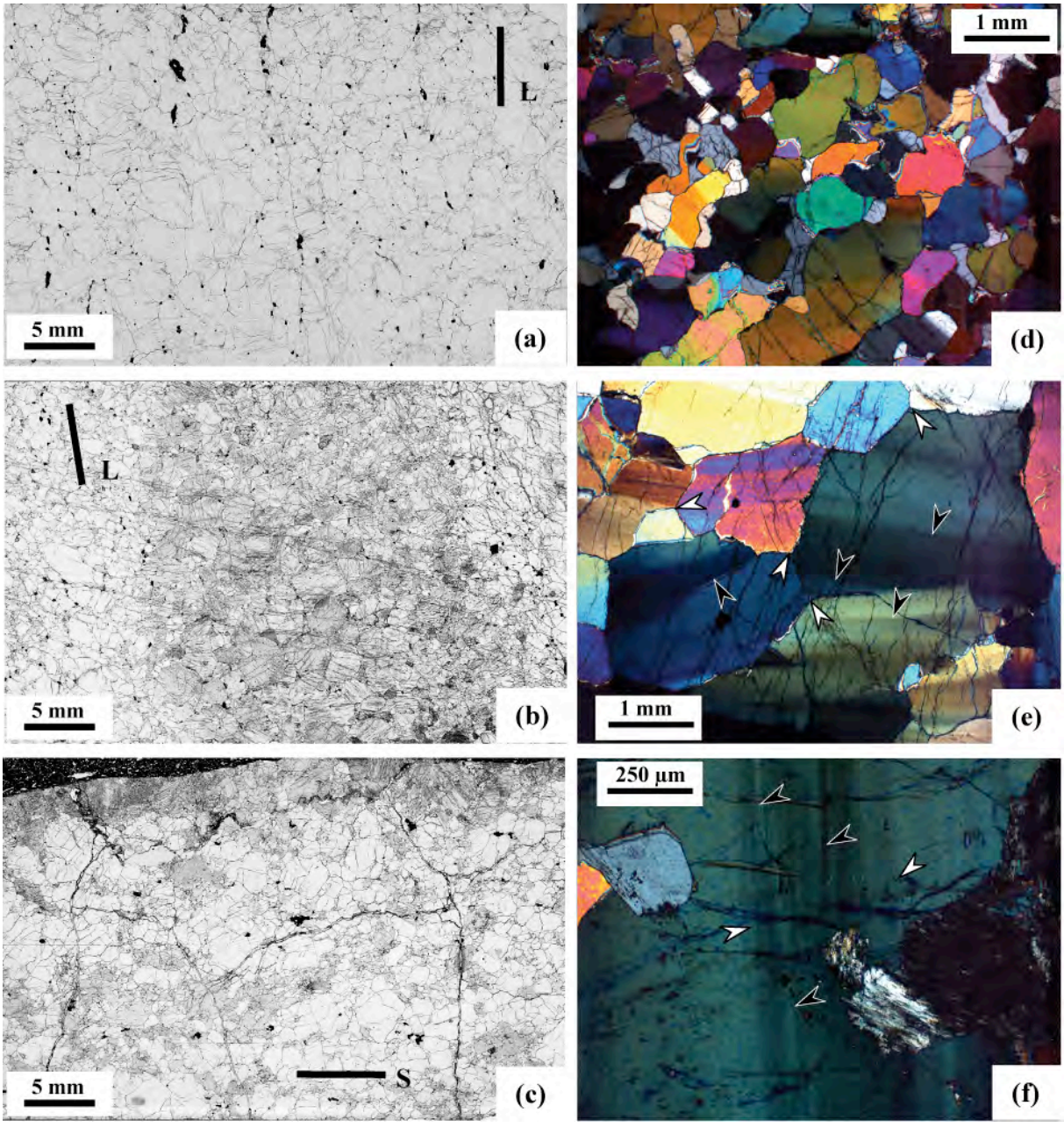

Figure 2

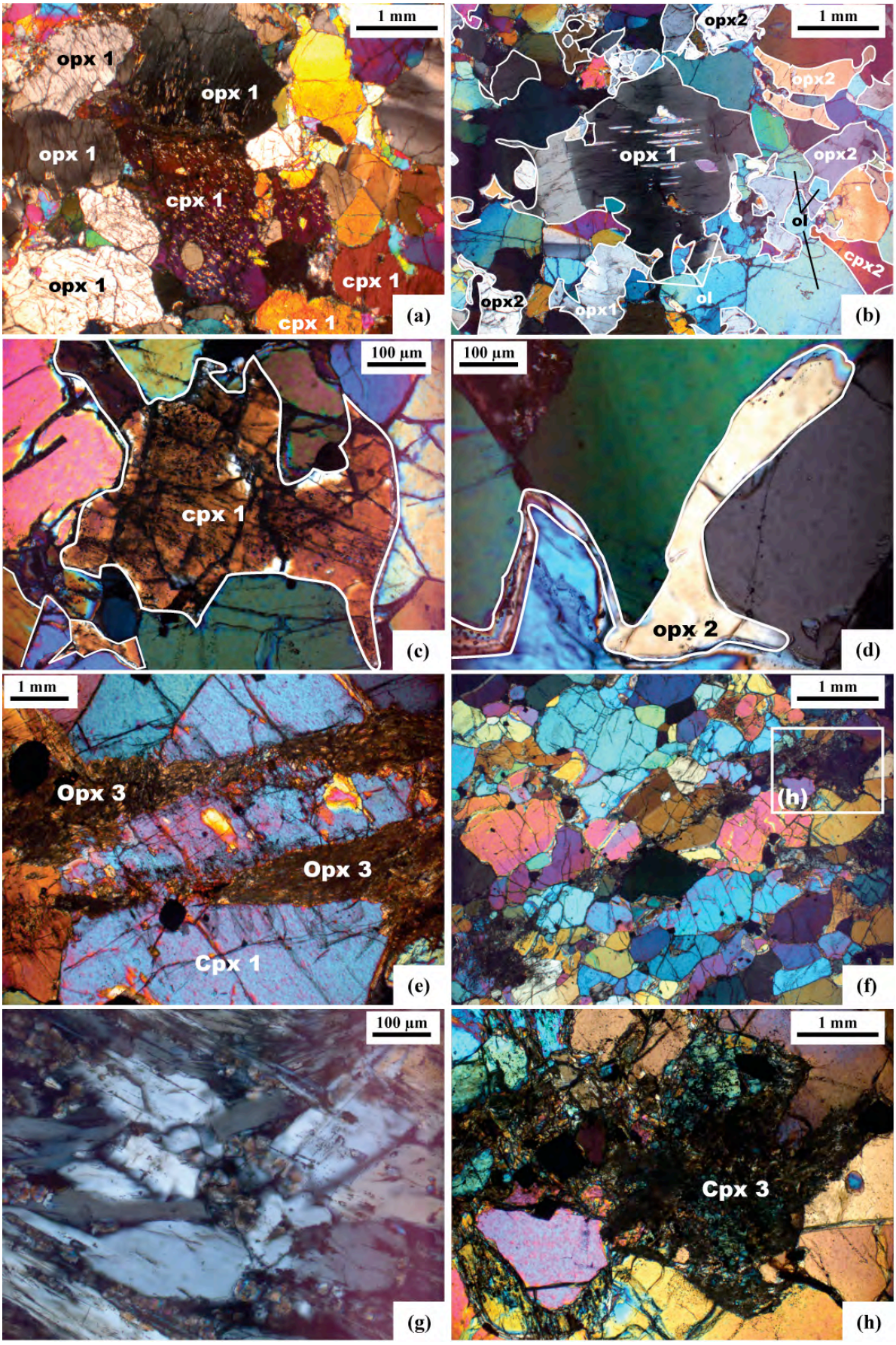
1 mm
opx 1
opx 1
opx 1
cpx 1
opx 1
cpx 1
cpx 1
(a)
opx2
1 mm
opx2
opx 1
opx2
ol
cpx2
opx2
opx1
ol
(b)
100 µm
cpx 1
(c)
100 µm
opx 2
(d)
1 mm
Opx 3
Opx 3
Cpx 1
(e)
1 mm
(h)
(f)
100 µm
(g)
1 mm
Cpx 3
(h)

Figure 3

Olivine
Orthopyroxene
Clinopyroxene
[100]
[010]
[001]
55-2B J=10.46
54-2A J=9.25
56-2A J=7.79
55-2A J=5.24
54-2D J=4.13
56-2H J=3.44
56-2T J=3.34
33-2A J=3.25

Figure 4

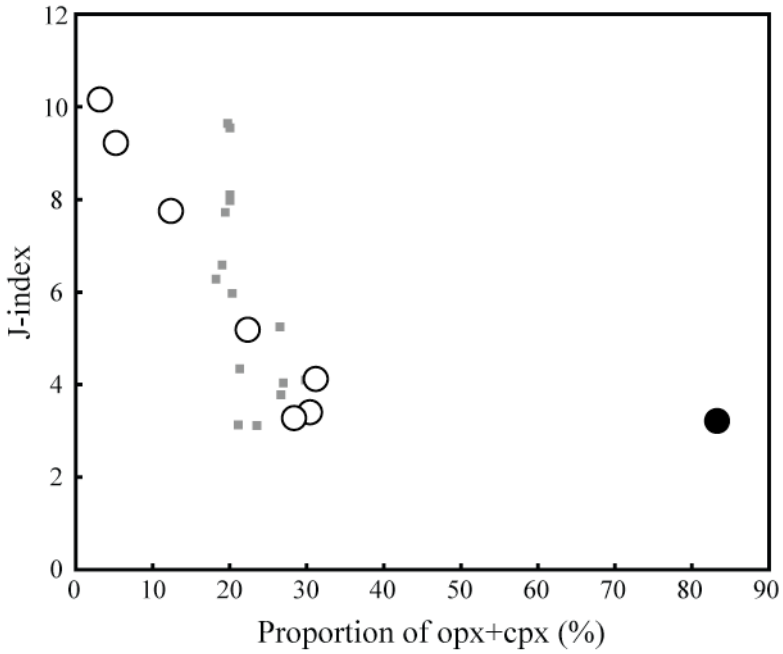
J-index
Proportion of opx+cpx (%)
0
2
4
6
8
10
12
0
10
20
30
40
50
60
70
80
90

Figure 5

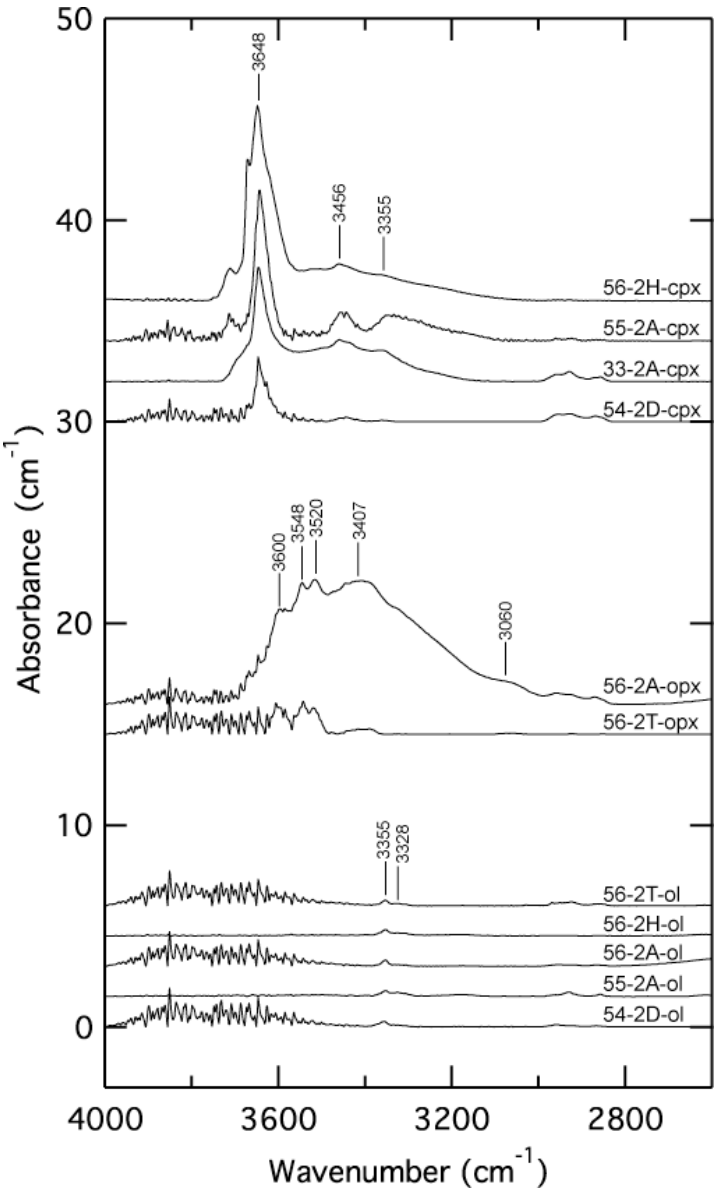
50
40
30
20
10
0
Absorbance (cm-1)
4000
3600
3200
2800
Wavenumber (cm-1)
3648
3456
3355
56-2H-cpx
55-2A-cpx
33-2A-cpx
54-2D-cpx
3600
3548
3520
3407
3060
56-2A-opx
56-2T-opx
3355
3328
56-2T-ol
56-2H-ol
56-2A-ol
55-2A-ol
54-2D-ol

Figure 6

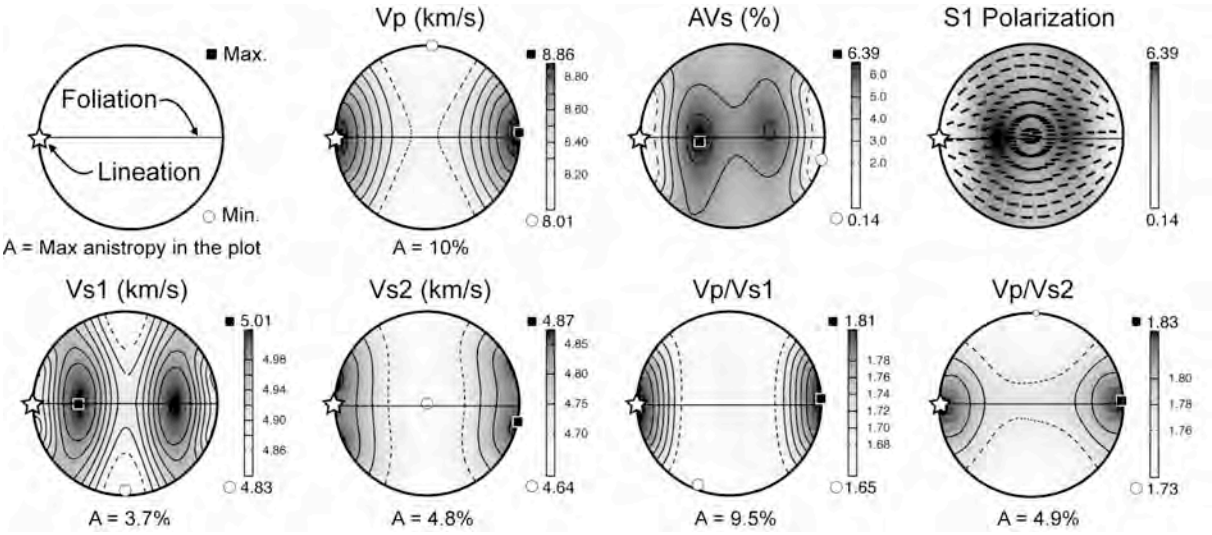
Max.
Foliation
Lineation
Min.
A = Max anistropy in the plot
Vp (km/s)
8.86
8.80
8.60
8.40
8.20
8.01
A = 10%
AVs (%)
6.39
6.0
5.0
4.0
3.0
2.0
0.14
S1 Polarization
6.39
0.14
Vs1 (km/s)
5.01
4.98
4.94
4.90
4.86
4.83
A = 3.7%
Vs2 (km/s)
4.87
4.85
4.80
4.75
4.70
4.64
A = 4.8%
Vp/Vs1
1.81
1.78
1.76
1.74
1.72
1.70
1.68
1.65
A = 9.5%
Vp/Vs2
1.83
1.80
1.78
1.76
1.73
A = 4.9%

Figure 7

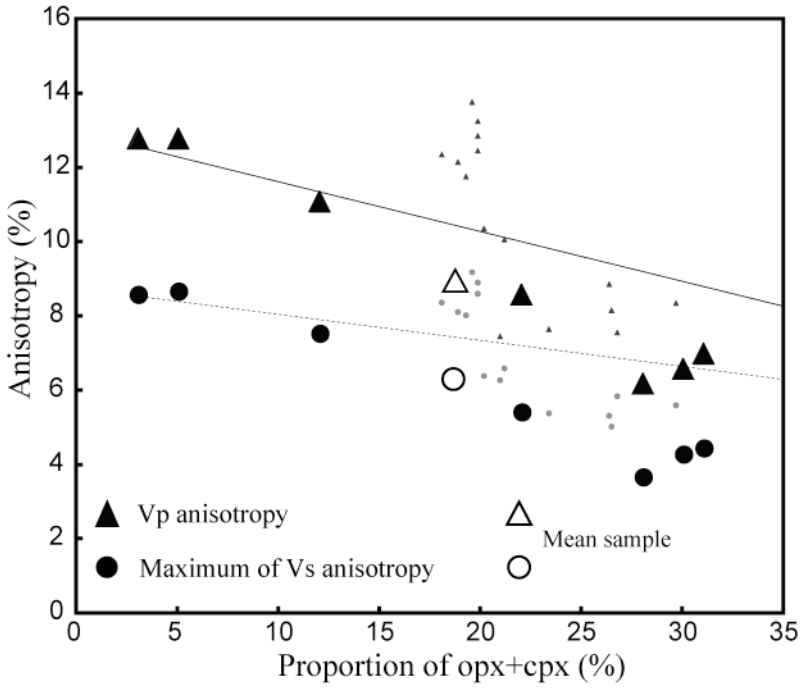
Anisotropy (%)
Proportion of opx+cpx (%)
Vp anisotropy
Maximum of Vs anisotropy
Mean sample

Figure 8

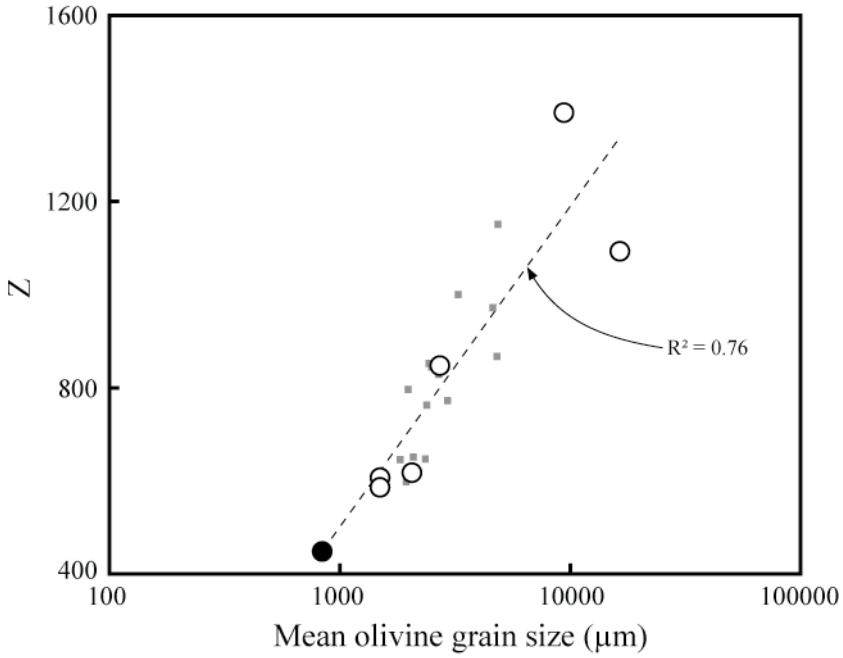
1600
1200
800
400
Z
100
1000
10000
100000
Mean olivine grain size (μm)
R² = 0.76

Figure 9

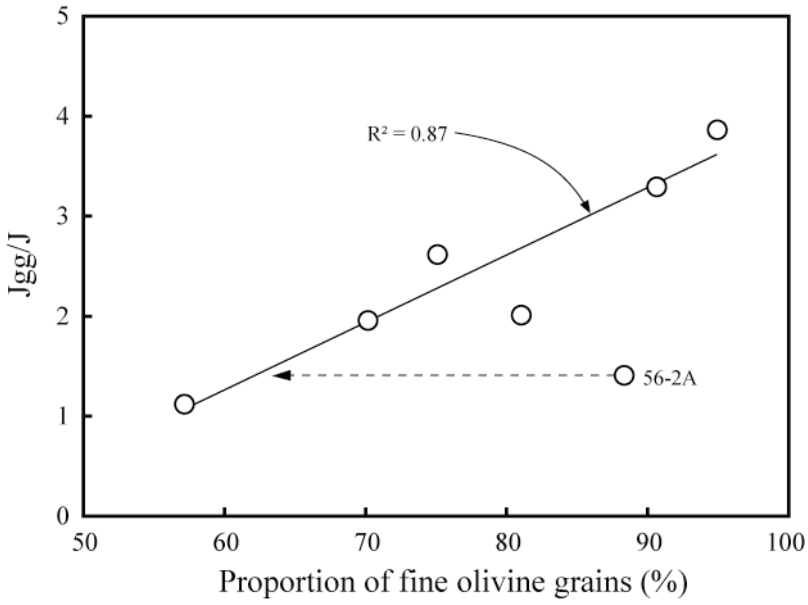
5
4
3
2
1
0
Jgg/J
R² = 0.87
56-2A
50
60
70
80
90
100
Proportion of fine olivine grains (%)

Figure 10

Table 1: olivine **g**rain size statistics (in μm)

Sample	Type	Olivine			Orthopyroxene			Clinopyroxene			Pyroxene
		Mean	Std.	Max.	Mean	Std.	Max.	Mean	Std.	Max.	content (%)
55-2B	D	1097	828	5291	0	0	0	485	84	649	3
54-2A	D	1396	1130	8300	0	0	0	463	127	716	5
56-2A	Hz	632	485	3607	0	0	0	0	0	0	12
55-2A	Hz	850	644	4397	605	402	2777	491	299	2130	22
54-2D	Lz	607	325	4525	432	253	1861	486	204	1850	31
56-2H	Lz	587	530	6060	452	348	3816	364	259	2254	30
56-2T	Hz	622	490	5503	586	442	3056	286	101	662	28
33-2A	O-Cpx	451	146	1316	343	198	818	684	528	4116	83

Data calculated from EBSD map and corrected by the geometric factor (1.2,Van der Wal et al., 1993)

Samples are classified in function of their J-index (cf. Fig. 6)

Std : standard deviation

Max = Maximum olivine grain size

Table 2: Water contents in olivine, orthopyroxene and clinopyroxene

Sample	Mineral	Microscope	Aperture size** (mm)	Section thickness (cm)	Water content* (wt ppm H_2O)	Water content* ($H/10^6$ Si)
33-2A	cpx-1	Hyperion	0.1x0.1	0.0320	204	2394
33-2A	cpx-2	Hyperion	0.1x0.1	0.0321	178	2091
33-2A	cpx-3	Hyperion	0.1x0.1	0.0322	117	1370
33-2A	cpx-4	Hyperion	0.1x0.1	0.0323	157	1845
33-2A	mean-cpx	-	-	-	166	1954
54-2A	ol-1	Hyperion	0.1x0.1	0.0315	1	22.52
54-2D	ol-1	Hyperion	0.1x0.1	0.0355	2	35
54-2D	ol-2	Hyperion	0.1x0.1	0.0355	1	21
54-2D	ol-3	Hyperion	0.1x0.1	0.0355	1	18
54-2D	cpx-1	Hyperion	0.1x0.1	0.0355	77	902
54-2D	cpx-2	Hyperion	0.1x0.1	0.0355	78	922
54-2D	mean-ol	-	-	-	2	25
54-2D	mean-cpx	-	-	-	78	912
55-2A	ol-1	Type A590	0.105	0.0280	4	68
55-2A	ol-2	Type A590	0.105	0.0280	3	51
55-2A	ol-3	Type A590	0.105	0.0280	2	32
55-2A	ol-4	Type A590	0.105	0.0280	2	32
55-2A	ol-5	Type A590	0.105	0.0280	3	45
55-2A	ol-6	Type A590	0.105	0.0280	2	26
55-2A	ol-7	Type A590	0.105	0.0280	1	24
55-2A	ol-8	Type A590	0.105	0.0280	1	23
55-2A	cpx-1	Type A590	0.120	0.0280	169	2028
55-2A	cpx-2	Type A590	0.120	0.0280	253	3045
55-2A	mean-ol	-	-	-	2	34
55-2A	mean-cpx	-	-	-	216	2462
56-2A	ol-1	Hyperion	0.1x0.1	0.0348	2	30
56-2A	ol-3	Hyperion	0.1x0.1	0.0348	1	18
56-2A	ol-4	Hyperion	0.1x0.1	0.0348	1	19
56-2A	opx-1	Hyperion	0.1x0.1	0.0348	431	4890
56-2A	mean-ol	Hyperion	-	-	1	24
56-2H	ol-1	Type A590	0.105	0.0330	2	33
56-2H	ol-2	Type A590	0.105	0.0330	2	36
56-2H	ol-3	Type A590	0.105	0.0330	2	35
56-2H	ol-4	Type A590	0.105	0.0330	2	26
56-2H	ol-5	Type A590	0.105	0.0330	2	26.985
56-2H	cpx-1	Type A590	0.105	0.0330	378	4443
56-2H	cpx-2	Type A590	0.105	0.0330	382	5875
56-2H	opx-1	Type A590	0.105	0.0330	249	2771
56-2H	mean-ol	-	-	-	2	30.944
56-2H	mean-cpx	-	-	-	380	4470
56-2T	ol-1	Hyperion	0.1x0.1	0.0353	1	18
56-2T	ol-2	Hyperion	0.1x0.1	0.0353	1	20
56-2T	ol-3	Hyperion	0.1x0.1	0.0353	2	32
56-2T	opx-1	Hyperion	0.1x0.1	0.0353	39	447
56-2T	opx-2	Hyperion	0.1x0.1	0.0353	38	431
56-2T	mean-ol	-	-	-	2	26
56-2T	mean-opx	-	-	-	39	439

*= using the calibration of Paterson (1982), water contents have ± 30% error

**Squared and circular aperture are noted with the form 0.1x0.1 and 0.105, respectively

Chapitre 5

Caractérisation des interactions entre déformation et transport réactionnel de fluides enrichis en silice par une approche expérimentale

5.1. Introduction

Les échantillons étudiés dans les chapitres précédents montrent une forte interaction entre la déformation et la percolation réactive de magma ou de fluides silicatés dans les roches du manteau supérieur en zone de supra-subduction. Les observations majeures sont : (1) la cristallisation des produits de réaction (pyroxènes secondaires) dans des bandes parallèle au structures de déformation, (2) la réduction de taille de grain de l'olivine dans ces zones de réaction , et (3) la réduction de l'intensité des OPR de l'olivine en fonction du degré d'enrichissement en pyroxène, ce qui implique une diminution de l'anisotropie sismique. Nous avons fait un certain nombre d'hypothèses pour expliquer ces caractéristiques. Ces hypothèses sont largement basées sur des études expérimentales où le magma est en équilibre avec la matrice solide (e.g., Hirth & Kohlstedt, 1995b; Holtzman et al., 2003a; Holtzman et al., 2003b; King et al., 2010). Cependant, les mécanismes de déformation des minéraux, de ségrégation magmatique, de réduction de taille de grain, lorsque l'on déforme une matrice solide en présence d'un fluide ou d'un magma en déséquilibre pétrologique avec celle-ci, n'ont jamais été explorés par des méthodes expérimentales.

Pour à cette problématique, j'ai entrepris une série d'expériences où un agrégat d'olivine est déformé en présence d'un fluide très riche en silice. Nous voulions tester si ceci entraine la cristallisation d'enstatite aux dépens de l'olivine selon la réaction :

$$Mg_2SiO_4 + SiO_2 \Rightarrow 2\ MgSiO_3$$

observée dans les xénolites du Kamchatka et de Papouasie Nouvelle Guinée. Cette réaction est possible dans le manteau supérieur car la composition des silicates dissous dans les fluides aqueux montre un forte composante enrichie en SiO_2 (Nakamura & Kushiro, 1974; Ryabchikov et al., 1982).

La principale difficulté pour préparer ces expériences concernait la génération du fluide. Dans le système SiO_2-H_2O, différents travaux montrent que le quartz est fusible ou dissout dans un fluide aqueux à partir de 1100°C pour des pressions inférieures à 500 MPa (e.g., Kennedy et al., 1962; Hack et al., 2007). Il faut aussi que le fluide ou le magma soit réparti de manière homogène dans l'agrégat afin d'étudier les interactions entre percolation et ségrégation qui pourrait être guidée par la déformation. Les échantillons expérimentaux sont donc composés d'un mélange de poudre d'olivine et de quartz, et d'eau distillée (cf. chapitre 5.2.2).

Pour réaliser ces expériences une presse de “Paterson” est utilisée. Cet appareil de haute pression et haute température permet de travailler aux températures qui règnent dans l’asthénosphère (maximum 1250°C) et sous des conditions hydrostatiques. Les mesures de contrainte sont très précises, et les échantillons sont volumineux (2-3 cm^3) ce qui rend l’observation des texture *post-mortem* aisée (c.f. chapitre 5.2.1)

Ce travail reste exploratoire et ne prétend pas résoudre entièrement la problématique étudiée. Le but était tout d'abord de s'initier à l'expérimentation en essayant de mettre en place un protocole satisfaisant pour ce type d’expériences. En effet, l’observation des textures, les mesures de l’OPR des minéraux ainsi que l’étude des données mécaniques montre que les résultats obtenus ne permettent pas de répondre aux questions initiales sur les interactions entre déformation et percolation réactive de fluides silicatés. Ces expériences permettent néanmoins de proposer des améliorations importantes à apporter au protocole expérimental.

5.2. Méthodes expérimentales et d’analyse

5.2.1. La presse Paterson

Un premier prototype de la presse de “Paterson” a été conçu par le Prof. Mervin S. Paterson (Paterson, 1970; Paterson, 1990) dans les années 1970, qui le commercialise depuis les années 1980. Aujourd’hui, 16 presses de Paterson sont en activité sur l’ensemble de la planète, pour l’essentiel dans des laboratoires de géologie. C’est un appareil de haute pression composé d’une enceinte à pression de gaz et équipé d’un chauffage interne (Figure 5.1). Le milieu de confinement est un gaz inerte: l’argon. Cette presse comporte un piston de déformation mobile à sa base permettant d’effectuer des expériences en compression uniaxiale, ainsi qu’un capteur de force interne (c’est-à-dire également sous pression, mais non chauffé) à l’enceinte de haute pression ce qui élimine une grande partie des imprécisions dues aux frottements lors des mesures effectuées avec un capteur de force externe. (Fig. 5.1). L’enceinte est suffisamment volumineuse afin de permettre l’utilisation d’échantillons de taille relativement importante pour le domaine des hautes pressions (jusqu’à 3 cm^3). Les échantillons ont, pour une expérience standard, une taille de ~ 20 mm de long pour 10 mm de diamètre. Le four utilisé est de « fabrication maison »; il est composé de 3 enroulements indépendants de fil de molybdène enroulés autour d’un tube d’alumine dense, et entouré de laine d’alumine. Le four est calibré après fabrication et également avant chaque série d’expériences pour garantir une zone de température quasi-constante (+/- 1-2 °C) sur une

longueur de 30 mm centrée sur l'échantillon. En effet, le gradient de température se doit d'être inférieur à 2°C sur toute la hauteur de l'échantillon afin d'assuré l'obtentions de données rhéologiques de qualité (déformation homogène avec une contrainte différentielle à ± 3 MPa).

La Presse Paterson de Géosciences Montpellier permet de travailler à des températures de 500-1250°C, des pressions de confinement de 100-450 MPa, généralement <300 MPa et à des taux de déformation allant de 10^{-3} à $10^{-6,5}$ s^{-1}. La résolution sur les mesures de déplacement et de forces est, respectivement, de 2 µm et 10 N.

Comparé à d'autres types de presses, celle-ci possède de nombreux avantages pour effectuer des expériences de déformation:

- Le milieu de confinement étant gazeux, la pression de confinement est réellement hydrostatique.
- La taille importante des échantillons (de l'ordre du centimètre cube).
- La stabilité et l'homogénéité de la température sur la toute la longueur de l'échantillon.
- Il n'y a que très peu de frottement entre le capteur de force interne et la colonne de déformation.

Ce type d'appareil présente néanmoins un désavantage non négligeable lorsque l'on travaille sur des processus mantelliques : la pression est limitée à 450 MPa, alors qu'il serait nécessaire de travailler à plus de 1 GPa pour caractériser le manteau supérieur.

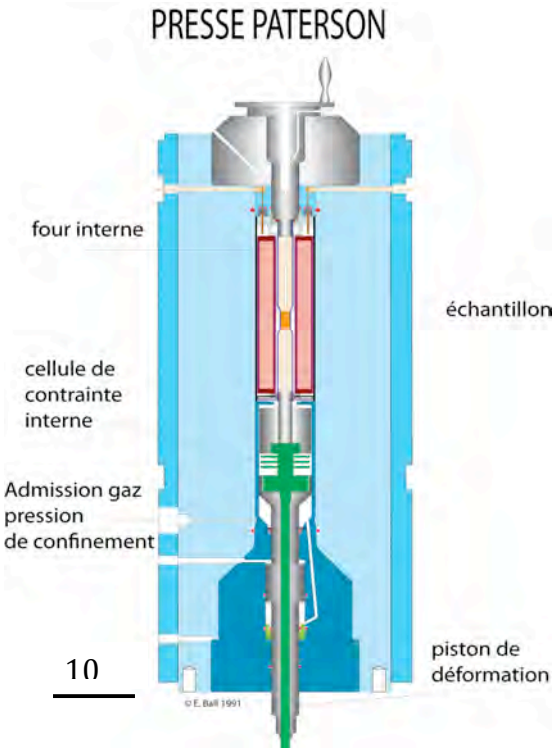

Figure 5.1 : Schémas représentant les

5.2.2. Préparations des expériences

La principale difficulté pour préparer ces expériences est de produire un fluide ou un magma enrichi en silice capable de réagir avec l'olivine pour créer de l'enstatite. De plus, ce fluide doit être réparti initialement de manière homogène dans l'agrégat afin d'étudier une possible ségrégation guidées par la déformation. Pour réaliser ces expériences l'idéal est donc de fabriquer un agrégat cristallin d'olivine et de quartz ou de silice amorphe hydratée.

Les échantillons sont donc composés d'un mélange:

- d'olivines de San Carlos (Arizona) de taille millimétrique pulvérisées par un broyeur à énergie fluide (Gribb & Cooper, 1998; Sundberg &Cooper, 2008) afin d'obtenir une poudre avec une taille de grain très fine et relativement homogène (2-10 µm). Une poudre fine est nécessaire afin d'obtenir une densification efficace (< 3% de porosité) durant les expériences de frittage à chaud (T >1200 °C).
- De la poudre de quartz (fournisseur Sigma Aldrich, 99.9% SiO_2) avec une taille de grain initiale d'environ 40 µm, cette dernière a ensuite été réduite par broyage manuel pendant au moins 20 minutes dans un mortier avec pilon en agate.
- D'eau distillée pour les expériences en conditions hydratées.

Avant mélange, les poudres sont séchées dans une étuve à 70°C pendant plus de 24h. La proportion de chaque poudre et la quantité d'eau distillée injectée sont détaillées dans le tableau 5.1. Le mélange est effectué manuellement dans le mortier en agate.

Deux types de capsules ont été utilisés:

- Pour les expériences en conditions hydratées, deux cylindres de nickel capables de s'emboîter parfaitement et fermés chacun à une extrémité sont utilisés comme capsule (Fig. 5.2). L'épaisseur finale de 1 mm de nickel en haut et en bas de la capsule permet d'éviter des pertes en eau importantes. On la nommera capsule double.
- Pour les expériences en conditions anhydres, un cylindre de nickel fin scellé à chaque extrémité par un disque de nickel (Fig. 5.2). On la nommera capsule simple.

Les dimensions de l'échantillon et des deux types de capsules avant expérience sont données dans le tableau 5.1 et figure 5.2.

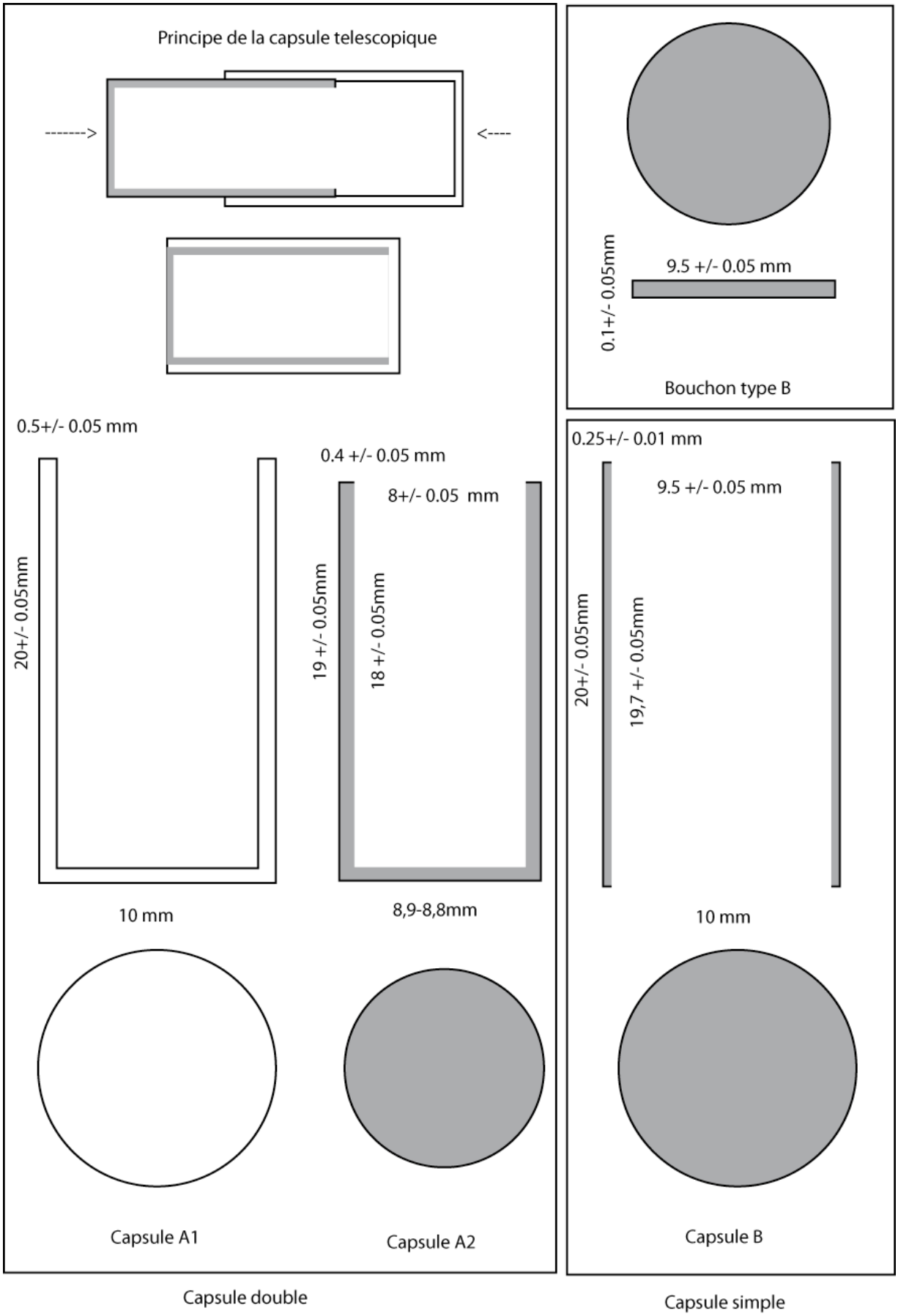

Figure 5.2 : Schémas et dimensions des capsules en Ni double et simple.

Une fois dans leur capsule, les mélanges de poudres sont frittés à froid (température ambiante) sous une pression uniaxiale de 200 MPa, par couches successives d'environ 2 mm. La double-capsule est ensuite placée dans la colonne schématisée dans la figure 5.3. Cet assemblage de pistons dans une jaquette en fer permet de transmettre la contrainte à l'échantillon. Celui-ci est encadré par deux disques d'alumines, puis par deux pistons biseautés d'alumines, deux pistons de zircone et enfin viennent les pistons en acier; des joints toriques supérieur et inférieur assurent l'étanchéité de la colonne. Les pistons d'alumine, de zircone et d'acier sont troués en leur centre pour permettre le passage du thermocouple de type-N (NiCrSi/NiSi) qui mesure la température à 3 mm de l'échantillon. Le rôle de la jaquette est double, elle permet de maintenir en place l'assemblage et de garantir l'étanchéité. En effet, sous l'effet de la pression de gaz, la jaquette est écrasée contre les pistons, l'échantillon et les joints.

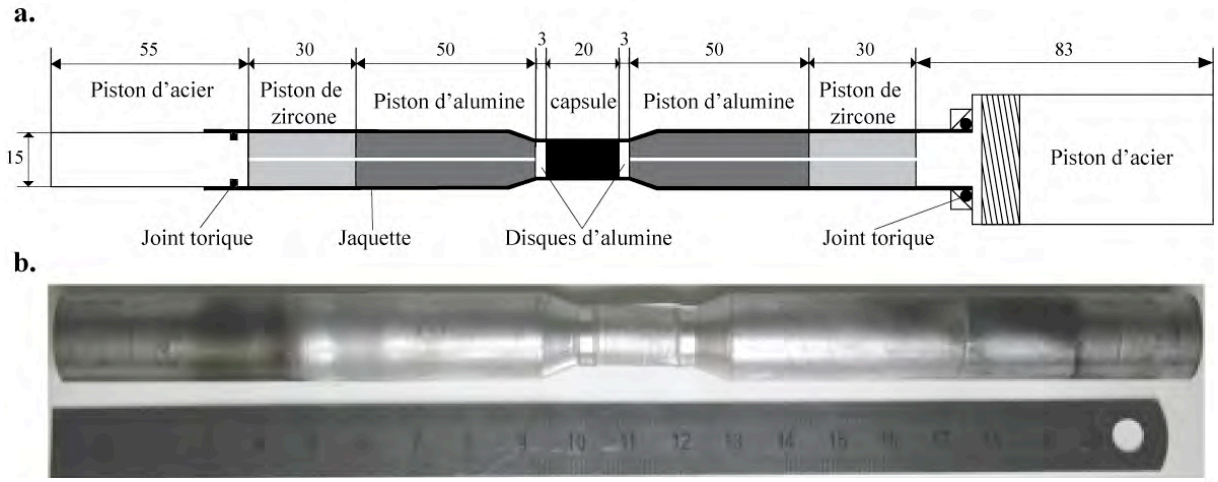

Figure 5.3 : (a) coupe schématique d'un assemblage échantillon, les cotes sont en millimètre. (b) photographie de l'assemblage de l'échantillon VSE1 après frittage à chaud. 300 MPa, 1200°C.

Les expériences de frittage à chaud sont faites à 1200°C, sous une pression de confinement de 300 MPa pendant 2 ou 3h (Tab. 5.1). La montée en température est faite à une vitesse ~10 °C/min. L'oxydation de la capsule de nickel permet de contrôler la fugacité d'oxygène autour du tampon Ni-NiO ce qui représente une valeur de $fO_2=10^{-2,6}$ Pa (O'Neill, 1987; Demouchy et al., 2007) au conditions de notre étude expérimentale. L'eau rajoutée à la poudre d'olivine et de quartz permet d'atteindre une fugacité d'eau maximale de 326 MPa (calculée en utilisant l'équation d'état de l'eau pur de (Pitzer & Sterner, 1994). À la fin de chaque expérience, la jaquette en fer et la capsule de nickel sont dissoutes dans de l'eau régale

(mélange à volume égal d'acide chlorhydrique et nitrique). Les lames minces sont ensuite coupées selon le diamètre de la section basale, dans la longueur de l'échantillon.

Trois échantillons ont subi une compression uniaxiale sous un taux de déformation constant (10^{-5} s^{-1}) sous une pression de confinement de 300 MPa et une température d'environs 1200°C. La trempe s'effectue par la diminution de la puissance électrique alimentant le four (100 °C/min), avec en parallèle une diminution de la pression de confinement (25 MPa/min).

Tableau 5.1: Conditions expérimentales et données mécaniques. Pression de confinement= 300±3 MPa

Ech. #	Capsule	Compo*	Type d'exp**	T (°C)	Duré (h:min)	Taux de def (s^{-1})	Contrainte déviatorique (MPa)	Déformation (%)
VSE1	double[1]	1	fc	1200	3:18			
VSE2	double	1	fc	1190	3:05			
			déf	1200	3:00	$1{,}02 \times 10^{-5}$	0	11
VSE3	double	1				Problème technique		
VSE4	double	2	fc	1215	2:00			
VSE5	double	2				Problème technique		
VSE6	double	2	fc	1216	2:20			
			déf	1220	2:50	$1{,}13 \times 10^{-5}$	53	10.2
VSE7	simple[2]	3	fc	1205	2:04			
VSE8	simple	3	fc	1210	2:24			
			def	1210	3:06	$1{,}04 \times 10^{-5}$	63	11.4

**Composition 1: matériel de départ: San Carlos olivine96%, quartz4%+40µl H2O.*

**Composition 2: matériel de départ: San Carlos olivine94%, quartz6%+40µl H2O.*

**Composition 3: matériel de départ: San Carlos olivine94%, quartz6% (anhydre)*

***fc: fritté à chaud ; déf: éxpérience de déformation en compression uniaxiale*
[1]Dimensions: longueur: 18 mm ; Diamètre: 8 mm
[2]Dimensions: longueur: 18 mm ; Diamètre: 10 mm

5.2.3. Traitement des données mécaniques et techniques d'analyse

Durant les expériences de déformations, la température, la pression, le déplacement et les forces interne et externe sont mesurés toutes les secondes. Le logiciel LabView permet d'enregistrer ces paramètres en temps réel. Sur la presse Paterson de Géosciences Montpellier, les forces sont mesurées en kilogramme-force, elles sont ensuite converties en Newton (1 kgf = 9,8 N). Comme la vitesse de déplacement est constante et que l'on connaît la longueur initiale de l'échantillon, il est aisé de calculer le taux de déformation. Le calcul de la contrainte déviatorique (σ) est plus délicat. Durant les expériences, la force s'applique sur tout l'assemblage (fer, nickel et échantillon), il faut alors effectuer une correction en soustrayant de la force totale mesurée (enregistrer *in-situ* par le capteur de force interne), la

force appliquée sur la capsule en nickel et celle sur la jaquette en fer pour ne garder que celle qui est appliquée sur l'échantillon. La contrainte appliquée sur l'échantillon est donc :

$$\sigma_{éch} = \frac{F_t - \sigma_{Ni} A_{Ni} - \sigma_{Fe} A_{Fe}}{A_{éch}}$$

où F_t est la force totale mesurée. σ_{Ni} et σ_{Fe}, sont les contraintes appliquées respectivement sur la capsule et la jaquette. La température, la vitesse de déformation ($\dot{\varepsilon}$) et la pression de confinement étant connues, il est possible de calculer σ_{Ni} et σ_{Fe} à partir de leurs lois de fluage de haute température (Frost & Ashby, 1982). $A_{éch}$, A_{Ni} et A_{Fe} sont les aires respectives des sections perpendiculaires à l'axe compression de l'échantillon, de la capsule et de la jaquette. La déformation étant en compression uniaxiale, l'échantillon cylindrique, la capsule, et la jaquette voient leur longueur diminuer et l'aire de leur section perpendiculaire à l'axe de compression augmenter, car le volume reste constant. Connaissant la variation de la hauteur de l'échantillon ainsi que son volume initial, on peut calculer $A_{éch}$, A_{Ni} et A_{Fe} à chaque pas de mesure. On obtient alors $\sigma_{éch}$ et la quantité de déformation (ε en %), ce qui permet de constituer les courbe de déformation traditionnelles.

Les concentrations en eau ont été obtenues par Spectroscopie Infra-Rouge à Transformé de Fourier (IRTF) au Laboratoire des Verres Colloïdes et Nanomatériaux (LVCN) de l'université de Montpellier II. La méthode utilisée est identique à celle décrite dans les chapitres 3 et 4. Cependant, ce type d'analyse nécessite une épaisseur de plusieurs centaines de micromètres libre de joints de grain. Un grain témoin d'olivine d'environ 3 mm de diamètre a donc été intégré dans l'échantillon VSE1, et, après expérience, poli jusqu'à une épaisseur de 300 µm suivant deux faces parallèles.

L'étude des textures et microstructures, la détermination des phases en présence ainsi que la mesure des orientations préférentiellement de réseaux des minéraux ont été faites avec un microscope à balayage (MEB) couplé à un système EBSD (système d'analyse de la diffusion des électrons rétro-diffusés). La méthode d'acquisition de données est similaire à celle décrite dans les chapitres précédents, cependant l'appareillage est différent. C'est un MEB CamScan X500FE CrystalProbe à pression variable appartenant à Géoscience Montpellier qui permet la mesure d'orientations cristallines (par EBSD) à très haute résolution (10 à 50 nm selon le matériel analysé). Contrairement au JEOL JEM5600, l'échantillon est placé dans la chambre d'analyse en position horizontale, le canon à électron est donc incliné de 70° par rapport à la verticale afin d'obtenir la géométrie idéale pour les analyses EBSD. Pour les mesures sur les échantillons expérimentaux, la tension est de 20 kV,

la distance focale d'environ 27 mm, et la pression dans la chambre pendant les analyses de 4-5 Pa. Le pas d'échantillonnage est de 0,5 µ m. Durant la période où les analyses des échantillons ont été faites, le CamScan X500FE CrystalProbe a subit des problèmes techniques récurrents. Les échantillons n'ont donc pas pu être tous analysés et certaines cartes sont incomplètes. Le taux d'indexation des cartes varie de 40 à 86%.

5.3 Résultats

5.3.1. Données mécaniques

Les mesures de force données par le capteur de force interne en fonction du temps pour les expériences de déformation VSE2, VSE6 et VSE8 sont présentées dans la figure 5.4. La vitesse de déplacement étant constante, il est alors possible de relier directement le temps et la quantité de déformation. Ce qui marque en priorité sur cette figure, est la différence entre les forces mesurées sur VSE2 qui sont très faibles (0,2-0,3 kN) comparé à VSE6 et VSE8, où les forces mesurées peuvent atteindre jusqu'à 4 kN. La figure 5.4c, où les corrections de jaquette et capsule ont été faites, montre que la contrainte déviatorique appliquée à VSE2 est inférieure ou égale à 0, ce qui signifie que toute la déformation a été accommodé par la jaquette en fer et la capsule de nickel. Ceci a été confirmé après l'expérience: la capsule exhibait deux bourrelets de nickel au contact des disques d'alumine, alors que l'échantillon n'avait subit aucun raccourcissement vertical. La capsule utilisée avait donc une épaisseur de nickel trop importante à chaque extrémité (~1 mm). Ceci nous a amené à modifier fabrication des capsules doubles (polissage pour avoir une épaisseur de 0,2 mm de Nickel aux extrémités) et réaliser deux nouvelles expériences. Pour les échantillons VSE6 et VSE8, on observe une augmentation brutale et quasi linéaire de la force appliquée jusqu'à environ 2000 s, puis la courbe s'infléchit. La force appliquée sur VSE8 est en moyenne plus importante de 8-10 MPa que sur VSE6. À partir de 5000 s, les deux courbes montrent des oscillations d'amplitude relativement importante (jusqu'à 1 kN) et corrélées à la variation de la température. En effet, sur cette période, la température était instable et a varié de ± 10 °C par rapport à la moyenne. Quelque soit l'expérience, pour chaque pic et creux de température (Figure 5.4b), il apparaît respectivement, entre 150 et 200 s plus tard, un creux et un pic de force (Figure 5.4a). Ces faibles variations de températures, dues à une instabilité du four, ont donc probablement induit les oscillations observées sur les courbes de force internes.

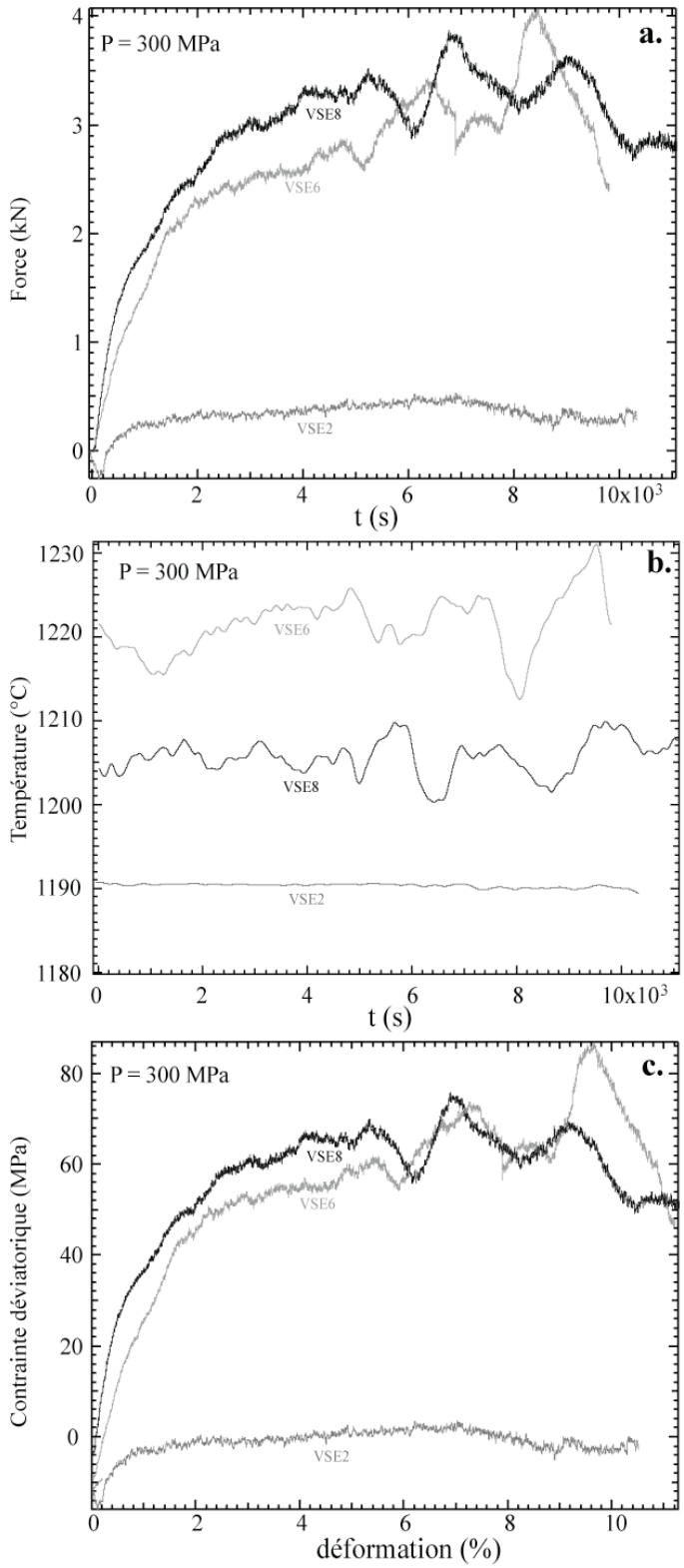

Figure 5.4: Courbes de déformation pour des agrégats d'olivine + quartz en conditions anhydres ou hydratées. (a) Force mesurée et (b) température appliquée sur l'assemblage de déformation en fonction du temps. (c) Contrainte déviatorique appliquée sur l'échantillon, calculée après correction des forces appliquées sur la capsule en nickel et la jaquette en fer, en fonction du pourcentage de déformation.

La contrainte déviatorique sur l'échantillon calculée pour chaque expérience en fonction du pourcentage de déformation est donnée dans la figure 5.4c. VSE2 n'ayant subit qu'une déformation de la capsule en nickel, nous nous intéresserons uniquement à VSE6 et VSE8. Pour une déformation inférieure à 0,2%, la contrainte est négative. Ceci est dû à la déformation de la capsule de nickel en contact avec les disques d'alumine ; plus elle est épaisse, plus la valeur négative sera importante. Si elle est trop épaisse, on ne déforme que la capsule comme pour VSE2. Jusqu'à environ 1,5% de déformation, les deux courbes sont quasiment linéaires et ont une pente forte. Cela correspond à la partie élastique de la déformation. Au-delà, le seuil de plasticité est atteint entre 40 et 60 MPa, les pentes décroissent et tendent à former un plateau. On atteint presque l'état d'équilibre (*quasi* steady-state). Cependant, à partir d'environ 6% de déformation, et à cause de l'instabilité en température du four, il n'est plus possible d'atteindre un réel état stationnaire. Une moyenne faite entre 3% et la valeur de déformation maximale donne néanmoins une bonne estimation de la contrainte déviatorique pour laquelle l'échantillon se déforme plastiquement. Les valeurs obtenues sont respectivement de 53 et 63 MPa pour VS6 et VS8 (Figure 5.4c et Tableau 5.1). Les oscillations de température induisent une incertitude de +/- 10 MPa.

5.3.2. Phases en présence, textures et microstructures

Seuls 4 échantillons ont été analysés par le MEB-EBSD (VSE4, VSE6, VSE7 et VSE8). Tous présentent une forte proportion d'olivine (>94%) et une très faible proportion de quartz et d'orthopyroxène (<6%). Ces deux phases étant mal indexées, il n'est pas possible d'avoir une estimation précise de la proportion de chacune, néanmoins l'enstatite semble être respectivement plus présente que le quartz dans les expériences en déformation et moins abondante que celui-ci dans les expériences dans des conditions statiques (Figure 5.5). Le polymorphe de l'enstatite qui cristallise sous les conditions de pression et de température des expériences (~300 MPa, ~1200 °C) est la protoenstatite (e.g., Smyth, 1974; Presnall, 1995). Smyth (1974) montre que la protoenstatite n'est pas stable à basse température, et que si la trempe se fait en quelques secondes ou plusieurs heures, elle se déstabilise respectivement en clinoenstatite ou orthoenstatite. Les expériences étudiées sont trempées en une douzaine de minutes, les deux phases ortho- et clinoenstatite devraient donc être présentes, cependant la clinoenstatite n'a jamais était formellement identifiée lors des analyses EBSD. Le polymorphe de l'enstatite présent dans les échantillons expérimentaux est donc essentiellement de l'orthoenstatite.

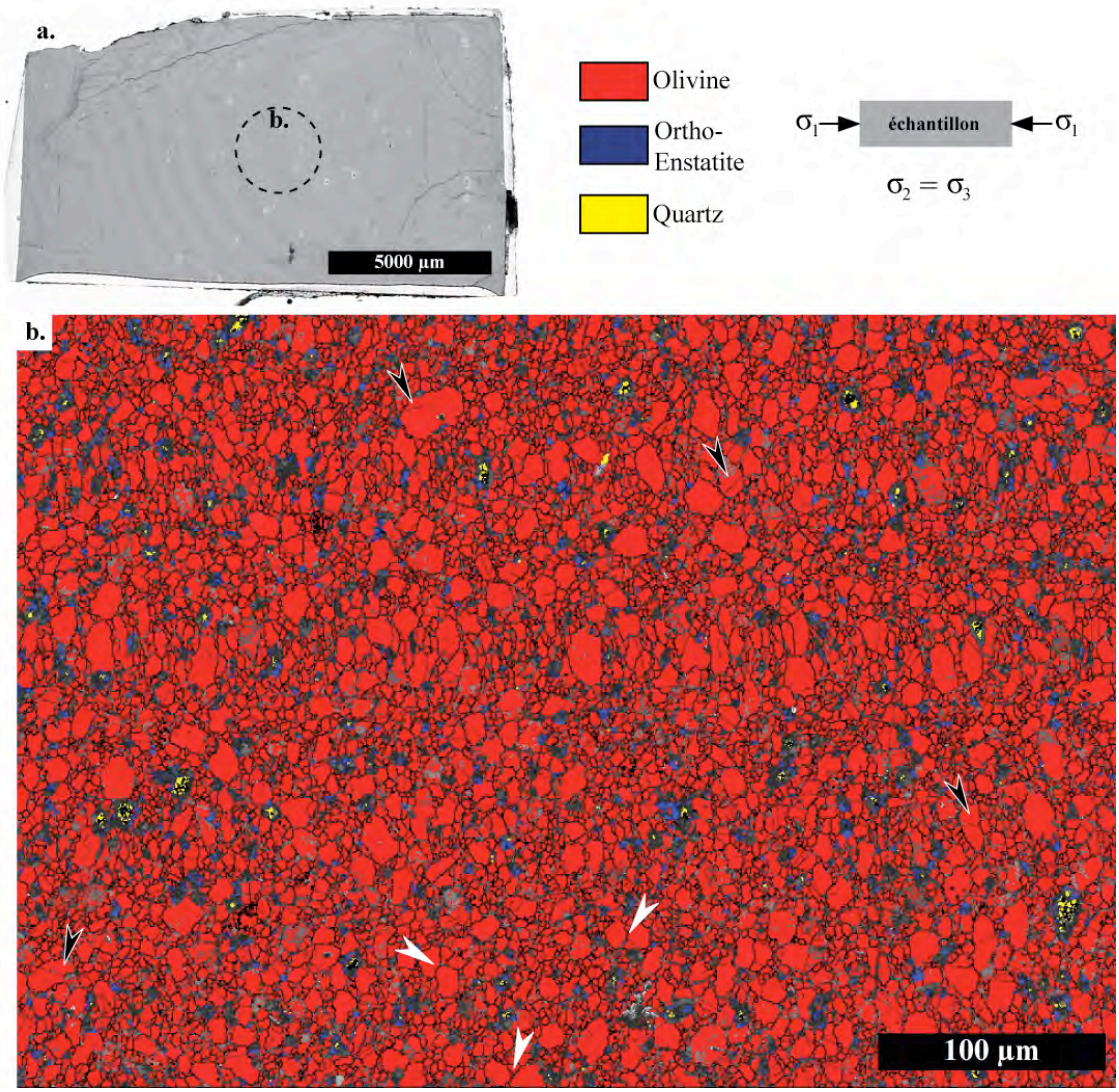

Figure 5.5: (a) Photographie de la lame mince taillée dans l'échantillon VSE6. Le cercle en pointillé indique la zone où se localise la carte EBSD (b). (b) carte EBSD montrant les phases en présence. Les flèches blanches et noires montrent respectivement les joints triples à 120° et les cristaux contenant des sous-joints. La bande horizontale d'olivines allongées perpendiculairement à la direction de compression résulte d'un problème de distorsion de l'image lors de l'indexation et non d'une déformation. L'indexation sur cette carte est de 86%.

La carte EBSD des phases minérales et orientations de l'expérience VSE6 est présentée dans la figure 5.5. Les autres cartes sont moins bien indexées, mais la figure 5.5 est représentative des textures observées dans les autres échantillons, déformés ou non. Quelque soient les conditions expérimentales, l'olivine montre une taille de grain allant de 2 à 30 µm. La moyenne se situe autour de 7,5 µm. Dans tous les échantillons, la répartition des grains de différents diamètres semble aléatoire. Les olivines présentent des joints de grain sinueux qui, très rarement, peuvent devenir rectilignes et former des joints triples à 120° (Figure 5.5). À part quelques rares gros cristaux d'olivine qui montrent des sous-joints dans les échantillons déformés, aucune microstructure de déformation n'a été identifiée. Les cristaux d'olivine dans

les échantillons déformés ne montrent pas d'aplatissement clair perpendiculairement à la direction de compression.

Les cristaux d'orthoenstatite et de quartz étant moins bien indexés, il est difficile d'établir une statistique de taille de grains correcte. Les données MEB-EBSD indiquent des tailles des grains allant de 2 à 11 µm pour le quartz et de 1 à 25 µm pour l'orthoenstatite. Les cristaux de quartz sont répartis aléatoirement dans les échantillons. Ils forment souvent des agrégats qui n'ont certainement pas été désagrégés lors du mélange des poudres. Les joints de grain quartz-quartz dans ces agrégats sont sinueux. Le quartz n'est que très rarement en contact avec l'olivine, ayant presque toujours une couronne d'orthoenstatite. Les cristaux d'orthoenstatite apparaissent aussi parfois isolés. Dû aux problèmes d'indexation, la forme des grains d'orthoenstatite reste indéterminée. Aucune microstructure de déformation n'a été identifiée dans les cristaux de quartz et d'orthoenstatite.

5.3.3. Orientation préférentielle de réseau

Quelque soit les conditions de l'expérience, l'olivine montre une faible OPR; cette dernière est néanmoins cohérente entre les différents échantillons (Figure 5.6). Les axes [100] forment une guirlande dans le plan perpendiculaire à la direction de compression (elle est identique pour le fritté à froid et les expériences de déformation). Les axes [001] montrent une tendance similaire mais moins marquée. Les axes [010] sont préférentiellement orientés parallèlement à la direction de compression. L'olivine présente donc une OPR dite axiale-[010] cohérente avec le régime de déformation imposé.

Comme pour l'olivine, tous les échantillons montrent une OPR de l'orthoenstatite. Cependant, celle-ci est plus forte que les OPR de l'olivine (Figure 5.6). Les axes [001] montrent une orientation préférentielle dans le plan d'extension dans une direction faisant un angle de 30-45° avec le plan de la lame mince. Le maximum de concentration des axes [010] fait un angle très faible avec la direction de compression. Cette tendance est bien marquée pour les échantillons VSE6 et VSE7, alors que l'orientation préférentielle de réseau de l'orthoenstatite est quasiment aléatoire pour VSE4 et faible pour VSE8. Excepté pour VSE4, les axes [100] montrent une orientation préférentielle dans le plan d'extension à peu près perpendiculaire à celle des axes [001].

Seul l'échantillon VSE6 montre une OPR du quartz. Elle reste néanmoins relativement faible. Le maximum de concentration des axes [001] se situe dans le plan d'extension et fait un faible angle avec la perpendiculaire au plan de la lame mince. Les autres échantillons ne montrent pas clairement une orientation préférentielle de réseau du quartz.

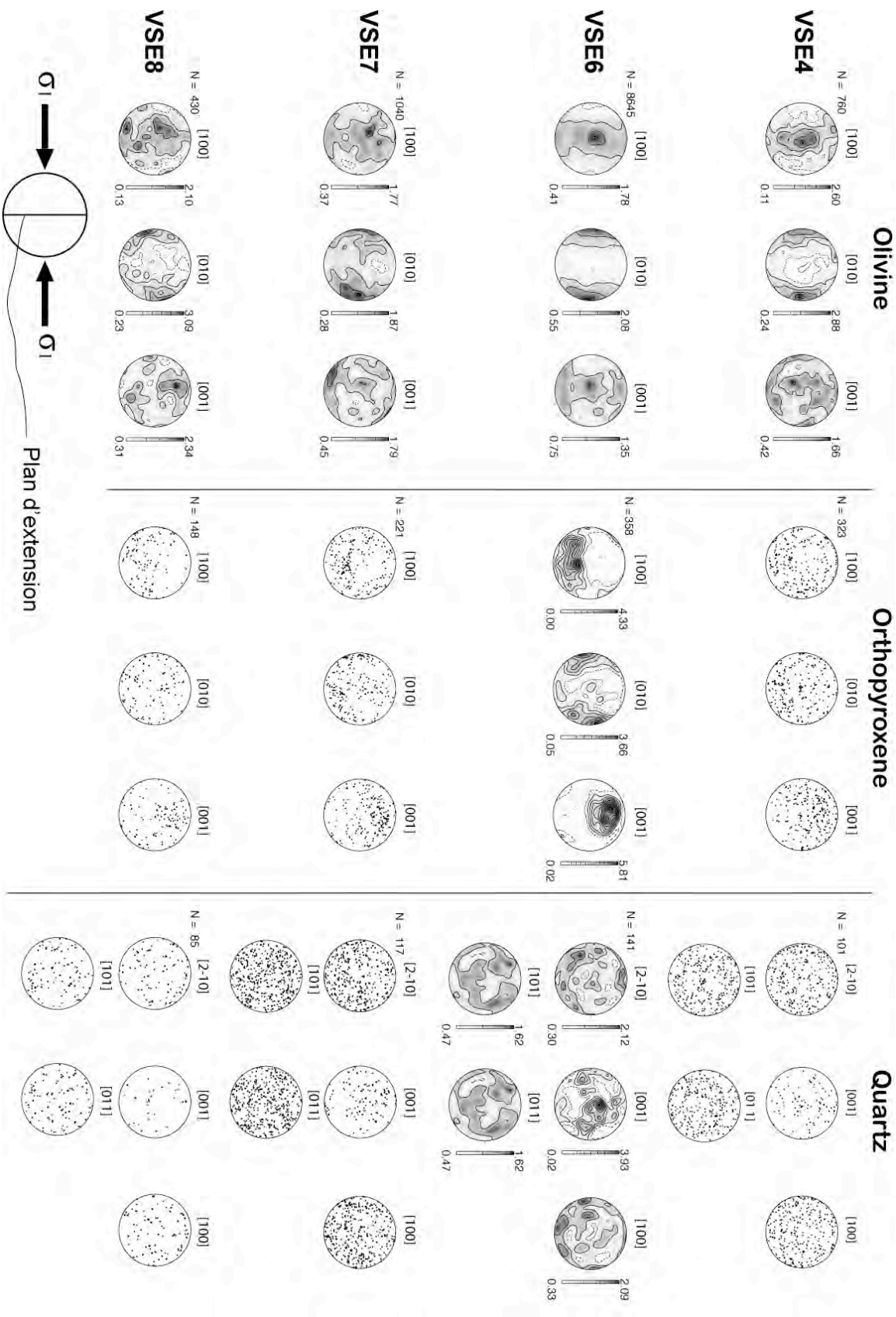

Figure 5.6: Orientations préférentielles de réseau de l'olivine, de l'orthoenstatite et du quartz des échantillons VSE4, VSE6, VSE7 et VSE8. Projections stéréographiques dans l'hémisphère inférieur, les contours sont montré pour 0,5 multiples de la distribution uniforme, N correspond au nombre de grain mesuré.

5.4 Discussion - conclusion

5.4.1 Déformation en présence d'un fluide réactif et/ou d'eau ?

Les échantillons expérimentaux étudiés sont composés d'environ 94% d'olivine. C'est donc ce minéral qui contrôle la rhéologie. Lorsque un agrégat d'olivine est déformé en présence d'eau ou de faible proportion de magma, la contrainte déviatorique nécessaire pour le déformer à une vitesse de déformation donnée (résistance mécanique) baisse considérablement (Blacic, 1972; Mackwell et al., 1985; Karato et al., 1986; Hirth & Kohlstedt, 1995a; Hirth & Kohlstedt, 1995b; Mei & Kohlstedt, 2000a; Mei & Kohlstedt, 2000b; Mei et al., 2002; Zimmerman & Kohlstedt, 2004). À partir de l'équation (2) présentée dans partielle chapitre 1.2.2, il est possible de construire les lois de fluage de l'olivine pour des conditions de pression et température et pour des tailles de grain qui correspondent aux expériences de déformation VSE6 et VSE8 (Figure 5.7). Les paramètres utilisés pour tracer les lois de fluage d'un agrégat d'olivine en présence d'eau, de faible fraction de magma ou sans ni l'un ni l'autre proviennent, respectivement, des travaux de Mei & Kohlstedt (2000a; 2000b), Hirth & Kohlstedt (1995a; 1995b) et Hirth & Kohlstedt 2003). Le comportement rhéologique des échantillons VSE6 et VSE8 peut être parfaitement expliqué par les lois de fluage établies pour un agrégat d'olivine anhydre et sans magma (figure 5.7). La différence de contrainte déviatorique (~10 MPa) calculée sur ces deux échantillons s'explique par la différence de température (10°C) entre les deux expériences mettant en évidence la sensibilité de la rhéologie de l'olivine à la température. Ces résultats montrent que ces échantillons n'ont pas été déformés dans des conditions sursaturées en eau, différemment des expériences de Mei & Kohlstedt (2000a,b), et que si une fusion partielle a eu lieur, celle-ci a produit des concentrations en magma très faibles. Ceci implique que les capsules utilisées pour les expériences hydratées ne sont donc pas efficaces pour garder l'eau dans le système, ou alors que fugacité en eau n'était pas assez importante pour modifier la rhéologie de l'olivine et/ou provoquer la fusion ou la dissolution du quartz.

Afin de mesurer la concentration en eau dans l'olivine, un monocristal d'olivine d'environ 300 µm a été placé dans l'échantillon VSE1. Cependant, suite à un problème de polissage il n'a pas pu être correctement analysé. Il n'est donc actuellement pas possible de connaître la concentration en eau dans les olivines des expériences hydratées.

Une autre hypothèse pour expliquer le comportement mécanique de type "anhydre" de ces agrégats serait la formation d'un fluide riche en silice qui aurait réagit avec l'olivine

entrainant la déshydratation de celle ci durant le fritté à chaud, avant l'application de la contrainte déviatorique. Si tel est le cas, la présence de quartz à la fin des expériences tend à montrer que l'hydratation des échantillons n'était pas suffisante pour le dissoudre totalement. Par ailleurs, les couronnes d'orthoenstatite systématiques autour du quartz suggèrent plutôt une réaction à l'état solide.

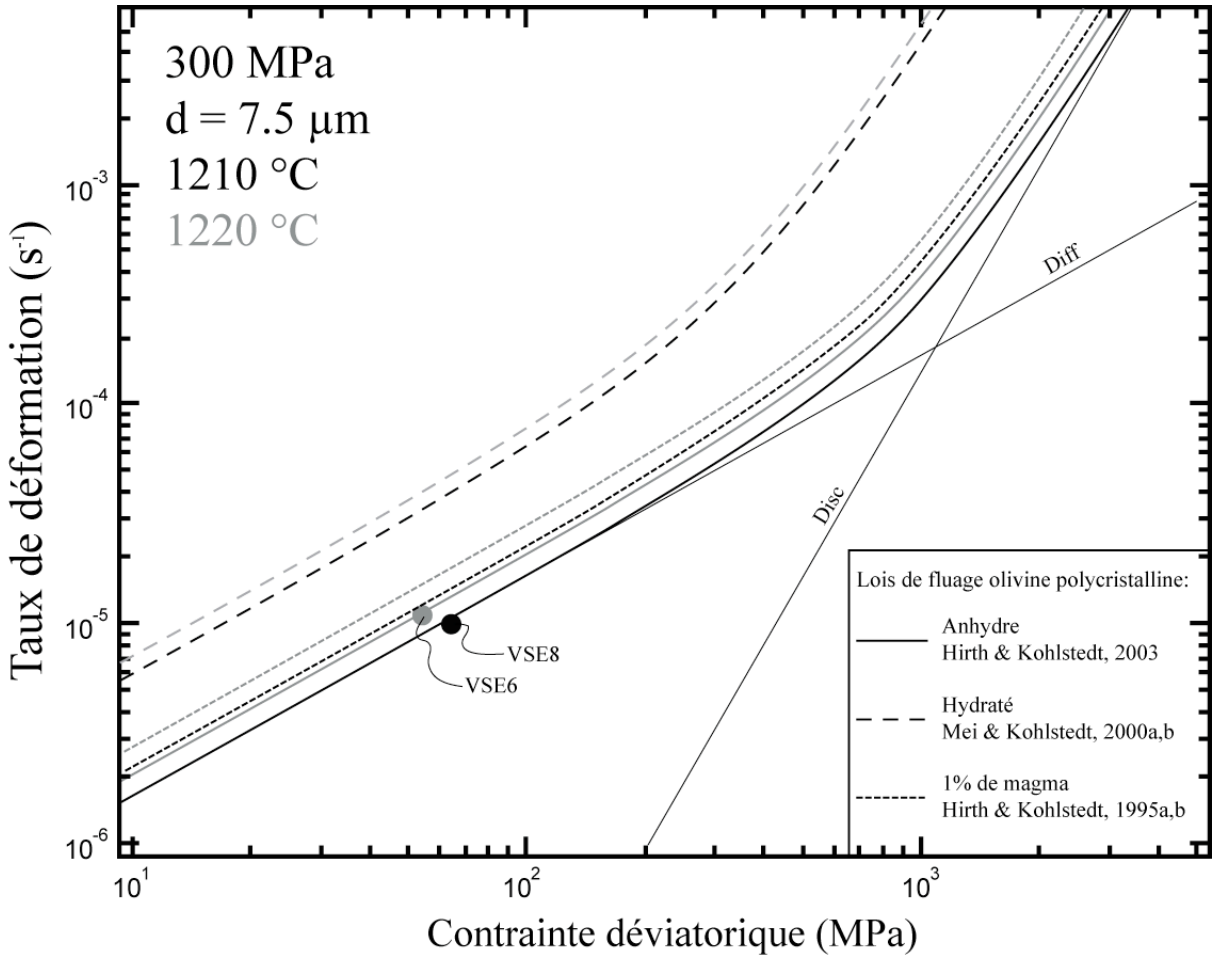

Figure 5.7: Comparaison entre les données mécaniques des échantillons VSE6 et VSE8 et les lois de fluages calculées pour un agrégats d'olivine anhydre, hydraté, ou contenant 1% de magma, en utilisant les pression, températures et tailles de grain des expériences de déformation. Les courbes nommées "Disc" et "Diff" correspondent respectivement aux termes $\dot{\varepsilon}_{diffusion}$ et $\dot{\varepsilon}_{dislocation}$ de l'équation (2) décrite dans la partie 1.2.2 pour la loi de fluage d'un agrégat d'olivine anhydre déformé à 1210 °C.

5.4.2 Mécanismes de déformation

Les OPR axiales-[010] de l'olivine sont cohérentes avec une déformation en compression uniaxiale (e.g., Tommasi et al., 1999). Ces OPR sont aussi semblables à celles

que l'on obtient après un fritté à froid (D. Mainprice, communication personnelle, 2010). Le fait que les OPR de l'olivine soient similaires entre les échantillons des expériences en conditions statiques et dynamiques signifie que l'OPR a été acquise durant le fritté à froid et que l'essentiel de la déformation a été accommodé par des processus de diffusion. L'absence de microstructures de déformation dans la plupart des cristaux d'olivine, excepté les plus gros appuie cette hypothèse. Les donnés mécaniques, qui montrent que les échantillons ont été déformés dans les domaines de contrainte et taux de déformation où le comportement rhéologique de l'agrégat est essentiellement contrôlé par la loi de fluage diffusion, corrobore également cette hypothèse (Figure 5.7).

Comme pour l'olivine, les OPR de l'orthoenstatite sont similaires dans les échantillons déformés ou non. Ceci indique que cette OPR ne résulte pas d'une déformation à haute température, ni à basse température étant donné que l'orthoenstatite n'est pas présente lors du fritté à froid. Pour les mêmes raisons, l'hypothèse d'une cristallisation orientée sous contrainte est écartée. Un phénomène d'épitaxie entre l'orthoenstatite et l'olivine ou le quartz pourrait expliquer ces OPR. Cependant l'analyse des OPR d'orthoenstatite ne met pas en évidence des corrélations claires. On observe seulement un parallélisme du maximum des axes [010] de l'orthoenstatite et de l'olivine, et, seulement pour l'échantillon VSE6, le maximum des axes [001] de l'enstatite fait un angle faible avec les axe [001] du quartz. Sans une étude détaillée des relations cristallographiques locales entre l'orthoenstatite et des minéraux voisins, qui reste encore à réaliser, il n'est pas possible de discuter cette hypothèse. Il sera néanmoins très complexe d'identifier des relations d'épitaxie car, lors des expériences, ce n'est pas l'orthoenstatite qui cristallise mais la protoenstatite. Une autre possibilité à prendre en compte pourrait être un biais d'échantillonnage. Même si ce problème est rare, il peut arriver que, pour une phase minéralogique donnée, une orientation particulière soit préférentiellement indexée par le MEB-EBSD. Nous prévoyons dans le futur d'analyser des lames coupées perpendiculairement à l'axe du cylindre pour tester cette hypothèse.

5.4.3 Conclusion

Cette série d'expériences ne permet pas de caractériser vraiment les interactions entre déformation et percolation réactive de magma ou de fluide. Les résultats montrent, en effet, que la cristallisation d'orthopyroxènes semble résulter au moins partiellement d'une réaction à l'état solide entre l'olivine et le quartz, plutôt qu'entre l'olivine et un fluide riche en silice. Les données mécaniques sont cohérentes avec des lois de fluage établies pour des agrégats

d'olivine anhydre et sans magma ou fluides. Les OPR de l'olivine et de l'orthopyroxène semblent avoir subit respectivement des biais de préparation et de mesure.

Ce travail permet néanmoins d'identifier et de résoudre des problèmes directement liés au protocole expérimental et aux analyses. Les solutions et améliorations à y apporter sont :

- Pour régler le problème de l'hydratation des échantillons afin de créer un fluide ou un magma riche en silice, il suffirait soit de mettre plus d'eau distillée (> 100 μL) s'il n'y a pas de problème d'étanchéité, soit d'améliorer le scellement des capsules (soudure à l'arc en gelant la capsule par bain d'azote liquide).
- L'olivine est déformée essentiellement par des processus de diffusion, ce qui ne correspond pas aux observations faites dans les échantillons naturels (cf. chapitre 2,3 et 4). Les mécanismes de déformations étant très sensible à la taille des cristaux (e.g., Mei & Kohlstedt, 2000a; Zhang et al., 2000; Hirth & Kohlstedt, 2003), une poudre avec des tailles de grains plus importante (>50 μm, idéalement 300-500 μm).
- Une étude cristallographique détaillée de l'orthopyroxene devrait permettre d'identifier quel polymorphe de l'enstatite est présent, et de voir si il y a des relations épitaxiques entre l'enstatite et l'olivine ou le quartz.
- L'identification d'un biais d'indexation de l'orthopyroxene peut être aisément mis en évidence en mesurant les OPR dans les lames coupées dans des orientations différentes relativement à l'axe du cylindre.

Ce travail était exploratoire. En effet, aucune étude expérimentale de ce type n'a encore été publiée. Les protocoles pour étudier cette problématique étaient à mettre en œuvre. Cette série d'expériences permettra donc, pour les études futures dans ce domaine, d'éviter un certain nombre de difficultés.

Chapitre 6

Conclusions et Perspectives

6.1 Conclusions

Ce travail apporte de nouvelles contraintes sur les interactions entre la déformation et les processus d'hydratation et de percolation de magma ou de fluides et leurs implications sur les propriétés sismiques dans le coin mantellique. Il se base sur l'analyse d'échantillons naturels. Les résultats obtenus sont quelque peu différents des études expérimentales qui étaient jusqu'à présent les seules méthodes utilisées pour répondre à cette question. Les résultats majeurs de cette étude ont des implications sur l'interprétation des directions de polarisation rapide des ondes S et des rapports Vp/Vs dans le manteau au-dessus des zones de subduction.

Deux types d'échantillons naturels ont été étudiés. Le premier est la zone des tectonites à spinelles du massif péridotitique de Ronda en Espagne (chapitre 2; Soustelle et al., 2009). Cette zone représente la partie lithosphérique du massif qui est séparée d'un domaine asthénosphérique ayant subit un fusion partielle et de recristallisation de grande ampleur par un front de recristallisation (Van der Wal & Bodinier, 1996; Van der Wal & Vissers, 1996; Garrido & Bodinier, 1999; Lenoir et al., 2001; Vauchez & Garrido, 2001). Cette configuration résulte d'un phénomène d'érosion thermique lié à un amincissement lithosphérique en contexte de subduction (C. Marchesi, communication personnelle 2010). Le deuxième type d'échantillon sont des xénolites de manteau équilibrées dans le domaine de stabilité du spinelle et extraites par des volcans situés au dessus d'une subduction active (Avacha, Kamchatka) ou stoppée récemment (Lihir, Papouasie-Nouvelle-Guinée). Ces échantillons étaient localisés au-dessus de la zone de fusion partielle du coin mantellique et ont donc subi la percolation des magma ou des fluides produits par la subduction (chapitre 3; Soustelle et al., 2010; chapitre 4). Il est donc possible de comparer les processus qui ont affecté les tectonites à spinelle de Ronda, les xénolites du Kamchatka et de Papouasie-Nouvelle-Guinée.

L'étude structurale, pétrologique et géochimique des tectonites à spinelles de Ronda montre que les magmas générés dans la zone de fusion partielle ont percolé et refertilisé ce domaine lithosphérique. Cet épisode de refertilisation se traduit pas la cristallisation d'orthopyroxène et de clinopyroxène (± spinelle) aux dépens de l'olivine. De telles réactions ont aussi été observées dans les xénolites de péridotites du Kamachatka et de Papouasie-Nouvelle-Guinée qui montrent respectivement un enrichissement en orthopyroxène et en orthopyroxène+clinopyroxène (±amphibole±phlogopite) qui s'est fait aux dépens de l'olivine.

Les différentes réactions suggèrent que les fluides ou magmas n'étaient pas de même nature selon les localités. Quelque soit leur provenance, les observation structurales et microstructurales dans toutes ces péridotites montrent que la percolation de fluide ou de magma ont été synchrone d'un événement de déformation à haute température sous de faibles contraintes (e.g., 13 MPa pour les xénolites du Kamchatka). Le parallélisme systématiquement observé entre les structures de déformation (foliation, linéation) et les zones d'enrichissement en pyroxènes d'échelle plurimétrique (Ronda) à millimétrique (xénolites) suggère qu'il y a eu un contrôle de la déformation sur la percolation. Ce processus a aussi été mis en évidence dans des expériences de déformation d'un agrégat cristallin en présence de magma (e.g., Holtzman et al., 2003a; Holtzman et al., 2003b; King et al., 2010), cependant le parallélisme entre les bandes enrichies en magma et les structures de déformation n'y est jamais observé.

Les olivines des tectonites à spinelles de Ronda montrent des OPR de type axiale [010] cohérentes avec le régime tectonique qui a affecté ce domaine lors de l'événement d'amincissement lithosphérique. Les olivines des xénolites du Kamchatka et de Papouasie-Nouvelle-Guinée ont, elles, des OPR de type axiale [100] qui résulterait de l'activation simultanée des plans de glissement (010) et (001). L'étude détaillée de ces OPR et l'observation des dislocations (chapitre 3; Soustelle et al., 2010) montrent que [100] est toujours la direction de glissement dominante dans l'olivine, et qu'elle est toujours parallèle à la linéation. Contrairement aux expériences, l'analyse des échantillons naturels montre que la déformation en présence de magma ou fluides n'implique pas une modification de l'OPR de l'olivine menant à une orientation préférentielle des [001] parallèlement à la direction de fluage. La mesure des concentrations et l'analyse de la solubilité de l'eau dans l'olivine aux conditions P,T correspondant au domaine de stabilité du spinelle, ainsi que l'estimation des paléo-contraintes sur les échantillons du Kamchatka, montrent que la faible hydratation des olivine a pu induire l'activation simultané des deux plans de glissement (010) et (001). Cependant, même pour une olivine saturée en eau dans le domaine de stabilité du spinelle, l'hydratation n'est pas suffisante pour que la direction de glissement dominante dans l'olivine évolue de [100] à [001]. La percolation réactive syn-cinématique de magma ou de fluide a néanmoins un impact non négligeable sur les OPR de l'olivine. En effet, la cristallisation des pyroxènes durant la déformation provoque une désorientation et une décroissance de la taille des cristaux d'olivine, ce qui entraine une baisse de l'intensité de l'OPR de l'olivine en fonction de la proportion modale de pyroxène.

Les propriétés sismiques ont été calculées seulement sur les xénolites de péridotites du Kamchatka et de Papouasie-Nouvelle-Guinée (chapitre 3; Soustelle & Tommasi, 2010; chapitre 4). Les systèmes de glissement dominants dans l'olivine pour ces échantillons étant {0kl}[100], cela implique que la direction de polarisation rapide des ondes S dans la partie supérieure du coin mantellique est parallèle à la direction d'écoulement du manteau. Cependant, la percolation réactive de fluide ou de magma a entrainé un enrichissement en pyroxène associé à une décroissance de l'intensité des OPR de l'olivine, ce qui a pour conséquence une baisse non négligeable de l'anisotropie. Si cette réduction n'est pas prise en compte, elle peut induire une sous-estimation de l'épaisseur de la couche anisotrope d'environs 25-35%. Un tel enrichissement en orthopyroxène a déjà été proposé pour expliquer les faibles rapports Vp/Vs (<1,7) observés dans le manteau avant arc de certaines zones de subduction. Cependant le calcul des variations du rapport Vp/Vs en fonction de la proportion d'orthopyroxène montre que ce processus ne peut permettre d'atteindre de telles valeurs. Les chapitres 3.2 (Soustelle & Tommasi, 2010) et 4 montrent que la prise en compte de l'anisotropie des ces péridotites, en considérant la géométrie de la déformation et les directions de propagation des ondes P et S dans le coin mantellique, permet d'expliquer des rapports Vp/Vs < 1.7.

L'enrichissement en pyroxène ne peut à lui seul expliquer la baisse d'anisotropie (cf. chapitre 4). Ce sont donc les mécanismes de déformation de l'olivine qui on été affectés durant la percolation réactive de fluide ou de magma. Cependant l'observation de ces échantillons naturels a seulement permis d'établir des hypothèses sur cette question. Le chapitre 6 est une étude exploratoire qui décrit une séries d'expériences dont le but était de déformer un agrégat d'olivine en présence d'un fluide riche en silice afin de provoquer une percolation réactionnelle syn-cinématique précipitant de l'enstatite aux dépens de l'olivine. Elles avaient pour objectif de contraindre les mécanismes de déformation de l'olivine lors d'une percolation réactive, et de voir si le déséquilibre entre le fluide et la matrice solide pouvait expliquer les différences observées entre les expériences de déformation magma/roche à l'équilibre et les échantillons naturels. Cependant, l'étude des échantillons expérimentaux montre que le protocole utilisé n'est pas encore au point.

6.2 Perspectives

Les résultats obtenus sur les deux séries de xénolites de manteau des zones de subduction du Kamchatka et de Papouasie-Nouvelle-Guinée sont très similaires. Ceci tend à suggérer que les processus d'interaction entre déformation et percolation réactive de fluide ou de magma décrits dans cette étude pourraient être étendues à l'ensemble des zones de subduction. Cependant, le contexte géodynamique pouvant être très différent d'une zone à l'autre, même si les xénolites échantillonnant le coin mantellique sont rares, ce type d'étude devrait être étendu à l'ensemble des zones où l'on trouve se type de roches afin de s'affranchir de chaque particularité et d'en tirer des généralités sur les processus de déformation du manteau en présences de magma ou de fluide et leur implication sur les propriétés sismiques.

Les échantillons étudiés lors de cette thèse sont tous des péridotites à spinelle. Cela signifie qu'ils nous renseignent uniquement sur les processus mantelliques qui se produisent à moins de ~70 km de profondeur. La pression a cependant un effet non négligeable sur e comportement de l'olivine, modifiant l'activité des systèmes de glissement (e.g., Mainprice et al., 2005) et la solubilité de l'eau (e.g.,Keppler & Bolfan-Casanova, 2006); ces processus entrainent tous les deux des modification de l'OPR et donc de l'anisotropie sismique. La pression joue aussi un rôle sur la composition des silicates dissouts dans les fluides (e.g., Nakamura & Kushiro, 1974; Ryabchikov et al., 1982), ce qui peut entrainer des variations sur les réactions et sur les angle diédraux, donc sur les mécanismes de percolation. Pour compléter notre compréhension de la déformation du coin mantellique il faudrait donc étudier des échantillons de péridotites à grenats. De telles roches ne peuvent être extraites par des volcans de zones de subduction actives car elle se situe bien en dessous du domaine où le magma migre par fracturation. Cependant, il arrive que des peridotites à grenat du coin mantellique soient exhumées le long du chenal de subduction et se retrouvent dans les zones de sutures des chaines de montagnes. C'est le cas, par exemple, des péridotites à grenat du massif d'Ulten dans les Alpes italiennes (Scambelluri et al., 2006).

Le travail expérimental démarré ici sur l'effet de la réaction sur les interactions entre déformation et percolation de fluide ou de magma nécessite d'être poursuivi. En effet, c'est un domaine qui a été encore très peu exploré et qui pourrait apporter de nombreuses réponses sur les mécanismes de déformation, non seulement dans le coin mantellique mais dans toutes les zones ou une matrice solide se déforme en présence d'un liquide pas à l'équilibre.

Références (hors articles)

Arai, S., Ishimaru, S. and Okrugin, V., 2003. Metasomatized harzburgite xenoliths from Avacha volcano as fragments of mantle wedge of the Kamchatka arc: Implication for the metasomatic agent. The Island Arc, 12(2): 233-246.

Arai, S. and Kida, M., 2000. Origin of fine-grained peridotite xenoliths from Iraya volcano of Batan Island, Philippines: deserpentinization or metasomatism at the wedge mantle beneath an incipient arc? Island Arc, 9(4): 458-471.

Arcay, D., Doin, M.P., Tric, E., Bousquet, R. and de Capitani, C., 2006. Overriding plate thinning in subduction zones: Localized convection induced by slab dehydration. Geochemistry Geophysics Geosystems, 7(2): doi:10.1029/2005GC001061.

Avé-Lallemant, H.G. and Carter, N.L., 1970. Syntectonic recrystallization of olivine and modes of flow in the upper mantle. Geological Society of America Bulletin, 81: 2003-2020.

Backus, G.E., 1965. Possible forms of seismic anisotropy of the uppermost mantle under oceans Journal of Geophysical Research, 70: 3429-3439.

Bai, Q., Mackwell, S.J. and Kohlstedt, D.L., 1991. High-Temperature Creep of Olivine Single-Crystals .1. Mechanical Results for Buffered Samples. Journal of Geophysical Research-Solid Earth and Planets, 96(B2): 2441-2463.

Ben Ismail, W. and Mainprice, D., 1998. An olivine fabric database: an overview of upper mantle fabrics and seismic anisotropy. Tectonophysics, 296: 145-158.

Benioff, H., 1949. Seismic evidence for the fault origin of oceanic deeps. The Geological Society of America Bulletin, 60(12): 1837-1856.

Blacic, J.D., 1972. Effect of water on the experimental deformation of olivine. In: H.C. Heard, I.Y. Borg, N.L. Carter and C.B. Rayleigh (Editors), Flow and Fracture of Rocks. Geophysical Monograph. American Geophysical Union, Washington, pp. 109-115.

Boudier, F., Baronnet, A. and Mainprice, D., 2010. Serpentine Mineral Replacements of Natural Olivine and their Seismic Implications: Oceanic Lizardite versus Subduction-Related Antigorite. Journal of Petrology, 51(1-2): 495-512.

Buttles, J. and Olson, P., 1998. A laboratory model of subduction zone anisotropy. Earth and Planetary Science Letters, 164: 245-262.

Cagnioncle, A.-M., Parmentier, E.M. and Elkins-Tanton, L.T., 2007. Effect of solid flow above a subducting slab on water distribution and melting at convergent plate boundaries Journal of geophysical Research, 112: B09402.

Coleman, P.J. and Kroenke, L.W., 1981. Subduction without volcanism in the Solomon Island arc. Geo-Marine Letters, 1: 129-134.

Connolly, J.A.D. and Podladchicov, Y.Y., 2007. Decompaction weackening and channelling instability in ductile porous media: Implications for asthenospheric melt segregation. Journal of Geophysical Research, 112: B10205.

Connolly, J.A.D. and Podladchikov, Y.Y., 1998. Compaction-driven fluid flow in viscoelastic rock. Geodinamica Acta, 11(2-3): 55-84.

Costa, F. and Chakraborty, S., 2008. The effect of water on Si and O diffusion rates in olivine and implications for transport properties and processes in the upper mantle Physics of the Earth and Planetary Interiors, 166: 11-29.

Crampin, S. and Booth, D.C., 1985. Shear-wave polarization near the Noth Anatolian fault, II, Interpretation in term ofs of vrack-induced anisotropy. Geophysical Journal of the Royal Astronomical Society, 83: 75-92.

Currie, C.A., Huismans, R.S. and Beaumont, C., 2008. Thinning of continental backarc lithosphere by flow-induced gravitational instability. Earth and Planetary Science Letters, 269: 436-447.

Davies, J.H. and Stevenson, D.J., 1992. Physical model of source region of subduction zone volcanics. J. Geophys. Res., 97: 2037-2070.

Demouchy, S., 2004. Water in the Earth's interior: Thermodynamics and kinetics of hydrogen incorporation in olivine and wadsleyite, Universität Bayreuth, Bayreuth, 165 pp.

Demouchy, S., Jacobsen, S.D., Gaillard, F. and Stern, C.R., 2006. Rapid magma ascent recorded by water diffusion profiles in mantle olivine. Geology, 34(6): 429-432.

Demouchy, S., Mackwell, S.J. and Kohlstedt , D.L., 2007. Influence of hydrogen on Fe–Mg interdiffusion in (Mg,Fe)O and implications for Earth's lower mantle. Contributions to Mineralogy and Petrology, 154: 279-289.

Drew, D.A., 1983. Mathematical modeling of two phase flow Annual Reviews of Fluid Mechanics, 15: 261-291.

Durham, W.B., Goetze, C. and Blake, B., 1977. Plastic-flow of oriented single-crystals of olivine. 2. Observations and interpretation of dislocation-structures Journal of geophysical Research, 82(36): 5755-5570.

Faccenda, M., Burlini, L., Gerya, T.V. and Mainprice, D., 2008. Fault-induced seismic anisotropy by hydration in subduction oceanic plates. Nature, 455: 1097-110.

Falus, G., Tommasi, A., Ingrin, J. and Szabo, C., 2008. Deformation and seismic anisotropy of the lithospheric mantle in the southeastern Carpathians inferred from the study of mantle xenoliths. Earth and Planetary Science Letters, 272: 50-64.

Forsyth, D. and Uyeda, S., 1975. On the relative importance of the driving forces of plate motion. Geophysical Journal of the Royal Astronomical Society, 43: 163-200.

Frost, H.J. and Ashby, M.F., 1982. deformation mechanism maps: the plasticity and creep of metals and ceramics. Pergamon Press, Oxford, UK.

Funiciello, F., Faccena, C., Giardini, D. and Regenauer-Lieb, K., 2003. Dynamics of retreating slabs: 2. Insights from three-dimensional laboratory experiments. Journal of Geophysical Research, 108: B4, 2207.

Garrido, C.J. and Bodinier, J.L., 1999. Diversity of mafic rocks in the Ronda peridotite: Evidence for pervasive melt-rock reaction during heating of subcontinental lithosphere by upwelling asthenosphere. Journal of Petrology, 40(5): 729-754.

Gerya, T.V. and Yuen, D.A., 2003. Rayleigh-Taylor instabilities from hydration and melting propel 'cold plumes' at subduction zones. Earth and Planetary Science Letters, 212(1-2): 47-62.

Grégoire, M. et al., 2007. Metasomatic interactions between slab-derived melts and depleted mantle: Insights from xenoliths within Monglo adakite (Luzon arc, Philippines). Lithos, 103(3-4): 415-430.

Gregoire, M., McInnes, B.I.A. and O'Reilly, S.Y., 2001. Hydrous metasomatism of oceanic sub-arc mantle, Lihir, Papua New Guinea - Part 2. Trace element characteristics of slab- derived fluids. Lithos, 59(3): 91-108.

Greve, S.M. and Savage, M.K., 2008. Strong vriations in seismic anisotropy across the Hikurangi subduction zone, North Island, New Zealand. Tectonophysics, 462: 7-21.

Greve, S.M. and Savage, M.K., 2009. Modelling seismic anisotropy variations across the Hikurangi subduction margin, New Zealand Earth and Planetary Science Letters, 285: 16-26.

Gribb, T.T. and Cooper, R.F., 1998. Low frequency shear attenuation in polycrystalline olivine: Grain boundary diffusion and the physical significance of the Andrade model for viscoelastic rheology. Journal of Geophysical Research, 103: 27267-27279.

Hack, A.C., Thompson, A.B. and Aerts, M., 2007. Phase relations involving hydrous silicate melts, aqueous fluid and minerals. In: A. Liebscher and C.A. Heinrich (Editors), Fluid-Fluid interactions. Reviews in Mineralogy and Geochemistry. Mineralogical Society of America, pp. 129-185.

Hall, C.E. and Parmentier, E.M., 2000. Spontaneous melt localization in a deforming solid with viscosity variations due to water weakening. Geophysical Research Letters, 27(1): 9-12.

Hammond, W.C. and Humphreys, E.D., 2000. Upper mantle seismic wave attenuation: ffect of realistic partial melt distribution. Journal of Geophysical Research, 105: 10,987-11,000.

Hess, H.H., 1964. Seismic anisotropy of the uppermost mantle under oceans. Nature, 203: 629-631.

Heuret, A., Lallemand, S., Funiciello, F., Piromallo, C. and Faccena, C., soumis. Characteristics of subduction-type seismogenic zones revisited. Geochemistry Geophysics Geosystems.

Hier-Majumder, S., Anderson, I.M. and Kohlstedt, D.L., 2004. Influence of Protons on Fe-Mg interdiffusion in olivine. Journal of geophysical Research, B2: B02202.

Hirth, G. and Kohlstedt, D.L., 1995a. Experimental Constraints on the Dynamics of the Partially Molten Upper-Mantle - Deformation in the Diffusion Creep Regime. Journal of Geophysical Research-Solid Earth, 100(B2): 1981-2001.

Hirth, G. and Kohlstedt, D.L., 1995b. Experimental constraints on the dynamics of the partially molten upper mantle 2. Deformation in the dislocation creep regime. Journal of Geophysical Research, 100(B8): 15,441-15,449.

Hirth, G. and Kohlstedt, D.L., 2003. Rheology of the upper mantle and the mantle wedge: A view from the experimentaliists, Inside the subduction factory. Geophysical Monograph. AGU.

Holtzman, B.K., Groebner, N.J., Zimmerman, M.E., Ginsberg, S.B. and Kohlstedt, D.L., 2003a. Stress-driven melt segregation in partially molten rocks. Geochemistry Geophysics Geosystems, 4: art. no.-8607.

Holtzman, B.K. and Kohlstedt, D.L., 2007. Stress-driven melt segregation and strain partitioning in partially molten rocks: Effects of stress and strain. Journal of Petrology, 48: 2379-2406.

Holtzman, B.K. et al., 2003b. Melt segregation and strain partitioning: Implications for seismic anisotropy and mantle flow. Science, 301(5637): 1227-1230.

Honda, S., Saito, M. and Nakakuki, T., 2002. Possible existence of small-scale convection under the back-arc Geophysical Research Letters, 29(21): 2043, doi:10.1029/2002GL015853.

Ionov, D.A., 2010. Petrology of Mantle Wedge Lithosphere: New Data on Supra-Subduction Zone Peridotite Xenoliths from the Andesitic Avacha Volcano, Kamchatka. Journal of Petrology, 51(1-2): 327-361.

Ionov, D.A., Bruegmann, G., Seitz, H.-M., Lahaye, Y. and Woodland, A.B., 2007. Peridotite xenoliths from the andesitic Avacha volcano, Kamchatka – any signatures of subduction metasomatism? Geochimica Et Cosmochimica Acta, 71(15 (S1)): A430. Abstr. 17th Goldschmidt Conf., Cologne.

Ishimaru, S., Arai, S., Ishida, Y., Shirasaka, M. and Okrugin, V., 2007. Melting and multi-stage metasomatism in the mantle wedge beneath a frontal arc inferred from highly

depleted peridotite xenoliths from the Avacha volcano, Southern Kamchatka. Journal of Petrology, 48(2): 395-433.
Jacobsen, S.D. et al., 2008. Effect of hydration on the elastic properties of olivine. Geophysical Research Letters, 35: L14303.
Jung, H. and Karato, S., 2001a. Water-induced fabric transitions in olivine. Science, 293(5534): 1460-1463.
Jung, H. and Karato, S.I., 2001b. Effects of water on dynamically recrystallized grain-size of olivine. Journal of Structural Geology, 23(9): 1337-1344.
Jung, H., Katayama, I., Jiang, Z., Hiraga, I. and Karato, S., 2006. Effect of water and stress on the lattice-preferred orientation of olivine. Tectonophysics, 421(1-2): 1-22.
Karato, S., 1989. Grain growth kinetics in olivine aggregates. Tectonophysics, 168: 255-273.
Karato, S., 2002. Mapping water content in the upper mantle. In: J. Eiler and G. Abers (Editors), The subduction factory.
Karato, S. and Jung, H., 1998. Water, partial melting and the origin of the seismic low velocity and high attenuation zone in the upper mantle. Earth and Planetary Science Letters, 157(3-4): 193-207.
Karato, S., Rubie, D.C. and Yan, H., 1993. Dislocation recovery in olivine under deep upper mantle conditions-Implications for creep and diffusion. Journal of geophysical Research, 20(5): 315-322.
Karato, S.-I., Jung, H., Katayama, I. and Skemer, P., 2008. Geodynamic significance of seismic anisotropy of the upper mantle: New insights from laboratory studies. Annual Reviews of Earth and Planetary Sciences, 36: 59-95.
Karato, S.I., Paterson, M.S. and Fitz Gerald, J.D., 1986. Rheology of Synthetic Olivine Aggregates - Influence of Grain-Size and Water. Journal of Geophysical Research-Solid Earth and Planets, 91(B8): 8151-8176.
Kawamoto, T., 2006. Hydrous phases and water transport in subduction slab. In: H. Keppler and J.R. Smyth (Editors), Water in nominally anhydrous minerals. Reviews in mineralogy & geochemistry. Geochemical Society & Mineralogical Society of America, Bayreuth Boulder, pp. 273-289.
Kawamoto, T. et al., 2004. Mg/Si ratio of aqueous fluids coexisting with forsterite and enstatite based on the phase relations in the Mg2SiO2-SiO2-H20 system. American Mineralogist, 89: 1433-1437.
Kelemen, P.B., Hirth, G., Shimizu, N., Spiegelman, M. and Dick, H.J.B., 1997. A review of melt migration processes in the adiabatically upwelling mantle beneath oceanic spreading ridges. Philosophical Transactions of the Royal Society of London Series a-Mathematical Physical and Engineering Sciences, 355(1723): 283-318.
Kelemen, P.B., Shimizu, N. and Salters, V.J.M., 1995. Extraction of Mid-Ocean-Ridge Basalt from the Upwelling Mantle by Focused Flow of Melt in Dunite Channels. Nature, 375(6534): 747-753.
Kendall, J.-M., 1994. Teleseismic arrivals at mid-ocean ridge: Effects of mantle melt and anisotropy. Geophysical Research Letters, 21: 301-304.
Kennedy, G.C., Heard, H.C., Wasserburg, G.J. and Newton, R.C., 1962. The upper 3 phases regin in system SiO2-H2O. American Journal of Science, 260: 501-521.
Keppler, H. and Bolfan-Casanova, N., 2006. Thermodynamics of water solubility and partitionning. In: H. Keppler and J.R. Smyth (Editors), Water in Nominally Anhydrous Minerals. Reviews in mineralogy & geochemistry. Geochemical society & Mineralogical society of America, Bayreuth-Boulder, pp. 193-230.
King, D.S.H., Zimmerman, M.E. and Kohlstedt , D.L., 2010. Stress-driven melt segregation in partially molten olivine-rich rocks deformed in torsion Journal of Petrology, 51: 21-42.

Kneller, E.A. and van Keken, P.E., 2008. The effects of three-dimensional slab geometry on deformation in the mantle wedge: implications for shear wave anisotropy. Geochemistry Geophysics Geosystems, 9: Q01003, doi:10.1029/2007GC001677.

Kohlstedt, D.L. and Holtzman, B.K., 2009. Shearing melt out of the Earth: An experimentalist's perspective on the influence of deformation on melt extraction. Annual Reviews of Earth and Planetary Sciences 37: 561-593.

Lallemand, S., 1999. La subduction océanique. Gordon and Breach, Newark, N.J.

Lassak, T.M., Fouch, M.J., Hall, C.E. and Kaminski, E., 2006. Seismic characterization of mantle flow in subduction systems: Can we resolve a hydrated mantle wedge. Earth and Planetary Science Letters, 243: 3-4.

Le Roux, V., Tommasi, A. and Vauchez, A., 2008. Feedback between melt percolation and deformation in an exhumed lithosphere–asthenosphere boundary. Earth and Planetary Science Letters, 274: 401-413.

Lenoir, X., Garrido, C.J., Bodinier, J.L., Dautria, J.M. and Gervilla, F., 2001. The recrystallization front of the Ronda peridotite: Evidence for melting and thermal erosion of subcontinental lithospheric mantle beneath the Alboran basin. Journal of Petrology, 42(1): 141-158.

Levin, V., Droznin, D., Park, J. and Gordeev, E., 2004. Detailled mapping of seismic anisotropy with local shear waves in southeastern Kamchatka. Geophysical Journal International, 158: 1009-1023.

Mackwell, S.J., Kohlstedt, D.L. and Paterson, M.S., 1985. The Role of Water in the Deformation of Olivine Single-Crystals. Journal of Geophysical Research-Solid Earth and Planets, 90(NB13): 1319-1333.

Mainprice, D. and Silver, P.G., 1993. Interpretation of SKS-waves using samples from the subcontinental lithosphere. Physics of the Earth and Planetary Interiors, 78: 257-280.

Mainprice, D., Tommasi, A., Couvy, H., Cordier, P. and Frost, D.J., 2005. Pressure sensitivity of olivine slip systems and seismic anisotropy of Earth's upper mantle. Nature, 433(7027): 731-733.

Mavko, G.M., 1980. Velocity and attenuation in partially molten rock. Journal of Geophysical Research, 85: 5412-5426.

McInnes, B.I.A., 1992. A glimpse of ephemeral subduction zone processes from Simberi island, Papua New Guinea, University of Ottawa, 235 pp.

McInnes, B.I.A., Gregoire, M., Binns, R.A., Herzig, P.M. and Hannington, M.D., 2001. Hydrous metasomatism of oceanic sub-arc mantle, Lihir, Papua New Guinea: petrology and geochemistry of fluid-metasomatised mantle wedge xenoliths. Earth and Planetary Science Letters, 188(1-2): 169-183.

McKenzie, D., 1984. The generation and compaction of partially molten rocks. Journal of Petrology, 25: 713-765.

Mei, S., Bai, W., Hiraga, T. and Kohlstedt, D.L., 2002. Influence of melt on the creep behavior of olivine-basalt aggregates under hydrous conditions. Earth and Planetary Science Letters, 201(3-4): 491-507.

Mei, S. and Kohlstedt, D.L., 2000a. Influence of water on plastic deformation of olivine aggregates 1. Diffusion creep regime. Journal of Geophysical Research-Solid Earth, 105(B9): 21457-21469.

Mei, S. and Kohlstedt, D.L., 2000b. Influence of water on plastic deformation of olivine aggregates 2. Dislocation creep regime. Journal of Geophysical Research-Solid Earth, 105(B9): 21471-21481.

Mibe, K., Fujii, T. and Yasuda, A., 1998. Connectivity of aqueous fluids in Earth's upper mantle. Geophysical Research Letters, 25: 1233-1236.

Mibe, K., Fujii, T. and Yasuda, A., 1999. Control of the location of the volcanic front in island arcs by aqueous fluid connectivity in the mantle wedge. Nature, 401(6750): 259-262.
Mizukami, T., Wallis, S.R. and Yamamoto, J., 2004. Naturals examples of olivine lattice preferred orientation patterns with a flow-normal a-axis maximum. Nature, 427: 432-436.
Nakamura, Y. and Kushiro, I., 1974. Composition of the gase phase in Mg2SiO4-SiO2-H2O at 15 kbar, carnegie Institution of Washington year Book, pp. 255-258.
Nicolas, A., 1986. A Melt Extraction Model Based on Structural Studies in Mantle Peridotites. Journal of Petrology, 27(4): 999-1022.
Nicolas, A. and Christensen, N.I., 1987. Formation of anisotropy in upper mantle peridotites - A review. In: K. Fuchs and C. Froidevaux (Editors), Composition, structure and dynamics of the lithosphere-asthenosphere system. Am. Geophys. Un., Washington, D.C., pp. 111-123.
O'Connell, R.J. and Budianski, B., 1974. Seismic velocities in dry and saturated craked solids. Journal of Geophysical Research, 79: 5412-5426.
O'Neill, H.S., 1987. Free energy of formation of NiO, CoO, Ni2SiO4, Co2SiO4. American Mineralogist, 72: 280-291.
Paterson, M.S., 1970. A high pressure high temperature apparatus for rock deformation. International Journal of Rock Mecanics and Mining since: 517-526.
Paterson, M.S., 1990. Rock deformation experimentation. In: A.D.e.al. (Editor), The brittle-ductile transition in rocks: The head volume. AGU, Washington, D.C., pp. 187-194.
Peslier, A. and Luhr, J., 2006. Hydrogen loss from olivines in mantle xenoliths from Simcoe (USA) and Mexico: Mafic alkalic magma ascent rates and water budget of the sub-continental lithosphere. Earth and Planetary Science Letters, 242(3-4): 302-319.
Peyton, V. et al., 2001. Mantle Flow at a Slab Edge: Seismic Anisotropy in the Kamchatka Region. Geophysical Research Letters, 28(2): 379-382.
Pitzer, K.S. and Sterner, S.M., 1994. Equation of state valid continuously from zero to extrem pressure for H2O and CO2. Journal of Chemical Physics, 101: 3111-3116.
Poli, S. and Schmidt, M.W., 2002. Petrology of subducted slabs. Annual Review of Earth and Planetary Sciences, 30: 207-235.
Presnall, D.C., 1995. Phase diagrams of Earth-forming minerals In: T.J. Arhens (Editor), Mineral Physics and Crystallography: A Handbook of Physical Constants. American Geophysical Union, Washington, pp. 248-268.
Ribe, N.M., 1986. Melt segregation driven by dynamic forcing. Geophysical Research Letters 13: 1462-1465.
Richter, F.M. and McKenzie, D., 1984. Dynamical model for melt segregation from a deformable rock matrix. Journal of Geology, 92: 729-740.
Riley, G.N.J. and Kohlstedt, D.L., 1990. An experimental study of melt migration in an olivine-melt system. In: M.P. Ryan (Editor), Magma Transport and Storage. John Wiley & Sons, New York, pp. 77-86.
Ryabchikov, I.D., Schreyer, W. and Abraham, K., 1982. Composition of aqueous fluid in equilibrium with pyroxenes and olivines at mantle pressure and temperature. Contribution to Mineralogy and Petrology, 79: 80-84.
Rytuba, J.J., McKee, E.H. and Cox, D., 1993. Geochronology and geochemistry of the Ladolam gold deposit, Lihir island, and gold deposits and volcanoes of Tabar and Tatau, Papua New Guinea. US Geological Survey Bulletin, 2039: 119-126.
Sato, H., Sacks, T. and Murase, G., 1989. The use of laboratory velocity data for estimating temperature and partial melt fraction in the low velocity zone: Comparisaon with heat

flow data and elecrtrical conductivity studies. Journal of Geophysical Research, 94: 5689-5704.
Scambelluri, M., Hermann, J., Morten, L. and Rampone, E., 2006. Melt- versus fluid-induced metasomatism in spinel to garnet wedge peridotites (Ulten zone, eastern Italian Alps): clues from trace element and Li abundance. Contribution to Mineralogy and Petrology, 151: 372-394.
Schellart, W.P., 2004. Quantifying the net slab pull force as a driving mechanism of plate tectonics. Geophysical Research Letters, 31: L07611.
Schmeling, H., 1985. Numerical models on the influence of partial melt on elastic, anelastic and electric properties of rocks. PartI: elasticity and anelasticity. Physics of the Earth and Planetary Interiors, 41: 34-57.
Silver, P.G. and Chan, W.W., 1988. Implications for continental structure and evolution from seismic anisotropy. Nature, 335: 34-39.
Skemer, P., Katayama, I. and Karato, S.I., 2006. Deformation fabrics of the Cima di Gagnone peridotite massif, Central Alps, Switzerland: evidence of deformation at low temperature in presence of water. Contribution to Mineralogy and Petrology, 152(1): 43-51.
Sleep, N.H., 1988. Trapping of melt by veins and dykes. Journal of Geophysical Research, 93: 10255-10272.
Smyth, J.R., 1974. Experimental study on the polymorphism of entatite. American Mineralogist, 59: 345-352.
Sobolev, S.V. et al., 1996. Upper mantle temperatures from teleseismic tomography of French Massif Central including effects of composition, mineral reactions, anharmonicity, anelasticity and partial melt. Earth and Planetary Science Letters, 139(1-2): 147-163.
Soustelle, V. and Tommasi, A., 2010. Seismic properties of the supra-subduction mantle: Constraints from peridotite xenoliths from the Avacha volcano, southern Kamchatka. Geophysical Research Letters 37: L13307.
Soustelle, V., Tommasi, A., Bodinier, J.-L., Garrido, C.J. and Vauchez, A., 2009. Deformation and reactive melt transport in the mantle lithosphere above a large-scale partial melting domain: the Ronda peridotite massif, S Spain. Journal of Petrology, 50(7): 1235-1266.
Soustelle, V., Tommasi, A., Demouchy, S. and Ionov, D.A., 2010. Deformation and Fluid-Rock Interaction in the Supra-subduction Mantle: Microstructures and Water Contents in Peridotite Xenoliths from the Avacha Volcano, Kamchatka. Journal of Petrology, 51(1-2): 363-394.
Spence, D.A., Sharp, P. and Turcotte, D.L., 1987. Buoyancy-driven crack propagation: a mechanism for magma migration. Journal of Fluid Mechanic, 174: 135-153.
Spence, D.A. and Turcotte, D.L., 1985. Magma-driven propagation of cracks. Journal of Geophysical Research, 90: 575-580.
Spiegelman, M., 1993. Physics of melt extraction: Theory, implications and applications. Phil. Trans. Roy. Soc. London A, 342: 23-41.
Stern, R.J., 2002. Subduction zones. Reviews of Geophysics, 40(4): art. no.-1012.
Stevenson, D.J., 1989. Spontaneous small-scale melt segregation in partial melts undergoing deformation. Geophysical Research Letter, 16: 1067-1070.
Sundberg, M. and Cooper, R.F., 2008. Crystallographic preferred orientation produced by diffusional creep of harzburgite: Efects of chemical interactions among phases during plastic flow. Journal of Geophysical Research, 113: B12208.
Takei, Y., 1998. Constitutive mechanical relations of solid-liquid composites in terms of grain-boundary continuity. Journal of Geophysical Research, 103: 10,183-10,204.

Takei, Y., 2000. Accoustic properties of partially molten media studied o a simple binary system with a controlable dihedral angle. Journal of Geophysical Research, 103: 16,665-16,682.

Tasaka, M., Michibayashi, K. and Mainprice, D., 2008. B-type olivine fabrics developed in the fore-arc side of the mantle wedge along a subducting slab. Earth and Planetary Science Letters, 272(3-4): 747-757.

Tommasi, A., Tikoff, B. and Vauchez, A., 1999. Upper mantle tectonics: three-dimensional deformation, olivine crystallographic fabrics and seismic properties. Earth and Planetary Science Letters, 168(1-2): 173-186.

Tommasi, A., Vauchez, A., Godard, M. and Belley, F., 2006. Deformation and melt transport in a highly depleted peridotite massif from the Canadian Cordillera: Implications to seismic anisotropy above subduction zones Earth and Planetary Science Letters, 252: 245-259.

Tommasi, A., Vauchez, A. and Ionov, D.A., 2008. Deformation, static recrystallization, and reactive melt transport in shallow subcontinental mantle xenoliths (Tok Cenozoic volcanic field, SE Siberia). Earth and Planetary Science Letters, 272: 65-77.

Van der Wal, D. and Bodinier, J.L., 1996. Origin of the recrystallisation front in the Ronda peridotite by km-scale pervasive porous melt flow. Contributions to Mineralogy and Petrology, 122(4): 387-405.

Van der Wal, D. and Vissers, R.L.M., 1996. Structural petrology of the Ronda peridotite, SW Spain: Deformation history. Journal of Petrology, 37(1): 23-43.

Vauchez, A. and Garrido, C.J., 2001. Seismic properties of an asthenospherized lithospheric mantle: constraints from lattice preferred orientations in peridotite from the Ronda massif. Earth and Planetary Science Letters, 192(2): 235-249.

Wadati, K., 1928. Shallow and deep earthquakes. Geophysical Magazine, 1: 162-202.

Wadati, K., 1935. On the activity of deep-focus earthquakes in the Japan Islands and neighbourhoods. Geophysical Magazine, 8: 305-325.

Wagner, L.S., Beck, S. and Zandt, G., 2005. Upper mantle structure in the south central Chilean subduction zone (30° to 36°S). Journal of geophysical Research, 110: B01308.

Wagner, L.S., Beck, S., Zandt, G. and Ducea, M.N., 2006. Depleted lithosphere, cold, trapped asthenosphere, and frozen melt puddles above the flat slab in central Chile and Argentina. Earth and Planetary Science Letters, 245: 289-301.

Watson, B., E., Brenan, J., M. and Baker, D., R., 1990. Distribution of fluids in the continental mantle. In: M.A. Menzies (Editor), Continental Mantle. Clarendon Press, Oxford, pp. 111-125.

Weertman, J., 1971. Theory of water-filled crevasses in glaciers to the vertical magma transport beneath ocean ridges Journal of Geophysical Research, 76: 1171-1183.

Yoder, H.S. and Tilley, C.E., 1962. Origin of basalt magmas: an experimental study of natural and synthetic rock systems. Journal of Petrology, 3: 342-532.

Zhang, H. et al., 2004. High-resolution subducting-slab structure beneath nothern Honshu, Japan, revealed by double-difference tomography. Geology, 32(4): 361-364.

Zhang, S., Karato, S.-I., Fitz Gerald, J., Faul, U.H. and Zhou, Y., 2000. Simple shear deformation of olivine aggregates Tectonophysics, 316: 133-152.

Zimmerman, M.E. and Kohlstedt, D.L., 2004. Rheological Properties of Partially Molten Lherzolite Journal of Petrology, 45(2): 275-298.